

Journal of Mechanics of Materials and Structures

Volume 14, No. 3

May 2019



JOURNAL OF MECHANICS OF MATERIALS AND STRUCTURES

msp.org/jomms

Founded by Charles R. Steele and Marie-Louise Steele

EDITORIAL BOARD

ADAIR R. AGUIAR	University of São Paulo at São Carlos, Brazil
KATIA BERTOLDI	Harvard University, USA
DAVIDE BIGONI	University of Trento, Italy
MAENGHYO CHO	Seoul National University, Korea
HUILING DUAN	Beijing University
YIBIN FU	Keele University, UK
IWONA JASIUK	University of Illinois at Urbana-Champaign, USA
DENNIS KOCHMANN	ETH Zurich
MITSUTOSHI KURODA	Yamagata University, Japan
CHEE W. LIM	City University of Hong Kong
ZISHUN LIU	Xi'an Jiaotong University, China
THOMAS J. PENCE	Michigan State University, USA
GIANNI ROYER-CARFAGNI	Università degli studi di Parma, Italy
DAVID STEIGMANN	University of California at Berkeley, USA
PAUL STEINMANN	Friedrich-Alexander-Universität Erlangen-Nürnberg, Germany
KENJIRO TERADA	Tohoku University, Japan

ADVISORY BOARD

J. P. CARTER	University of Sydney, Australia
D. H. HODGES	Georgia Institute of Technology, USA
J. HUTCHINSON	Harvard University, USA
D. PAMPLONA	Universidade Católica do Rio de Janeiro, Brazil
M. B. RUBIN	Technion, Haifa, Israel

PRODUCTION production@msp.org

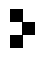
SILVIO LEVY Scientific Editor

See msp.org/jomms for submission guidelines.

JoMMS (ISSN 1559-3959) at Mathematical Sciences Publishers, 798 Evans Hall #6840, c/o University of California, Berkeley, CA 94720-3840, is published in 10 issues a year. The subscription price for 2019 is US \$635/year for the electronic version, and \$795/year (+\$60, if shipping outside the US) for print and electronic. Subscriptions, requests for back issues, and changes of address should be sent to MSP.

JoMMS peer-review and production is managed by EditFLOW® from Mathematical Sciences Publishers.

PUBLISHED BY

 **mathematical sciences publishers**
nonprofit scientific publishing

<http://msp.org/>

© 2019 Mathematical Sciences Publishers

EXPERIMENTAL AND NUMERICAL ENERGY ABSORPTION STUDY OF ALUMINUM HONEYCOMB STRUCTURE FILLED WITH GRADED AND NONGRADED POLYURETHANE FOAM UNDER IN-PLANE AND OUT-OF-PLANE LOADING

ALIREZA MOLAIEE AND SEYED ALI GALEHDARI

This study aims to investigate the effect of honeycomb structure filled with graded and nongraded polyurethane foam on reaction force during energy absorption under in-plane and out-of-plane loadings. Three types of aluminum AL5052 honeycomb structures without filling, with graded filling and with nongraded filling were manufactured and subjected to quasistatic compression loading. In order to investigate the effect of reaction force and energy absorption capacity, honeycomb cores with different densities were selected. Afterward, the behavior of honeycomb structures was numerically simulated in the ABAQUS software. The results of finite element analysis show that using foam filling in honeycomb structures increases energy absorption. The structures filled with graded foam, shows better performance with the rate of stiffness reduction from impact location compared to those filled with nongraded foam. Energy absorption for graded foam structure occurs at a longer time period comparing to nongraded one. The energy absorption capacity of the structure under out-of-plane loading is much higher than in-plane loading, but its reaction force is very high. The results of empirical tests are greatly similar to that of numerical studies. Therefore, it is possible to use simulation in ABAQUS environment for solving more complex problems.

A list of symbols can be found on page 321.

1. Introduction

In the recent years according to the importance of energy absorption in different industries, impact absorbers, especially honeycomb structures have gained increased attention. Inspired from natural structures, it is possible to create optimized structures with higher energy absorption capabilities. Human and bird bone structures are among the most efficient natural impact absorbers. In bones, sponge-like structure leads to impact absorption and the damage lessening to joints [Koch 1917]. Another natural example of impact absorption is the banana structure and its peel which protects the soft core of the fruit from outside forces [Ali et al. 2008]. Due to the high strength to weight ratio and high energy absorption up to 70% of the initial height, honeycomb structures have gained increased importance in various industries, especially in the aerospace industry [Bitzer 1997]. Various structures and materials are used to manufacture honeycomb structures. The most common honeycomb structures are hexagonal structures made from aluminum and filled polymer foams. Polymer foams are among the cheapest materials and have characteristics such as heat resistance, waterproofing and soundproofing and are also cost-efficient.

Keywords: honeycomb structure, energy absorption, in-plane loading, out-of-plane loading, graded foam, ABAQUS, experimental test.

Some of the recent studies have investigated the mechanical properties of polymer foams. Various types of polymer foams have been investigated but polyurethane foams are less frequently used. Deshpande and Fleck [2001] investigated the behaviors of two types of PVC (polyvinyl chloride) foams for a wide range of tensile and compression strains. Seo et al. [2004] studied the effects of compression on small packages of hard polyurethane and polystyrene foams. They investigated foam characteristics at different densities using compression test and calculated stress-strain charts, Young modulus and Poisson coefficient of foams based on their density.

Some studies have investigated the filling of honeycomb structures with polymer foams. Akay and Hanna [1990] studied the behaviors of honeycomb structures and sandwich panels filled with foam using force-bending equipment and scanned foam samples using ultrasonic waves. Hanssen et al. [2000] created a program made from 96 tests for axial deformation and investigated the effects of foam density on energy absorption of structures with thin walls filled with aluminum foam. Suvorov and Dvorak [2005] investigated general deformation of sandwich structures under average impact speeds of 10 m/s and 20 m/s caused by the impact between boat and docks. They selected carbon-vinyl ester plates and used foam nucleus made from PVC H100 and flexible polyurethane foam between carbon-vinyl ester plates. They concluded that energy absorption is directly related to distance and initial velocity of a projectile. Song et al. [2010] investigated the dynamic compression behavior of three-dimensional foam structures with Voroni geometry using finite element analysis and empirical tests. They also investigated the effects of irregularities in cell structure, impact loading, relative compression and hardness strain on deformation of the structure. Galehdari et al. [2015] proposed an analytical equation for plateau stress using exponential hardening model in honeycomb structures. They also extracted the equation for specific energy absorption of honeycomb structures using locking strain and strain energy. In order to validate these equations, they simulated five different aluminum types with exponential hardening model in ABAQUS software. They also carried out an impact test on a graded honeycomb structure in order to validate the results of the numerical analysis. A comparison showed a good agreement between their numerical and empirical results. Also, Galehdari and Khodarahmi [2016] designed a graded honeycomb structure for shock absorption in helicopter seats during a crash-landing. They simulated this structure in ABAQUS environment. Alavi Nia and Sadeghi [2010] carried out an empirical study for investigating the response of empty and filled honeycomb structures under quasistatic loadings. They used five different empty and foam-filled honeycomb structures made from Al-5052-H39 alloy and concluded that use of foam filling can increase energy absorption up to 300%. Zarei Mahmoudabadi and Sadighi [2011] carried out an empirical investigation about the effect of filling honeycomb structures with polyurethane under out-of-plane conditions. They reported that increasing loading speed from quasistatic to dynamic increases stress level in the stress-strain chart of both empty and foam-filled honeycomb structures while filling under out-of-plane conditions has no significant effects on energy absorption. Mozafari et al. [2016] investigated foam-filled honeycomb sandwich panels under in-plane impact loading and analysed them by numerical methods. They used three different aluminum honeycombs filled with three different polyurethane foam and studied their energy absorption capacity by quasistatic compression test. Ebrahimi et al. [2018] have studied the energy absorption characterization of functionally graded foam (FGF) filled tubes under axial loading experimentally. The FGF tubes are filled axially by gradient layers of polyurethane foams of different densities. Finally, the results of experimental test show that an FGF filled tube has excellent energy absorption capacity compared to the ordinary uniform foam-filled with

the same weight. Shahravi et al. [2019] have designed a polyurethane foam-filled thin-walled aluminum grooved circular tubes. The tubes are shaped with the inner and the outer circular grooves at different positions along the axis. They investigated the effects of the grooves distance, tube diameter, grooves depth, foam density, and tube thickness on the crashworthiness parameters of grooved circular tubes. Also, Yu et al. [2018] studied static axial crushing and energy absorption of density-graded aluminum foam-filled square metal columns experimentally and theoretically. It was shown that the density-graded aluminum foam-filled square metal column is a novel topological structure with higher energy absorption, higher load-carrying capacity and much higher crushing force efficiency.

Regarding the above-mentioned researches, except for tubes, the graded foam has not been used in honeycomb structures under in-plane or out-of-plane loading in honeycomb energy absorbers. The current study aims to investigate aluminum honeycomb structures filled with graded and nongraded polyurethane foams.

2. Problem definition

Honeycomb structures have better performance when they are subjected to out-of-plane loading direction. In some cases, such as impact absorbers for protecting an occupant against the crash, impacts might occur from in-plane direction. Therefore, it is important to investigate the behavior of honeycomb structures for in-plane loading. Two types of loading are shown in Figure 1.

The utilized honeycomb structure is made from 16 separate rows with 10 cells in each row. The dimensions of the aluminum honeycomb structure are determined based on the MIL-C-7438G standard (Table 1).

The polyurethane is a closed-cell material created from isocyanate and polyol. This foam has different densities depending on the ratio of isocyanate and polyol which are mixed together under pressure and heat. The mixture then shows a volume increase of 20 to 30 times in a few seconds creating a compact, uniform foam structure with any desirable thickness (Figure 2, left).

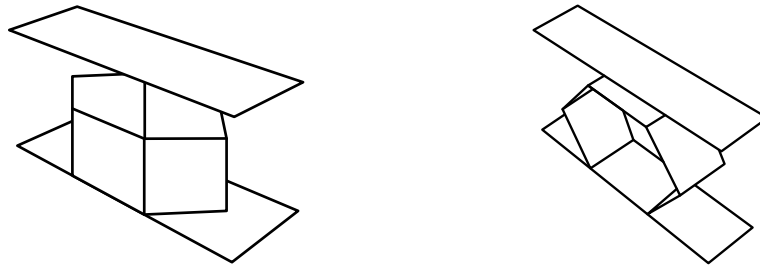


Figure 1. Loading conditions: out-of-plane (left) and in-plane (right).

Foil thickness (mm)	Cell size (mm)	Height (mm)	Width (mm)	Length (mm)
0.018	3.175	12.7	50	50

Table 1. Aluminum honeycomb structure dimensions.

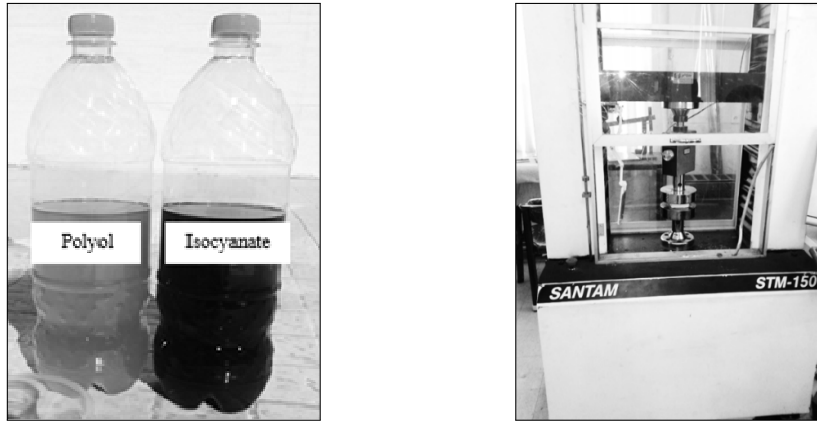


Figure 2. Left: polyol and isocyanate combined for the production of polyurethane foam. Right: Santam test machine.

Polyol weight (g)	Isocyanate weight (g)	Polyol to isocyanate weight composition ratio	Density (kg/m ³)
11	11	1	70
9	13	0.69	80
7	14	0.5	90
5	15	0.33	100

Table 2. The weight of ingredients combined with polyurethane foam.

In order to determine the mechanical behavior of foams used to fill the structures, these foams were subjected to compression test. The Santam (STM-150) equipment was used for compression test of polyurethane foams (Figure 2, right).

To this end, foams were cut with dimensions of 24.5 mm × 70 mm × 70 mm in accordance with the ASTM C365 standard. The polyol and isocyanate parts were mixed with ratios presented in Table 2 to produce foam with densities of 70 kg/m³, 80 kg/m³, 90 kg/m³ and 100 kg/m³. The density of the foam increases with increase in the ratio of isocyanate to polyol. For example, a ratio of 1 : 1 (isocyanate : polyol) has a density of 70 kg/m³ while a ratio of 2 : 1 has a density of 90 kg/m³ and a ratio of 3 : 1 leads to a density of 100 kg/m³.

3. Numerical simulation

In order to investigate the energy absorption of different honeycomb structures, a finite element simulation was performed in ABAQUS software. The rows in the structure are made from Al 5052-O alloy with a density of 2680 kg/m³, elasticity modulus of 70.3 GPa and the Poisson ratio of 0.33. Mechanical properties of Al 5052-O alloy are determined using the ASTM B209M standard in which yield and ultimate strength are equal to 65 MPa and (170~215) MPa respectively. A finite element model of the structure under in-plane loading is shown in Figure 3.

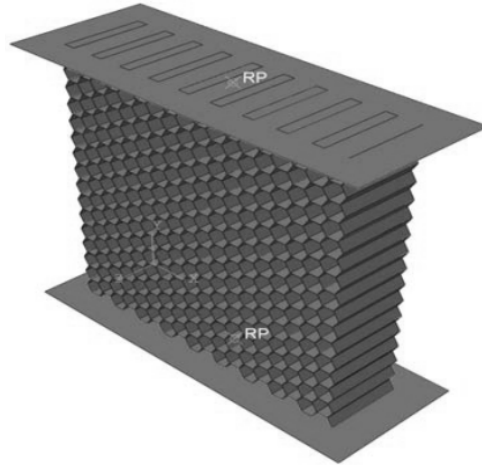


Figure 3. Finite element model of the structure under in-plane loading.

Movement is applied through a rigid plate placed above the honeycomb structure. This structure is attached to another rigid plate on the bottom side. The force is applied at the reference point of the rigid plate and all degrees of freedom of this plate except in moving direction are the constraint. All degrees of freedom of the lower rigid plate are also fixed. A four-node shell S4R element was used for meshing of honeycomb structure while two-line, four-node R3D4 element was used for meshing of the above and below rigid plate plates. For the S4R element, shear strain is assumed to be constant along the thickness. Since the structure has regular geometry and is made from thin metal sheets, a four-node shell element is used. Kinematic and penalty surfaces to surface interaction were used for contact between the upper plate and lower one and the structure, respectively.

In order to investigate the effects of filling honeycomb structure with foam, light-weight polyurethane foam was used as the filling phase. Material properties including density, elastic behavior, and crushable foam were defined in the material properties module. Foam with a density of 100 kg/m^3 , elasticity modulus of 10.1 MPa and Poisson coefficient of zero was selected as nongraded foam. To model the foam crushable in ABAQUS environment, h and ν_p parameters must be defined. The first parameter, h , is the ratio of initial Mises to initial hydrostatic compression while the second parameter, ν_p , is the plastic Poisson coefficient. The final value of the compression yield stress ratio was equal to 1 while the plastic Poisson's ratio was 0. The assumption of full adhesion was used for determining the contact between foam and honeycomb structure. A linear, six-node C3D8R element was used for meshing of foams.

In order to investigate the structures with graded foams, different foam densities with properties shown in Table 2 were used. The order of graded foam in the structure is shown in Figure 4.

For out-of-plane loading on the aluminum honeycomb structure, the in-plane model was rotated for 90 degrees (Figure 5).

4. Experimental tests

In order to carry out an empirical investigation on the behavior of honeycomb structures, some test specimens were prepared for each of the five models. Al-5052-O aluminum honeycomb sample was

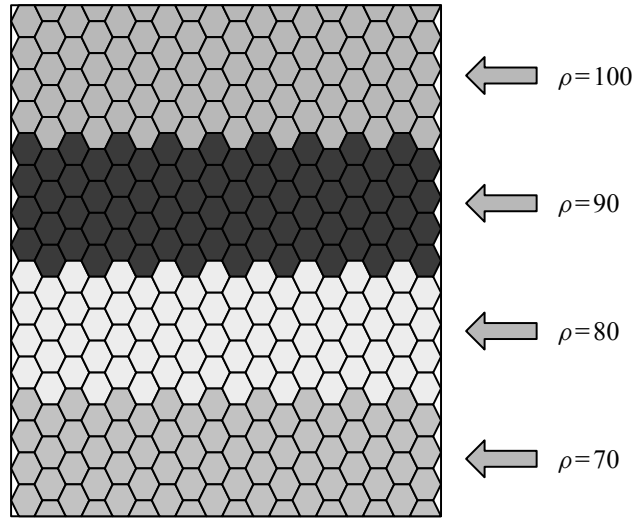


Figure 4. Graded foam arrangement order.

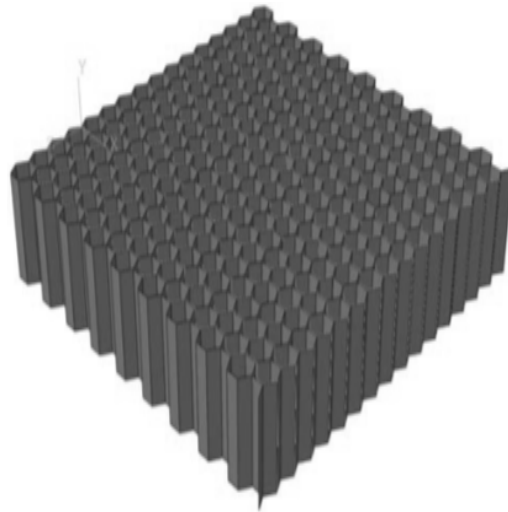


Figure 5. Out-of-plane loading on honeycomb structure model.

purchased from Hexcel Co. with dimensions of 50 mm × 50 mm (specifications are shown in Table 1). Then, this structure was used to prepare three types of structures without foam (empty structures), a structure filled with nongraded foam and a structure filled with graded foam. Names of test specimen which are subjected under quasistatic loadings are listed in Table 3.

The test specimens were subjected to compression test with the loading rate 2 mm/min using Santam machine.

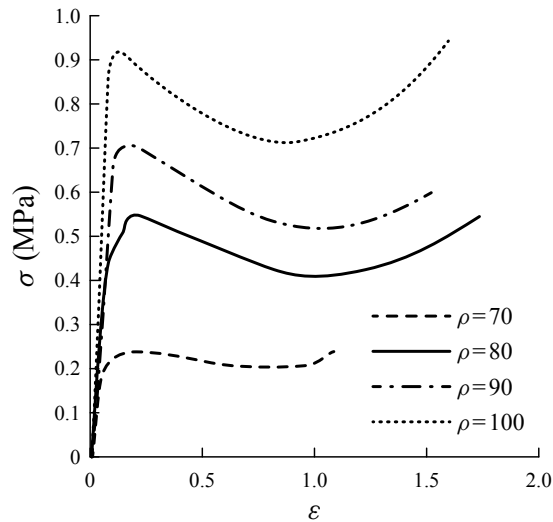
Loading type	Sample type	Sample name
In-plane	Without foam	H-NF-I-S
	With nongraded foam	H-FN-I-S
	With graded foam	H-FG-I-S
Out-of-plane	Without foam	H-NF-O-S
	With nongraded foam	H-FN-O-S

Table 3. Names of the test specimen.

5. Results and discussion

The stress-strain graph of polyurethane foams resulted from compression tests for different densities is shown in Figure 6. Based on the compression test results, mechanical properties of polyurethane foam are presented in Table 4.

5.1. Numerical results. Numerical analyses were carried out using Dynamic/Explicit solver and results were presented in various graphs. One of the important parameters in energy absorbers is the magnitude

**Figure 6.** Stress-strain graph of polyurethane foam for different densities.

Elasticity Module, E (MPa)	Yield Stress, σ_y (MPa)	Density, ρ (kg/m ³)
3.3	0.21	70
5.1	0.5	80
5.5	0.7	90
10.1	0.9	100

Table 4. Mechanical mechanical properties of the polyurethane foam.

of the structure's reaction force, as well as magnitude and duration of energy absorption. A suitable absorber needs to absorb the maximum amount of energy during the highest possible time with the minimum reaction force. Kinetic energy applied to the structure is transformed into its internal energy which is the sum of strain energy and plastic deformation energy. In order to achieve more accurate numerical results, mesh dependency is checked for all numerical simulations. As a sample, the load-displacement graph of nongraded foam filled honeycomb structure under in-plane quasistatic loading for different element sizes is shown in Figure 7.

According to Figure 7, the results have proper convergence for three sizes of element. So, 0.003 m element size is selected for numerical analysis. The displacement contours for in-plane quasi-loading of different structures are shown in Figure 8.

The deformation pattern of all three structures is X-mode. However, the X-mode deformation is wider for empty structure and its center is located at the structure's center of mass. However, in the nongraded foam-filled structure, the center of X is located higher than the structure's center and is again further

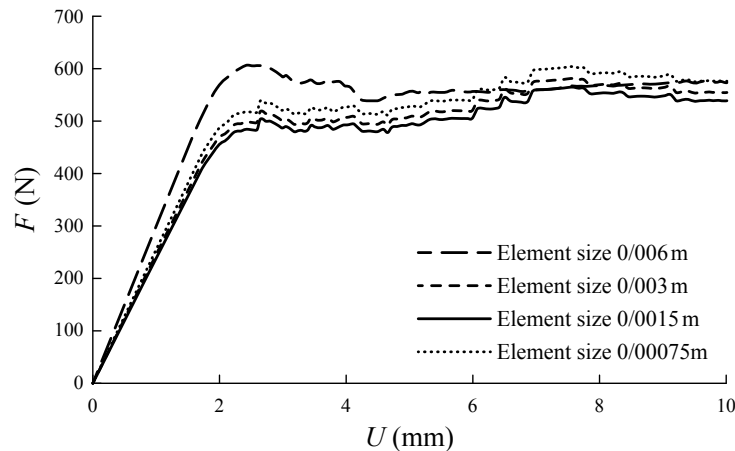


Figure 7. Load-displacement graph of nongraded foam-filled honeycomb structure under in-plane quasistatic loading for different element sizes.

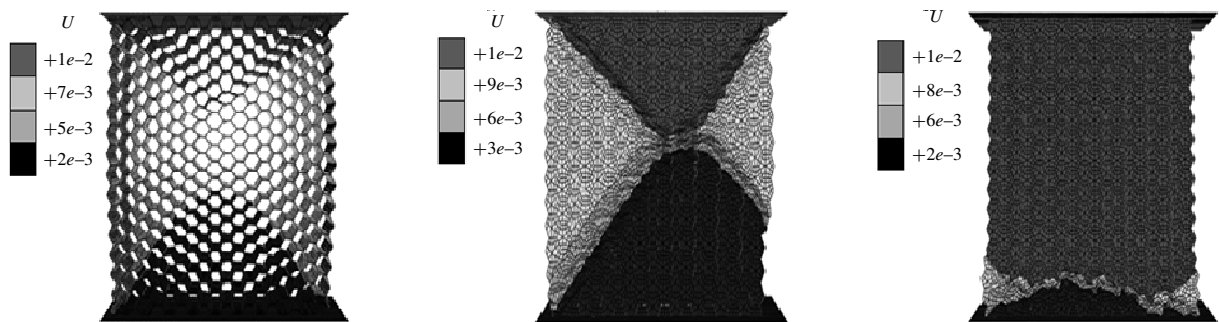


Figure 8. Structure's deformation contour for in-plane quasistatic loading for without foam (left), nongraded foam (middle) and graded foam models (right).

away from the structure's center in graded foam-filled structure. Deformation contours acquired from the out-of-plane quasistatic simulation for both structures are presented in Figure 9.

The results of numerical simulation for five models (Table 3) under quasistatic static loads are shown in different graphs. In these graphs, the reaction on force is measured at the lower plate and displacement is measured at the upper plate. The force-displacement graph for in-plane quasistatic simulation is presented in Figure 10 (left).

For in-plane quasistatic loadings of the empty structure, force increases in a smooth pattern while this increase in the nongraded foam-filled structure is irregular and step by step and shows a larger increase. On the other hand, this increase in the graded foam-filled structure shows smaller variations. In quasistatic, in-plane loading, the behaviors of all three structures are close to one another but the foam-filled structures absorb more energy and have a higher reaction force. The area under the graph for the graded foam-filled structure is also lower than nongraded structure. Force-displacement graph for quasistatic simulation in out-of-plane conditions is shown in Figure 10 (right).

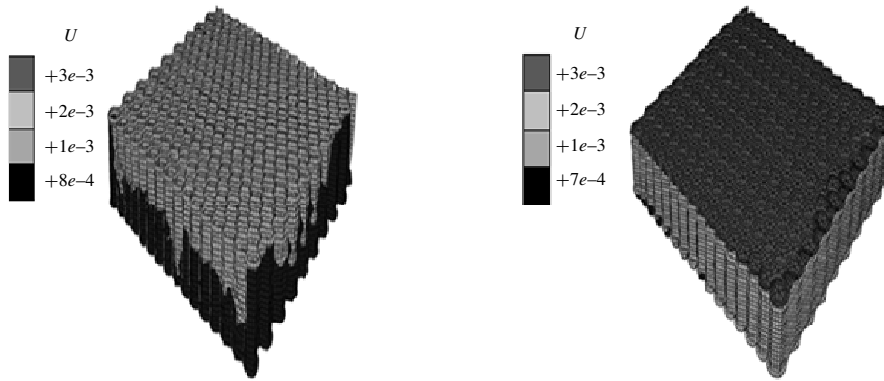


Figure 9. Structure's deformation contour for out-of-plane quasistatic loading for without foam (left) and nongraded foam models (right).

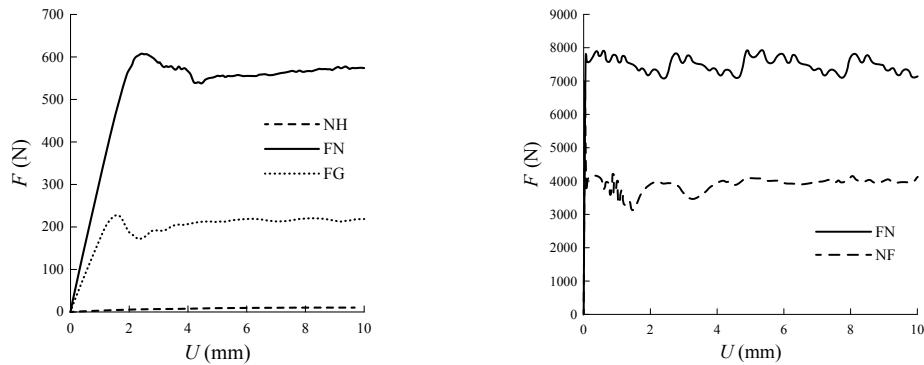


Figure 10. Left: the in-plane quasistatic reaction force-displacement graph. Right: the out-of-plane quasistatic force-displacement graph.

For out-of-plane quasistatic loading, the empty structure shows a sudden increase in force and small oscillations at the end. The nongraded foam-filled structure also shows a sudden increase in force but experiences larger oscillations at the end. For this case, behaviors of both structures are close to one another but the foam-filled structure causes higher reaction forces.

5.2. Experimental results. The final deformation modes of three structures for in-plane quasistatic tests are shown in Figure 11.

The empty structure shows X-shaped deformation mode under in-plane quasistatic loads while the nongraded foam-filled structure shows uniform deformation and the graded foam-filled structure has only expanded on the lower side which shows a distribution of lower force toward the lower surface. This can be one of the advantages of this structure. The final deformation modes of structures for out-of-plane quasistatic tests are shown in Figure 12.

It can be seen that empty structure has wrinkled under out-of-plane loadings while the nongraded foam-filled structure shows uniform deformation. Force-displacement graph of in-plane quasistatic test for different structures is presented in Figure 13 (left).

The applied force in quasistatic loading for empty structure increases irregularly and step by step. This increase in the nongraded foam-filled structure is around 36 times higher and shows a harmonic increase but with a sharp slope. In graded form-filled structure, this value is almost half of nongraded structure



Figure 11. Final deformation modes of three structures for in-plane quasistatic tests for without foam (left), nongraded graded foam (middle) and graded foam models (right).

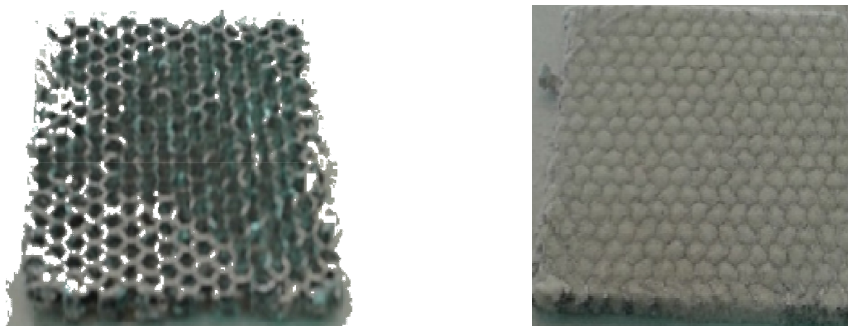


Figure 12. Final deformation modes of structures for out-of-plane quasistatic tests for without foam (left) and nongraded foam models (right).

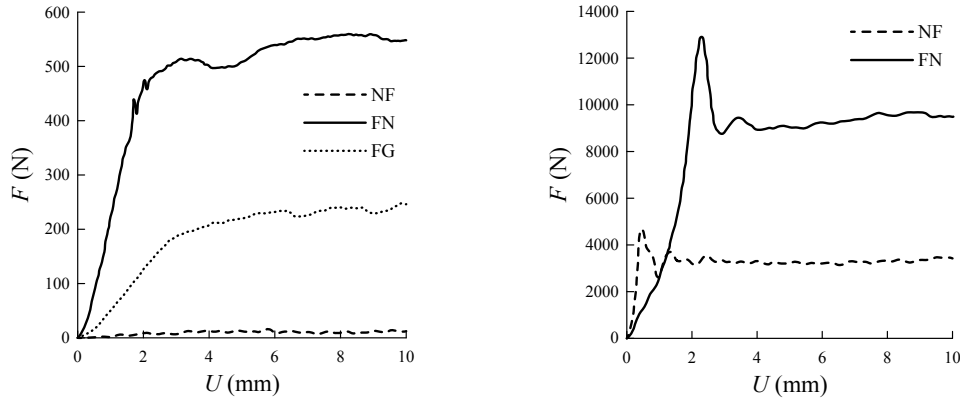


Figure 13. Left: in-plane quasistatic force-displacement graph. Right: out-of-plane quasistatic force-displacement graph.

and this increase is significantly slower and occurs in four steps. This is due to using four different foams in this structure. Reaction force in the nongraded foam-filled structure is the largest and the force for the structure with graded foam is around half of the nongraded structure. However, the increase in the graded structure is slower which is one of the advantages of this structure. Force-displacement displacement graph for the out-of-plane quasistatic static test for different structures is shown in Figure 13 (right).

The force applied during quasistatic static loading for empty structure shows a 250 times increase compared to in-plane conditions and then continues with an attenuating peak. In the structure with nongraded foam filling, this increase is 3 times of empty structure but this increase had a lower slope. The force transferred in structure with nongraded foam is significantly higher and increases with a lower slope. This means that the foam-filled structure not only absorbs more energy but also transfers a lower amount of force.

5.3. Comparison between numerical and experimental results. Figure 14 shows a comparison between force-displacement results of in-plane quasistatic tests and the results of numerical simulation for different models.

The empirical and numerical results for the empty structure are almost similar to one another. The difference between results in the nongraded foam-filled structure is even smaller. The difference between empirical and numerical results for the graded foam-filled structure is also small. In general, the results of numerical and empirical studies show good agreement with each other. So, the numerical simulation method is verified and applicable to other models. The comparison between out-of-plane quasistatic empirical tests and numerical results for different models are presented in Figure 15.

These results are almost identical for empty structure. Addition of foam filling causes a small difference between numerical and empirical results. However, the results still have good agreement with one another.

5.4. Comparison between in-plane and out-of-plane loadings. The results of in-plane and out-of-plane plane loadings for different models are compared as shown in Figure 16.

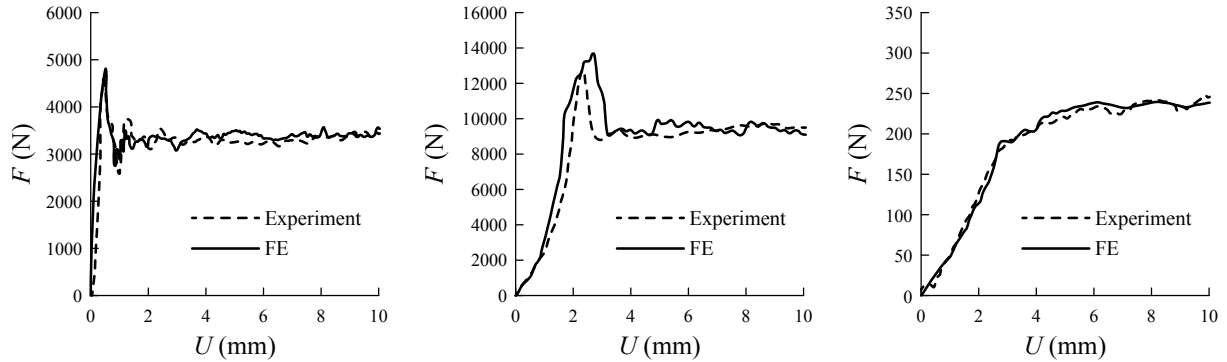


Figure 14. Comparison between in-plane loading for experimental and numerical results: empty structure (left), nongraded foam-filled structure (middle) and graded foam-filled structure (right).

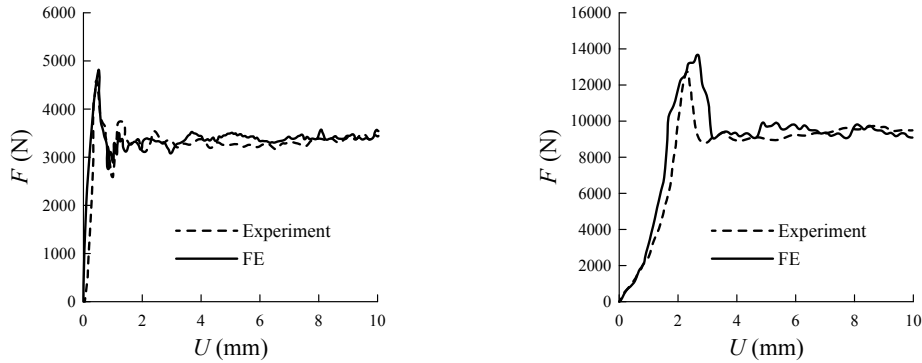


Figure 15. Comparison between the numerical and experimental results for out-of-plane loading for without foam (left) and nongraded foam models (right).

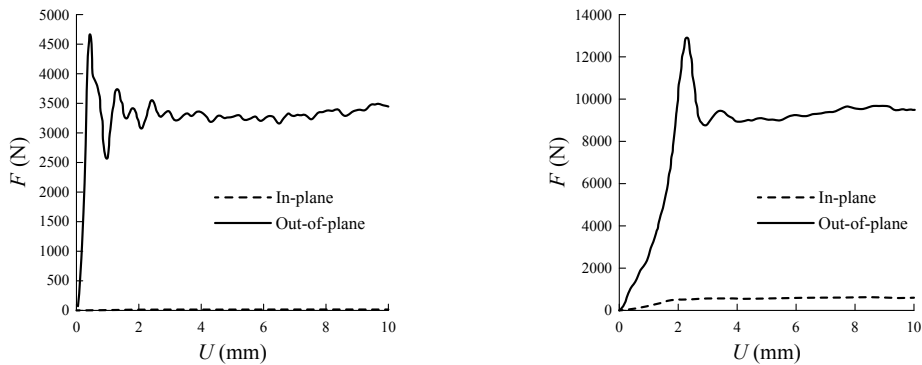


Figure 16. Comparison between the results of in-plane and out-of-plane loadings for without foam (left) and nongraded foam models (right).

In the out-of-plane loading, hallow structure applies a significantly higher force but shows a very high reaction force at the initial impact time while the nongraded foam-filled structure applies a force three times higher than the empty structure but reaction force reaches maximum magnitude at the later time. For the in-plane conditions, despite the fact that structure applies a significantly smaller force, this force decreases slowly overtime. This is more obvious in nongraded graded, foam-filled structure.

6. Conclusion

For in-plane loading, filling the structure with foam means that structure can absorb a higher amount of energy but simultaneously show a higher reaction force. Using graded filling in a way that structure stiffness increases downward and away from the location of the applied force increases energy absorption time and force transfer. This means that compared to structures with nongraded foam filling, graded structures absorb a lower amount of energy but this energy is absorbed with high reaction force during a longer time. The variation of the foam density is very important in energy absorption. It's better to increase the density of foam from the place of the impact load through the outer side of the energy absorber. For the structures with graded foam, the injury will be less regarding the structure with uniform density. When the energy absorber is used to protect a human, uniform reaction force and its transfer time are more important than the amount of absorbed energy. Therefore the application of honeycomb structures filled with graded foam is recommended. In out-of-plane loading, a foam-filled structure absorbs a higher amount of energy and also shows a milder reaction force.

In general, the results of the numerical simulation are close to that of empirical tests except in some parts of various graphs which require further investigation. The reasons for differences between numerical and empirical results can be manufacturing conditions and environmental factors. This means that numerical simulation results for behaviors of all five structures were validated using empirical tests. So, the numerical simulation method in ABAQUS software can be used to simulate the energy absorption of different honeycomb structures.

List of symbols

F	force (N)	U	displacement (mm)
FG	graded foam-filled structure	ε	strain
FN	nongraded foam-filled structure	ρ	density (kg/m ³)
NF	empty structure	σ	stress (MPa)

References

- [Akay and Hanna 1990] M. Akay and R. Hanna, "A comparison of honeycomb-core and foam-core carbon-fibre/epoxy sandwich panels", *Composites* **21**:4 (1990), 325–331.
- [Alavi Nia and Sadeghi 2010] A. Alavi Nia and M. Z. Sadeghi, "The effects of foam filling on compressive response of hexagonal cell aluminum honeycombs under axial loading-experimental study", *Mater. Des.* **31**:3 (2010), 1216–1230.
- [Ali et al. 2008] M. Ali, A. Qamhiyah, D. Flugrad, and M. Shakoar, "Theoretical and finite element study of a compact energy absorber", *Adv. Eng. Softw.* **39**:2 (2008), 95–106.
- [Bitzer 1997] T. Bitzer, *Honeycomb technology: materials, design, manufacturing, applications and testing*, Chapman & Hall, London, 1997.
- [Deshpande and Fleck 2001] V. S. Deshpande and N. A. Fleck, "Multi-axial yield behaviour of polymer foams", *Acta Mater.* **49**:10 (2001), 1859–1866.

- [Ebrahimi et al. 2018] S. Ebrahimi, N. Vahdatazad, and G. H. Liaghat, “Experimental characterization of the energy absorption of functionally graded foam filled tubes under axial crushing loads”, *J. Theor. Appl. Mech. (Warsaw)* **48**:1 (2018), 76–89.
- [Galehdari and Khodarahmi 2016] S. A. Galehdari and H. Khodarahmi, “Design and analysis of a graded honeycomb shock absorber for a helicopter seat during a crash condition”, *Int. J. Crashworthiness* **21**:3 (2016), 231–241.
- [Galehdari et al. 2015] S. A. Galehdari, M. Kadkhodayan, and S. Hadidi-Moud, “Analytical, experimental and numerical study of a graded honeycomb structure under in-plane impact load with low velocity”, *Int. J. Crashworthiness* **20**:4 (2015), 387–400.
- [Hanssen et al. 2000] A. G. Hanssen, M. Langseth, and O. S. Hopperstad, “Static and dynamic crushing of circular aluminium extrusions with aluminium foam filler”, *Int. J. Impact Eng.* **24**:5 (2000), 475–507.
- [Koch 1917] J. C. Koch, “The laws of bone architecture”, *Am. J. Anat.* **21**:2 (1917), 177–298.
- [Mozafari et al. 2016] H. Mozafari, S. Khatami, H. Molatefi, V. Crupi, G. Epasto, and E. Guglielmino, “Finite element analysis of foam-filled honeycomb structures under impact loading and crashworthiness design”, *Int. J. Crashworthiness* **21**:2 (2016), 148–160.
- [Seo et al. 2004] K. S. Seo, J. C. Lee, K. S. Bang, and H. S. Han, “Shock absorbing evaluation of the rigid polyurethane foam and Styrofoam applied to a small transportation package”, in *14th International Symposium on the Packaging and Transportation of Radioactive Materials (PATRAM 2004)* (Berlin, Germany), 2004.
- [Shahravi et al. 2019] S. Shahravi, M. J. Rezvani, and A. Jahan, “Multi-response optimization of grooved circular tubes filled with polyurethane foam as energy absorber”, *J. Optimiz. Ind. Eng.* **12**:1 (2019), 133–149.
- [Song et al. 2010] Y. Song, Z. Wang, L. Zhao, and J. Luo, “Dynamic crushing behavior of 3D closed-cell foams based on Voronoi random model”, *Mater. Des.* **31**:9 (2010), 4281–4289.
- [Suvorov and Dvorak 2005] A. P. Suvorov and G. J. Dvorak, “Dynamic response of sandwich plates to medium-velocity impact”, *J. Sandw. Struct. Mater.* **7**:5 (2005), 395–412.
- [Yu et al. 2018] X. Yu, Q. Qin, J. Zhang, S. He, C. Xiang, M. Wang, and T. J. Wang, “Crushing and energy absorption of density-graded foam-filled square columns: experimental and theoretical investigations”, *Compos. Struct.* **201** (2018), 423–433.
- [Zarei Mahmoudabadi and Sadighi 2011] M. Zarei Mahmoudabadi and M. Sadighi, “A study on the static and dynamic loading of the foam filled metal hexagonal honeycomb — theoretical and experimental”, *Mater. Sci. Eng. A* **530** (2011), 333–343.

Received 4 Jun 2018. Revised 4 Jul 2019. Accepted 2 Aug 2019.

ALIREZA MOLAIEE: alireza.m.1392@gmail.com

Department of Mechanical Engineering, Najafabad Branch, Islamic Azad University, Najafabad, Iran

SEYED ALI GALEHDARI: ali.galehdari@pmc.iaun.ac.ir

Department of Mechanical Engineering, Najafabad Branch, Islamic Azad University, Najafabad, Iran

TRANSIENT THERMAL STRESSES IN A LAMINATED SPHERICAL SHELL OF THERMOELECTRIC MATERIALS

YUE LIU, KAI FA WANG AND BAOLIN WANG

Thermoelectric materials have many potential applications in engineering such as in thermoelectric generators, waste heat recovery industry, thermoelectric cooling devices. They can also be used in thermal protection system of supersonic space shuttles to reduce their surface temperatures. On the other hand, multilayered spherical shell structures are important structure type for thermoelectric material applications. This paper presents a transient analysis model to predict the temperature field and the associated thermal stresses in a laminated thermoelectric spherical shell subjected to a sudden temperature increase on its outer surface. The effects of applied electric current density, thermal conductivity and thickness of laminated shells on the temperature and thermal stress distributions have been obtained and shown graphically. Numerical results show that the maximum tensile hoop stress in the laminated shells can be reduced significantly at a specific applied electric current density. The thermal conductivity ratio of laminated shells has significant impact on the maximum stress level in the shells. When the thermal conductivity ratio of the inner layer to the outer layer increases, the maximum tensile hoop stress increases but the maximum compressive hoop stress decreases.

1. Introduction

Thermoelectric materials can achieve energy conversion between electricity and heat and are widely applied to engineering applications [Riffat and Ma 2003]. For example, thermoelectric devices can be used for thermoelectric power generation, refrigeration and thermal protection system [Chowdhury et al. 2009; DiSalvo 1999; Zhang et al. 2016; Han et al. 2014; O'Brien et al. 2008; Li et al. 2005]. They also have potential applications in high-temperature superconductor cables in space solar energy stations. Applications of the thermoelectric conversion technology is calling for high efficiency thermoelectric materials [Huang and Duang 2000; Tian et al. 2015]. Thus thermoelectric materials have attracted attentions in the field of materials science. Zhang et al. [2018b] successfully realized n-type BiCuSeO and Seebeck coefficient of BiCuSeO was improved through introducing extra Bi/Cu to fill the Bi/Cu vacancies. Pothin et al. [2018] finished theoretical and experimental work on the tellurium doping of thermoelectric ZnSb and investigated the influence of tellurium on the phase stabilities. In addition, the requirements of structural strength and reliability of the thermoelectric intelligent devices call for a better understanding of the mechanics properties. Thus stress analysis of thermoelectric materials has attracted more and more attentions. A theoretical model to analyze the thermoelectric conversion efficiency of a cracked material provided by Zhang et al. [2017a]. Later, they also studied the effect of cracking on the thermoelectric properties under combined electrical and temperature loadings [2017b]. Song et al. [2018] analyzed

Keywords: thermoelectric material, laminated structure, superconductor cable, high temperature, thermal stress, thermal protection system.

the thermoelectric field near an elliptic inhomogeneity in an open circuit by using the complex-variable method. Wang [2015] studied effective material properties of thermoelectric composite materials with elliptical fibers. Liu et al. [2017a] provided a mechanical model of a thermoelectric thin film bonded to an elastic substrate. Applications of the thermoelectric conversion techniques in spacecraft have also attracted more and more attentions. The reason is that when the spacecraft cruise at high velocity, there is a severe heating on their outer surface. However, for safe operation, the temperature on the interior of the spacecraft should not be too high. As a result, there is the large temperature difference between the in-wall and the outer surface of spacecraft. It is the prerequisite of the use of the thermoelectric conversion techniques. In addition, the features of thermoelectric materials and devices make them very attractive for meeting the need of the thermal protection system of spacecraft. For example, the features of them include large operating temperature range, easy to control, reliable operation, layout flexibility, adaptability.

Thermoelectric cylindrical and spherical shells are more and more applied to the thermoelectric devices and many researchers studied them in recent years. Yang et al. [2014] obtained thermoelectric field distributions in both homogeneous shell and core-shell composites and analyzed the effective thermoelectric properties of the core-shell composites. Zhang et al. [2018a] studied the effects of interface layers on the performance of annular thermoelectric generators. Liu et al. [2018] presented a transient model to investigate the dynamic characteristics of laminated thermoelectric cylindrical shells and studied the transient thermal stress fields. In engineering practice, the temperature at the outer surface of thermoelectric spherical shell may be suddenly increased, such as for thermal protection system [Hegde et al. 2012; Lu and Liu 2012]. In order to make the design of thermoelectric devices satisfy the requirements of structural strength, dynamic characteristics of thermoelectric spherical shell should be studied. Suggested by the previous studies [Ching and Chen 2007; Frostig and Thomsen 2007; Qin 2005; Qiu et al. 2018; Wu et al. 2016], the transient thermal stress in the thermoelectric shell structures should be researched. In addition, laminated thermoelectric shells attract more and more attention [Liu et al. 2018; Yang et al. 2014]. The dynamic characteristics of laminated spherical shells of thermoelectric materials should be also studied. To our best knowledge, investigation of transient characteristics of homogeneous thermoelectric spherical shell and laminated thermoelectric spherical shells is very limited.

The aim of current paper is to propose a transient model to study the transient temperature and thermal stress fields in both homogeneous and laminated thermoelectric spherical shells. By using the technique of separation of variables, we obtain the solutions for temperatures at the steady-state and the transient-state. Some numerical calculations are performed to study the transient characteristics of spherical shell. The influences of applied electric current density, thermal conductivity and the thickness of laminated spherical shells on the temperature field and thermal stress field are investigated. This research can provide some guidelines for the design and optimization of thermoelectric shell devices.

2. Transient model of the homogeneous thermoelectric spherical shell

Figure 1 shows a homogeneous thermoelectric spherical shell, where r is the radial coordinate (radius), r_1 is the internal radius and r_2 is the external radius of thermoelectric shell. Note that t denotes time. Assume that thermoelectric shell is at an initial constant temperature T_1 . For time $t > 0$, the temperature of external surface ($r = r_2$) is changed to T_2 and kept at T_2 . For thermoelectric materials, the basic

governing equations in transient state can be expressed as [Wang 2017]

$$\nabla \cdot \mathbf{j} = 0, \quad (1)$$

$$-\nabla \cdot \mathbf{q} - \mathbf{j} \cdot \nabla V = \rho c \frac{\partial T}{\partial t}, \quad (2)$$

$$\mathbf{j} = -\sigma \nabla V - \sigma s \nabla T, \quad (3)$$

$$\mathbf{q} = -\sigma s T \nabla T - (\kappa + \sigma s^2 T) \nabla T, \quad (4)$$

where T and V are, respectively, temperature and electric potential; \mathbf{j} and \mathbf{q} are, respectively, electric current density and heat flux vector; σ , κ , s , ρ and c are, respectively, electric conductivity, thermal conductivity, Seebeck coefficient, mass density and specific heat. In this work, the symmetric problem is considered so that temperature, electric potential and electric current density depend only on radial coordinate r . The governing equation for electric current density is rewritten as $\mathrm{d}j/\mathrm{d}r + 2j/r = 0$, where j is the magnitude of current density. As a result, j can be obtained as $j = C/r^2$. A special case is considered and applied electric current density is independent on time, therefore C is a constant. From (1) to (4), the governing equation for transient temperature can be obtained as

$$\nabla^2 T + \frac{j^2}{\kappa \sigma} = \frac{\rho c}{\kappa} \frac{\partial T}{\partial t}. \quad (5)$$

For 1-D problem of $T(r, t)$, equation (5) can be rewritten as

$$\frac{1}{r} \frac{\partial^2}{\partial r^2} (rT) + \frac{j^2}{\kappa \sigma} = \frac{\rho c}{\kappa} \frac{\partial T}{\partial t}. \quad (6)$$

The solution to (6) can be expressed as $T(r, t) = T_s(r) + T_h(r, t)$, where $T_s(r)$ is the steady part of the solution, $T_h(r, t)$ is the transient part of the solution. Subscripts s and h denote the steady and the transient part, respectively. For 1-D problem of $T_s(r)$, the governing equation can be expressed as

$$\frac{1}{r} \frac{\mathrm{d}^2}{\mathrm{d}r^2} (rT_s) + \frac{j^2}{\kappa \sigma} = 0, \quad (7)$$

and boundary conditions are $T_s(r_1) = T_1$ and $T_s(r_2) = T_2$. For 1-D problem of $T_h(r, t)$, the governing equation can be expressed as

$$\frac{1}{r} \frac{\partial^2}{\partial r^2} (rT_h) = \frac{\rho c}{\kappa} \frac{\partial T_h}{\partial t}, \quad (8)$$

and corresponding boundary conditions are $T_h(r_1, t) = 0$ and $T_h(r_2, t) = 0$, initial condition is $T_h(r, 0) = T_1 - T_s(r)$. New variables $W_s(r)$ and $W_h(r, s)$ are introduced by the transform $W_s(r) = rT_s(r)$ and $W_h(r, t) = rT_h(r, t)$. Thus (7) and (8) can be rewritten as

$$\frac{\mathrm{d}^2 W_s}{\mathrm{d}r^2} + \frac{rj^2}{\kappa \sigma} = 0, \quad (9)$$

$$\frac{\partial^2 W_h}{\partial r^2} = \frac{\rho c}{\kappa} \frac{\partial W_h}{\partial t}. \quad (10)$$

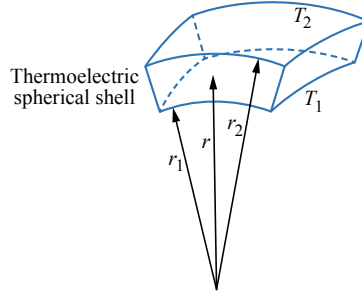


Figure 1. The homogeneous thermoelectric spherical shell.

2.1. The temperature field. Substituting the expression of j into (9) gives

$$W_s = -\frac{C^2}{2\kappa\sigma} \frac{1}{r} + C_1 r + C_2, \quad (11)$$

where C_1 and C_2 are unknown constants. From boundary conditions C_1 and C_2 can be solved as

$$C_1 = \frac{r_2 T_2 - r_1 T_1}{r_2 - r_1} - \frac{C^2}{2r_1 r_2 \kappa \sigma}, \quad C_2 = r_1 T_1 + \frac{C^2}{2r_1 \kappa \sigma} - C_1 r_1. \quad (12)$$

The solution to (10) can be expressed as [Hahn and Özişik 2012]

$$W_h(r, t) = \sum_{n=1}^{\infty} \exp\left(-\frac{\kappa}{\rho c} \beta_n^2 t\right) \frac{2}{r_2 - r_1} \sin(\beta_n r) \int_{r_1}^{r_2} \sin(\beta_n r) [r T_1 - W_s(r)] dr, \quad (13)$$

where $\beta_n = \pi n / (r_2 - r_1)$, $n = 1, 2, 3, \dots$. Thus $T(r, t)$ can be obtained as $T(r, t) = [W_s(r) + W_h(r, t)]/r$.

2.2. The thermal stress field. In this case, only radial strain ε_r and hoop strain ε_θ are nonzero. The expressions of them are, respectively, $\varepsilon_r = du/dr$ and $\varepsilon_\theta = u/r$, where u is radial displacement. The equation of stress equilibrium is $d\sigma_r/dr + 2(\sigma_r + \sigma_\theta)/r = 0$. Stress-strain equations are

$$\sigma_r = \frac{E}{(1+\nu)(1-2\nu)} [(1-\nu)\varepsilon_r + 2\nu\varepsilon_\theta - (1+\nu)\alpha\Delta T], \quad (14a)$$

$$\sigma_\theta = \frac{E}{(1+\nu)(1-2\nu)} [\varepsilon_\theta + \nu\varepsilon_r - (1+\nu)\alpha\Delta T], \quad (14b)$$

where E , ν and α are Young's modulus, Poisson's ratio and thermal expansion coefficient of the thermoelectric spherical shell, respectively. Note that ΔT is temperature increment measured relative to the initial temperature, which can be expressed as $\Delta T = T(r, t) - T_1$ in this case. Substituting (14a), (14b) and the expressions of ε_r and ε_θ into equilibrium equation gives

$$\frac{d}{dr} \left[\frac{1}{r^2} \frac{d}{dr} (r^2 u) \right] = \frac{1+\nu}{1-\nu} \alpha \frac{d}{dr} (\Delta T). \quad (15)$$

The solution to (15) is

$$u = \frac{1+\nu}{1-\nu} \frac{\alpha}{r^2} \int_{r_1}^r \Delta T r^2 dr + ar + \frac{b}{r^2}. \quad (16)$$

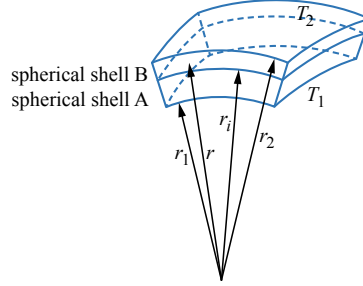


Figure 2. The laminated thermoelectric spherical shells.

Thus (14a) and (14b) can be rewritten as

$$\sigma_r = -\frac{2\alpha E}{1-\nu} \frac{1}{r^3} \int_{r_1}^r \Delta T r^2 dr + \frac{Ea}{1-2\nu} - \frac{1}{r^3} \frac{2Eb}{1+\nu}, \quad (17a)$$

$$\sigma_\theta = \frac{\alpha E}{1-\nu} \frac{1}{r^3} \int_{r_1}^r \Delta T r^2 dr + \frac{Ea}{1-2\nu} + \frac{1}{r^3} \frac{Ea}{1+\nu} - \frac{\alpha E \Delta T}{1-\nu}, \quad (17b)$$

where a and b are constants. When internal and external surfaces of the shell are stress free, a and b can be obtained as

$$a = \frac{2(1-2\nu)b}{r_1^3(1+\nu)}, \quad b = \frac{\alpha(1+\nu)}{1-\nu} \frac{r_1^3}{r_2^3 - r_1^3} \int_{r_1}^{r_2} \Delta T r^2 dr. \quad (18a)$$

When internal surface of shell is fixed and external surface is stress free, a and b can be obtained as

$$a = -\frac{b}{r_1^3}, \quad b = -\frac{2\alpha}{1-\nu} \frac{(1-2\nu)(1+\nu)r_1^3}{[r_2^3(1+\nu) + 2(1-2\nu)r_1^3]} \int_{r_1}^{r_2} \Delta T r^2 dr. \quad (18b)$$

When both internal and external surfaces of shell are fixed, a and b can be obtained as

$$a = -\frac{b}{r_1^3}, \quad b = -\frac{1+\nu}{1-\nu} \frac{r_1^3 \alpha}{r_1^3 - r_2^3} \int_{r_1}^{r_2} \Delta T r^2 dr. \quad (18c)$$

3. The transient model of the laminated thermoelectric spherical shell

As shown in Figure 2, laminated thermoelectric spherical shell is considered which consists of two homogeneous thermoelectric shells, A and B. The interface of the two shells is at r_i . Note that r_1 and r_2 express, respectively, the internal radius of spherical shell A and the external radius of spherical shell B. Assume that initially the laminated thermoelectric spherical shell is at a constant temperature T_1 . For time $t > 0$, temperature of the external surface of shell B ($r = r_2$) is changed to T_2 and kept at T_2 . Similar to the method in Section 2, the temperature field of shell A is $T_A(r, t) = T_{As}(r) + T_{Ah}(r, t)$ and temperature field of shell B is $T_B(r, t) = T_{Bs}(r) + T_{Bh}(r, t)$. The subscripts A and B denote, respectively, the shell A and shell B.

3.1. The temperature field. Similar to the method in Section 2, new variables $W_{As}(r)$, $W_{Bs}(r)$ are introduced by the transform $W_{As}(r) = rT_{As}(r)$ and $W_{Bs}(r) = rT_{Bs}(r)$. These new variables should satisfy (9).

The expressions of them can be obtained as

$$W_{As} = -\frac{C_A^2}{2\kappa_A\sigma_A} \frac{1}{r} + C_{A1}r + C_{A2}, \quad W_{Bs} = -\frac{C_B^2}{2\kappa_B\sigma_B} \frac{1}{r} + C_{B1}r + C_{B2}, \quad (19)$$

where C_{A1} , C_{A2} , C_{B1} and C_{B2} are constants; σ_A , κ_A , s_A , are, respectively, electric conductivity, thermal conductivity and Seebeck coefficient of spherical shell A, and σ_B , κ_B , s_B , are, respectively, electric conductivity, thermal conductivity and Seebeck coefficient of spherical shell B. From boundary conditions we have the equations as

$$r_1 T_1 = -\frac{C^2}{2\kappa_A\sigma_A} \frac{1}{r_1} + C_{A1}r_1 + C_{A2}, \quad r_2 T_2 = -\frac{C^2}{2\kappa_B\sigma_B} \frac{1}{r_2} + C_{B1}r_2 + C_{B2}. \quad (20a)$$

In addition, temperature, electric current density and heat flux are continuous at the interface [Yang et al. 2014], we have the equation as

$$-\frac{C_A^2}{2\kappa_A\sigma_A} \frac{1}{r_i} + C_{A1}r_i + C_{A2} = -\frac{C_B^2}{2\kappa_B\sigma_B} \frac{1}{r_i} + C_{B1}r_i + C_{B2}, \quad (20b)$$

$$C_A = C_B = C, \quad (20c)$$

$$(s_A T_{As} j_A - \kappa_A \nabla T_{As})|_{r=r_i} = (s_B T_{Bs} j_B - \kappa_B \nabla T_{Bs})|_{r=r_i}. \quad (20d)$$

From (20a) to (20d), C_{A1} , C_{A2} , C_{B1} and C_{B2} can be obtained as

$$C_{A1} = -\frac{(\kappa_B r_i^2 \Gamma_1 + \Gamma_3)(r_i - r_2)}{\Gamma_2(r_i - r_2) + (r_i - r_1)\kappa_B r_i^2}, \quad C_{A2} = r_1 T_1 + \frac{C^2}{2r_1\kappa_A\sigma_A} - C_{A1}r_1, \quad (21a)$$

$$C_{B1} = \Gamma_1 + C_{A1} \frac{r_i - r_1}{r_i - r_2}, \quad C_{B2} = r_2 T_2 + \frac{C^2}{2r_2\kappa_B\sigma_B} - C_{B1}r_2, \quad (21b)$$

where

$$\Gamma_1 = \frac{r_1 T_1 - r_2 T_2}{r_i - r_2} + \left(\frac{r_i - r_1}{r_1\kappa_A\sigma_A} + \frac{r_2 - r_i}{r_2\kappa_B\sigma_B} \right) \frac{C^2}{2r_i(r_i - r_2)}, \quad \Gamma_2 = C(s_A - s_B)(r_i - r_1) - [(\kappa_A - \kappa_B)r_1 + \kappa_B r_i]r_i,$$

$$\Gamma_3 = \frac{(\sigma_A - \sigma_B)C^2}{2\sigma_A\sigma_B} + \frac{(r_i - r_1)C^2}{2r_1r_i\kappa_A\sigma_A} [C(s_A - s_B) + r_i(\kappa_A - \kappa_B)] + r_1 T_1 [C(s_A - s_B) + r_i(\kappa_A - \kappa_B)].$$

Similar to Section 2.1, $T_{Ah}(r, t)$ and $T_{Bh}(r, t)$ should satisfy (8). The boundary conditions and continuous conditions are

$$T_{Ah}(r_1, t > 0) = 0, \quad (22a)$$

$$T_{Ah}(r_i, t > 0) = T_{Bh}(r_i, t > 0), \quad (22b)$$

$$\kappa_A \frac{\partial T_{Ah}(r, t)}{\partial r} = \kappa_B \frac{\partial T_{Bh}(r, t)}{\partial r}, \quad r = r_i, \quad t > 0, \quad (22c)$$

$$T_{Bh}(r_2, t > 0) = 0. \quad (22d)$$

The initial conditions for $T_{Ah}(r, t)$ and $T_{Bh}(r, t)$ are

$$T_{Ah}(r, 0) = T_1 - T_{As}(r), \quad T_{Bh}(r, 0) = T_1 - T_{Bs}(r). \quad (23)$$

$T_{Ah}(r, t)$ and $T_{Bh}(r, t)$ are [Hahn and Özişik 2012]

$$T_{Ah}(r, t) = \sum_{n=1}^{\infty} \exp(-\beta_n^2 t) \frac{1}{N_n} \varphi_{An}(r) \times \left\{ \rho_A c_A \int_{r_1}^{r_i} r^2 \varphi_{An}(r) [T_1 - T_{As}(r)] dr + \rho_B c_B \int_{r_i}^{r_2} r^2 \varphi_{Bn}(r) [T_1 - T_{Bs}(r)] dr \right\}, \quad (24a)$$

$$T_{Bh}(r, t) = \sum_{n=1}^{\infty} \exp(-\beta_n^2 t) \frac{1}{N_n} \varphi_{Bn}(r) \times \left\{ \rho_A c_A \int_{r_1}^{r_i} r^2 \varphi_{An}(r) [T_1 - T_{As}(r)] dr + \rho_B c_B \int_{r_i}^{r_2} r^2 \varphi_{Bn}(r) [T_1 - T_{Bs}(r)] dr \right\}, \quad (24b)$$

where ρ_A, c_A are, respectively, mass density and specific heat of spherical shell A, ρ_B, c_B are, respectively, mass density and specific heat of spherical shell B, and

$$N_n = \rho_A c_A \int_{r_1}^{r_i} r^2 \varphi_{An}^2(r) dr + \rho_B c_B \int_{r_i}^{r_2} r^2 \varphi_{Bn}^2(r) dr, \\ \varphi_{An} = A_{1n} \frac{1}{r} \sin\left(\frac{\beta_n}{\sqrt{\omega_A}} r\right) + B_{1n} \frac{1}{r} \cos\left(\frac{\beta_n}{\sqrt{\omega_A}} r\right), \quad \varphi_{Bn} = A_{2n} \frac{1}{r} \sin\left(\frac{\beta_n}{\sqrt{\omega_B}} r\right) + B_{2n} \frac{1}{r} \cos\left(\frac{\beta_n}{\sqrt{\omega_B}} r\right),$$

where $A_{1n}, B_{1n}, A_{2n}, B_{2n}, \beta_n$ are the unknown constants and $\omega_A = \kappa_A / (\rho_A c_A)$, $\omega_B = \kappa_B / (\rho_B c_B)$. $A_{1n}, B_{1n}, A_{2n}, B_{2n}$ and β_n are listed in Appendix A. Thus $T_A(r, t)$ and $T_B(r, t)$ can be obtained as $T_A(r, t) = W_{As}(r)/r + T_{Ah}(r, t)$ and $T_B(r, t) = W_{Bs}(r)/r + T_{Bh}(r, t)$.

3.2. The thermal stress field. Similar to the method in Section 2.2, displacement and stresses in thermoelectric spherical shell A and B can be obtained as

$$u_A = \frac{1 + \nu_A}{1 - \nu_A} \frac{\alpha_A}{r^2} \int_{r_1}^r \Delta T_A r^2 dr + a_{11} r + \frac{b_{12}}{r^2}, \quad (25a)$$

$$\sigma_{Ar} = -\frac{2\alpha_A E_A}{1 - \nu_A} \frac{1}{r^3} \int_{r_1}^r \Delta T_A r^2 dr + \frac{E_A a_{11}}{1 - 2\nu_A} - \frac{1}{r^3} \frac{2E_A b_{12}}{1 + \nu_A}, \quad (25b)$$

$$\sigma_{A\theta} = \frac{\alpha_A E_A}{1 - \nu_A} \frac{1}{r^3} \int_{r_1}^r \Delta T_A r^2 dr + \frac{E_A a_{11}}{1 - 2\nu_A} + \frac{1}{r^3} \frac{E_A b_{12}}{1 + \nu_A} - \frac{\alpha_A E_A \Delta T_A}{1 - \nu_A}, \quad (25c)$$

$$u_B = \frac{1 + \nu_B}{1 - \nu_B} \frac{\alpha_B}{r^2} \int_{r_i}^r \Delta T_B r^2 dr + a_{21} r + \frac{b_{22}}{r^2}, \quad (26a)$$

$$\sigma_{Br} = -\frac{2\alpha_B E_B}{1 - \nu_B} \frac{1}{r^3} \int_{r_i}^r \Delta T_B r^2 dr + \frac{E_B a_{21}}{1 - 2\nu_B} - \frac{1}{r^3} \frac{2E_B b_{22}}{1 + \nu_B}, \quad (26b)$$

$$\sigma_{B\theta} = \frac{\alpha_B E_B}{1 - \nu_B} \frac{1}{r^3} \int_{r_i}^r \Delta T_B r^2 dr + \frac{E_B a_{21}}{1 - 2\nu_B} + \frac{1}{r^3} \frac{E_B b_{22}}{1 + \nu_B} - \frac{\alpha_B E_B \Delta T_B}{1 - \nu_B}, \quad (26c)$$

where a_{11}, b_{12}, a_{21} and b_{22} are unknown constants; E_A, ν_A and α_A are, respectively, Young's modulus, Poisson's ratio and thermal expansion coefficient of spherical shell A, and E_B, ν_B and α_B are, respectively, Young's modulus, Poisson's ratio and thermal expansion coefficient of spherical shell B. Assumed that

	s (VK ⁻¹) $\times 10^{-6}$	σ (Sm ⁻¹) $\times 10^3$	κ (Wm ⁻¹ K ⁻¹)	ρ (kgm ⁻³)	c (Jkg ⁻¹ K ⁻¹)	α (K ⁻¹) $\times 10^{-5}$	E (GPa)	ν
Shell A	200	110	1.6	7740	154.4	1.68	47	0.3
Shell B	233	47.2	1.22	6760	190	0.42	160	0.4

Table 1. Thermoelectric properties of thermoelectric spherical shells A and B [Antonova and Looman 2005; Clin et al. 2009; Gao et al. 2011; Jin 2013; Yang et al. 2014].

radial displacement and radial stress of spherical shell A and B are continuous at the interface. It means $u_A(r_i) = u_B(r_i)$ and $\sigma_{Ar}(r_i) = \sigma_{Br}(r_i)$. a_{11} , b_{12} , a_{21} and b_{22} are listed in Appendix B.

4. Numerical examples and discussions

The internal and external radii of thermoelectric spherical shell are, respectively, assumed as $r_1 = 0.05$ m and $r_2 = 0.055$ m, as shown in Figure 1. For laminated spherical shells, the internal and external radii are, respectively, assumed as $r_1 = 0.05$ m and $r_2 = 0.055$ m as shown in Figure 2. The material properties of thermoelectric spherical shell A and shell B are listed in Table 1 [Antonova and Looman 2005; Clin et al. 2009; Gao et al. 2011; Jin 2013; Liu et al. 2017b; Yang et al. 2014]. In addition, assume that material properties of homogeneous thermoelectric spherical shell are the same as thermoelectric shell A in Table 1. Assume that temperature applied on internal surface T_1 is equal to 300 K and temperature applied on the external surface T_2 is equal to 1300 K. In addition, V_1 is applied electric potential on internal surface and value of V_1 is assumed to be zero. A typical value of the electric current density $j_0 = 3 \times 10^6$ A m⁻² [Wang 2017] is used as the reference value. Assume that the reference electric current density is applied on internal surface of spherical shell. Thus the value of reference constant C_0 is equal to 7500.

4.1. The transient temperature field. Figure 3 shows the temperature profile of homogeneous thermoelectric spherical shell. It is noted that in Figure 3 the normalized current density j/j_0 is assumed to be 1. It shows that temperatures gradually increase with time and become almost steady as time exceeds 20 s in current case. The distribution of temperature is nonlinear, due to Joule heating. Figure 4 shows the influence of applied electric current density on steady-state temperature field of homogeneous thermoelectric spherical shell. Clearly, temperature profiles for positive electric current and negative electric current are almost coincident. This means that direction of applied electric current density does not affect the temperature distribution. The reason is that temperature field of homogeneous thermoelectric spherical shell is affected by the square of applied electric current density j , which can be found from the equation (11).

Figure 5 shows the temperature profile of laminated thermoelectric spherical shells. The normalized electric current density j/j_0 is assumed to be 1. In this case, temperature increases with time and finally approaches the steady state when time exceeds 20 s. Figure 6 shows the effect of electric current density on steady-state temperature field of laminated thermoelectric spherical shell. Due to thermoelectric effect, heat flux in thermoelectric material is obtained as $q = sTj - \kappa \nabla T$, which is affected by electric current density j . For laminated thermoelectric spherical shells, continuous condition of heat flux is that $q_A = q_B$

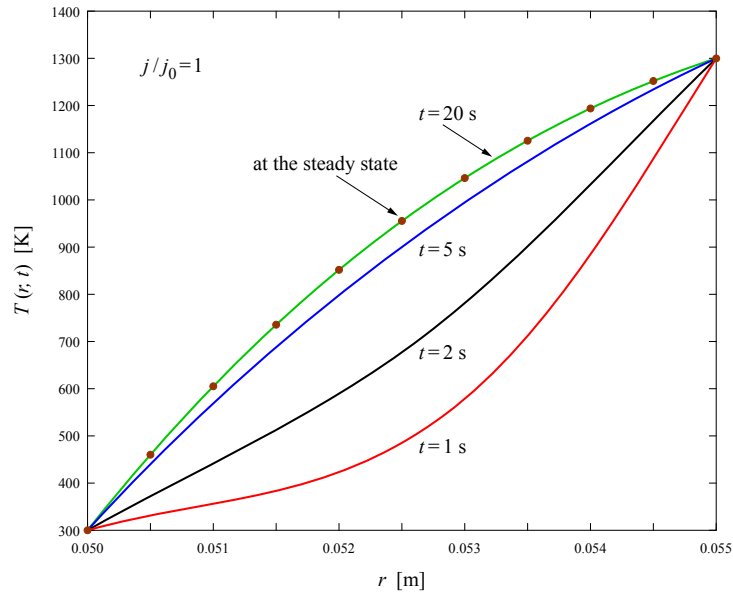


Figure 3. Distribution of transient temperature in homogeneous thermoelectric spherical shell for $j/j_0 = 1$.

at interface. On the other hand, temperature field is affected by the square of electric current density j which can be found from governing equation (9). Thus temperature field of laminated spherical shells

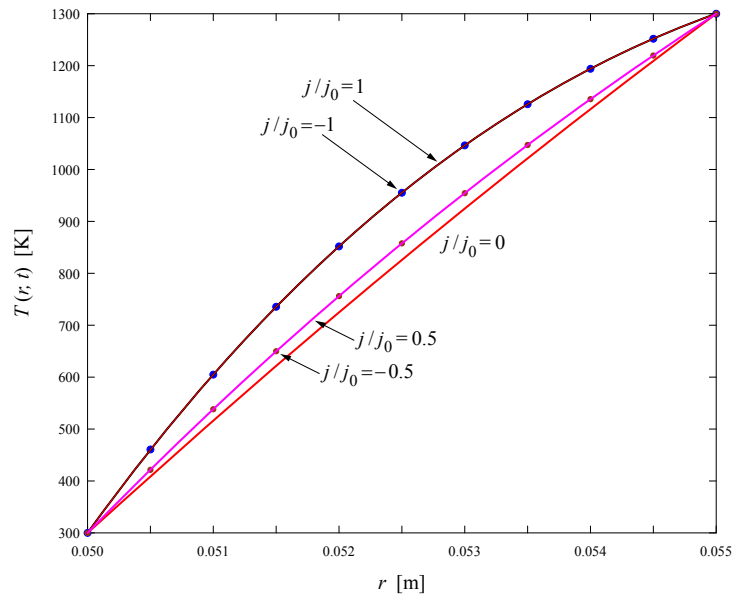


Figure 4. The influence of applied current density on the temperature field of homogeneous thermoelectric spherical shell under steady state.

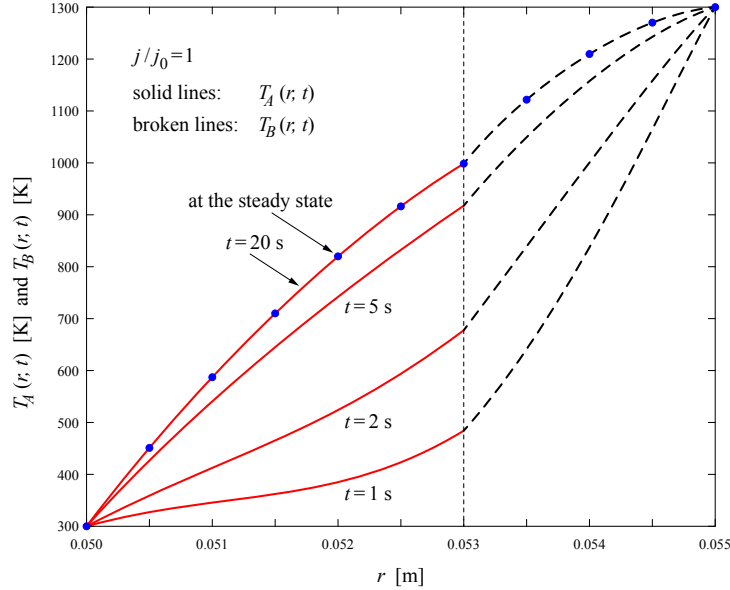


Figure 5. Distribution of transient temperature in laminated thermoelectric spherical shell for $j/j_0 = 1$.

is dependent on the first and second power of electric current density. Both direction and magnitude of applied current density can affect temperature distribution. If Seebeck coefficient s is equal to zero (ignore thermoelectric effect), heat flux will be independent of j and temperature field will be affected only by the second power of electric current density.

4.2. The transient thermal stress field. Considering the most common practical situation, the radial stresses at the both internal and external surfaces are assumed to be zero in this subsection. Since the maximum hoop stress is higher than that of radial stress in this case, only distributions of hoop stress are given. As mentioned above, temperature field keep almost steady state as time is greater than 20 s. In addition, the change of temperature field is obvious with time t varying from 0 s to 10 s and when time t varying from 10 s to 20 s, the change of temperature field is not obvious. Thus the dynamic variations of hoop stress from 0 s to 10 s are given in this subsection.

Figure 7 shows dynamic hoop stress variations at internal and external surfaces of the homogeneous thermoelectric spherical shell. Since temperature applied on external surface T_2 is higher than initial temperature (hot shock), the region near external surface (r_2) is in compressive, whereas a tensile zone is developed at internal surface (r_1). Before temperature of spherical shell reaches the steady-state, hoop stress at external surface decreases with time and hoop stress at internal surface increases with time. The transient thermal stress field for positive current density is the same as that for the negative current density. In current case, the maximum compressive stress is at r_2 when time is equal to zero and the maximum tensile stress is at r_1 when the stress field reaches steady state. Figure 8 shows dynamic hoop stress variations at interface, internal and external surfaces of laminated thermoelectric spherical shells. When temperature on external surface (r_2) is changed to T_2 ($T_2 > \text{initial temperature}$), the region near external surface of shell B (r_2) is in compressive, whereas a tensile zone is developed at interface of shell B (r_i).

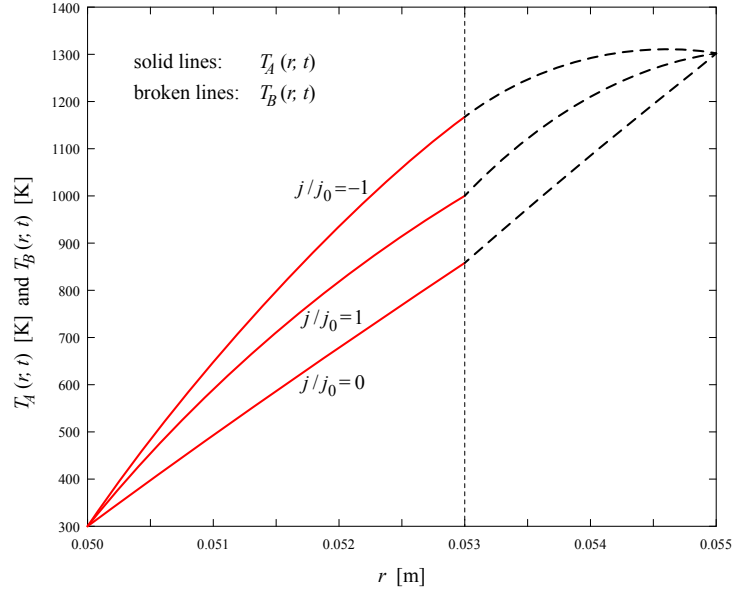


Figure 6. The influence of applied current density on the temperature field of laminated thermoelectric spherical shell under steady state.

Due to continuous condition at interface, interface of shell A (r_i) is in tensile in a short time after hot shock ($t < 0.5$ s). When temperature of laminated spherical shells reaches the steady-state, shell A and shell B at interface have the same temperature. In current case, thermal expansion coefficient of shell A is bigger than that of shell B. Thus interface surface of shell A is in compressive at steady-state. Hoop stress at interface $\sigma_{A\theta}(r_i, t)$ therefore is tensile at the beginning and finally is compressive. Temperature distribution is dependent on both direction and magnitude of applied current density. Thus the transient thermal stress profiles for positive current density is different from that for negative electric current, as shown in Figure 8. In this case, the maximum compressive stress is at external surface of shell B (r_2) when time is equal to zero and the maximum tensile stress is at interface of shell B (r_i) when the stress field reaches steady state.

4.3. The influences of thermal conductivity. Many studies show that reducing the thermal conductivity can improve the thermoelectric figure of merit (ZT) but it can also cause thermomechanical issues [Kim et al. 2016]. Thus the influence of thermal conductivity on the thermal stress field should be studied. Figure 9 shows the influence of thermal conductivity on the maximum compressive and tensile hoop stresses. Note that in Figure 9, $\sigma_{\theta}(r_2, 0)$ and $s_{\theta s}(r_1)$ are the maximum compressive hoop stress and maximum tensile hoop stress in the shells, respectively. It can be seen that if applied electric current density increases and thermal conductivity decreases, the maximum compressive stress decreases but the maximum tensile stress increases. Influence of thermal conductivity on the maximum tensile stress is more significant than that on the maximum compressive stress. This means that even though lowering thermal conductivity can enhance the thermoelectric figure of merit (ZT), it is also likely to cause the structural reliability concerns. Therefore, when we design thermoelectric spherical shell devices, a balance between the thermoelectric performance and structural reliability issue should be made.

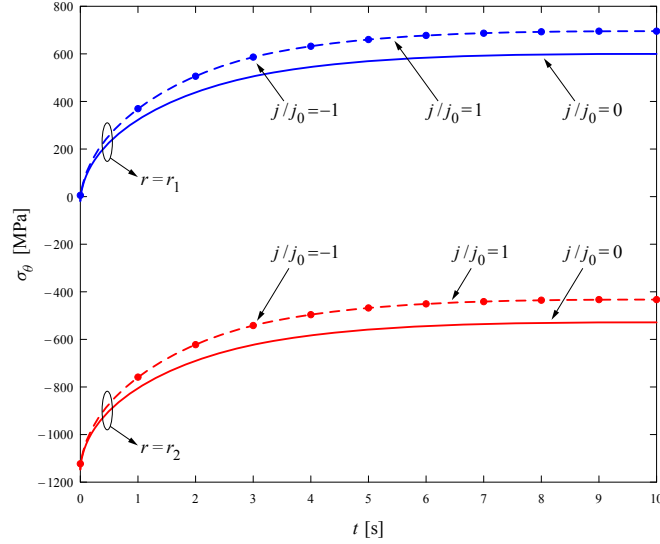


Figure 7. The dynamic hoop stress variations at the internal and external surfaces of homogeneous thermoelectric spherical shell (the applied temperature at the internal and external surfaces of shell are, respectively, 300 K and 1300 K).

Figures 10 and 11 show the influence of thermal conductivity on maximum tensile hoop stress and maximum compressive hoop stress of laminated spherical shells, respectively. Note that $\sigma_{B\theta s}(r_i)$ is the maximum tensile hoop stress of laminated shells in Figure 10 and $\sigma_{B\theta}(r_2, 0)$ is the maximum compressive

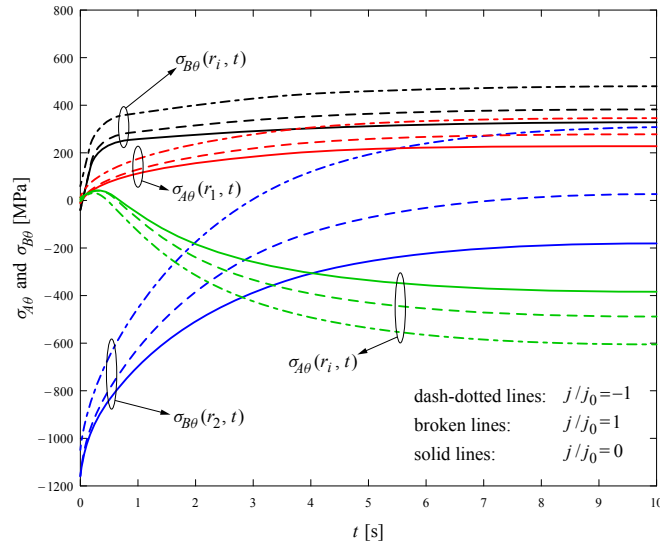


Figure 8. The dynamic hoop stress variations at the interface and the internal and external surfaces of laminated thermoelectric spherical shells (the applied temperature at the internal and external surfaces of shell are, respectively, 300 K and 1300 K).

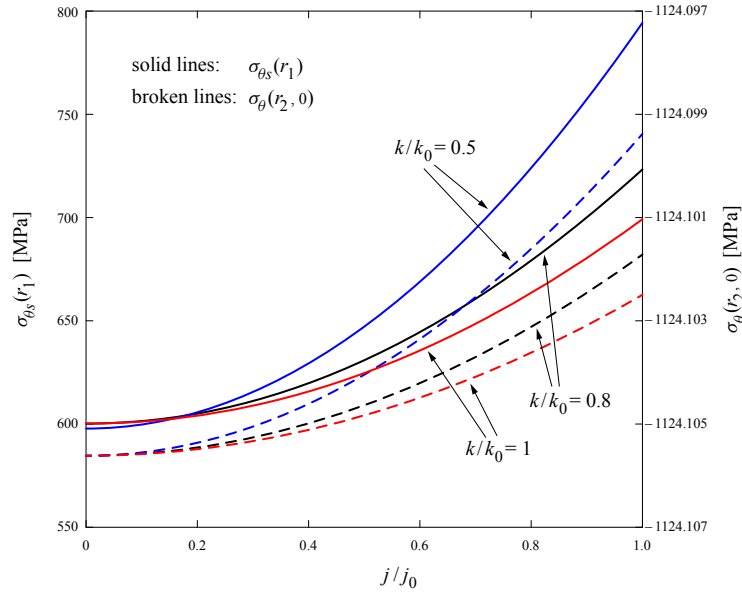


Figure 9. The influence of thermal conductivity on the maximum compressive and tensile hoop stresses in homogeneous thermoelectric spherical shell ($j_0 = C_0/r^2$ where $C_0 = 7500$, $\kappa_0 = 1.6 \text{ W m}^{-1} \text{ K}^{-1}$).

hoop stress of laminated shells in Figure 11. For laminated thermoelectric spherical shells, temperature is a function of the first and second power of electric current density j . In current case, maximum

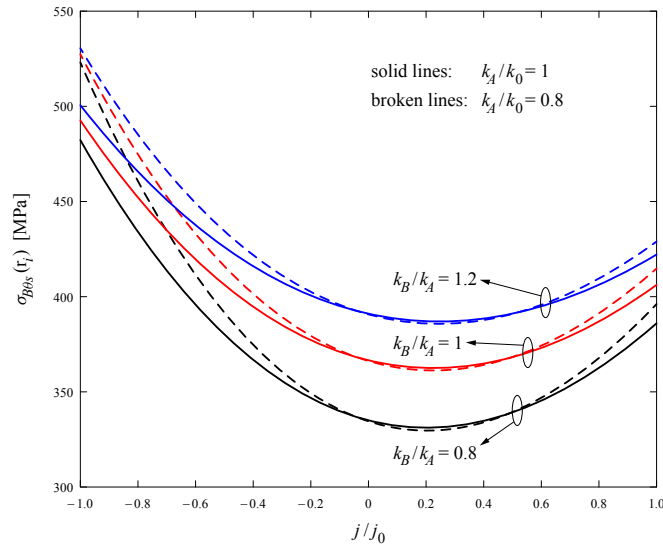


Figure 10. The influence of thermal conductivity on the maximum tensile hoop stress in laminated thermoelectric spherical shells ($j_0 = C_0/r^2$ where $C_0 = 7500$, $\kappa_0 = 1.6 \text{ W m}^{-1} \text{ K}^{-1}$).

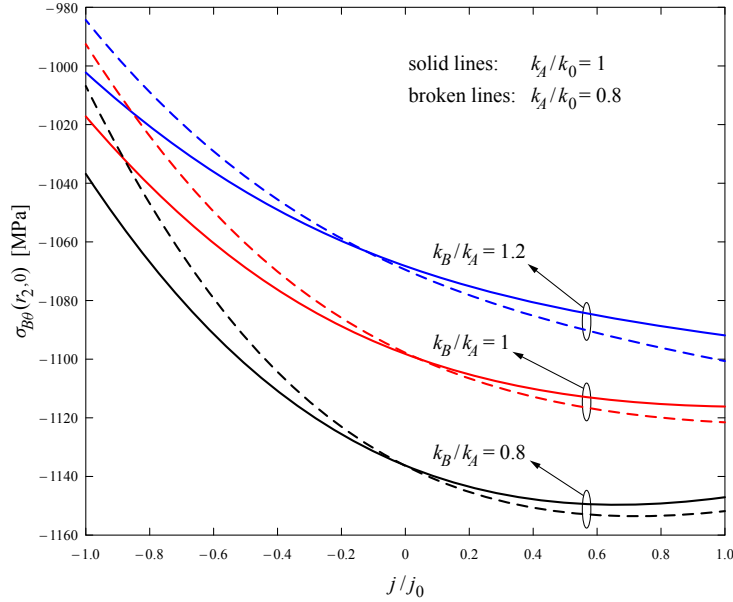


Figure 11. The influence of thermal conductivity on the maximum compressive hoop stress in laminated thermoelectric spherical shells ($j_0 = C_0/r^2$ where $C_0 = 7500$, $\kappa_0 = 1.6 \text{ W m}^{-1} \text{ K}^{-1}$).

tensile hoop stress reaches the lowest value when the value of j/j_0 is around 0.2. When the thermal conductivity ratio of shell A to shell B increases, the maximum tensile hoop stress increases and the maximum compressive hoop stress decreases.

4.4. The influences of the thickness of laminated shells. Figures 12 and 13 show, respectively, influence of the thickness of laminated shells on the maximum tensile and compressive hoop stresses. When the laminated thermoelectric spherical shells are used in thermal protection system of supersonic space shuttles, there is the large temperature difference between external surface and internal surface. Thus assumed that T_2 is equal to 1300 K and 1600 K and T_1 is equal to 300 K in this subsection. As mentioned above, $\sigma_{B\theta s}(r_i)$ and $\sigma_{B\theta}(r_2, 0)$ are, respectively, the maximum tensile and compressive hoop stresses of laminated shells in Figures 12 and 13. It is noted that increasing r_i means that the radial thickness of shell B becomes thinner and that of shell A becomes thicker when the radii of internal and external surfaces keep constant. The value of maximum tensile stress is the lowest when the interface is on the middle of laminated shell. It is noted that these lines do not intersect at one point for $T_2 = 1300 \text{ K}$ or 1600 K, as shown in Figure 13.

5. Conclusion

This work constructs a transient mechanical model for laminated thermoelectric spherical shells, considering the coupling of the heat transfer and electric conduction. Notably, a computational code with good human-machine dialogue interface was developed. The code allows us to graphically input data and output the results. The models can evaluate the thermal and mechanical characteristics of materials

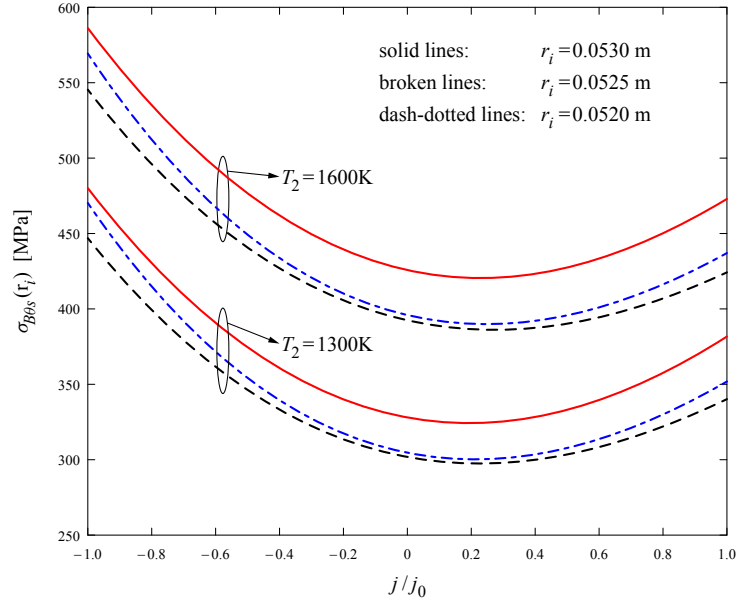


Figure 12. The influence of the thickness of laminated shells on the maximum tensile hoop stress in the thermoelectric spherical shell ($j_0 = C_0/r^2$ where $C_0 = 7500$, $r_1 = 0.05$ m, $r_2 = 0.055$ m, $T_1 = 300$ K).

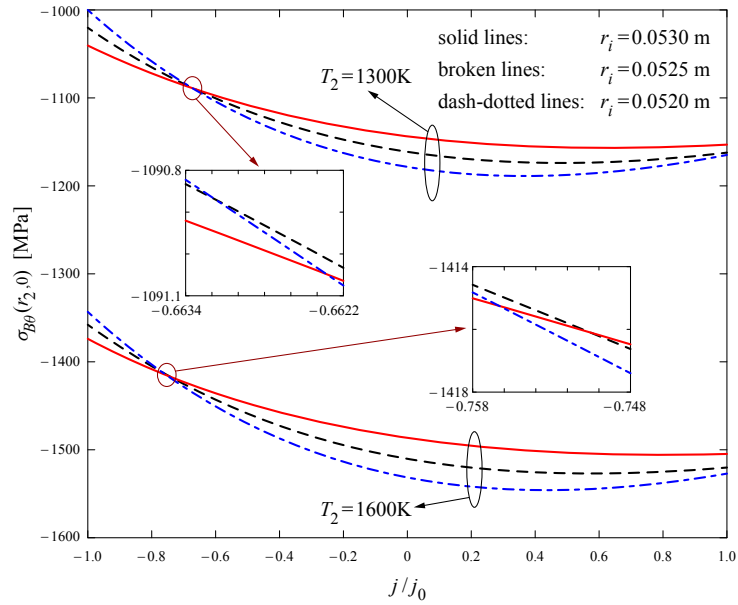


Figure 13. The influence of the thickness of laminated shells on the maximum compressive hoop stress in the thermoelectric spherical shell ($j_0 = C_0/r^2$ where $C_0 = 7500$, $r_1 = 0.05$ m, $r_2 = 0.055$ m, $T_1 = 300$ K).

for temperatures higher than 1300 K, which are very possibly happen thermal protection system of future supersonic space shuttle, and for temperatures as low as 77 K that is possible for high-temperature superconductors in space solar energy station. Numerical results show that specifying the applied electric current density may reduce the maximum tensile stress in the laminated shells. For laminated spherical shells, additional attention for the thermal conductivity ratio of shell A to shell B should be paid. If the thermal conductivity ratio of laminated shells increases, the maximum tensile hoop stress increases but the maximum compressive hoop stress decreases.

Appendix A

First, φ_{An} and φ_{Bn} should satisfy the following equations [Hahn and Özişik 2012]

$$\varphi_{An}(r_1) = 0, \quad (A1)$$

$$\varphi_{An}(r_i) = \varphi_{Bn}(r_i), \quad (A2)$$

$$\kappa_A \frac{d\varphi_{An}(r)}{dr} = \kappa_B \frac{d\varphi_{Bn}(r)}{dr}, \quad r = r_i, \quad (A3)$$

$$\varphi_{Bn}(r_2) = 0. \quad (A4)$$

Substituting $\varphi_{An}(r)$ and $\varphi_{Bn}(r)$ into (A1) to (A4) gives

$$0 = A_{1n} \frac{1}{r_1} \sin\left(\frac{\beta_n}{\sqrt{\omega_A}} r_1\right) + B_{1n} \frac{1}{r_1} \cos\left(\frac{\beta_n}{\sqrt{\omega_A}} r_1\right), \quad (A5)$$

$$A_{1n} \frac{1}{r_i} \sin\left(\frac{\beta_n}{\sqrt{\omega_A}} r_i\right) + B_{1n} \frac{1}{r_i} \cos\left(\frac{\beta_n}{\sqrt{\omega_A}} r_i\right) = A_{2n} \frac{1}{r_i} \sin\left(\frac{\beta_n}{\sqrt{\omega_B}} r_i\right) + B_{2n} \frac{1}{r_i} \cos\left(\frac{\beta_n}{\sqrt{\omega_B}} r_i\right), \quad (A6)$$

$$\begin{aligned} & \frac{\kappa_A}{\kappa_B} A_{1n} \left[\frac{\beta_n}{\sqrt{\omega_A}} \cos\left(\frac{\beta_n}{\sqrt{\omega_A}} r_i\right) - \frac{1}{r_i} \sin\left(\frac{\beta_n}{\sqrt{\omega_A}} r_i\right) \right] \\ & - \frac{\kappa_A}{\kappa_B} B_{1n} \left[\frac{1}{r_i} \cos\left(\frac{\beta_n}{\sqrt{\omega_A}} r_i\right) + \frac{\beta_n}{\sqrt{\omega_A}} \sin\left(\frac{\beta_n}{\sqrt{\omega_A}} r_i\right) \right] \\ & = A_{2n} \left[\frac{\beta_n}{\sqrt{\omega_B}} \cos\left(\frac{\beta_n}{\sqrt{\omega_B}} r_i\right) - \frac{1}{r_i} \sin\left(\frac{\beta_n}{\sqrt{\omega_B}} r_i\right) \right] \\ & - B_{2n} \left[\frac{1}{r_i} \cos\left(\frac{\beta_n}{\sqrt{\omega_B}} r_i\right) + \frac{\beta_n}{\sqrt{\omega_B}} \sin\left(\frac{\beta_n}{\sqrt{\omega_B}} r_i\right) \right], \quad (A7) \end{aligned}$$

$$0 = A_{2n} \frac{1}{r_2} \sin\left(\frac{\beta_n}{\sqrt{\omega_B}} r_2\right) + B_{2n} \frac{1}{r_2} \cos\left(\frac{\beta_n}{\sqrt{\omega_B}} r_2\right). \quad (A8)$$

Without loss of generality, we choose $A_{1n} = 1$ [Hahn and Özişik 2012] and A_{1n} , B_{1n} , A_{2n} and B_{2n} can be obtained as

$$A_{1n} = 1, \quad (A9)$$

$$B_{1n} = -\tan\left(\frac{\beta_n}{\sqrt{\omega_A}} r_1\right), \quad (A10)$$

$$A_{2n} = \frac{\cos(\beta_n/\sqrt{\omega_A} r_i) \tan(\beta_n/\sqrt{\omega_A} r_1) - \sin(\beta_n/\sqrt{\omega_A} r_i)}{\cos(\beta_n/\sqrt{\omega_B} r_i) \tan(\beta_n/\sqrt{\omega_B} r_2) - \sin(\beta_n/\sqrt{\omega_B} r_i)}, \quad (\text{A11})$$

$$B_{2n} = -A_{2n} \tan\left(\frac{\beta_n}{\sqrt{\omega_B}} r_2\right). \quad (\text{A12})$$

Equations (A5), (A6), (A7) and (A8) can be expressed in the matrix form. From the requirement that determinant of the coefficients in the matrix should be zero, values of β_n can be obtained.

Appendix B

Three different boundary conditions are considered: Case 1, both internal and external surfaces of laminated thermoelectric spherical shell are stress free; Case 2, internal surface of shell is fixed, and external surface is stress free; Case 3, both internal and external surfaces of shell are fixed. a_{11} , b_{12} , a_{21} and b_{22} are

$$a_{11} = \Omega_1 b_{12}, \quad (\text{B1})$$

$$b_{12} = \frac{r_i \Omega_3 - \Lambda_5}{\Lambda_1} + \frac{\Lambda_2}{\Lambda_1} b_{22}, \quad (\text{B2})$$

$$a_{21} = \Omega_3 + \Omega_2 b_{22}, \quad (\text{B3})$$

$$b_{22} = \frac{\Lambda_1 \Lambda_6 + \Lambda_3 (r_i \Omega_3 - \Lambda_5) - \Omega_3 \Lambda_1 \Lambda_7}{\Lambda_1 \Lambda_4 - \Lambda_2 \Lambda_3}, \quad (\text{B4})$$

where

$$\begin{aligned} \Lambda_1 &= r_i \Omega_1 + \frac{1}{r_i^2}, \quad \Lambda_2 = r_i \Omega_2 + \frac{1}{r_i^2}, \quad \Lambda_3 = \frac{E_A \Omega_1}{1 - 2\nu_A} - \frac{1}{r_i^3} \frac{2E_A}{1 + \nu_A}, \quad \Lambda_4 = \frac{E_B \Omega_2}{1 - 2\nu_B} - \frac{1}{r_i^3} \frac{2E_B}{1 + \nu_B}, \\ \Lambda_5 &= \frac{1 + \nu_A}{1 - \nu_A} \frac{\alpha_A}{r_i^2} \int_{r_1}^{r_i} \Delta T_A r^2 dr, \quad \Lambda_6 = -\frac{2\alpha_A E_A}{1 - \nu_A} \frac{1}{r_i^3} \int_{r_1}^{r_i} \Delta T_A r^2 dr, \quad \Lambda_7 = \frac{E_B}{1 - 2\nu_B}, \\ \Omega_1 &= \begin{cases} \frac{2(1-2\nu_A)}{r_1^3(1+\nu_A)}, & \text{for case 1,} \\ -\frac{1}{r_1^3}, & \text{for case 2 and case 3,} \end{cases} \quad \Omega_2 = \begin{cases} \frac{2(1-2\nu_B)}{r_2^3(1+\nu_B)}, & \text{for case 1 and case 2,} \\ -\frac{1}{r_2^3}, & \text{for case 3,} \end{cases} \\ \Omega_3 &= \begin{cases} \frac{2\alpha_B(1-2\nu_B)}{1-\nu_B} \frac{1}{r_2^3} \int_{r_i}^{r_2} \Delta T_B r^2 dr, & \text{for case 1 and case 2,} \\ -\frac{1+\nu_B}{1-\nu_B} \frac{\alpha_B}{r_2^3} \int_{r_i}^{r_2} \Delta T_B r^2 dr, & \text{for case 3.} \end{cases} \end{aligned}$$

Acknowledgment

This research was supported by the Research Innovation Fund of Shenzhen City of China (project nos. JCYJ20170413104256729, JCYJ20170811160538023), the National Natural Science Foundation of China (project nos. 11672084, 11602072, 11972133).

References

[Antonova and Looman 2005] E. E. Antonova and D. C. Looman, "Finite elements for thermoelectric device analysis in ANSYS", pp. 215–218 in *ICT 2005. 24th International Conference on Thermoelectrics* (Clemson), 2005.

- [Ching and Chen 2007] H. K. Ching and J. K. Chen, “Thermal stress analysis of functionally graded composites with temperature-dependent material properties”, *J. Mech. Mater. Struct.* **2**:4 (2007), 633–653.
- [Chowdhury et al. 2009] I. Chowdhury, K. Prasher, R. Lofgreen, G. Chrysler, S. Narasimhan, R. Mahajan, D. Koester, R. Alley, and R. Venkatasubramanian, “On-chip cooling by superlattice-based thin-film thermoelectrics”, *Nat. Nanotechnol.* **4** (2009), 235–238.
- [Clin et al. 2009] T. Clin, S. Turenne, D. Vasilevskiy, and R. A. Masut, “Numerical simulation of the thermomechanical behavior of extruded bismuth telluride alloy module”, *J. Electron. Mater.* **38**:7 (2009), 994–1001.
- [DiSalvo 1999] F. J. DiSalvo, “Thermoelectric cooling and power generation”, *Science* **285**:5428 (1999), 703–706.
- [Frostig and Thomsen 2007] Y. Frostig and O. T. Thomsen, “Buckling and nonlinear response of sandwich panels with a compliant core and temperature-dependent mechanical properties”, *J. Mech. Mater. Struct.* **2**:7 (2007), 1355–1380.
- [Gao et al. 2011] J.-L. Gao, Q.-G. Du, X.-D. Zhang, and X.-Q. Jiang, “Thermal stress analysis and structure parameter selection for a Bi_2Te_3 -based thermoelectric module”, *J. Electron. Mater.* **40**:5 (2011), 884–888.
- [Hahn and Özişik 2012] D. W. Hahn and M. N. Özişik, *Heat conduction*, 3rd ed., John, 2012.
- [Han et al. 2014] X.-Y. Han, J. Wang, and H.-F. Cheng, “Investigation of thermoelectric SiC ceramics for energy harvesting applications on supersonic vehicles leading-edges”, *Bull. Mater. Sci.* **37**:1 (2014), 127–132.
- [Hegde et al. 2012] G. M. Hegde, V. Kulkarni, M. Nagaboopathy, and K. P. J. Reddy, “Structure and morphology studies of chromium film at elevated temperature in hypersonic environment”, *Bull. Mater. Sci.* **35**:3 (2012), 341–345.
- [Huang and Duang 2000] B. J. Huang and C. L. Duang, “System dynamic model and temperature control of a thermoelectric cooler”, *Int. J. Refriger.* **23**:3 (2000), 197–207.
- [Jin 2013] Z.-H. Jin, “Buckling of thin film thermoelectrics”, *Int. J. Fract.* **180**:1 (2013), 129–136.
- [Kim et al. 2016] H. S. Kim, T. Wang, W. Liu, and Z. Ren, “Engineering thermal conductivity for balancing between reliability and performance of bulk thermoelectric generators”, *Adv. Funct. Mater.* **26**:21 (2016), 3678–3686.
- [Li et al. 2005] Y.-Z. Li, C. Wei, L. Yuan, and J. Wang, “Simulation of micro spacecraft active temperature control system using thermoelectric cooler”, *Chinese J. Mech. Eng.* **41** (2005), 149–152. in Chinese.
- [Liu et al. 2017a] Y. Liu, B. L. Wang, and C. Zhang, “Mechanical model for a thermoelectric thin film bonded to an elastic infinite substrate”, *Mech. Mater.* **114** (2017), 88–96.
- [Liu et al. 2017b] Y. Liu, B. L. Wang, and C. Zhang, “Thermoelastic behavior of a thermoelectric thin-film attached to an infinite elastic substrate”, *Philos. Mag.* **97**:1 (2017), 43–57.
- [Liu et al. 2018] Y. Liu, K. F. Wang, and B. L. Wang, “Mechanics modeling of dynamic characteristics of laminated thermoelectric cylindrical shells”, *Appl. Thermal Eng.* **136** (2018), 730–739.
- [Lu and Liu 2012] H.-B. Lu and W.-Q. Liu, “Numerical investigation on properties of attack angle for an opposing jet thermal protection system”, *Chinese Phys. B* **21**:8 (2012), 084401.
- [O’Brien et al. 2008] R. C. O’Brien, R. M. Ambrosi, N. P. Bannister, S. D. Howe, and H. V. Atkinson, “Safe radioisotope thermoelectric generators and heat sources for space applications”, *J. Nucl. Mater.* **377**:3 (2008), 506–521.
- [Pothin et al. 2018] R. Pothin, R. M. Ayril, A. Berche, P. Ziolkowski, G. Oppitz, and P. Jund, “Computational and experimental analysis on Te-doped ZnSb thermoelectric material”, *Mater. Res. Bull.* **101** (2018), 90–99.
- [Qin 2005] Q.-H. Qin, “2D Green’s functions of defective magneto-electroelastic solids under thermal loading”, *Eng. Anal. Bound. Elem.* **29**:6 (2005), 577–585.
- [Qiu et al. 2018] Y. Qiu, H. Wu, J. Wang, J. Lou, Z. Zhang, A. Liu, and G. Chai, “The enhanced piezoelectricity in compositionally graded ferroelectric thin films under electric field: a role of flexoelectric effect”, *J. Appl. Phys.* **123**:8 (2018), 084103.
- [Riffat and Ma 2003] S. B. Riffat and X. Ma, “Thermoelectrics: a review of present and potential applications”, *Appl. Thermal Eng.* **23**:8 (2003), 913–935.
- [Song et al. 2018] K. Song, H. P. Song, and C. F. Gao, “Unavoidable electric current caused by inhomogeneities and its influence on measured material parameters of thermoelectric materials”, *J. Appl. Phys.* **123**:12 (2018), 124105.
- [Tian et al. 2015] H. Tian, X. Sun, Q. Jia, X. Liang, G. Shu, and X. Wang, “Comparison and parameter optimization of a segmented thermoelectric generator by using the high temperature exhaust of a diesel engine”, *Energy* **84** (2015), 121–130.

- [Wang 2015] Y.-Z. Wang, “Effective material properties of thermoelectric composites with elliptical fibers”, *Appl. Phys. A Mater. Sci. Process.* **119**:3 (2015), 1081–1085.
- [Wang 2017] B. L. Wang, “A finite element computational scheme for transient and nonlinear coupling thermoelectric fields and the associated thermal stresses in thermoelectric materials”, *Appl. Thermal Eng.* **110** (2017), 136–143.
- [Wu et al. 2016] H. Wu, L. Li, G. Chai, F. Song, and T. Kitamura, “Three-dimensional thermal weight function method for the interface crack problems in bimaterial structures under a transient thermal loading”, *J. Therm. Stresses* **39**:4 (2016), 371–385.
- [Yang et al. 2014] Y. Yang, C. Gao, and J. Li, “The effective thermoelectric properties of core-shell composites”, *Acta Mech.* **225**:4-5 (2014), 1211–1222.
- [Zhang et al. 2016] G. Zhang, K. Jiao, Z. Niu, H. Diao, Q. Du, H. Tian, and G. Shu, “Power and efficiency factors for comprehensive evaluation of thermoelectric generator materials”, *Int. J. Heat Mass Transf.* **93** (2016), 1034–1037.
- [Zhang et al. 2017a] A. B. Zhang, B. L. Wang, J. Wang, J. K. Du, C. Xie, and Y. A. Jin, “Thermodynamics analysis of thermoelectric materials: influence of cracking on efficiency of thermoelectric conversion”, *Appl. Thermal Eng.* **127** (2017), 1442–1450.
- [Zhang et al. 2017b] A. B. Zhang, B. L. Wang, J. Wang, J. K. Du, and C. Xie, “Effect of cracking on the thermoelectric conversion efficiency of thermoelectric materials”, *J. Appl. Phys.* **121**:4 (2017), 045105.
- [Zhang et al. 2018a] A. B. Zhang, B. L. Wang, D. D. Pang, L. W. He, J. Lou, J. Wang, and J. K. Du, “Effects of interface layers on the performance of annular thermoelectric generators”, *Energy* **147** (2018), 612–620.
- [Zhang et al. 2018b] X. Zhang, D. Feng, J. He, and L.-D. Zhao, “Attempting to realize n-type BiCuSeO”, *J. Solid State Chem.* **258** (2018), 510–516.

Received 21 Nov 2018. Revised 8 Apr 2019. Accepted 1 Jun 2019.

YUE LIU: 750310541@qq.com

Harbin Institute of Technology, Shenzhen, 518055, China

KAI FA WANG: wangkf@hit.edu.cn

Harbin Institute of Technology, Shenzhen, 518055, China

BAOLIN WANG: wangbl@hit.edu.cn

Harbin Institute of Technology, Shenzhen, 518055, China

TUNING THE PROPAGATION CHARACTERISTICS OF THE TRAPPED AND RELEASED STRONGLY NONLINEAR SOLITARY WAVES IN 1-D COMPOSITE GRANULAR CHAIN OF SPHERES

BIN WU, HEYING WANG, XIUCHENG LIU, MINGZHI LI, ZONGFA LIU AND CUNFU HE

After a chain composed of light particles is inserted into a one-dimensional heavy granular chain of spheres, the formed composite chain can trap strongly nonlinear solitary waves (SNSWs) in a light sectional chain. The light sectional chain can reduce the peak amplitude of pulse waves imposed on the objects contacting with the end particle of the chain. However, the effects of the light sectional chain's properties on the propagation velocity and amplitude of both the trapped and output pulse waves are unclear. In this study, finite element models with optimal parameters were established to investigate the multireflection behaviors of the output pulse waves. Both the simulation and experimental results demonstrated that the light sectional chain could act as a physical regulator to tune the properties of the output pulse waves in the composite chain. When the material of the light particle was fixed, both the propagation velocity and amplitude of the output pulse waves exhibited the exponentially downward trend as the number of light particles increased. Compared to the light sectional chain of Brass, the PTFE chain could cause more serious attenuation on the amplitude of the pulse waves and reduce the propagation velocity of the output pulse waves. Similar phenomena had been reported in simulation results only at the nanoscale. Even at the macroscale, the investigated composite chain could quantitatively tune the propagation characteristics of the trapped and output pulse waves by adjusting the material and number of light particles.

1. Introduction

Strongly nonlinear solitary waves (SNSWs), which are derived from the nonlinearity of the Hertzian contact interactions between spherical particles, in one-dimensional granular chains have been widely explored due to the unique properties [Nesterenko 1983; Daraio et al. 2006a; Potekin et al. 2013; Nesterenko et al. 2005], such as independence of their width on amplitude and strong dependence of speed on amplitude. Wave dynamics in one-dimensional granular chains have been extensively investigated in the last twenty years to reveal the behavior of wave propagation in the granular chains and various potential applications have been reported, such as the design of metamaterials and metadevices [Gantzounis et al. 2013; Kim et al. 2017; Xu and Nesterenko 2017; Raney et al. 2016], nondestructive material evaluations [Rizzo et al. 2015], energy harvesting [Li and Rizzo 2015a; 2015b; Rizzo and Li 2017], and even medical hyperthermia [Spadoni and Daraio 2010]. The effects of particle material properties and impact condition on the formation and propagation velocity of SNSWs supported by 1-D chain of homogeneous elastic spherical particles have been reported [Meidani et al. 2015; Ngo et al. 2011; 2013; Khatri et al. 2012].

Keywords: 1-D composite granular chain, strongly nonlinear solitary waves, propagation characteristics tuning, energy trapping.

To reveal the wave propagation behavior in granular chains subjected to external impact, Nguyen and Brogliato [2014] and Brogliato [2016] published monographs to introduce and summarize the available theoretical approaches and computation tools. Theoretical expression about the energetical coefficient of restitution related with plastic (residual) indentation are first given in [Nguyen and Brogliato 2014]. Further study was reported by Zhao et al. [2008] to clarify the wave behavior in a column of beads colliding against a wall through adjusting the energetical restitution coefficient of a bistiffness compliant contact model. Falcon et al. [1998] found that spheres could be modelled as rigid bodies with localized deformation based on the Hertz' elasticity at the contact points. Kuninaka and Hayakawa [2009] partially determined dissipation during binary collision of nanoparticles through molecular dynamics and macroscopic collision model. Takato et al. [2018] obtained inelastic contact force between nanoparticles based on Hertz contact mechanics by molecular dynamics model. Many finite element methods had been developed to simulate the propagation properties of waves in one-dimensional particle chains [Musson and Carlson 2014; 2016; Ngo et al. 2011; Kim et al. 2015] since the attenuation caused by the plastic deformation generated between contacting particles could be calculated more accurately [Musson and Carlson 2014; 2016].

The composite granular chain with multisectional chains of spherical particles endows pulse waves with certain propagation characteristics [Przedborski et al. 2015; Vergara 2005; Hong and Xu 2002] and can act as a container to trap the energy of pulse waves in a particular section of chain [Nesterenko et al. 1995; Daraio et al. 2006b; Sen et al. 2008; Carretero-González et al. 2009]. In a composite granular chain of spherical particles, which is divided into two heavy sections and one light section, the leakage of trapped energy demonstrates a power-law behavior over time [Hong 2005; Wang et al. 2007; Xu and Zheng 2017]. The power-law behavior of the trapped energy release is attributed to the back-and-forth reflection of the sequence of pulse waves bouncing between the heavy-light and light-heavy interfaces. The bouncing behavior of the output pulse waves predicted by the theoretical model [Xu and Zheng 2017; Khatri 2012] was not confirmed or discussed by experimental tools yet. In addition, no dissipation on collisions is taken into account, so it is predicted that the output pulse waves move freely in the light section of chain without energy dissipation. The prediction remains to be experimentally explored.

Daraio et al. [2006b] experimentally investigated the reflection and transmission behaviors of pulse waves at the interface between steel particle and PTFE particle in composite granular chains. When pulse waves passed through heavy steel particles and entered the light PTFE section of chain, pulse waves decompose into a sequence of solitary waves with slower velocity and lower amplitude than that of incident pulse waves. In the design of a fine granular protector, the amplitude of the final output pulse waves of the composite granular chain is more concerned, but the energy dissipation and velocity variation of pulse waves in the light chain are seldom considered [Daraio et al. 2006b]. The effect of the number of particles in the light chain on the features of output pulse waves is still unknown.

The behavior of solitary waves propagating along the light section of chain in 1-D composite granular chain constructed by inserting a series of short single-walled carbon nanotubes into C_{60} system was simulated at the nanoscale [Xu and Zheng 2017]. A concept of energy tunnel was proposed based on the truth that both the propagation velocity and the energy carried by the solitary waves continuously decayed as the number of the carbon nanotubes increased. The interesting phenomenon of energy tunnel arose from the increase in the internal energy in carbon nanotubes with the consumption of the energy

of solitary waves passing through carbon nanotubes, but the phenomenon had not been verified at the macroscale [Xu and Zheng 2017].

Therefore, in this study, it is hypothesized that the energy tunnel phenomenon occurs in 1-D composite granular chain of particles at the macroscale. Both the finite element simulation and proof-of-concept experiments were performed to investigate the propagation characteristics of the trapped and output pulse waves in 1-D composite granular chain of particles. The simulation and experimental results confirmed the hypothesis. During the propagation of output pulse waves in the light sectional chain, the propagation velocity of pulse waves successively decreased due to the accumulation effect of the deformation energy storage. As the number of light particles increased, both the propagation velocity and amplitude of the output pulse waves in the end heavy chain demonstrated the exponentially downward trend.

This paper is organized as follows. In Section 2, based on Hertzian contact theory, the pulse waves in 1-D composite granular chain of spheres as well as the reflections of the output pulse waves are introduced. In Section 3, finite element models are established and the parameters of the models are optimized. The propagation characteristics of the trapped and output pulse waves is numerically investigated and discussed. In Section 4, the experimental setup is presented and simulation results are compared with experimental results. Finally, the conclusion is drawn in Section 5.

2. Fundamental theory

One-dimensional granular chain is a collection of macroscopic discrete particles whose dimensions are comparable to those of the overall system and so large that the thermal motion of particles may be ignored [Nesterenko 1983]. In a monatomic granular chain composed of N spherical particles shown in Figure 1 (top), the applied static force F_0 results in a small deformation at the contact area of adjacent particles and a relative displacement of δ_0 between the centers of two adjacent particles is generated. Under the action of an external impact F_d imposed along the particle alignment direction, the displacement of the center of individual particle is u_n ($n = 1, 2, \dots, N$). If the chain is uncompressed ($F_0 = 0$) or weakly precompressed ($F_0 \ll F_d$, resulting in $|u_{n+1} - u_n|/\delta_0 \gg 1$), the formation of strongly nonlinear solitary waves (SNSWs) in the chain is dominated by Hertzian contact law due to the balance of dispersion and interparticle nonlinearity. The contact force F between two adjacent particles is expressed as [Hertz 1881; Nesterenko 2001]

$$F(\delta) = \begin{cases} A\delta^{3/2}, & \delta > 0 \\ 0, & \delta < 0, \end{cases} \quad (1)$$

where δ represents the relative displacement of the centers of two adjacent particles. The contact stiffness A during compression can be calculated as [Nesterenko 2001]

$$A = \frac{4E_1E_2(1/R_1 + 1/R_2)^{-1/2}}{3[E_2(1 - \nu_1^2) + E_1(1 - \nu_2^2)]},$$

where R_1 and R_2 are the radii of the particles, and E_1 , E_2 , ν_1 , and ν_2 are Young's modulus and Poisson's ratio of the two particles' material, respectively. The motion equation for each particle is

$$\ddot{u}_n = A(\delta_0 - u_n + u_{n-1})^{3/2} - A(\delta_0 - u_{n+1} + u_n)^{3/2}. \quad (2)$$

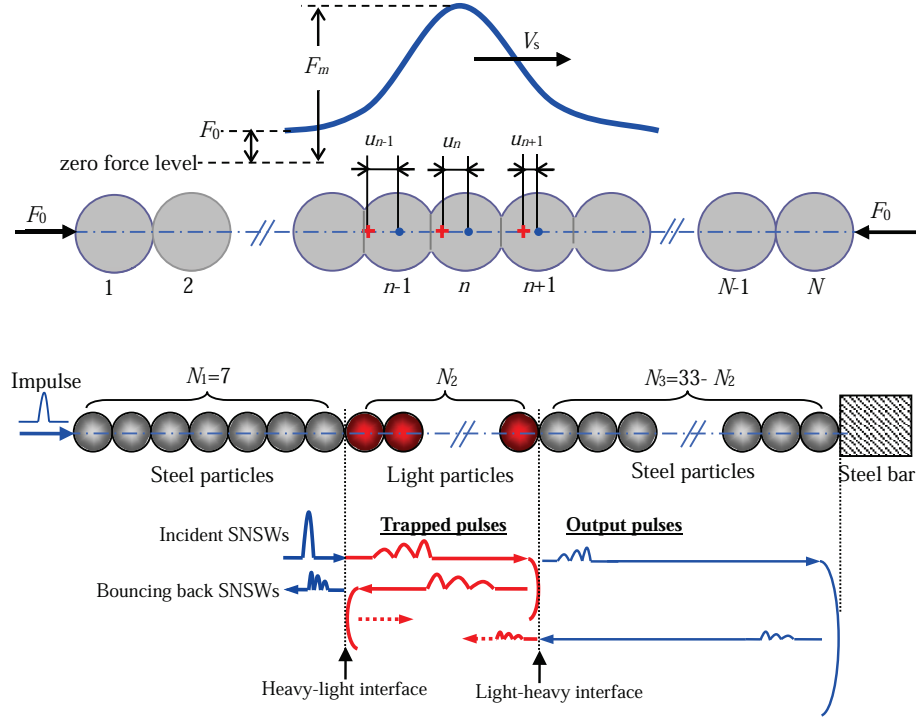


Figure 1. One-dimensional diagram of uniform granular chain (top) and composite granular chain for supporting strongly nonlinear solitary waves (bottom).

In a 1-D chain composed of identical spherical particles, the propagation velocity of SNSWs V_s can be expressed as a function of the ratio of static and the maximum dynamic force $f_r = F_m/F_0$, where F_m includes static precompression force F_0 [Nesterenko 2001]:

$$V_s = 0.9314 \left(\frac{4E^2 F_0}{a^2 \rho^3 (1 - \nu^2)^2} \right)^{1/6} \frac{1}{(f_r^{2/3} - 1)} \left\{ \frac{4}{15} [3 + 2f_r^{5/3} - 5f_r^{2/3}] \right\}^{1/2}. \quad (3)$$

When the chain is uncompressed, equation (3) can be simplified as

$$V_s = 0.6802 \left(\frac{2E}{a \rho^{3/2} (1 - \nu^2)} \right)^{1/3} F_d^{1/6}. \quad (4)$$

The maximum contact force F_m among the particles during the propagation of solitary waves remains constant in nondissipative systems [Nesterenko 2001]. In reality, energy dissipation is unavoidable. However, it is still difficult to accurately predict energy dissipation of SNSWs along its propagation due to the factors of contact plasticity, inelastic restitution of the particles, reflection at interface, and friction between the chain and its holder [Wang and Nesterenko 2015; Rosas and Lindenberg 2003; Rosas et al. 2008]. Therefore, in the subsequent finite element simulation, the propagation behavior of pulse waves in 1-D granular chain was only investigated for nondissipative systems. Energy attenuation of pulse waves along its propagation in the composite chain was evaluated by experimental tools.

In the case, the composite granular chain is composed of a total of 40 spherical particles which have the identical diameter of 10 mm and can be divided into three sections. Seven steel particles are placed in the first section of the chain (referred to heavy section) to generate a pulse close to steady strongly nonlinear solitary wave when impact force applied on the first particle is of significantly short duration or due to impact by striker with mass equal or less than mass of particles in the chain. The second section of the chain includes a certain amount (varying in the range of 3–24) of particles of lower Young's modulus and density (referred as light section) compared to steel particles. The third section of the chain (heavy section) is also composed of steel particles and its last particle directly contacts with a steel bar.

The propagation of the pulse waves along the composite granular chain is more complex than that in a chain composed of identical particles. It is already known that the incident SNSWs from the heavy sectional chain are transformed into an oscillatory pulse which on later stage is split into a sequence of strongly nonlinear solitary waves [Nesterenko et al. 1995; Daraio et al. 2006b; Sen et al. 2008]. Energy reflections do not occur unless pulse waves travel from the light section to the heavy section. As a result, the sequence of pulse waves propagating along the light section bounce back and forth between the light-heavy and heavy-light interfaces (Figure 1, bottom), as suggested by the reported interesting energy trapping behavior [Wang et al. 2007]. Due to the energy trapping effect, the peak amplitude of the output pulse waves transmitted into the third sectional chain is lower than that of the impact applied on the first sectional chain. Therefore, the composite granular chain can work as a protector to mitigate the strength of external impact applied on the steel bar.

For the composite granular chain shown in Figure 1 (bottom), the energy of pulse waves transmitted into the third section of the chain can be tunable by employing particles of different materials. To improve the performance of the protector, soft materials with a small Young's modulus and density are generally recommended for the light sectional chain. However, the effect of the length of the light section on the quantity of energy transmitted into the third section of the chain has not been reported yet. In addition, the reflection behavior of the trapped sequence of pulse waves at the light-heavy interface was also not experimentally observed or discussed.

3. Numerical modeling

3.1. Descriptions of the FE model. To simulate the propagation of pulse waves in the composite granular chain, inspired by the report in [Musson and Carlson 2014], finite element models were developed in COMSOL. The penalty function was employed to solve the contact problem among the particles in 1-D granular chain of spherical particles. First, a 1-D chain composed of identical elastic spherical particles was modeled to optimize the mesh size, penalty factor, and solver by comparing the simulated results with that predicted with (4). Second, a 1-D composite granular chain shown in Figure 1 (bottom) was modeled with the optimal numerical scheme to investigate the propagation characteristics of the trapped and output pulses.

Two-dimensional axial symmetry operation was applied in the model shown in Figure 2 (top left) to obtain a 1-D chain composed of fifteen stainless steel particles. The properties of the stainless steel are listed in Table 1. To save computational resources, the diameter of the particles was selected as 4.76 mm, which was smaller than that of the particles in the composite granular chain. The last particle at the

bottom of the chain contacted with a stainless steel cylinder, whose diameter and height were about 20 mm and 10 mm, respectively.

Starting from the contact point between two adjacent particles, the arc with the length of $\pi/18$ is defined as the contact boundary. A contact pair shown in Figure 2 (top right) consists of a *source* and *destination* contact boundary. The contact force was transferred from the *source* contact boundary to the *destination* contact boundary. The displacements of the centers of all the particles were fixed as zero in r direction to limit the rotation and translation. The fixed constraint was applied to the bottom surface of the cylinder and the remaining surfaces of the entire model had free boundaries.

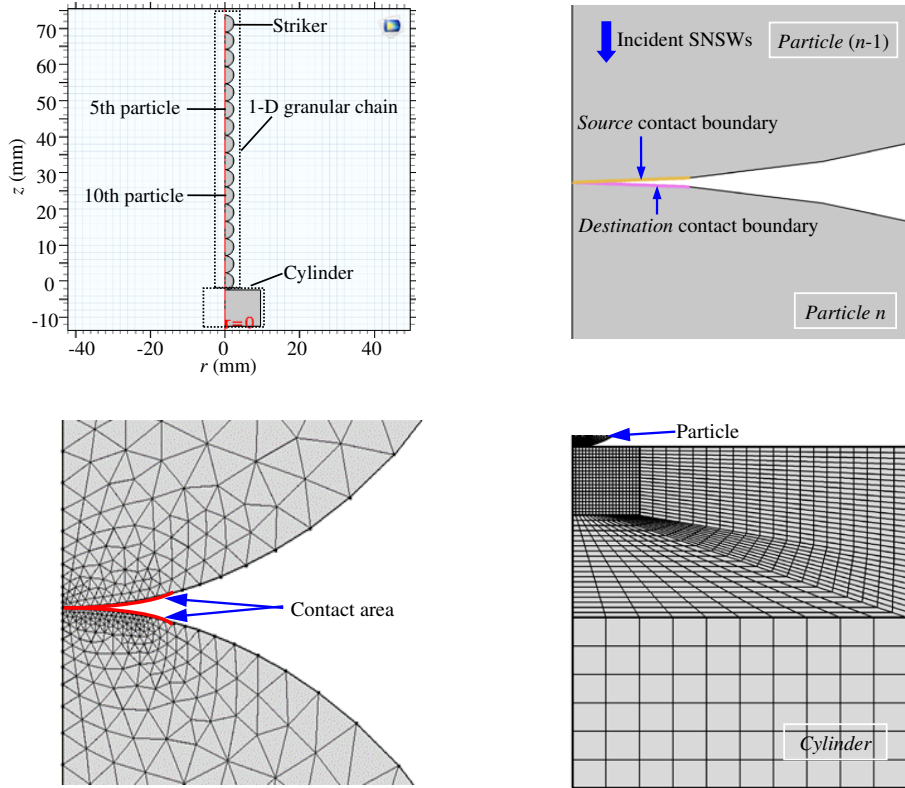


Figure 2. Finite element simulation model of 1-D granular chain. Top: geometrical configuration of the entire model (left) and the contact pair (right). Bottom: meshing results of the contact area between two adjacent particles (left) and between the last particle of the chain and the bottom cylinder (right).

materials	density (g/m ³)	Young's modulus (GPa)	Poisson's ratio
stainless steel	7925	209	0.28
Brass	8398	103	0.34
PTFE	1870	1.46	0.46

Table 1. Properties of granular materials.

The contact pair was discretized with free three-noded elements and then the particles were meshed with free triangular nodes by the automatic generation algorithm. To achieve the more accurate solution, the *destination* contact boundary employed the finer mesh than that of the *source* contact boundary after repeated trials. The meshing operation of the cylinder was performed according to the procedures recommended by the case of *Cylinder Roller Contact* in COMSOL. In the cylinder, the mesh size near the contact area between the particle and the top surface of the cylinder was much smaller than that of the region far away from the contact area.

The top stainless steel particle of the chain acted as a striker with an initial speed of 0.626 m/s and then the propagation of SNSWs in the chain was simulated in the finite element models established above. The mesh size and the penalty factor, which determined the performance of the penalty function on solving the contact problem, were optimized with the single factor analysis method. The relative errors between the simulated velocities of the SNSWs and the results predicted by the Hertzian contact theory were used as a criterion for evaluating the effects of the mesh size and penalty factor on the computation accuracy of the FE model.

3.2. Parameter optimization.

3.2.1. Mesh size. The penalty factor was fixed as a constant with a value of $\eta = 1$ and *constant* solver was employed to give the solutions of the solitary wave propagation. The profile of the contact force at the interaction zone between two adjacent particles was extracted from the simulation results when the minimal mesh size (β) of the model was gradually reduced from 0.2 mm to 0.01 mm.

The contact force profiles corresponding to the contact pair of the 5th and 6th particles and the contact pair of the tenth and eleventh particles are plotted in Figure 3. The time interval between the two peaks of the contact force profiles is divided by the distance of five-time diameters of the particle to estimate the propagation velocity (V_{sw}) of the solitary wave.

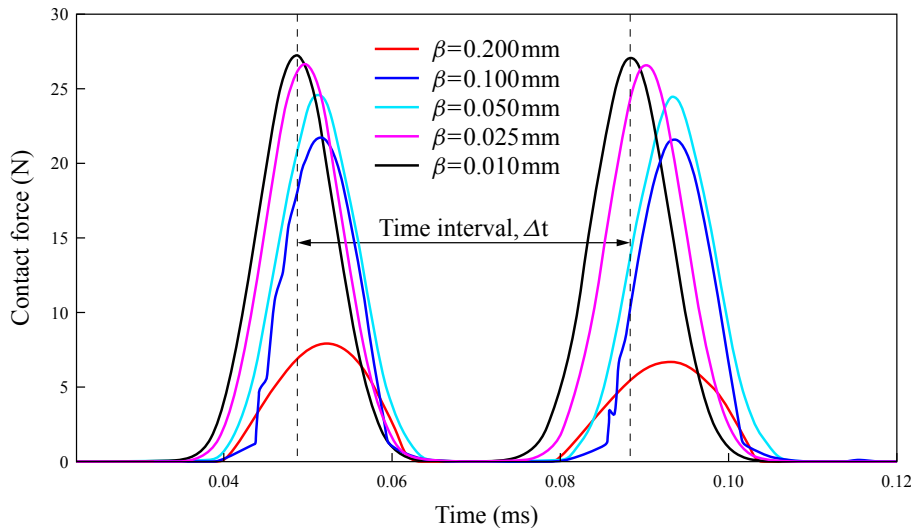


Figure 3. Profiles of contact force obtained from the model with different mesh sizes.

model no.	mesh size (mm)	contact force (N)	velocity of SNSWs		time consumption
			value (m/s)	error (%)	
1	0.2–0.4	7.92	590	20.00	9 min 24 s
2	0.1–0.2	21.71	569	2.14	18 min 49 s
3	0.05–0.1	24.55	566	4.63	31 min 16 s
4	0.025–0.05	26.62	586	2.58	1 h 9 min
5	0.01–0.02	27.17	599	0.76	3 h 21 min 3 s

Table 2. Performances of the models with different mesh sizes.

As indicated in (4), for the granular chain of a given material, the velocity of the SNSWs is proportional to the value of $F_m^{1/6}$. When the minimal mesh size of 0.2 mm was selected in the model, the obtained maximum contact force was significantly lower than that of other cases and a relative error between the simulated value of V_{sw} and the theoretical velocity of SNSWs was 20.00%. When the minimal mesh size decreased from 0.2 mm to 0.1 mm, the maximum contact force in the simulation substantially increased from 7.92 N to 21.71 N and the obtained relative error of the velocity was decreased to 2.14%. However, the profile of the contact force was not smooth especially in the initial stage of the contact, indicating that the model could not achieve the high-precision simulation of the propagation of SNSWs.

Therefore, the model utilizing the smaller mesh size was further investigated. When the minimal mesh size was alternatively selected as 0.05 mm, 0.025 mm, and 0.01 mm, the calculation error of velocity and simulation time are summarized in Table 2. The FE models are solved by the COMSOL software which is run in a computer with two processors of Intel Xeon X5650 (RAM: 64 GB, main frequency: 2.66 GHz). In the simulation cases, the minimal calculation error of 0.67% could be realized after the longest simulation time with the smallest mesh size of 0.01 mm (Case 5). To balance the calculation error and simulation time, the minimal mesh size was selected as 0.025 mm in the subsequent simulation even though the calculation error was slightly higher than that in Case 5. The total number of degree of freedom in the selected model solution is 115634.

3.2.2. Penalty factor and solver. For the purpose of solving some optimization problems, an additional function (penalty function) should be added to the original objective function in order to obtain an augmented objective function [Greenberg and Pierskalla 1970]. The penalty function is generally used to transform the constrained optimization problem into an unconstrained optimization problem [Bellmore et al. 1970; Hinch and Saint-Jean 1999]. The penalty factor η is an important parameter of the penalty function.

The similar simulation procedure as previously discussed is used to investigate the effect of penalty factor η in the penalty function on the calculation error of velocity. When the value of η gradually increases from 1.1 to 1.5 with a step of 0.1, the high-quality contact force profiles can be obtained with the *Constant* solver. The simulated values of F_m and velocities are listed in Table 3. The relative error of velocity continuously decreases from 2.47% to 1.57% as the penalty factor increases from 1.1 to 1.4. As for the case of $\eta = 1.5$, the simulation results show that the maximum contact force further increases compared to the case of $\eta = 1.4$, thus leading to an increase in propagation velocity according to (4). Surprisingly, the velocity estimated from the simulation results is about 590 m/s (Table 3), which

penalty factor, η	contact force, F (N)	velocity of solitary wave, V_{sw}	
		values (m/s)	errors (%)
1.1	26.71	587	2.47
1.2	26.77	590	2.01
1.3	26.81	592	1.70
1.4	26.86	592	1.57
1.5 (constant solver)	27.36	590	2.36
1.5 (automatic solver)	27.22	595	0.40

Table 3. Results obtained from the model with different penalty factors and solvers.

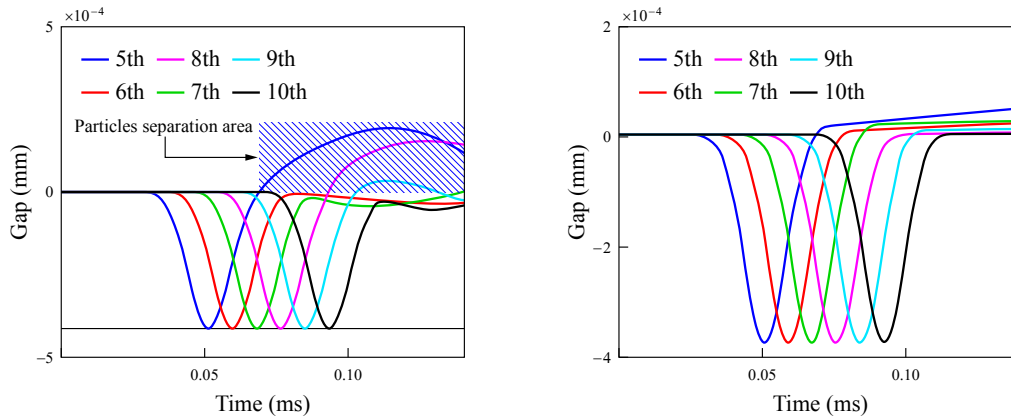


Figure 4. Gap between two adjacent particles obtained from the model with constant solver (left) and automatic solver (right).

is slower than that obtained in the case of $\eta = 1.4$. As shown in Figure 4, the value of the gap at the contact point between the 5th and 6th particles remains to be negative due to the compression before the time of 0.6 ms. Then it has the positive sign, indicating that the separation phenomenon of particles occurs during the propagation of SNSWs. The similar behavior can also be observed from the results extracted at the 10th contact pair. The separation phenomenon of the particles may induce the second impact among the particles [Wang and Nesterenko 2015; Rosas et al. 2008].

To solve the problem of the *Constant* solver, the *Automatic* solver was adopted to provide more convincing results (Figure 4, right). Although slight separation could be concluded from the profile of gap versus time, the velocity calculation error significantly decreased to 0.4% (Table 3).

With the optimal parameters of mesh size ($\beta = 0.025$ mm) and penalty factor ($\eta = 1.5$), the solutions of the model provided by *Automatic* solver were used to explore the relationship between the contact force and the relative displacement between the centers of the 5th and 6th particles. The results in Figure 5 demonstrated that the dependency of the dynamic contact force on the relative displacement yielded a power function with an exponent of 1.554, which was close to the value of 1.5 suggested by the Hertzian contact law [Hertz 1881]. The results in Figure 5 and Table 3 proved that the finite element model with

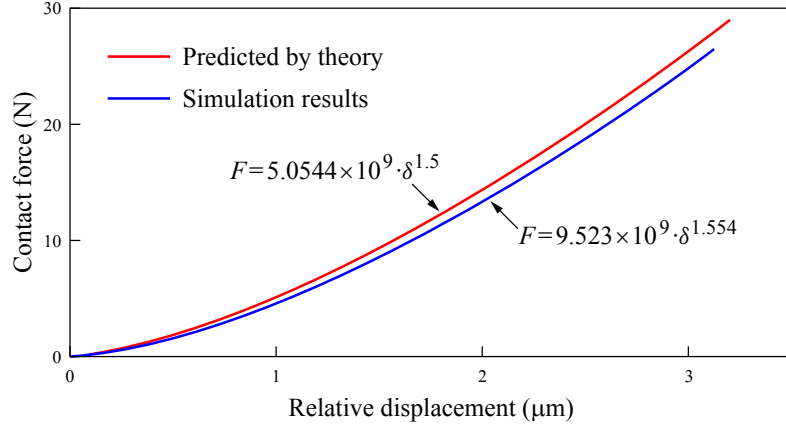


Figure 5. Comparison between the predicted and simulated results of the dependency of contact force on the relative displacement.

optimal parameters and solver could be applied to accurately simulate the propagation of SNSWs in 1-D granular chain of spheres.

3.3. Propagation behaviors of pulse waves in composite chain. The finite element model together with its optimal parameters (mesh size, penalty factor, and solver) obtained in Section 3.2 was used to investigate the propagation of SNSWs in a 1-D composite granular chain of spheres (Figure 1, bottom). In the simulation model, the material of the spherical particles in the light sectional chain was alternatively selected as Brass and PTFE, whose properties are listed in Table 1.

The initial speed of the striker particle was fixed at 0.626 m/s in all the simulation models. Due to the energy trapping effect governed by the light-heavy and heavy-light interfaces, the propagation behaviors of pulse waves in the light chain was complicated. So far, the multiple reflection behavior of the pulse waves in the light chain was seldom explored with simulation tools. Here, as an example, the simulation results obtained from the model with $N_2 = 6$ particles in the light section were extracted to observe the reflection behavior of output pulse waves in the composite chain. The profile of contact force versus time shown in Figure 6 was extracted from the contact pair formed with the third and fourth particles in the light section.

In the model with light sectional chain of Brass, one round of back and forth reflections can be identified in the profile shown in Figure 6 (left). The pulse waves reflected from the light-heavy interface are in the form of a single impulse, which is referred to back reflection wave (BRW). When the BRW returns to the heavy-light interface, partial energy of BRW will be reflected again to generate the forth reflection wave (FRW). When the original incident pulse wave passes through the heavy-light interface, as suggested in the previous study [Hong and Xu 2002], partial energy of the pulse waves is stored in the particles in the form of compressive deformation. The BRW imposes propulsive force onto the contact area at the heavy-light interface and consequently deformation recovery happens, thus leading to additional impact on the light section and generating a delayed forth reflection wave (DFRW) (Figure 6, left).

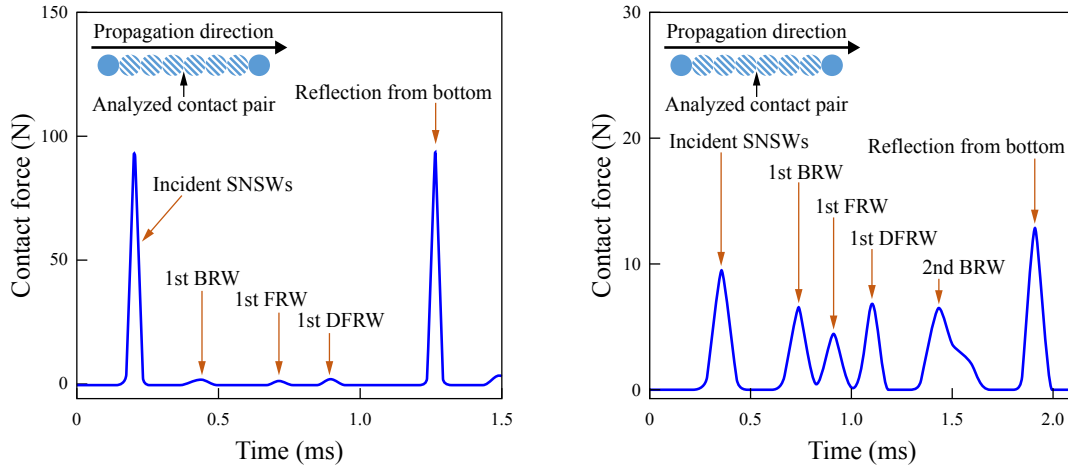


Figure 6. Profiles of contact force extracted at the analyzed contact pair in the model of composite chain with the light sectional chain of Brass (left) and PTFE (right).

Similar reflection behavior of pulse waves at the first round of back and forth reflections can be observed in the case with the light chain of PTFE. As sketched in Figure 6 (right), two reflected wave packets are respectively generated by the mechanism of interface reflection and the deformation recovery and can be identified during the process of the first forth reflection of pulse waves. The contact stiffness between PTFE particle and steel particle was much lower than that between Brass particle and steel particle. As emphasized in the previous report [Daraio et al. 2006b], for the fixed incident pulse waves, the amount of energy reflected at the contact pair with low contact stiffness was higher than that in the case of high contact stiffness. Accordingly, in the case with the light chain of PTFE, the ratio of energy of BRW to the output pulses transmitted through the light-heavy interface was much higher than that in the case with the light chain of Brass. In other words, a larger amount of energy of pulse waves was trapped inside the light chain of PTFE compared to that in the light chain of Brass.

In the third section of the composite chain, the propagation velocity of pulse waves was determined by the peak contact force at the contact pair [Rosas and Lindenberg 2003]. In the composite chain with the light chain of PTFE, the amount of energy (or peak contact force) transmitted into the third section chain was much smaller than that in the case with light chain of Brass. Thus, the output pulses of the composite chain propagated more slowly in the case with the light chain of PTFE than that in the case of Brass chain. The propagation time of the pulse waves reflected from the bottom cylinder was around 1.85 ms, which was longer than the propagation time of 1.25 ms estimated from Figure 6 (left). The delay of pulse waves reflected from the bottom cylinder allowed the longer time window to observe the reflection behavior of pulse waves in the light section and the second back reflection wave could also be captured (Figure 6, right).

To carefully investigate the energy transmission efficiency (λ) of pulse waves at the light-heavy interface, the profiles of contact force were extracted at the second contact pair in the third sectional chain. With the increase in the number of light particles, the results of the contact force profiles for the cases with the light chains of Brass and PTFE are plotted in Figure 7 (left and right, respectively). The amount

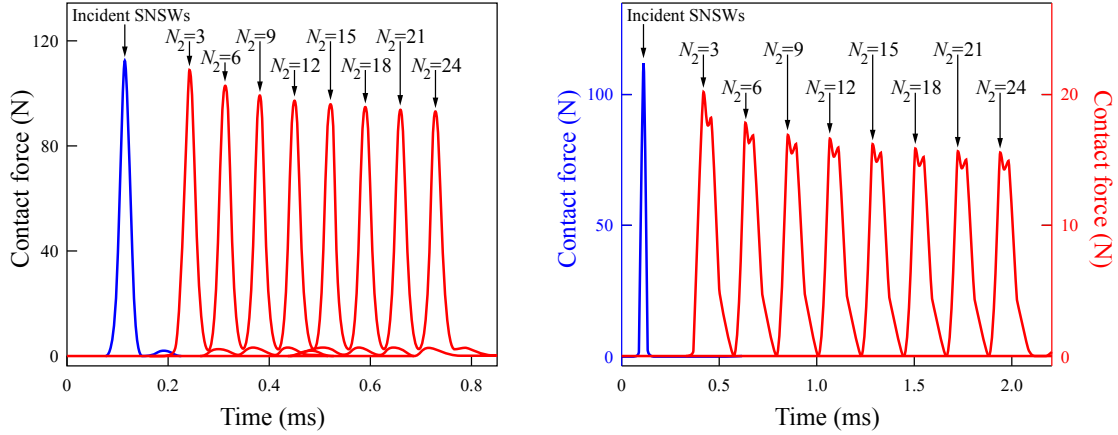


Figure 7. Effects of the number of light particles on the transmitted pulse waves in the model of composite chain with the light section of Brass (left) and PTFE (right).

of the energy of incident pulse waves was fixed due to the constant impact condition imposed on the composite chain. Hence, the effect of the length of light section on the energy transmission efficiency λ could be evaluated by verifying the results in Figure 7.

For both cases of the composite chain, the peak contact force of the transmitted (or output) pulses demonstrated the exponentially decreasing trend with the increase in the value of N_2 . During the propagation of the pulse waves in the first chain, the total energy density of the pulse waves (including the elastic energy and kinematic energy) retains as constant (see Figure 8). This confirmed that the energy dissipation caused by material attenuation and friction is not considered in the simulation model.

However, the total energy of the pulse waves in the light section chain demonstrates successive attenuation as the propagation of the pulse waves (see Figure 8). The maximum compressive stress in the contact area of Brass sphere is changed from 1200 MPa to 1110 MPa, and for the PTFE sphere is changed from 35 MPa to 20 MPa. The Young's modulus of the light spheres is much lower than that of the steel spheres used in the first chain. As a result, the maximum compressive stress in the contact area of two light spheres may exceed the yield strength of the material of Brass and PTFE. Therefore, plastic

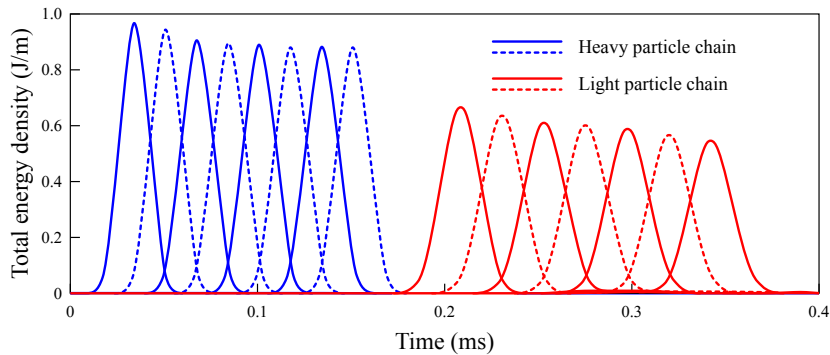


Figure 8. The total energy density of the heavy particles and light particles.

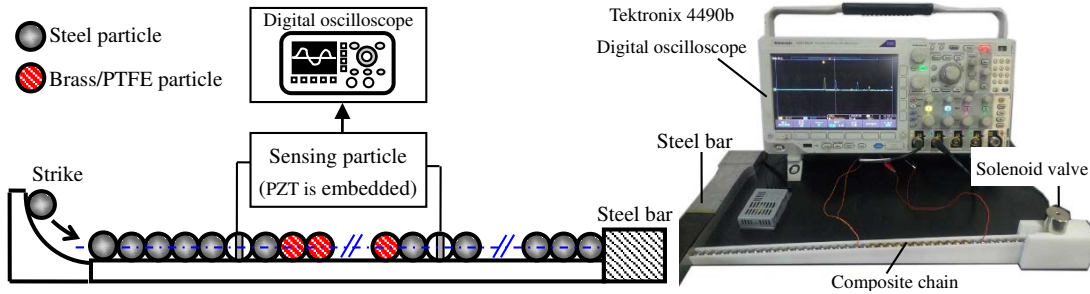


Figure 9. Schematic diagram (left) and photo of the experimental setup (right).

deformation occurs at the contact area of two light spheres and part of the pulse waves' energy is stored in the form of plastic deformation. The decay of the output energy of pulses was attributed to plastic deformation when pulse waves passed through the light section [Musson and Carlson 2014; 2016].

The profile of the contact force extracted from the case of PTFE showed two peaks. We believed that the collision between the incident pulse waves and the BRW induced secondary collisions at the light-heavy interface. The time interval between the two collisions was short and the output pulses were overlapped to exhibit the double-peak character. The double-peak character in the waveform of transmitted pulse waves was confirmed by subsequent experimental results. The decay of energy transmission efficiency is quantitatively analyzed in Section 4.

4. Experimental verification and discussion

Experimental observation of the propagation behavior of pulse waves was conducted in a one-dimensional composite granular chain composed of 40 spherical particles (see in Figure 9). The diameter of all the particles was identical to that used in the simulation model. The configuration of the composite chain was also identical to that illustrated in Figure 1 (bottom). Two sensing particles were respectively used to replace the sixth particle in the first sectional chain and the second particle in the third sectional chain to sense the propagation of pulse waves. Each sensing particle was made by cutting a steel particle into halves and embedding a PZT wafer between the two halves [Daraio et al. 2006a; 2006b]. The sandwich structure of the sensing particle was boned with epoxy and the voltage signals output by the PZT wafer was acquired by a Tektronix 4490b digital oscilloscope with a sampling frequency of 10 MHz.

The well-arranged composite chain was placed in a plastic holder with an inclination angle of 3° in order to achieve the intact contact between every two adjacent particles [Leonard et al. 2014]. A solenoid valve was used to hold and release the steel striker particle with a diameter of 10 mm. The distance between the center of striker and the center of the first particle in the chain was adjusted to be around 20 mm and the estimated speed of the impact imposed on the composite chain was about 0.626 m/s.

The light chain was alternatively fulfilled with the particles of Brass and PTFE. Figure 10 shows the signal of pulse waves measured by the two sensing particles in the experimental tests. As predicted with the simulation results in Figure 7, in the two cases, the peak voltage induced by the propagation of pulse waves demonstrated the exponential attenuation behavior with the increase in the propagation distance.

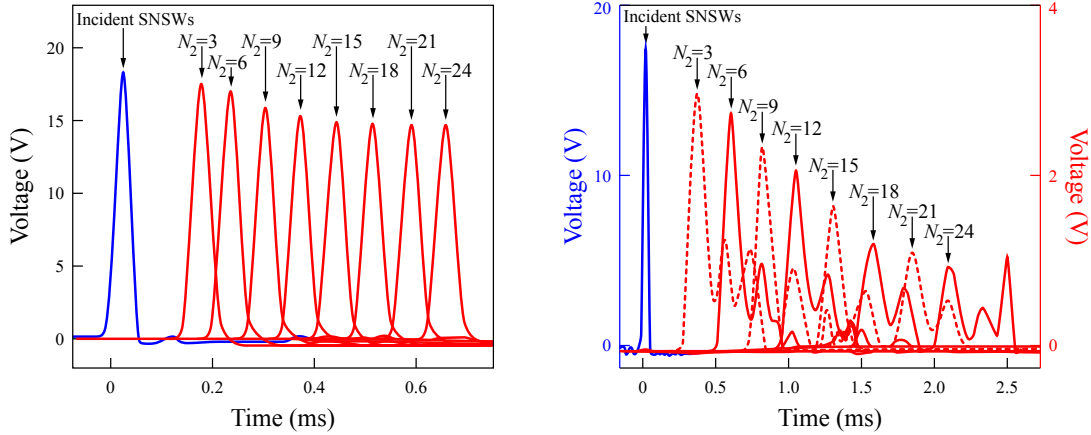


Figure 10. Effects of the number of light particles on the transmitted pulse waves in the experiment of composite chain with the light section of Brass (left) and PTFE (right).

The ratio of the peak amplitude of incident pulse waves to the peak amplitude of output pulses was treated as the energy transmission efficiency (λ). In addition, the time interval (Δt) between the peak voltages of the incident and transmitted pulse waves were estimated. The propagation distance (L) was divided by the time interval (Δt) to estimate the propagation velocity (V_{sw}) of the pulse waves. The estimated results of λ and V_{sw} are plotted in Figure 11.

Experimental results were compared with simulation results based on the results shown in Figure 11. For the composite chain with the light section of Brass, the measured propagation velocity of pulse waves exponentially decayed from the initial value of 469 m/s ($N_2 = 3$) to around 424 m/s ($N_2 = 24$). The measured value of V_{sw} was lower than the predicted value and the error might come from the mismatch of material properties between the true particle and the particle in the simulation model. Among the investigated cases, the maximum relative error between the simulated propagation velocity and measured propagation velocity was about 4.2%. In the case with the light chain of PTFE, the curve fitted to the predicted data was close to that fitted to the measured data (Figure 11, right). In the initial stage ($N_2 = 1$), the prediction error of propagation velocity was about 17.1%. When the value of N_2 was larger than 3, the prediction error dramatically decreased below 2.3%, indicating that the previously established finite element models possessed the good prediction performance in the propagation velocity of the pulse waves in the investigated composite chain.

In the studied two cases of the composite chain, both the measured and predicted results of energy transmission efficiency showed the exponential decay trend. Hence, the light sectional chain had the effects of velocity reduction and amplitude attenuation on the input pulse waves transmitted from the first sectional chain. The propagation velocity and the amplitude of the output pulses were determined by both the material properties and the number of light particles in the simulation results. Erenow, the phenomenon similar to that demonstrated in Figure 11, was only reported at the nanoscale in simulation studies. The results in Figure 11 indicated that even at the macroscale the investigated composite chain was able to quantitatively tune the amplitude and propagation velocity of pulse waves by adjusting the number of particles in the light sectional chain.

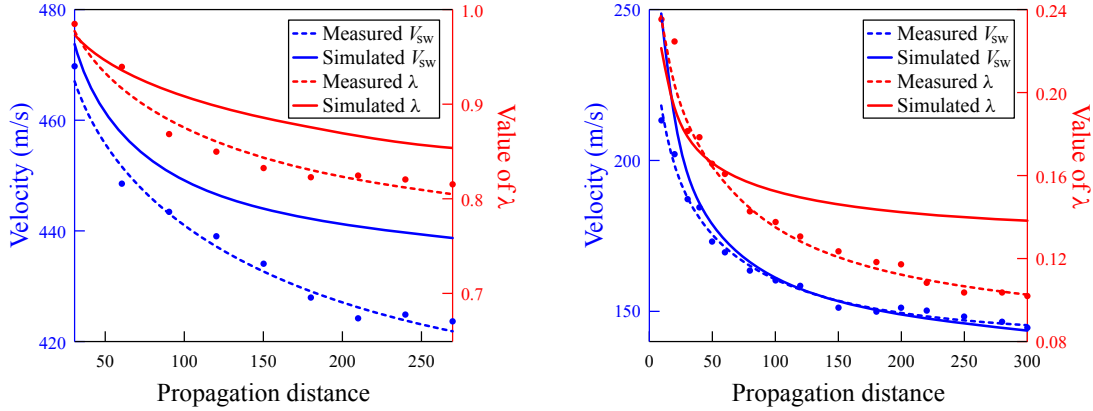


Figure 11. Amplitude and velocity obtained by the experiment and simulation for the particles with the low elastic modulus: Brass particles (left) and PTFE particles (right).

At the initial stage ($N_2 = 3$), the prediction error of the value of λ was as small as 0.53% for the case with the light chain of Brass and a prediction error was 1.3% for the case with the light chain of PTFE. When the number of Brass (or PTFE) particles was larger than 6, the difference between the measured energy transmission efficiency and the predicted energy transmission efficiency increased with the increase in the propagation distance. In the experiment, along with the propagation of pulse waves in the light chain, the inevitable friction between the particles and the plastic holder caused additional energy dissipation to pulse waves. The longer propagation distance corresponded to the more dissipated energy. The accumulation effect of the energy dissipation led to the continuously increasing error between the measured and predicted values of λ .

The light sectional chain can act as a physical regulator to control the properties of the output pulse waves. When the number of light particles was fixed, compared to the light Brass chain, the light PTFE chain caused the more serious attenuation on the amplitude of the pulse waves and more significantly decreased the propagation velocity of the output pulse waves. When the material of the light particle was selected, the dependency of both the propagation velocity and the amplitude of the output pulse waves on the number of light particle could be predicted with the proposed finite element simulation model. However, the predicted values of V_{sw} and λ were larger than corresponding actual results because the mechanical frictions in the system of composite chain were not considered in the simulation model.

5. Conclusion

The propagation characteristics of the trapped and output strongly nonlinear solitary waves in 1-D composite granular chain of spherical particles were explored in this study. Finite element simulation was performed with optimal mesh size, penalty factor, and solver and the obtained results confirmed that the energy tunnel behavior, which had been reported at the nanoscale [Xu and Zheng 2017], was also applicable to the composite chain at the macroscale. More precisely, the propagation velocity and the amplitude of the finally output pulse waves in the composite chain could be tuned by adjusting the material and the number of light particles.

Though the energy dissipation caused by viscoplastic deformation of particles or friction was not considered in the simulation model, the total energy of the pulse waves in the light section chain successively decays as the propagation of the pulse waves. This is because plastic deformation occurs at the contact area of two light spheres and part of the pulse waves' energy is stored in the form of plastic deformation. As a result, the propagation velocity and the amplitude of the output pulse waves could be exponentially reduced by increasing the number of light particles.

Verification experiments were performed to confirm the conclusions obtained from simulations. However, in the experiments unavoidable energy dissipation of SNSWs along its propagation occurs due to viscoplastic deformation of particles and friction. Thus the finite element simulation results has a systemic overestimation in predicting the propagation velocity and the amplitude of the output pulse waves. However, the established finite element simulation model could be used to investigate the multireflection behavior of the output pulse waves and reveal the effects of the configuration and material of the light sectional chain on the properties of the output pulse waves.

Acknowledgements

This study was supported by the National Natural Science Foundation of China (Project No. 11572011) and the International Research Cooperation Seed Fund of Beijing University of Technology (Project No. 2018A07).

References

- [Bellmore et al. 1970] M. Bellmore, H. J. Greenberg, and J. J. Jarvis, "Generalized penalty-function concepts in mathematical optimization", *Oper. Res.* **18**:2 (1970), 229–252.
- [Brogliato 2016] B. Brogliato, *Nonsmooth mechanics: models, dynamics and control*, Springer, London, 2016.
- [Carretero-González et al. 2009] R. Carretero-González, D. Khatri, M. A. Porter, P. G. Kevrekidis, and C. Daraio, "Dissipative solitary waves in granular crystals", *Phys. Rev. Lett.* **102**:2 (2009), 024102.
- [Daraio et al. 2006a] C. Daraio, V. F. Nesterenko, E. B. Herbold, and S. Jin, "Tunability of solitary wave properties in one-dimensional strongly nonlinear phononic crystals", *Phys. Rev. E* **73**:2 (2006), 026610.
- [Daraio et al. 2006b] C. Daraio, V. F. Nesterenko, E. B. Herbold, and S. Jin, "Energy trapping and shock disintegration in a composite granular medium", *Phys. Rev. Lett.* **96**:5 (2006), 058002.
- [Falcon et al. 1998] E. Falcon, C. Laroche, S. Fauve, and C. Coste, "Collision of a 1-D column of beads with a wall", *Eur. Phys. J. B* **5**:1 (1998), 111–131.
- [Gantzounis et al. 2013] G. Gantzounis, M. Serra-Garcia, K. Homma, J. M. Mendoza, and C. Daraio, "Granular metamaterials for vibration mitigation", *J. Appl. Phys.* **114**:9 (2013), 093514.
- [Greenberg and Pierskalla 1970] H. J. Greenberg and W. P. Pierskalla, "Surrogate mathematical programming", *Oper. Res.* **18**:5 (1970), 924–939.
- [Hertz 1881] H. Hertz, "On the contact of elastic solids", *J. Reine Angew. Math.* **92** (1881), 156–171.
- [Hinch and Saint-Jean 1999] E. J. Hinch and S. Saint-Jean, "The fragmentation of a line of balls by an impact", *Proc. R. Soc. Lond. A* **455**:1989 (1999), 3201–3220.
- [Hong 2005] J. Hong, "Universal power-law decay of the impulse energy in granular protectors", *Phys. Rev. Lett.* **94**:10 (2005), 108001.
- [Hong and Xu 2002] J. Hong and A. Xu, "Nondestructive identification of impurities in granular medium", *Appl. Phys. Lett.* **81**:25 (2002), 4868–4870.
- [Khatri 2012] D. Khatri, *Non-destructive evaluation of material system using highly nonlinear acoustic waves*, Ph.D. thesis, California Institute of Technology, 2012, Available at <https://thesis.library.caltech.edu/7022/>.

- [Khatrri et al. 2012] D. Khatrri, D. Ngo, and C. Daraio, “Highly nonlinear solitary waves in chains of cylindrical particles”, *Granul. Matter* **14**:1 (2012), 63–69.
- [Kim et al. 2015] E. Kim, R. Chaunsali, H. Xu, J. Jaworski, J. Yang, P. G. Kevrekidis, and A. F. Vakakis, “Nonlinear low-to-high-frequency energy cascades in diatomic granular crystals”, *Phys. Rev. E* **92**:6 (2015), 062201. also in arXiv:1505.05556v2.
- [Kim et al. 2017] E. Kim, J. Yang, H.-Y. Hwang, and C. W. Shul, “Impact and blast mitigation using locally resonant woodpile metamaterials”, *Int. J. Impact Eng.* **101** (2017), 24–31.
- [Kuninaka and Hayakawa 2009] H. Kuninaka and H. Hayakawa, “Simulation of cohesive head-on collisions of thermally activated nanoclusters”, *Phys. Rev. E* **79**:3 (2009), 031309. also in arXiv:0812.5035v2.
- [Leonard et al. 2014] A. Leonard, C. Chong, P. G. Kevrekidis, and C. Daraio, “Traveling waves in 2D hexagonal granular crystal lattices”, *Granul. Matter* **16**:4 (2014), 531–542. also in arXiv:1305.0171v1.
- [Li and Rizzo 2015a] K. Li and P. Rizzo, “Energy harvesting using an array of granules”, *J. Vib. Acoust. (ASME)* **137**:4 (2015), 041002.
- [Li and Rizzo 2015b] K. Li and P. Rizzo, “Energy harvesting using arrays of granular chains and solid rods”, *J. Appl. Phys.* **117**:21 (2015), 215101.
- [Meidani et al. 2015] M. Meidani, E. Kim, F. Li, J. Yang, and D. Ngo, “Tunable evolutions of wave modes and bandgaps in quasi-1D cylindrical phononic crystals”, *J. Sound Vib.* **334** (2015), 270–281.
- [Musson and Carlson 2014] R. W. Musson and W. Carlson, “Simulation of solitary waves in a monodisperse granular chain using COMSOL multiphysics: localized plastic deformation as a dissipation mechanism”, *Granul. Matter* **16**:4 (2014), 543–550.
- [Musson and Carlson 2016] R. W. Musson and W. Carlson, “Plastic deformation in a metallic granular chain”, *Comput. Part. Mech.* **3**:1 (2016), 69–82.
- [Nesterenko 1983] V. F. Nesterenko, “Propagation of nonlinear compression pulses in granular media”, *J. Appl. Mech. Tech. Phys.* **24**:5 (1983), 733–743.
- [Nesterenko 2001] V. F. Nesterenko, *Dynamics of heterogeneous materials*, Springer-Verlag, New York, 2001.
- [Nesterenko et al. 1995] V. F. Nesterenko, A. N. Lazaridi, and E. B. Sibiriyakov, “The decay of soliton at the contact of two “acoustic vacuums””, *J. Appl. Mech. Tech. Phys.* **36**:2 (1995), 166–168.
- [Nesterenko et al. 2005] V. F. Nesterenko, C. Daraio, E. B. Herbold, and S. Jin, “Anomalous wave reflection at the interface of two strongly nonlinear granular media”, *Phys. Rev. Lett.* **95**:15 (2005), 158702.
- [Ngo et al. 2011] D. Ngo, D. Khatrri, and C. Daraio, “Highly nonlinear solitary waves in chains of ellipsoidal particles”, *Phys. Rev. E* **84**:2 (2011), 026610.
- [Ngo et al. 2013] D. Ngo, S. Griffiths, D. Khatrri, and C. Daraio, “Highly nonlinear solitary waves in chains of hollow spherical particles”, *Granul. Matter* **15**:2 (2013), 149–155.
- [Nguyen and Brogliato 2014] N. S. Nguyen and B. Brogliato, *Multiple impacts in dissipative granular chains*, Springer, Berlin, 2014.
- [Potekin et al. 2013] R. Potekin, K. R. Jayaprakash, D. M. McFarland, K. Remick, L. A. Bergman, and A. F. Vakakis, “Experimental study of strongly nonlinear resonances and anti-resonances in granular dimer chains”, *Exp. Mech.* **53**:5 (2013), 861–870.
- [Przedborski et al. 2015] M. A. Przedborski, T. A. Harroun, and S. Sen, “Localizing energy in granular materials”, *Appl. Phys. Lett.* **107**:24 (2015), 244105. also in arXiv:1601.02656v1.
- [Raney et al. 2016] J. R. Raney, N. Nadkarni, C. Daraio, D. M. Kochmann, J. A. Lewis, and K. Bertoldi, “Stable propagation of mechanical signals in soft media using stored elastic energy”, *Proc. Nat. Acad. Sci. USA* **113**:35 (2016), 9722–9727.
- [Rizzo and Li 2017] P. Rizzo and K. Li, “Analysis of the geometric parameters of a solitary waves-based harvester to enhance its power output”, *Smart Mater. Struct.* **26** (2017), 075004.
- [Rizzo et al. 2015] P. Rizzo, A. Bagheri, and E. La Malfa Ribolla, “Highly nonlinear solitary waves for the NDT of slender beams”, pp. 173–177 in *Emerging Technologies in Non-Destructive Testing VI: Proceedings of the 6th International Conference on Emerging Technologies in Nondestructive Testing* (Brussels), 2015.

- [Rosas and Lindenberg 2003] A. Rosas and K. Lindenberg, “Pulse dynamics in a chain of granules with friction”, *Phys. Rev. E* **68**:4 (2003), 041304. also in arXiv:cond-mat/0307080v1.
- [Rosas et al. 2008] A. Rosas, A. H. Romero, V. F. Nesterenko, and K. Lindenberg, “Short-pulse dynamics in strongly nonlinear dissipative granular chains”, *Phys. Rev. E* **78**:5 (2008), 051303.
- [Sen et al. 2008] S. Sen, J. Hong, J. Bang, E. Avalos, and R. Doney, “Solitary waves in the granular chain”, *Phys. Rep.* **426**:2 (2008), 21–66.
- [Spadoni and Daraio 2010] A. Spadoni and C. Daraio, “Generation and control of sound bullets with a nonlinear acoustic lens”, *Proc. Nat. Acad. Sci. USA* **107**:16 (2010), 7230–7234.
- [Takato et al. 2018] Y. Takato, M. E. Benson, and S. Sen, “Small nanoparticles, surface geometry and contact forces”, *Proc. R. Soc. A* **474**:2211 (2018), 20170723.
- [Vergara 2005] L. Vergara, “Scattering of solitary waves from interfaces in granular media”, *Phys. Rev. Lett.* **95**:10 (2005), 108002.
- [Wang and Nesterenko 2015] S. Y. Wang and V. F. Nesterenko, “Attenuation of short strongly nonlinear stress pulses in dissipative granular chains”, *Phys. Rev. E* **91**:6 (2015), 062211.
- [Wang et al. 2007] P. J. Wang, J. H. Xia, Y. D. Li, and C. S. Liu, “Crossover in the power-law behavior of confined energy in a composite granular chain”, *Phys. Rev. E* **76**:4 (2007), 041305.
- [Xu and Nesterenko 2017] Y. Xu and V. F. Nesterenko, “Strongly nonlinear stress waves in dissipative metamaterials”, *AIP Conf. Proc.* **1793**:1 (2017), 120005.
- [Xu and Zheng 2017] J. Xu and B. Zheng, “Quantitative tuning nanoscale solitary waves”, *Carbon* **111** (2017), 62–66.
- [Zhao et al. 2008] Z. Zhao, C. Liu, and B. Brogliato, “Energy dissipation and dispersion effects in granular media”, *Phys. Rev. E* **78**:3 (2008), 031307.

Received 24 Jan 2019. Revised 1 Aug 2019. Accepted 7 Aug 2019.

BIN WU: wb@bjut.edu.cn

College of Mechanical Engineering and Applied Electronics Technology, Beijing University of Technology,
Chaoyang District, 100 Pingleyuan Village, Beijing 100124, China

HEYING WANG: whyne2015@emails.bjut.edu.cn

College of Mechanical Engineering and Applied Electronics Technology, Beijing University of Technology,
Chaoyang District, 100 Pingleyuan Village, Beijing 100124, China

XIUCHENG LIU: xiuchliu@bjut.edu.cn

College of Mechanical Engineering and Applied Electronics Technology, Beijing University of Technology,
Chaoyang District, 100 Pingleyuan Village, Beijing 100124, China

MINGZHI LI: lmz1001@emails.bjut.edu.cn

College of Mechanical Engineering and Applied Electronics Technology, Beijing University of Technology,
Chaoyang District, 100 Pingleyuan Village, Beijing 100124, China

ZONGFA LIU: lzf@haust.edu.cn

College of Civil Engineering, Henan University of Science and Technology, Luolong District, 263 Kaiyuan Avenue,
Luoyang 471023, China

CUNFU HE: hecunfu@bjut.edu.cn

College of Mechanical Engineering and Applied Electronics Technology, Beijing University of Technology,
Chaoyang District, 100 Pingleyuan Village, Beijing 100124, China

ACCURATE BUCKLING ANALYSIS OF PIEZOELECTRIC FUNCTIONALLY GRADED NANOTUBE-REINFORCED CYLINDRICAL SHELLS UNDER COMBINED ELECTRO-THERMO-MECHANICAL LOADS

SHENGBO ZHU, YIWEN NI, JIABIN SUN,
ZHENZHEN TONG, ZHENHUAN ZHOU AND XINSHENG XU

An accurate axial buckling analysis of piezoelectric functionally graded nanotube-reinforced composite cylindrical shells under combined electro-thermo-mechanical loads is performed in the Hamiltonian system. The Hamiltonian form of governing buckling equations is established based on the symplectic geometry and Reissner's shell theory. Exact solutions are expressed in terms of symplectic eigenfunctions which have five possible forms. A detailed parametric study is conducted to demonstrate the influences of geometrical parameters, boundary conditions, reinforcement nanotubes and their distribution patterns on the symplectic eigenfunctions. Furthermore, the effects of distribution patterns of nanotubes, electric voltage and temperature rise on critical buckling stresses are investigated.

1. Introduction

In recent years, nanocomposite have received increasingly attention in both scientific and industrial communities [Zeighampour and Tadi Beni 2014; Tadi Beni et al. 2015; 2016; Tadi Beni and Mehralian 2016; Mehralian et al. 2016a; 2016b; 2017a; 2017b; Mehralian and Tadi Beni 2016; 2017a; 2017b; 2018; Jamal-Omidi and ShayanMehr 2017; Kheibari and Beni 2017; Hajmohammad et al. 2018; Kamarian et al. 2018; Rafiee et al. 2019]. Piezoelectric polymers, as a kind of piezoelectric composite, usually offer low density, high toughness and high electromechanical effects, which cannot be realized with piezoelectric ceramics or single crystals [Ueberschlag 2001]. Recently, in order to enhance the performance of such piezoelectric polymers, boron nitride nanotubes (BNNTs) and carbon nanotubes (CNTs) with functionally graded (FG) distribution in the matrix were introduced to reinforce the piezoelectric polymer [Ghorbanpour Arani et al. 2016; Mohammadimehr et al. 2016]. The strength, electrical and thermal conductivity of piezoelectric FG nanotube reinforced composites (NTRC) are greatly improved so that the proposed composites become potential candidates for fabricating the key component of intelligent devices and equipment, such as FG-NTRC hybrid laminated beams [Fan and Wang 2016], FG-NTRC beams with piezoelectric layers [Rafiee et al. 2013; Yang et al. 2015; Wu et al. 2016] and FG-NTRC plates with piezoelectric layers [Rafiee et al. 2014; Wu and Chang 2014; Mohammadimehr et al. 2016; Hajmohammad et al. 2017; Keleshteri et al. 2017]. The cylindrical shells made of piezoelectric FG-NTRC are also ones of the important fundamental components. Hence, the stability analysis of piezoelectric FG-NTRC cylindrical shells under combined electro-thermo-mechanical loads is of great importance for the design and evaluation of the fundamental structures.

Zhenhuan Zhou is the corresponding author.

Keywords: axial buckling, functionally graded materials, piezoelectric nanotube-reinforced composite, cylindrical shell, analytical solution, symplectic method.

The nature for buckling of piezoelectric cylindrical shells has been well studied in the literature. Mohammadimehr et al. [2014], Ganesan and Kadoli [2003], Sheng and Wang [2010] investigated the buckling of piezoelectric FG cylindrical shells by using the finite element method. Mirzavand et al. [2016], Fard and Bohlooly [2017], Sun et al. [2016; 2018] investigated the axial buckling, thermal buckling and postbuckling of piezoelectric cylindrical shells by the Galerkin method. Dai and Zheng [2011] analyzed the buckling and postbuckling of piezoelectric fiber reinforced composite cylindrical shell by the Ritz energy method. Mehralian et al. [2016a] investigated the buckling of anisotropic piezoelectric cylindrical shells by using the generalized differential quadrature (GDQ) method. Farajpour et al. [2017] investigated the vibration, buckling and smart control of piezoelectric nanoshells by using the GDQ method. Zhu et al. [2017] investigated the size-dependent effect on the torsional buckling of FG cylindrical nanoshell covered with piezoelectric nanolayers by using the GDQ method. Mirzavand et al. [2010; 2013], Dai et al. [2013] investigated the thermal buckling and postbuckling of piezoelectric FG cylindrical shells by using the finite difference method. Shen [2001; 2002a; 2002b; 2005; 2009; 2010], Shen and Li [2002], Shen and Noda [2007], Shen and Xiang [2007] analyzed the buckling and postbuckling of piezoelectric FG cylindrical shells by the singular perturbation method. Sahmani et al. [2016] studies the nonlinear buckling and postbuckling of piezoelectric cylindrical nanoshells by using the singular perturbation method. Mirzavand and Eslami [2007; 2011], Khoa et al. [2019] obtained exact solutions for buckling and postbuckling of piezoelectric FG cylindrical shells.

In contrast, there are only a few studies on the stability behaviors of piezoelectric shells made of NTRC. Ghorbanpour Arani et al. [2012a; 2012b; 2014] and MosallaieBarzoki et al. [2012; 2013] investigated the axial buckling, torsional buckling and dynamic buckling of piezoelectric NTRC cylindrical shells under electro-thermo-mechanical loads by using the energy method and harmonic differential quadrature method. Salehi-Khojin and Jalili [2008] obtained exact solutions for buckling of simply supported piezoelectric NTRC cylindrical shells under electro-thermo-mechanical loads. For the piezoelectric FG-NTRC, most of the existing literature were concentrated on the buckling of beams or plates [Rafiee et al. 2013; 2014; Wu and Chang 2014; Yang et al. 2015; Fan and Wang 2016; Mohammadimehr et al. 2016; Wu et al. 2016; Hajmohammad et al. 2017; Keleshteri et al. 2017]. The stability of piezoelectric FG-NTRC cylindrical shells was rarely reported in the open literature. Ansari et al. [2016] investigated the postbuckling of FG-NTRC cylindrical shells with piezoelectric layers under electro-thermo-mechanical loads by using the Ritz energy approach. Ninh [2018] analyzed the thermal torsional postbuckling of FG-NTRC cylindrical shells with sur-bonding piezoelectric layers by using the Galerkin method. SafarPour et al. [2019] obtained critical external voltage of rotating piezoelectric FG-NTRC cylindrical shells by using the GDQ method.

In view of the literature, it is found that the stability analysis of piezoelectric NTRC cylindrical shells is very limited, especially for piezoelectric FG-NTRC cylindrical shells. Most of the work were performed based on numerical methods, e.g., energy method [Ghorbanpour Arani et al. 2012a; 2012b; Mosallaie Barzoki et al. 2012; Ansari et al. 2016; Ninh 2018], GDQ method [Mosallaie Barzoki et al. 2013; Ghorbanpour Arani et al. 2014; SafarPour et al. 2019]. Analytical solutions were only reported by Salehi-Khojin and Jalili [2008], which was derived by the trial functions. Although the numerical approach could directly aid the engineering design, the analysis of data may be very time-consuming. In this case, analytical solutions could provide an efficient way to the rapid design and evaluation of such cylindrical shells.

Motivated by this, we employ a new Hamiltonian-based method [Wang and Qin 2007; Chen and Zhao 2009; Yao et al. 2009; Lim and Xu 2010; Sun et al. 2013; 2014a; 2014b; Li et al. 2015; Ni et al. 2017; 2018] to find exact solutions for buckling of piezoelectric FG-NTRC cylindrical shells under combined electro-thermo-mechanical loads. By introducing a total unknown vector, the high-order governing differential equations for buckling of the shell is reduced into a set of low-order ordinary equations. Thus, the buckling problem of the piezoelectric FG-NTRC shell is regarded as an eigenproblem in the symplectic space so that the exact solutions can be directly represented by the symplectic eigenfunctions. Unlike the single-formed solution obtained by the classical analytical treatments, the present solutions have five possible forms which highly depend on the geometrical parameters, circumference wave numbers, reinforcement nanotubes and their distribution patterns. Numerical examples are provided to reveal the effects of key influencing factors on the expressions of symplectic eigenfunctions and critical buckling stresses.

This paper is organized as follows. Following this introduction, modeling of piezoelectric FG-NTRC cylindrical shells under combined electro-thermo-mechanical loads is established. The basic equations are presented in Section 3. The Hamiltonian form of governing buckling equations and exact solutions are given in Sections 4 and 5, respectively. Numerical examples are provided in Section 6. Finally, the conclusions are summarized in Section 7.

2. Modeling of piezoelectric NTRC cylindrical shells

Consider a piezoelectric FG-NTRC cylindrical shell with external electric voltage θ_0 , temperature field $T(z)$ and axial compression F in Figure 1 (left). The geometries are taken as length L , radius R and thickness h . It is referred to a shell coordinate system (x, θ, z) where x , θ and z are in the axial, circumferential and outward normal directions of the middle surface of shell. The displacements along x -, θ - and z - axes are specified by u , v and w , respectively.

The NTRC is made from a mixture of NTs and an isotropic matrix. Four distribution patterns of the NTs along the thickness direction are considered in the present study, as shown in Figure 1 (right). The corresponding volume fractions of NTs are as follows [Ghorbanpour Arani et al. 2016; Mohammadimehr et al. 2016]:

$$\text{Uniformly distribution (UD):} \quad V_{NT} = V_{NT}^*, \quad (1a)$$

$$\text{FG-X:} \quad V_{NT} = 2(|z|/h) V_{NT}^*, \quad (1b)$$

$$\text{FG-O:} \quad V_{NT} = 2(2 - 2|z|/h) V_{NT}^*, \quad (1c)$$

$$\text{FG-V:} \quad V_{NT} = (1 + 2z/h) V_{NT}^*, \quad (1d)$$

where V_{NT}^* is total volume fraction of the NTs and it ranges from 0 to 0.5.

It is considered that the constituents of NTRC are orthotropic and homogeneous along the principal axis. The effective material properties of NTRC are evaluated by using the representative volume element based on micromechanical models. The mechanical, electrical and thermal properties are expressed as [Ghorbanpour Arani et al. 2016; Mosallaie Barzoki et al. 2012; Salehi-Khojin and Jalili 2008; Tan and

Tong 2001a; 2001b]:

$$c_{11} = \frac{c_{11}^{NT} c_{11}^M}{V_{NT} c_{11}^M + V_M c_{11}^{NT}}, \quad c_{12} = c_{11} \left(V_{NT} \frac{c_{12}^{NT}}{c_{11}^{NT}} + V_M \frac{c_{12}^M}{c_{11}^M} \right), \quad (2a)$$

$$c_{22} = V_{NT} c_{22}^{NT} + V_M c_{22}^M, \quad c_{66} = \frac{c_{66}^{NT} c_{66}^M}{V_{NT} c_{66}^M + V_M c_{66}^{NT}},$$

$$e_{31} = c_{11} \left(V_{NT} \frac{e_{31}^{NT}}{c_{11}^{NT}} + V_M \frac{e_{31}^M}{c_{11}^M} \right), \quad e_{32} = V_{NT} e_{32}^{NT} + V_M e_{32}^M, \quad (2b)$$

$$\varepsilon_{11} = V_{NT} \varepsilon_{11}^{NT} + V_M \varepsilon_{11}^M, \quad \varepsilon_{22} = V_{NT} \varepsilon_{22}^{NT} + V_M \varepsilon_{22}^M, \quad \varepsilon_{33} = V_{NT} \varepsilon_{33}^{NT} + V_M \varepsilon_{33}^M, \quad (2c)$$

$$\beta_1 = V_{NT} \beta_1^{NT} + V_M \beta_1^M, \quad \beta_2 = V_{NT} \beta_2^{NT} + V_M \beta_2^M, \quad (2d)$$

$$p_3 = V_{NT} p_3^{NT} + V_M p_3^M, \quad (2e)$$

where V_M is the volume fractions of matrix which satisfies $V_{NT} + V_M = 1$; c_{11}^i , c_{12}^i , c_{22} and c_{66}^i are elasticity constants; e_{31}^i and e_{32}^i are piezoelectric constants; ε_{11}^i , ε_{22}^i and ε_{33}^i are dielectric constants; β_1^i and β_2^i are thermal moduli; p_3^i is pyroelectric constant; “ $i = NT$ ” and “ $i = M$ ” represent the NTs and matrix, respectively.

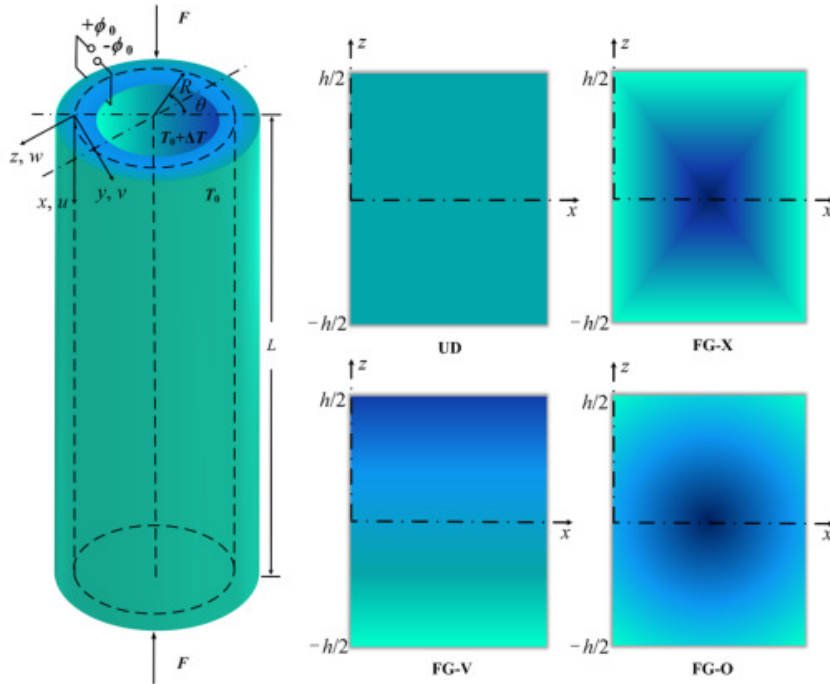


Figure 1. A piezoelectric NTRC cylindrical shell. Left: geometry of a piezoelectric NTRC cylindrical shell with thermal load, electric voltage and axial compression. Right: four distribution patterns of NTs.

3. Formulations of piezoelectric NTRC cylindrical shells

According to Reissner's shell theory [Leissa 1993], the strain components on the middle surface of the piezoelectric NTRC cylindrical shell are expressed as

$$\varepsilon_x = \frac{\partial u}{\partial x} - \frac{\partial^2 w}{\partial x^2} z, \quad (3a)$$

$$\varepsilon_\theta = \frac{1}{R} \frac{\partial v}{\partial \theta} + \frac{w}{R} - \frac{1}{R^2} \left(\frac{\partial^2 w}{\partial \theta^2} - \frac{\partial v}{\partial \theta} \right) z, \quad (3b)$$

$$\gamma_{x\theta} = \frac{\partial v}{\partial x} + \frac{1}{R} \frac{\partial u}{\partial \theta} - \frac{1}{R} \left(2 \frac{\partial^2 w}{\partial \theta \partial x} - \frac{\partial v}{\partial x} \right) z. \quad (3c)$$

To simplify the manipulation, the electric potential which satisfies the Maxwell equation can be assumed as a combination of cosine and linear variation, i.e., [Wang 2002; Pietrzakowski 2008; Lang and Xuewu 2013; Ke et al. 2014; Mehralian et al. 2016a; Mehralian and Tadi Beni 2017b; 2018]

$$\tilde{\phi}(x, \theta, z) = -\cos(\beta z) \phi(x, \theta) + \frac{2z\phi_0}{h}, \quad (4)$$

where $\beta = \pi/h$; ϕ is electric potential induced by elastic deformation; ϕ_0 is the applied uniform electric voltage marked in Figure 1 (left).

The electric field $\mathbf{E} = \{E_x, E_\theta, E_z\}^T$ are written as [Ke et al. 2014]

$$E_x = -\frac{\partial \tilde{\phi}}{\partial x} = \cos(\beta z) \frac{\partial \phi}{\partial x}, \quad (5a)$$

$$E_\theta = -\frac{1}{R+z} \frac{\partial \tilde{\phi}}{\partial \theta} = \frac{\cos(\beta z)}{R+z} \frac{\partial \phi}{\partial \theta}, \quad (5b)$$

$$E_z = -\frac{\partial \tilde{\phi}}{\partial z} = -\beta \sin(\beta z) \phi - \frac{2\phi_0}{h}. \quad (5c)$$

The thermo-electro-mechanical constitutive equation for piezoelectric cylindrical shell under the plane stress state is given by [Ke et al. 2014]

$$\begin{Bmatrix} \sigma_x \\ \sigma_\theta \\ \sigma_{x\theta} \end{Bmatrix} = \begin{bmatrix} c_{11} & c_{12} & 0 \\ c_{12} & c_{22} & 0 \\ 0 & 0 & c_{66} \end{bmatrix} \begin{Bmatrix} \varepsilon_x \\ \varepsilon_\theta \\ \gamma_{x\theta} \end{Bmatrix} - \begin{bmatrix} 0 & 0 & e_{31} \\ 0 & 0 & e_{32} \\ 0 & 0 & 0 \end{bmatrix} \begin{Bmatrix} E_x \\ E_\theta \\ E_z \end{Bmatrix} - \begin{Bmatrix} \beta_1 \\ \beta_2 \\ 0 \end{Bmatrix} T(z), \quad (6a)$$

$$\begin{Bmatrix} D_x \\ D_\theta \\ D_z \end{Bmatrix} = \begin{bmatrix} 0 & 0 & 0 \\ 0 & 0 & 0 \\ e_{31} & e_{32} & 0 \end{bmatrix} \begin{Bmatrix} \varepsilon_x \\ \varepsilon_\theta \\ \gamma_{x\theta} \end{Bmatrix} + \begin{bmatrix} \varepsilon_{11} & 0 & 0 \\ 0 & \varepsilon_{22} & 0 \\ 0 & 0 & \varepsilon_{33} \end{bmatrix} \begin{Bmatrix} E_x \\ E_\theta \\ E_z \end{Bmatrix} + \begin{Bmatrix} 0 \\ 0 \\ p_3 \end{Bmatrix} T(z), \quad (6b)$$

where σ_{ij} and D_i are stress and electric displacement components, respectively.

Integrating (6), the force, moment and generalized electric displacement resultants of the cylindrical shell are obtained as

$$\{N_x, N_\theta, N_{x\theta}\}^T = \int_{-h/2}^{h/2} \{\sigma_x, \sigma_\theta, \sigma_{x\theta}\}^T dz, \quad (7a)$$

$$\{M_x, M_\theta, M_{x\theta}\}^T = \int_{-h/2}^{h/2} \{\sigma_x, \sigma_\theta, \sigma_{x\theta}\}^T z dz, \quad (7b)$$

$$\{\Lambda_x, \Lambda_\theta, \Lambda_{x\theta}\}^T = \int_{-h/2}^{h/2} -R \left\{ \cos(\beta z) D_x, \frac{\cos(\beta z)}{R+z} D_\theta, \beta \sin(\beta z) D_z \right\}^T dz. \quad (7c)$$

The relations between the shear forces and moments can be expressed as

$$Q_x = \frac{\partial M_x}{\partial x} + \frac{1}{R} \frac{\partial M_{x\theta}}{\partial \theta} \quad \text{and} \quad Q_\theta = \frac{\partial M_{x\theta}}{\partial x} + \frac{1}{R} \frac{\partial M_\theta}{\partial \theta}. \quad (8)$$

The prebuckling state can be considered as uniform deformation or axisymmetric deformation and has a significant effect only for a particularly short and thick cylindrical shell [Yamaki 1984; Teng 1996; Rotter 2014; Teng and Rotter 2014]. In the present study, since the displacement and angle of rotation are very small, the prebuckling state is assumed as a uniform deformation. When the external loads increase to a certain extent, another new equilibrium state will appear on the basis of the original equilibrium state under external disturbance. The bifurcation buckling of the structure occurs at this time, and the governing equation of linear buckling for the state of stability is established. The corresponding state variables can be divided into

$$\{u, v, w, \phi\} = \{u^0, v^0, w^0, \phi^0\} + \{u^1, v^1, w^1, \phi^1\}, \quad (9a)$$

$$\{E_x, E_\theta, E_z\} = \{E_x^0, E_\theta^0, E_z^0\} + \{E_x^1, E_\theta^1, E_z^1\}, \quad (9b)$$

$$\{D_x, D_\theta, D_z\} = \{D_x^0, D_\theta^0, D_z^0\} + \{D_x^1, D_\theta^1, D_z^1\}, \quad (9c)$$

$$\{N_x, N_\theta, N_{x\theta}\} = \{N_x^0, N_\theta^0, N_{x\theta}^0\} + \{N_x^1, N_\theta^1, N_{x\theta}^1\}, \quad (9d)$$

$$\{M_x, M_\theta, M_{x\theta}\} = \{M_x^0, M_\theta^0, M_{x\theta}^0\} + \{M_x^1, M_\theta^1, M_{x\theta}^1\}, \quad (9e)$$

$$\{\Lambda_x, \Lambda_\theta, \Lambda_{x\theta}\} = \{\Lambda_x^0, \Lambda_\theta^0, \Lambda_{x\theta}^0\} + \{\Lambda_x^1, \Lambda_\theta^1, \Lambda_{x\theta}^1\}, \quad (9f)$$

$$\{Q_x, Q_\theta\} = \{Q_x^0, Q_\theta^0\} + \{Q_x^1, Q_\theta^1\}, \quad (9g)$$

where the superscripts “0” and “1” correspond to the prebuckling quantities and infinitesimal increments. The corresponding resultant forces in prebuckling state can be obtained as $N_x^0 = N_e^0 + N_t^0 + N_m^0$ where $N_e^0 = -2 \int_{-h/2}^{h/2} e_{31} \phi_0 / h dz$, $N_t^0 = \int_{-h/2}^{h/2} \beta_1 T(z) dz$ and $N_m^0 = F / 2\pi R$ represent the internal forces caused by external electric voltage, temperature rise and external axial compression, respectively.

Substituting (3) and (6) into (7), internal forces and generalized electric displacements for the state of stability can be simplified as

$$N_x^1 = A_{11} \frac{\partial u^1}{\partial x} + \frac{A_{12}}{R} \left(\frac{\partial v^1}{\partial \theta} + w^1 \right) - B_{11} \frac{\partial^2 w^1}{\partial x^2} - \frac{B_{12}}{R^2} \left(\frac{\partial^2 w^1}{\partial \theta^2} - \frac{\partial v^1}{\partial \theta} \right), \quad (10a)$$

$$N_\theta^1 = A_{21} \frac{\partial u^1}{\partial x} + \frac{A_{22}}{R} \left(\frac{\partial v^1}{\partial \theta} + w^1 \right) - B_{21} \frac{\partial^2 w^1}{\partial x^2} - \frac{B_{22}}{R^2} \left(\frac{\partial^2 w^1}{\partial \theta^2} - \frac{\partial v^1}{\partial \theta} \right), \quad (10b)$$

$$N_{x\theta}^1 = A_{66} \left(\frac{\partial v^1}{\partial x} + \frac{\partial u^1}{R \partial \theta} \right) - \frac{B_{66}}{R} \left(2 \frac{\partial^2 w^1}{\partial x \partial \theta} - \frac{\partial v^1}{\partial x} \right), \quad (10c)$$

$$M_x^1 = B_{11} \frac{\partial u^1}{\partial x} + \frac{B_{12}}{R} \left(\frac{\partial v^1}{\partial \theta} + w^1 \right) - D_{11} \frac{\partial^2 w^1}{\partial x^2} - \frac{D_{12}}{R^2} \left(\frac{\partial^2 w^1}{\partial \theta^2} - \frac{\partial v^1}{\partial \theta} \right) + E_{31} \phi^1, \quad (10d)$$

$$M_\theta^1 = B_{21} \frac{\partial u^1}{\partial x} + \frac{B_{22}}{R} \left(\frac{\partial v^1}{\partial \theta} + w^1 \right) - D_{21} \frac{\partial^2 w^1}{\partial x^2} - \frac{D_{22}}{R^2} \left(\frac{\partial^2 w^1}{\partial \theta^2} - \frac{\partial v^1}{\partial \theta} \right) + E_{32} \phi^1, \quad (10e)$$

$$M_{x\theta}^1 = B_{66} \left(\frac{\partial v^1}{\partial x} + \frac{\partial u^1}{R \partial \theta} \right) - \frac{D_{66}}{R} \left(2 \frac{\partial^2 w^1}{\partial x \partial \theta} - \frac{\partial v^1}{\partial x} \right), \quad (10f)$$

$$\Lambda_x^1 = -R X_{11} \frac{\partial \phi^1}{\partial x}, \quad (10g)$$

$$\Lambda_\theta^1 = -R X_{22} \frac{\partial \phi^1}{\partial \theta}, \quad (10h)$$

$$\Lambda_z^1 = R E_{31} \frac{\partial^2 w^1}{\partial x^2} + \frac{E_{32}}{R} \left(\frac{\partial^2 w^1}{\partial \theta^2} - \frac{\partial v^1}{\partial \theta} \right) + R X_{33} \phi^1, \quad (10i)$$

where

$$\{A_{ij}, B_{ij}, D_{ij}\} = \int_{-h/2}^{h/2} c_{ij} \{1, z, z^2\} dz \quad (i, j = 1, 2, 6),$$

are components of the extensional, coupling and bending stiffness, $A_{12} = A_{21}$, $B_{12} = B_{21}$ and $D_{12} = D_{21}$,

$$\begin{aligned} \{E_{31}, E_{32}\} &= \int_{-h/2}^{h/2} \{e_{31}, e_{32}\} \beta z \sin(\beta z) dz, & X_{11} &= \int_{-h/2}^{h/2} \varepsilon_{11} \cos^2(\beta z) dz, \\ X_{22} &= \int_{-h/2}^{h/2} \varepsilon_{22} \frac{\cos^2(\beta z)}{(R+z)^2} dz, & X_{33} &= \int_{-h/2}^{h/2} \varepsilon_{33} \beta^2 \sin^2(\beta z) dz. \end{aligned}$$

The governing equations for the state of stability can be obtained as [Ke et al. 2014]

$$\frac{\partial N_x^1}{\partial x} + \frac{\partial N_{x\theta}^1}{R \partial \theta} = 0, \quad \frac{\partial N_{x\theta}^1}{\partial x} + \frac{\partial N_\theta^1}{R \partial \theta} + \frac{Q_\theta^1}{R} = 0, \quad (11a)$$

$$\frac{\partial Q_x^1}{\partial x} + \frac{\partial Q_\theta^1}{R \partial \theta} - \frac{N_\theta^1}{R} - N_x^0 \frac{\partial^2 w^1}{\partial x^2} = 0, \quad \frac{\partial \Lambda_x^1}{\partial x} + \frac{\partial \Lambda_\theta^1}{\partial \theta} + \Lambda_z^1 = 0. \quad (11b)$$

Two types of end conditions at $x = 0$ and L are considered here [Chen et al. 1996; Hussein and Heyliger 1998; Saviz et al. 2007; Ke et al. 2014; Sun et al. 2016], i.e.,

$$\text{Clamped (C):} \quad u^1 = v^1 = w^1 = \frac{\partial w^1}{\partial x} = \phi^1 = 0, \quad (12a)$$

$$\text{Simply supported (S):} \quad \frac{\partial u^1}{\partial x} = v^1 = w^1 = M_x^1 = \phi^1 = 0. \quad (12b)$$

4. Governing equations in Hamiltonian system

To obtain the analytical solutions of (11), the Hamiltonian description is introduced here. Define \mathbf{q} and \mathbf{p} as the original vector and its dual vector in the Hamiltonian system, respectively. The original vector is assumed as a vector consisting of displacements, angle of rotation and electric potential, i.e.,

$$\mathbf{q} = \{q_1, q_2, q_3, q_4, q_5\}^T = \{u^1, v^1, w^1, \theta_\theta^1, \phi^1\}^T, \quad (13)$$

where ϕ_θ^1 is the angle of rotation,

$$\theta_\theta^1 = \frac{v^1}{R} - \frac{1}{R} \frac{\partial w^1}{\partial \theta}. \quad (14)$$

The Lagrangian density function L_C is introduced as [Ke et al. 2014]

$$\begin{aligned} L_C = & -\frac{R}{2} \int_{-h/2}^{h/2} (D_x^1 E_x^1 + D_\theta^1 E_\theta^1 + D_z^1 E_z^1) dz \\ & + \frac{R}{2} \left[A_{11} \left(\frac{\partial u^1}{\partial x} \right)^2 + A_{22} \left(\frac{\dot{v}^1}{R} + \frac{w^1}{R} \right)^2 + 2A_{12} \frac{\partial u^1}{\partial x} \left(\frac{\dot{v}^1}{R} + \frac{w^1}{R} \right) + A_{66} \left(\frac{\partial v^1}{\partial x} + \frac{\dot{u}^1}{R} \right)^2 \right. \\ & - 2 \frac{B_{66}}{R} \left(\frac{\partial v^1}{\partial x} + \frac{\dot{u}^1}{R} \right) \left(2 \frac{\partial \dot{w}^1}{\partial x} - \frac{\partial v^1}{\partial x} \right) - 2B_{11} \frac{\partial u^1}{\partial x} \frac{\partial^2 w^1}{\partial x^2} \\ & - 2B_{12} \left(\frac{\dot{v}^1}{R} + \frac{w^1}{R} \right) \frac{\partial^2 w^1}{\partial x^2} + 2 \frac{B_{12}}{R} \frac{\partial u^1}{\partial x} \dot{\theta}_\theta^1 + 2 \frac{B_{22}}{R} \left(\frac{\dot{v}^1}{R} + \frac{w^1}{R} \right) \dot{\theta}_\theta^1 \\ & \left. + D_{11} \left(\frac{\partial^2 w^1}{\partial x^2} \right)^2 - 2 \frac{D_{12}}{R} \frac{\partial^2 w^1}{\partial x^2} \dot{\theta}_\theta^1 + \frac{D_{22}}{R} (\dot{\theta}_\theta^1)^2 + \frac{D_{66}}{R} \left(2 \frac{\partial \dot{w}^1}{\partial x} - \frac{\partial v^1}{\partial x} \right)^2 \right] \\ & + \left[2B_{66} \left(\frac{\partial \dot{u}^1}{R \partial x} + \frac{\partial^2 v^1}{\partial x^2} \right) + \frac{B_{22}}{R^2} (\dot{v}^1 + v^1 - R\theta_\theta^1) + B_{12} \frac{\partial \dot{u}^1}{R \partial x} \right. \\ & \left. - D_{12} \frac{\partial^2 \dot{w}^1}{R \partial x^2} + \frac{D_{22}}{R^2} \ddot{\theta}_\theta^1 + 2D_{66} \left(2 \frac{\partial^2 \theta_\theta^1}{\partial x^2} - \frac{\partial^2 v^1}{R \partial x^2} \right) \right] (\dot{w}^1 - v^1 + R\theta_\theta^1), \quad (15) \end{aligned}$$

where $(\dot{}) = \partial()/\partial\theta$.

The corresponding dual vector \mathbf{p} can be obtained by (15)

$$\mathbf{p} = \frac{\delta L_C}{\delta \dot{\mathbf{q}}} = \{p_1, p_2, p_3, p_4, p_5\}^T = \{N_{x\theta}^1, N_\theta^1, V_\theta^1, M_\theta^1, \Lambda_\theta^1\}^T, \quad (16)$$

where equivalent shear forces V_θ^1 can be expressed by

$$V_\theta^1 = Q_\theta^1 + \frac{\partial M_{x\theta}^1}{\partial x}. \quad (17)$$

From (14), we have

$$\dot{w}^1 = v^1 - R\theta_\theta^1. \quad (18)$$

Substituting (18) into (10), we have

$$\dot{u}^1 = \left(\frac{B_{66}}{A_{66}} - R \right) \frac{\partial v^1}{\partial x} - 2R \frac{B_{66}}{A_{66}} \frac{\partial \theta_\theta^1}{\partial x} + \frac{R}{A_{66}} N_{x\theta}^1, \quad (19)$$

$$\dot{v}^1 = R \frac{\kappa_3}{\kappa_2} \frac{\partial u^1}{\partial x} + R \frac{\kappa_5}{\kappa_2} \frac{\partial^2 w^1}{\partial x^2} - w^1 + R \frac{D_{22}}{\kappa_2} N_\theta^1 - R \frac{B_{22}}{\kappa_2} M_\theta^1 + R \frac{B_{22}E_{32}}{\kappa_2} \phi^1, \quad (20)$$

$$\dot{\theta}_\theta^1 = -R \frac{\kappa_4}{\kappa_2} \frac{\partial u^1}{\partial x} + R \frac{\kappa_6}{\kappa_2} \frac{\partial^2 w^1}{\partial x^2} - R \frac{B_{22}}{\kappa_2} N_\theta^1 + R \frac{A_{22}}{\kappa_2} M_\theta^1 - R \frac{A_{22}E_{32}}{\kappa_2} \phi^1, \quad (21)$$

$$\dot{\phi}^1 = -\frac{1}{RX_{22}} \Lambda_\theta^1. \quad (22)$$

Substituting (10), (18), (20) and (21) into (11), we have

$$\dot{N}_{x\theta}^1 = R \left(\frac{\kappa_{10}}{D_{22}\kappa_2} \frac{\partial^2 u^1}{\partial x^2} + \frac{\kappa_{11}}{D_{22}\kappa_2} \frac{\partial^3 w^1}{\partial x^3} + \frac{\kappa_3}{\kappa_2} \frac{\partial N_\theta^1}{\partial x} - \frac{\kappa_4}{\kappa_2} \frac{\partial M_\theta^1}{\partial x} + E_{32} \frac{\kappa_4}{\kappa_2} \frac{\partial \phi^1}{\partial x} \right). \quad (23)$$

Substituting (10), (17) and (18) into (11), we have

$$\dot{N}_\theta^1 = -\frac{\kappa_9}{R} \frac{\partial^2 v^1}{\partial x^2} + 2\kappa_9 \frac{\partial^2 \theta_\theta^1}{\partial x^2} + \left(\frac{B_{66}}{A_{66}} - R \right) \frac{\partial N_{x\theta}^1}{\partial x} - V_\theta^1. \quad (24)$$

Substituting (10), (17), (18), (20) and (21) into (11), we have

$$\begin{aligned} \dot{V}_\theta^1 = -R \left[\frac{\kappa_{11}}{D_{22}\kappa_2} \frac{\partial^3 u^1}{\partial x^3} + \frac{\kappa_{12}}{D_{22}\kappa_2} \frac{\partial^4 w^1}{\partial x^4} + \frac{\kappa_5}{\kappa_2} \frac{\partial^2 N_\theta^1}{\partial x^2} + \frac{\kappa_6}{\kappa_2} \frac{\partial^2 M_\theta^1}{\partial x^2} + \left(E_{31} - \frac{\kappa_6}{\kappa_2} E_{32} \right) \frac{\partial^2 \phi^1}{\partial x^2} \right] \\ + N_\theta^1 + RN_x^0 \frac{\partial^2 w^1}{\partial x^2}. \end{aligned} \quad (25)$$

Substituting (10), (17), (18) and (19) into (8), we have

$$\dot{M}_\theta^1 = 2\kappa_9 \frac{\partial^2 v^1}{\partial x^2} - 4R\kappa_9 \frac{\partial^2 \theta_\theta^1}{\partial x^2} - 2R \frac{B_{66}}{A_{66}} \frac{\partial N_{x\theta}^1}{\partial x} + RV_\theta^1. \quad (26)$$

Substituting (10) into (11), we have

$$\begin{aligned} \dot{\Lambda}_\theta^1 = -R \left[E_{32} \frac{\kappa_4}{\kappa_2} \frac{\partial u^1}{\partial x} + \left(E_{31} - \frac{\kappa_6}{\kappa_2} E_{32} \right) \frac{\partial^2 w^1}{\partial x^2} + \frac{E_{32}B_{22}}{\kappa_2} N_\theta^1 - \frac{E_{32}A_{22}}{\kappa_2} M_\theta^1 - X_{11} \frac{\partial^2 \phi^1}{\partial x^2} \right. \\ \left. + \left(X_{33} + \frac{A_{22}E_{32}^2}{\kappa_2} \right) \phi^1 \right], \end{aligned} \quad (27)$$

where $\kappa_1 = A_{11}D_{22} - B_{12}^2$, $\kappa_2 = A_{22}D_{22} - B_{22}^2$, $\kappa_3 = B_{22}B_{12} - A_{12}D_{22}$, $\kappa_4 = A_{22}B_{12} - A_{12}B_{22}$, $\kappa_5 = B_{12}D_{22} - B_{22}D_{12}$, $\kappa_6 = A_{22}D_{12} - B_{22}B_{12}$, $\kappa_7 = B_{12}D_{12} - B_{11}D_{22}$, $\kappa_8 = D_{12}^2 - D_{11}D_{22}$, $\kappa_9 = (A_{66}D_{66} - B_{66}^2)/A_{66}$, $\kappa_{10} = \kappa_3^2 - \kappa_1\kappa_2$, $\kappa_{11} = \kappa_3\kappa_5 - \kappa_7\kappa_2$ and $\kappa_{12} = \kappa_8\kappa_2 + \kappa_5^2$.

In view of (18)–(27), the Hamiltonian governing equations can be represented in a matrix form of

$$\dot{\boldsymbol{\psi}} = \mathbf{H}\boldsymbol{\psi}, \quad (28)$$

where $\boldsymbol{\psi} = \{\mathbf{q}^T, \mathbf{p}^T\}^T$ is a total unknown vector; \mathbf{H} is the Hamiltonian operator matrix in Appendix A.

The associated end conditions (12) are rewritten in the Hamiltonian form:

$$\text{C:} \quad q_1 = q_2 = q_3 = \frac{\partial q_3}{\partial x} = q_5 = 0, \quad (29a)$$

$$\text{S:} \quad \frac{\partial q_1}{\partial x} = q_2 = q_3 = \frac{\kappa_{11}}{D_{22}\kappa_2} \frac{\partial q_1}{\partial x} + \frac{\kappa_{12}}{D_{22}\kappa_2} \frac{\partial^2 q_3}{\partial x^2} + E_{31}q_5 + \frac{\kappa_5}{\kappa_2} p_2 + \frac{\kappa_6}{\kappa_2} p_4 = q_5 = 0. \quad (29b)$$

5. Symplectic eigenvalue problem and buckling equation

According to the Hamiltonian matrix, the method of separation of variables is available to solve the governing equation (28) [Lim and Xu 2010]. Assuming that $\boldsymbol{\psi}(x, \theta) = \boldsymbol{\eta}(x)e^{\mu\theta}$, the eigenvalue equation for (28) has the form of

$$\mathbf{H}\boldsymbol{\eta}_n = \mu\boldsymbol{\eta}_n, \quad (30)$$

where $\mu = ni$ ($n = 0, \pm 1, \pm 2, \dots$) and $\boldsymbol{\eta}(x)$ are the symplectic eigenvalues and eigenfunctions, respectively. It is worthy of note that the eigenfunctions $\boldsymbol{\eta}_n$ can be divided into two groups: zero eigenfunctions $\boldsymbol{\eta}_0$ with $\mu = 0$ and nonzero eigenfunctions $\boldsymbol{\eta}_n$ with $\mu \neq 0$. The physical interpretations of $\boldsymbol{\eta}_0$ and $\boldsymbol{\eta}_n$ are the axisymmetric and nonaxisymmetric buckling solutions of the piezoelectric cylindrical shell, respectively. Thus, the zero eigenfunctions and nonzero eigenfunctions are solved separately.

5.1. Zero eigenfunction. Considering zero eigenfunctions, the eigenvalue equation has the form of $\mathbf{H}\boldsymbol{\eta}_0^{(1)} = 0$. In this case, characteristic equation is

$$\lambda^{10} + \xi_1^{(0)}\lambda^8 + \xi_2^{(0)}\lambda^6 + \xi_3^{(0)}\lambda^4 + \xi_4^{(0)}\lambda^2 + \xi_5^{(0)} = 0, \quad (31)$$

in which $\xi_i^{(0)}$ ($i = 1, 2, \dots, 5$) are the functions of compressive buckling load N_x^0 , which are elaborated in Appendix B.

The root of (31) are $\lambda_{1,2} = \pm i\alpha_1$, $\lambda_{3,4} = \pm i\alpha_2$, $\lambda_{5,6} = \pm \alpha_3$, $\lambda_7 = \lambda_8 = \lambda_9 = \lambda_{10} = 0$. Thus, the zero eigenfunctions can be represented by

Case I ($\mu = 0$):

$$\boldsymbol{\eta}_0^{(1)} = \mathbf{c}_1 \cos(\alpha_1 x) + \mathbf{c}_2 \sin(\alpha_1 x) + \mathbf{c}_3 \cos(\alpha_2 x) + \mathbf{c}_4 \sin(\alpha_2 x) + \mathbf{c}_5 e^{\alpha_3 x} + \mathbf{c}_6 e^{-\alpha_3 x} + \mathbf{c}_7 + \mathbf{c}_8 x + \mathbf{c}_9 x^2 + \mathbf{c}_{10} x^3, \quad (32)$$

where $\mathbf{c}_j = \{c_j^1, c_j^2, \dots, c_j^{10}\}^T$ ($j = 1, 2, \dots, 10$) are undetermined coefficient vectors. The physical interpretations of (32) are the axisymmetric buckling solutions of the piezoelectric cylindrical shell.

5.2. Nonzero eigenfunction. Considering nonzero eigenfunctions, the characteristic equation obtained from the eigenvalue equation $(\mathbf{H} - \mu \mathbf{I})\boldsymbol{\eta}_n = 0$ is written as

$$\lambda^{10} + \xi_1 \lambda^8 + \xi_2 \lambda^6 + \xi_3 \lambda^4 + \xi_4 \lambda^2 + \xi_5 = 0, \quad (33)$$

where, ξ_i ($i = 1, 2, \dots, 5$) are the functions of compressive buckling load and are elaborated in Appendix C. The symplectic eigenfunctions can be expressed by

$$\boldsymbol{\eta}_n = \sum_{i=1}^{10} \mathbf{c}_i e^{\lambda_i x}, \quad (34)$$

where λ_i ($i = 1, 2, \dots, 10$) are the roots of (33); $\mathbf{c}_j = \{c_j^1, c_j^2, \dots, c_j^{10}\}^T$ ($j = 1, 2, \dots, 10$) are undetermined coefficient vectors. Here, it should be pointed out that there are only ten independent coefficients. To simplify the manipulation, $\mathbf{c}^1 = \{c_1^1, c_2^1, \dots, c_{10}^1\}$ are chosen as the independent coefficients. Therefore, $\mathbf{c}^k = \{c_1^k, c_2^k, \dots, c_{10}^k\}$ ($k = 2, 3, \dots, 10$) can be represented by \mathbf{c}^1 .

According to λ and μ , the expressions of eigenfunction (34) can be grouped into five categories:

Case II ($\mu = \pm i$): $\lambda_{1,2} = \pm i\alpha_1$, $\lambda_{3,4} = \pm i\alpha_2$, $\lambda_{5,6} = \pm i\alpha_3$, $\lambda_{7,8} = \pm \alpha_4$, $\lambda_{9,10} = 0$,

$$\boldsymbol{\eta}_n^{(2)} = \mathbf{c}_1 \cos(\alpha_1 x) + \mathbf{c}_2 \sin(\alpha_1 x) + \mathbf{c}_3 \cos(\alpha_2 x) + \mathbf{c}_4 \sin(\alpha_2 x) + \mathbf{c}_5 \cos(\alpha_3 x) + \mathbf{c}_6 \sin(\alpha_3 x) + \mathbf{c}_7 e^{\alpha_4 x} + \mathbf{c}_8 e^{-\alpha_4 x} + \mathbf{c}_9 + \mathbf{c}_{10} x, \quad (35)$$

Case III ($\mu = \pm i$): $\lambda_{1,2} = \pm i\alpha_1$, $\lambda_{3,4} = \pm \alpha_2$, $\lambda_{5,6} = \pm \alpha_3$, $\lambda_{7,8} = \pm \alpha_4$, $\lambda_{9,10} = 0$,

$$\boldsymbol{\eta}_n^{(3)} = \mathbf{c}_1 \cos(\alpha_1 x) + \mathbf{c}_2 \sin(\alpha_1 x) + \mathbf{c}_3 e^{\alpha_2 x} + \mathbf{c}_4 e^{-\alpha_2 x} + \mathbf{c}_5 e^{\alpha_3 x} + \mathbf{c}_6 e^{-\alpha_3 x} + \mathbf{c}_7 e^{\alpha_4 x} + \mathbf{c}_8 e^{-\alpha_4 x} + \mathbf{c}_9 + \mathbf{c}_{10} x, \quad (36)$$

Case IV ($\mu \neq \pm i$): $\lambda_{1,2} = \pm i\alpha_1$, $\lambda_{3,4} = \pm i\alpha_2$, $\lambda_{5,6} = \pm \alpha_3$, $\lambda_{7,8} = \pm(\alpha_4 + i\alpha_5)$, $\lambda_{9,10} = \pm(\alpha_4 - i\alpha_5)$,

$$\boldsymbol{\eta}_n^{(4)} = \mathbf{c}_1 \cos(\alpha_1 x) + \mathbf{c}_2 \sin(\alpha_1 x) + \mathbf{c}_3 \cos(\alpha_2 x) + \mathbf{c}_4 \sin(\alpha_2 x) + \mathbf{c}_5 e^{\alpha_3 x} + \mathbf{c}_7 e^{\alpha_4 x} \cos(\alpha_5 x) + \mathbf{c}_8 e^{\alpha_4 x} \sin(\alpha_5 x) + \mathbf{c}_9 e^{-\alpha_4 x} \cos(\alpha_5 x) + \mathbf{c}_{10} e^{-\alpha_4 x} \sin(\alpha_5 x), \quad (37)$$

Case V ($\mu \neq \pm i$): $\lambda_{1,2} = \pm i\alpha_1$, $\lambda_{3,4} = \pm i\alpha_2$, $\lambda_{5,6} = \pm \alpha_3$, $\lambda_{7,8} = \pm \alpha_4$, $\lambda_{9,10} = \pm \alpha_5$,

$$\boldsymbol{\eta}_n^{(5)} = \mathbf{c}_1 \cos(\alpha_1 x) + \mathbf{c}_2 \sin(\alpha_1 x) + \mathbf{c}_3 \cos(\alpha_2 x) + \mathbf{c}_4 \sin(\alpha_2 x) + \mathbf{c}_5 e^{\alpha_3 x} + \mathbf{c}_6 e^{-\alpha_3 x} + \mathbf{c}_7 e^{\alpha_4 x} + \mathbf{c}_8 e^{-\alpha_4 x} + \mathbf{c}_9 e^{\alpha_5 x} + \mathbf{c}_{10} e^{-\alpha_5 x}, \quad (38)$$

Case VI ($\mu \neq \pm i$): $\lambda_{1,2} = \pm i\alpha_1$, $\lambda_{3,4} = \pm i\alpha_2$, $\lambda_{5,6} = \pm i\alpha_3$, $\lambda_{7,8} = \pm i\alpha_4$, $\lambda_{9,10} = \pm \alpha_5$,

$$\boldsymbol{\eta}_n^{(6)} = \mathbf{c}_1 \cos(\alpha_1 x) + \mathbf{c}_2 \sin(\alpha_1 x) + \mathbf{c}_3 \cos(\alpha_2 x) + \mathbf{c}_4 \sin(\alpha_2 x) + \mathbf{c}_5 \cos(\alpha_3 x) + \mathbf{c}_6 \sin(\alpha_3 x) + \mathbf{c}_7 \cos(\alpha_4 x) + \mathbf{c}_8 \sin(\alpha_4 x) + \mathbf{c}_9 e^{\alpha_5 x} + \mathbf{c}_{10} e^{-\alpha_5 x}, \quad (39)$$

where α_i ($i = 1, 2, \dots, 5$) are determined by (33). These nonzero eigenfunctions $\boldsymbol{\eta}_n^{(i)}$ ($i = 1, 2, \dots, 5$) represent the nonaxisymmetric buckling solutions of the piezoelectric FG-NTRC cylindrical shell.

Buckling equations and buckling mode shape functions can be determined by means of eigenfunctions $\boldsymbol{\eta}$ and end conditions. Substituting (35)–(39) into (29), one has $[\boldsymbol{\zeta}]_{10 \times 10}(\mathbf{c}^1)^T = 0$. For nontrivial solutions, the determinant of the coefficient matrix of $\boldsymbol{\zeta}$ should vanish. Thus, the compressive buckling loads $N_{mn} = N_m^0$ are the roots of $|\boldsymbol{\zeta}| = 0$. The buckling stresses is determined as $\sigma_{mn} = N_{mn}/h$, where m and n are the axial wave numbers and circumference wave numbers, respectively. The smallest value of σ_{mn} is the critical buckling stress σ_{cr} . The analytical buckling mode shape functions q_1 , q_2 and q_3 can be obtained by substituting the eigenvalues into the corresponding eigenfunctions.

6. Numerical examples and discussion

6.1. Validations. Since no available critical buckling load of piezoelectric FG-NTRC cylindrical shells is reported in the open literature, a simply supported piezoelectric FG cylindrical shell made of BaTiO₃/PZT-5A or BaTiO₃/PZT-4 is considered to verify the accuracy of the proposed method. The material properties for PZT-5A, PZT-4 and BaTiO₃ are taken as those in [Dong and Wang 2007; Sheng and Wang 2010]. The effective material properties P vary continuously in the thickness direction and can be expressed as $P(z) = (P_o - P_i)(1/2 + z/h)^k + P_i$ where k is the volume fraction exponent, P_o and P_i denote the property of the outer and inner surface of the shell, respectively. The nondimensional buckling load is defined as N_{cr}/N_{ocr} where

$$N_{ocr} = \frac{Eh^2}{R\sqrt{3(1-\nu^2)}}.$$

In the following numerical examples, a uniform temperature field is considered so that the temperature through the shell thickness rises uniformly by a certain amount $T(z) = \Delta T$. Variations of buckling loads for $m = n = 1$ versus k are plotted in Figure 2 with $L/R = 1$, $h/R = 0.01$, $N_m^0 = 0.2N_{ocr}$, $\phi_0 = 200$ V and $\Delta T = 200$ K. It can be seen that the trend of the present results are consistent with those reported by Sheng and Wang [2010] with minor errors. The errors are mainly caused by the difference of shell theories. The present results were obtained by Reissner's shell theory while the reference data were obtained by the first-order shear deformation theory. Furthermore, the relation between the buckling temperature rise for $m = n = 1$ and the electric voltage are shown in Figure 3 with $L/R = 1$, $h/R = 0.002$, $N_m^0 = 0.5N_{ocr}$ and $k = 1$. The present method again produces good agreement with the treatment in reference [Sheng and Wang 2010].

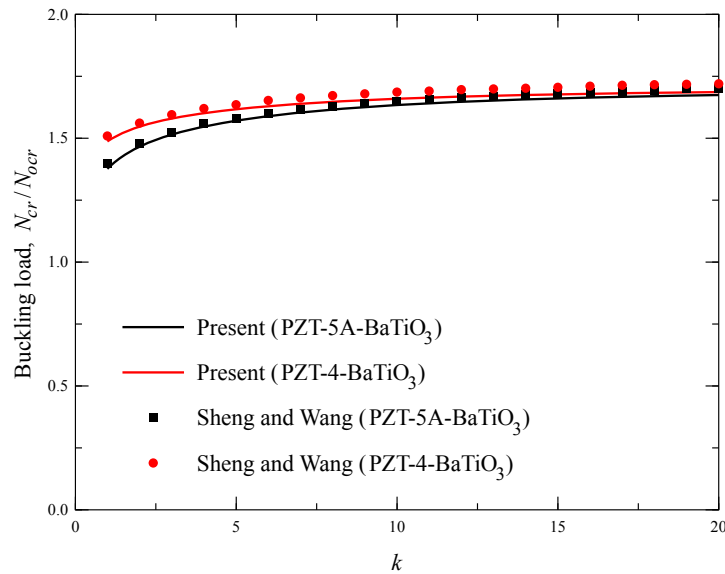


Figure 2. Comparison of the dimensionless buckling loads for S-S piezoelectric FG cylindrical shells with different volume fraction exponent k .

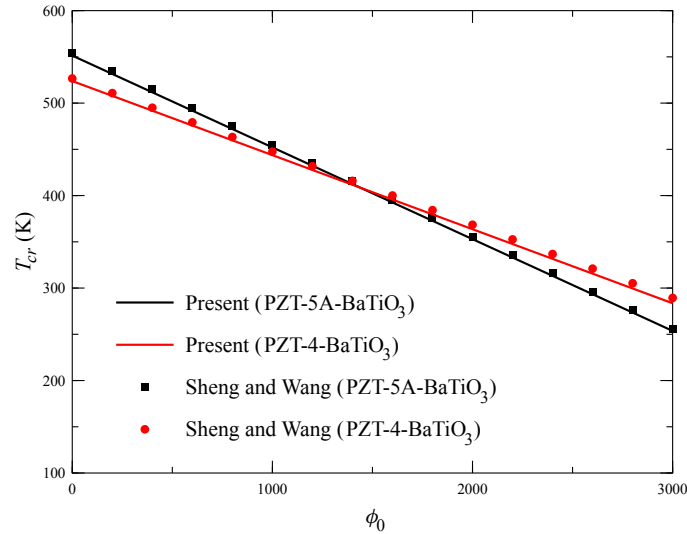


Figure 3. Comparison of the buckling temperature rise for S-S piezoelectric FG cylindrical shells with different ϕ_0 .

For a further verification, the present results are compared with those obtained by high-order shear deformation theory (HSDT). The critical buckling stresses of a clamped isotropic piezoelectric cylindrical shell made of PZT-A or PZT-B without electric voltage and temperature rise are computed and tabulated in Table 1. The material properties are selected as those in [Sun et al. 2016]. It is observed that the present data obtained by Rissiner's shell theory are in accordance with those of HSDT [Sun et al. 2016] with a maximum error 2.86%. The errors are mainly caused by the difference of shell theories. The critical buckling loads predicted by the HSDT are usually less than the Rissiner's shell theory when the shell is relatively thick.

	$h/R = 1/30$	$h/R = 1/35$	$h/R = 1/40$	$h/R = 1/45$	$h/R = 1/50$
$L/R = 1$					
Sun et al. (PZT-A)	1399.56	1199.57	1040.04	907.554	810.386
Present (PZT-A)	1433.91	1209.92	1043.43	913.969	808.000
Sun et al. (PZT-B)	1705.41	1447.32	1271.47	1120.34	997.118
Present (PZT-B)	1739.21	1481.68	1281.90	1110.33	991.122
$L/R = 4$					
Sun et al. (PZT-A)	1281.11	1098.76	962.878	855.604	770.723
Present (PZT-A)	1317.75	1106.98	965.451	849.869	766.702
Sun et al. (PZT-B)	1565.56	1325.56	1159.39	1031.84	929.486
Present (PZT-B)	1607.89	1354.65	1153.65	1027.62	930.291

Table 1. Comparison of the critical buckling stresses (MPa) for a piezoelectric cylindrical shell with different L/R and h/R .

6.2. Discussion on symplectic eigenfunctions. In the existing literature, analytical analyses for buckling of piezoelectric cylindrical shells were usually performed by the inverse or semiinverse methods under the classical Lagrangian system. Analytical solutions were obtained by introducing some trial functions (e.g., trigonometric functions). Consequently, the obtained solutions highly depend on the expressions of the predetermined functions. To overcome the above limitation of classical analytical treatments, the present study proposed a rigorous method for buckling of piezoelectric FG-NTRC shells under the Hamiltonian system. The obtained analytical solutions are directly expressed in terms of symplectic eigenfunctions without any trial functions. It is interesting to find from Section 5 that there exist five cases of symplectic eigenfunctions ((35)–(39)) for buckling of the shell, which implies the analytical solutions may have five possible forms. To reveal the effects of key influencing parameters on the expressions of symplectic eigenfunctions, a piezoelectric FG-NTRC cylindrical shell with $R = 0.1$ m, $V_{NT}^* = 0.2$, $\phi_0 = 10000$ V and $\Delta T = 10$ K is considered in this section. The material properties of CNT, BNNT and polyvinylidene fluoride (PVDF) are tabulated in Table 2 [Mosallae Barzoki et al. 2012; Mohammadimehr et al. 2016]. The buckling stresses, cases of symplectic eigenfunctions and their characteristic roots for three end conditions, various circumference wave number n , length L/R , thickness h/R , four distribution patterns of NTs and two kinds of reinforcement nanofiller are tabulated in tables 3–7.

From Table 3, it is clear that the end conditions do not affect the case of symplectic eigenfunctions regardless of circumference wave number n . It is also noted that the circumference wave number n has a significant influence on the case of symplectic eigenfunctions when n is small. However, the symplectic eigenfunctions always belong to Case V when n is large enough. Tables 4 and 5 present the buckling stresses, cases of symplectic eigenfunctions and their characteristic roots for various L/R and h/R . It is observed that the case of symplectic eigenfunctions have relations with the length and thickness of the shell when n is small. To further illustrate this, the variations of buckling stresses versus L/R and h/R with different n are plotted in figures 4 and 5. The influence of the reinforcement nanotubes (NT) and their distribution patterns on the case of symplectic eigenfunctions are investigated in tables 6 and 7, respectively. It is found that the piezoelectric FG-NTRC cylindrical shell with different reinforcement NTs and distribution patterns of NTs may produce different cases of symplectic eigenfunctions when n is small.

Property	CNT	BNNT	PVDF
c_{11} (GPa)	5824.9	2035	238.24
c_{22} (GPa)	7303.7	2035	23.6
c_{12} (GPa)	1019.37	692	3.98
c_{66} (GPa)	1944.5	672	6.43
e_{31} (C/m ²)	0	0.95	−0.135
e_{32} (C/m ²)	0	−0.45	−0.145
$\varepsilon_{11} = \varepsilon_{22} = \varepsilon_{33}$ (10 ^{−9} C/Vm)	0	0.17708	11.068
β_1 (10 ⁶ NK ^{−1} m ^{−2})	25.413	2.857	17.198
β_2 (10 ⁶ NK ^{−1} m ^{−2})	41.272	2.051	1.958

Table 2. Material properties of BNNT, CNT and PVDF.

n	Eigensolution	Characteristic roots					σ_{mn} (MPa)
		C-C					
0	Case I	31.8519i	25.6692i	347.781	0	0	3513.36
1	Case II	28.4520i	22.2538i	0.135052i	347.783	0	3096.72
2	Case VI	12.3684i	5.79333i	3.23354i	0.193372i	347.787	1843.09
5	Case V	9.83078i	4.04971i	0.852275	66.0224	347.817	391.08
10	Case V	16.2447i	10.2467i	1.65614	134.083	347.925	746.39
		C-S					
0	Case I	30.1889i	27.0832i	347.781	0	0	3450.14
1	Case II	26.8361i	23.7118i	0.133366i	347.783	0	3047.35
2	Case VI	11.0384i	8.09206i	2.58624i	0.193946i	347.787	1836.50
5	Case V	8.01563i	4.96564i	0.852544	66.0167	347.817	339.36
10	Case V	14.5183i	11.4651i	1.65615	134.083	347.925	687.53
		S-S					
0	Case I	28.9171i	28.2743i	347.781	0	0	3429.71
1	Case II	25.3615i	25.1327i	0.132797i	347.783	0	3030.60
2	Case VI	9.90976i	9.42478i	2.47125i	0.194116i	347.787	1834.56
5	Case V	6.33423i	6.28319i	0.852649	66.0145	347.817	319.43
10	Case V	13.2460i	12.5664i	1.65615	134.083	347.925	667.97

Table 3. Buckling stresses, cases of symplectic eigenfunctions and characteristic roots for a piezoelectric FG-NTRC cylindrical shell reinforced by CNTs with different end conditions (FG-O, $m = 1$, $L/R = 1$, $h/R = 0.01$).

From tables 4–7, it is worth to note that the influences of geometrical parameters, reinforcement NTs and their distribution patterns on the case of symplectic eigenfunctions only occur under the conditions of a small circumference wave number n . In other words, analytical solutions for buckling of the piezoelectric FG-NTRC cylindrical shell have a unique expression consisting of Case V symplectic eigenfunctions when n is large enough. The observations explain the reasons for the use of single-formed trial functions in the classical analytical method. In the buckling analysis of cylindrical shells, the circumference wave number n for the critical buckling stress usually decreases with the increase of L/R [Yamaki 1984]. The length of shells in most of theoretical studies usually selected less than 10 (e.g., [Mirzavand and Eslami 2007; Mirzavand and Eslami 2011; Salehi-Khojin and Jalili 2008]) so that n for the critical buckling stress is larger than 5. Thus, the analytical solutions only have a unique form (a series of Case V symplectic eigenfunctions) and the trial functions could produce accurate results. However, the specific trial functions will lead to errors when the circumference wave number n for the critical buckling stress is small (e.g., a very long shell).

At last, to get a better understanding of the buckling of piezoelectric FG-NTRC cylindrical shells, the corresponding buckling modes for C-C end condition in Table 3 are presented in Figure 6. The superscript and subscript of η are the case of symplectic eigenfunctions and the circumference wave

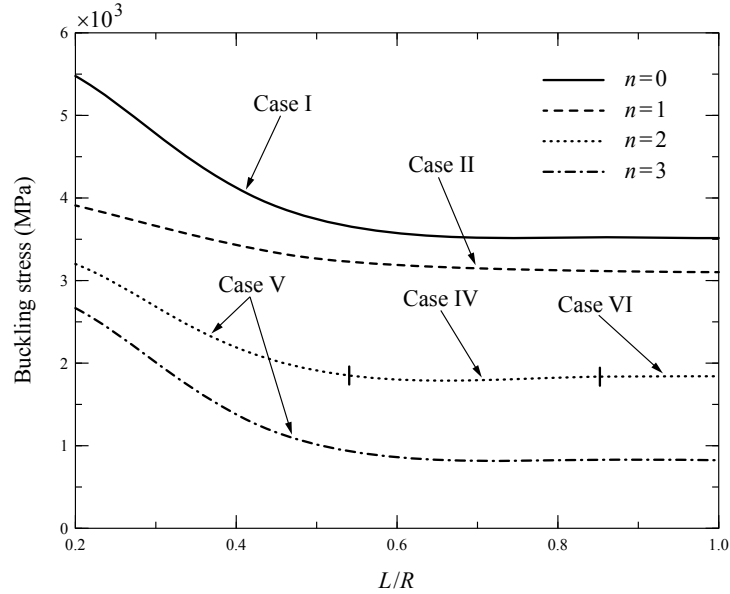


Figure 4. Variations of buckling stresses for a C-C piezoelectric FG-NTRC cylindrical shell reinforced by CNTs versus L/R with different n (FG-O, $m = 1$, $h/R = 0.01$).

number n . The color of the buckling modes is obtained by the “jet” type of the “colormap” function in Matlab. Different colors represent the displacement along the z -axes (i.e., w) of the cylindrical shell.

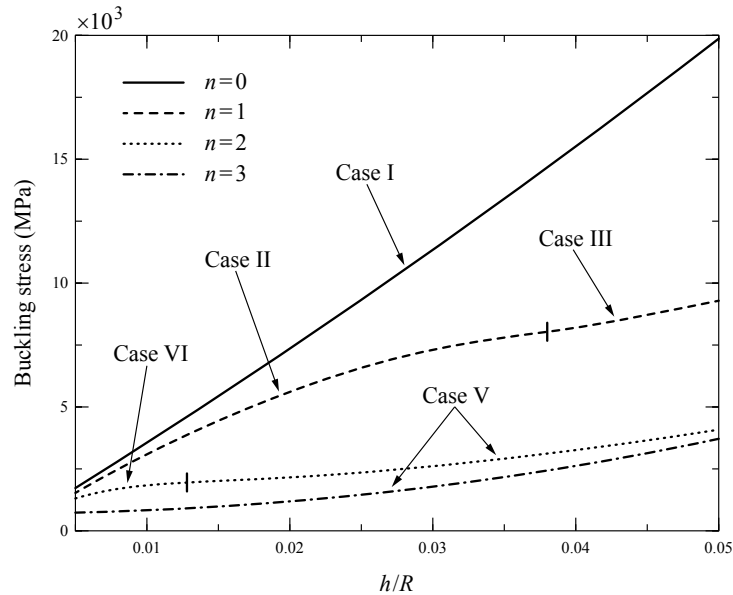


Figure 5. Variations of buckling stresses for a C-C piezoelectric FG-NTRC cylindrical shell reinforced by CNTs versus h/R with different n (FG-O, $m = 1$, $L/R = 1$).

n	Eigensolution	Characteristic roots					σ_{mn} (MPa)
		$L/R = 0.2$					
0	Case I	47.6496i	17.1589i	347.781	0	0	5485.46
1	Case II	37.9546i	15.2396i	0.165142i	347.783	0	3910.95
2	Case V	34.4650i	0.134607i	0.501912	19.2416	347.787	3215.40
3	Case V	32.2400i	0.400829i	0.561991	37.0153	347.794	2670.11
		$L/R = 0.5$					
0	Case I	35.1184i	23.2816i	347.781	0	0	3738.83
1	Case II	31.5626i	19.6989i	0.141165i	347.783	0	3272.59
2	Case V	16.5167i	0.188339i	2.18946	6.57829	347.787	1904.45
3	Case V	12.9775i	0.894441i	0.655560	35.3272	347.794	1014.58
		$L/R = 0.8$					
0	Case I	32.6248i	25.0611i	347.781	0	0	3555.36
1	Case II	29.1444i	21.6580i	0.136094i	347.783	0	3127.07
2	Case IV	12.8346i	0.193061i	347.787	$0.752660 \pm 4.18510i$		1846.69
3	Case V	8.44500i	1.31099i	0.693229	35.0258	347.794	848.51
		$L/R = 1$					
0	Case I	31.8519i	25.6692i	347.781	0	0	3513.36
1	Case II	28.4520i	22.2538i	0.135052i	347.783	0	3096.72
2	Case VI	12.3684i	5.79333i	3.23354i	0.193372i	347.787	1843.09
3	Case V	7.25032i	1.50749i	0.703436	34.9646	347.794	817.80

Table 4. Buckling stresses, cases of symplectic eigenfunctions and characteristic roots for a C-C piezoelectric FG-NTRC cylindrical shell reinforced by CNTs with different L/R (FG-O, $m = 1$, $h/R = 0.01$).

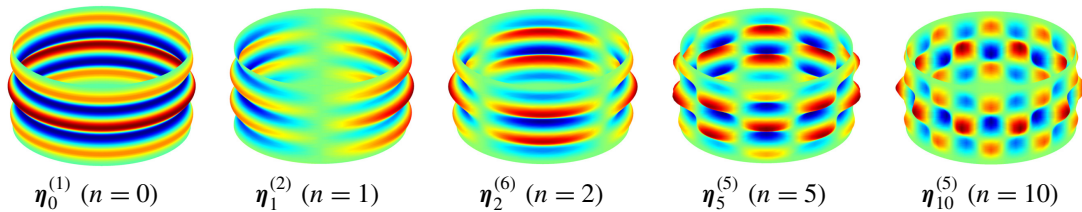


Figure 6. Buckling mode shapes for C-C piezoelectric FG-NTRC cylindrical shells with different n ($m = 1$, $L/R = 1$, $h/R = 0.01$).

6.3. Effects of the distribution patterns of NTs, electric voltage and temperature rise. To study the effects of the distribution patterns of NTs, electric voltage and temperature rise on the critical buckling stresses, a C-C piezoelectric NTRC cylindrical shell with $R = 0.1$ m, $L/R = 1$ and $h/R = 0.01$ is considered here. Variations of critical buckling stresses versus the volume fraction V_{NT} for different

reinforcement NTs and distribution patterns of NTs are plotted in Figure 7 with $\phi_0 = 10000$ V and $\Delta T = 10$ K. It is apparent that the critical buckling stress monotonically increases with the increasing V_{NT}^* regardless of the reinforcement NTs and their distribution patterns; the critical buckling stresses for the shell reinforced by CNTs are always larger than those reinforced by BNNTs. In addition, it is also worth to note that the FG distributions produce larger critical buckling stresses than the UD when V_{NT}^* is larger than a certain value. The observation implies the FG distributions of reinforcement NTs could improve the antibuckling performance of the piezoelectric FG-NTRC cylindrical shell. The corresponding critical buckling mode shapes for $V_{NT}^* = 0.4$ in Figure 7 are presented in Figure 8. It is clear that the critical buckling mode shapes for different reinforcement NTs and distribution patterns of NTs may have different n .

The critical buckling stresses for different applied electric voltages and temperature rises are tabulated in tables 8 and 9, respectively. The computation parameters are taken as $R = 0.1$ m, $L/R = 1$, $h/R = 0.01$, $N_{NT}^* = 0.2$, $\Delta T = 10$ K for Table 8 and $\phi_0 = 10000$ V for Table 9. It is observed that, for a specific

n	Eigensolution	Characteristic roots					σ_{mn} (MPa)
		$h/R = 0.005$					
0	Case I	47.1921i	34.6504i	695.562	0	0	1707.06
1	Case II	41.3313i	35.1534i	0.0853643i	695.563	0	1539.29
2	Case VI	36.5806i	24.0368i	0.483566i	0.105374i	695.565	1270.04
3	Case V	14.5791i	0.436957i	3.41190	12.3680	695.569	735.64
		$h/R = 0.01$					
0	Case I	31.8519i	25.6692i	347.781	0	0	3513.36
1	Case II	28.4520i	22.2538i	0.135052i	347.783	0	3096.72
2	Case VI	12.3684i	5.79333i	3.23354i	0.193372i	347.787	1843.09
3	Case V	7.25032i	1.50749i	0.703436	34.9646	347.794	817.80
		$h/R = 0.02$					
0	Case I	23.4341i	17.4449i	173.891	0	0	7363.67
1	Case II	18.1864i	12.1161i	0.258297i	173.893	0	5633.51
2	Case V	6.57791i	0.506629i	0.600103	22.4029	173.902	2135.58
3	Case V	7.07369i	1.83233i	0.531687	39.0081	173.916	1179.39
		$h/R = 0.05$					
0	Case I	16.1556i	10.1217i	69.5562	0	0	19912.16
1	Case III	7.76176i	0.451008	8.29977	69.5634	0	9295.67
2	Case V	6.41198i	0.751327i	0.355160	26.1836	69.5850	4087.02
3	Case V	7.03125i	1.90352i	0.501247	40.0669	69.6209	3708.66

Table 5. Buckling stresses, cases of symplectic eigenfunctions and characteristic roots for a C-C piezoelectric FG-NTRC cylindrical shell reinforced by CNTs with different h/R (FG-O, $m = 1$, $L/R = 1$).

n	Eigensolution	Characteristic roots					σ_{mn} (MPa)
		CNT					
0	Case I	30.1287i	24.0535i	283.790	0	0	3996.50
1	Case II	26.4194i	20.4406i	0.147932i	283.791	0	3461.30
2	Case V	8.56357i	0.527150i	2.01878	7.46659	283.797	1882.29
3	Case V	8.25457i	2.48970i	0.548627	36.2180	283.805	898.03
		BNNT					
0	Case I	23.0869i	17.0869i	284.368	0	0	2246.17
1	Case II	21.2855i	16.0233i	0.0974117i	284.370	0	1930.55
2	Case VI	16.8124i	10.5598i	0.533340i	0.211343i	284.375	1496.09
3	Case V	7.78340i	1.46291i	0.812484	12.9785	284.384	839.19

Table 6. Buckling stresses, cases of symplectic eigenfunctions and characteristic roots for a C-C piezoelectric FG-NTRC cylindrical shell with different reinforcement nanotubes (FG-X, $m = 1$, $L/R = 1$, $h/R = 0.01$).

reinforcement NT and distribution pattern, the critical buckling stress show a decreasing trend with the increase of electric voltage or temperature rise. Furthermore, it is also noted from the tabular data that the piezoelectric FG-NTRC cylindrical shell is insensitive to the electric voltage. For example, a 50×10^4 V electric voltage only leads to a 2.29% decrease of the critical buckling stress for the shell reinforced by CNT with FG-X distribution. In contrast, the piezoelectric NTRC cylindrical shell is very sensitive to the temperature rise. The critical buckling stresses significantly decreased by the temperature rise.

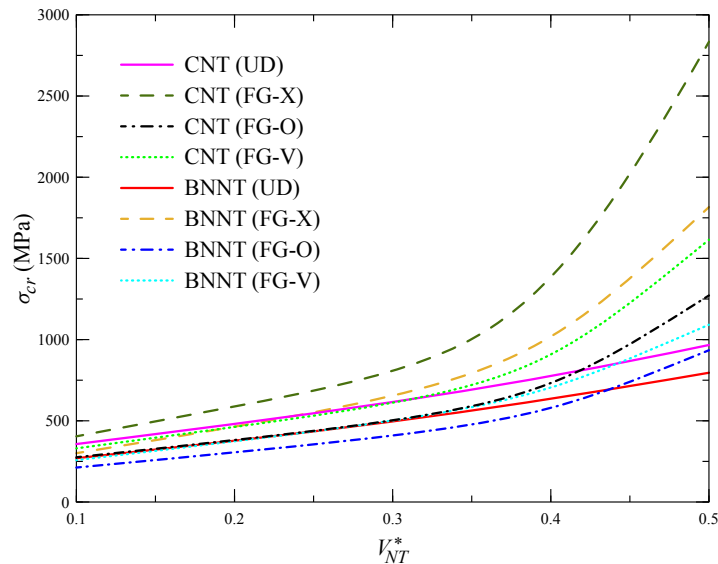


Figure 7. Critical buckling stresses (MPa) for C-C piezoelectric NTRC cylindrical shells with different V_{NT}^* .

n	Eigensolution	Characteristic roots					σ_{mn} (MPa)
		UD					
0	Case I	31.1433i	24.9141i	314.160	0	0	3718.79
1	Case II	27.4362i	21.4132i	0.142458i	314.162	0	3239.61
2	Case IV	9.43700i	0.334121i	314.167	$3.37294 \pm 2.77948i$		1823.08
3	Case V	7.86433i	2.20178i	0.577299	36.1523	314.175	837.58
		FG-X					
0	Case I	30.1287i	24.0535i	283.790	0	0	3996.50
1	Case II	26.4194i	20.4406i	0.147932i	283.791	0	3461.30
2	Case V	8.56357i	0.527150i	2.01878	7.46659	283.797	1882.29
3	Case V	8.25457i	2.48970i	0.548627	36.2180	283.805	898.30
		FG-O					
0	Case I	31.8519i	25.6692i	347.781	0	0	3513.36
1	Case II	28.4520i	22.2538i	0.135052i	347.783	0	3096.72
2	Case VI	12.3684i	5.79333i	3.23354i	0.193372i	347.787	1843.09
3	Case V	7.25032i	1.50749i	0.703436	34.9646	347.794	817.80
		FG-V					
0	Case I	31.0240i	24.8178i	314.160	0	0	3780.42
1	Case II	27.3637i	21.3602i	0.142141i	314.162	0	3300.07
2	Case IV	9.36739i	0.232799i	314.167	$3.17671 \pm 3.49833i$		1876.80
3	Case V	7.36768i	1.73605i	0.639055	35.7441	314.175	856.94

Table 7. Buckling stresses, cases of symplectic eigenfunctions and characteristic roots for a C-C piezoelectric FG-NTRC cylindrical shell reinforced by CNTs with different distribution patterns ($m = 1$, $L/R = 1$, $h/R = 0.01$).

7. Conclusion

The electro-thermo-mechanical buckling of a piezoelectric FG-NTRC cylindrical shell is investigated under the framework of Hamiltonian system. Exact solutions for buckling of piezoelectric FG-NTRC cylindrical shells are obtained and expressed in a series of symplectic eigenfunctions. Highly accurate buckling loads and analytical buckling shape functions are achieved simultaneously. The major conclusions are summarized as follows:

- (1) Exact solutions for buckling of piezoelectric FG-NTRC cylindrical shells have five possible forms, which highly depend on the geometrical parameters (L/R and h/R), circumference wave numbers, reinforcement nanotubes and their distribution patterns.
- (2) The influences of geometrical parameters (L/R and h/R), reinforcement NTs and their distribution patterns on expressions of symplectic eigenfunctions only occur when the circumference wave number n is small. Otherwise, the symplectic eigenfunctions only have a unique form (Case V).

Distribution	ϕ_0 (10^4 V)				
	-50	-25	0	25	50
CNT					
UD	488.913	482.232	475.550	468.868	462.187
FG-X	595.554	588.879	582.204	575.529	568.854
FG-O	389.925	383.250	376.575	369.900	363.225
FG-V	473.930	467.255	460.580	453.905	447.230
BNNT					
UD	383.596	378.388	373.181	367.974	362.766
FG-X	463.227	458.158	453.088	448.018	442.949
FG-O	311.640	306.571	301.501	296.431	291.362
FG-V	350.880	345.811	340.741	335.671	330.602

Table 8. Critical buckling stresses (MPa) for a C-C piezoelectric NTRC cylindrical shell with different electric voltage ϕ_0 .

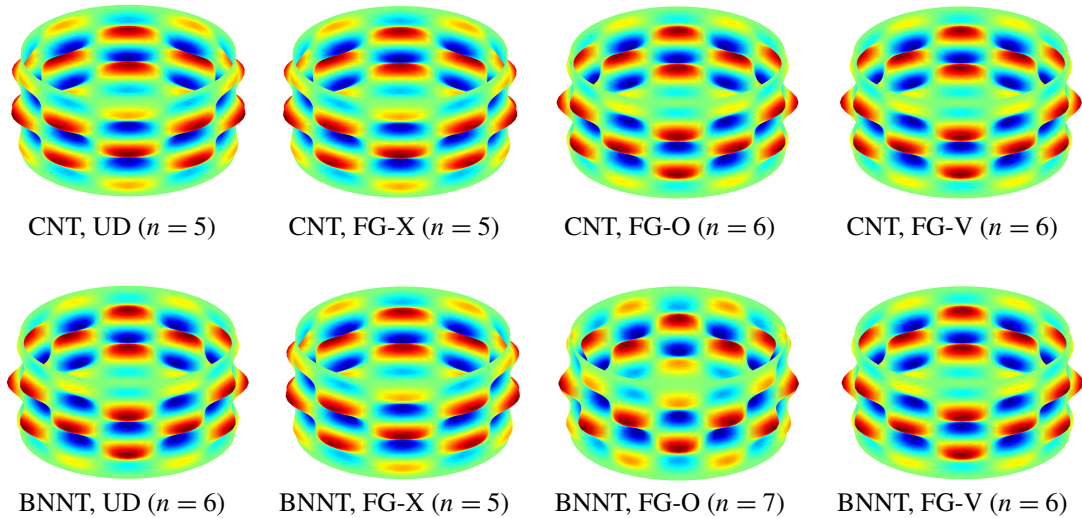


Figure 8. Critical buckling mode shapes for C-C piezoelectric NTRC cylindrical shells with different reinforcement NTs and distribution patterns ($L/R = 1$, $h/R = 0.01$).

- (3) The FG distribution of NTs could increase the carrying capacity of piezoelectric FG-NTRC cylindrical shells compared to uniform piezoelectric NTRC cylindrical shells. The FG-X shell produces the highest critical buckling stress.
- (4) The applied electric voltages and temperature rises could affect the carrying capacity of piezoelectric FG-NTRC cylindrical shells. The critical buckling stresses are sensitive to the temperature rise but insensitive to the electric voltage.

Distribution	ΔT				
	0	5	10	15	20
CNT					
UD	663.957	569.620	475.283	380.946	286.609
FG-X	770.611	676.274	581.937	487.600	393.263
FG-O	564.982	470.645	376.308	281.971	187.634
FG-V	648.987	554.650	460.313	365.976	271.639
BNNT					
UD	516.471	444.722	372.973	301.224	229.475
FG-X	596.383	524.634	452.885	381.136	309.387
FG-O	444.796	373.047	301.298	229.549	157.800
FG-V	484.036	412.287	340.538	268.789	197.040

Table 9. Critical buckling stresses (MPa) for a C-C piezoelectric NTRC cylindrical shell with different temperature rise ΔT .

Appendix A

$$\mathbf{H} = \begin{bmatrix} \mathbf{H}_1 & \mathbf{H}_2 \\ \mathbf{H}_3 & -\mathbf{H}_1^T \end{bmatrix}, \quad (\text{A.1})$$

$$\mathbf{H}_1 = \begin{bmatrix} 0 & \left(\frac{B_{66}}{A_{66}} - R\right) \frac{\partial}{\partial x} & 0 & -2 \frac{RB_{66}}{A_{66}} \frac{\partial}{\partial x} & 0 \\ \frac{R\kappa_3}{\kappa_2} \frac{\partial}{\partial x} & 0 & \frac{R\kappa_5}{\kappa_2} \frac{\partial^2}{\partial x^2} - 1 & 0 & \frac{RB_{22}E_{32}}{\kappa_2} \\ 0 & 1 & 0 & -R & 0 \\ -R \frac{\kappa_4}{\kappa_2} \frac{\partial}{\partial x} & 0 & R \frac{\kappa_6}{\kappa_2} \frac{\partial^2}{\partial x^2} & 0 & -\frac{RA_{22}E_{32}}{\kappa_2} \\ 0 & 0 & 0 & 0 & 0 \end{bmatrix}, \quad (\text{A.2})$$

$$\mathbf{H}_2 = \begin{bmatrix} \frac{R}{A_{66}} & 0 & 0 & 0 & 0 \\ 0 & \frac{RD_{22}}{\kappa_2} & 0 & -\frac{RB_{22}}{\kappa_2} & 0 \\ 0 & 0 & 0 & 0 & 0 \\ 0 & -\frac{RB_{22}}{\kappa_2} & 0 & \frac{RA_{22}}{\kappa_2} & 0 \\ 0 & 0 & 0 & 0 & -\frac{1}{RX_{22}} \end{bmatrix}, \quad (\text{A.3})$$

$$\mathbf{H}_3 = \begin{bmatrix} \frac{R\kappa_{10}}{D_{22}\kappa_2} \frac{\partial^2}{\partial x^2} & 0 & \frac{R\kappa_{11}}{D_{22}\kappa_2} \frac{\partial^3}{\partial x^3} & 0 & RE_{32} \frac{\kappa_4}{\kappa_2} \frac{\partial}{\partial x} \\ 0 & -\frac{\kappa_9}{R} \frac{\partial^2}{\partial x^2} & 0 & 2\kappa_9 \frac{\partial^2}{\partial x^2} & 0 \\ -\frac{R\kappa_{11}}{D_{22}\kappa_2} \frac{\partial^3}{\partial x^3} & 0 & -\frac{R\kappa_{12}}{D_{22}\kappa_2} \frac{\partial^4}{\partial x^4} + RN_x^0 \frac{\partial^2}{\partial x^2} & 0 & -R \left(E_{31} - \frac{\kappa_6}{\kappa_2} E_{32} \right) \frac{\partial^2}{\partial x^2} \\ 0 & 2\kappa_9 \frac{\partial^2}{\partial x^2} & 0 & -4R\kappa_9 \frac{\partial^2}{\partial x^2} & 0 \\ -RE_{32} \frac{\kappa_4}{\kappa_2} \frac{\partial}{\partial x} & 0 & -R \left(E_{31} - \frac{\kappa_6}{\kappa_2} E_{32} \right) \frac{\partial^2}{\partial x^2} & 0 & R \left(X_{11} \frac{\partial^2}{\partial x^2} - X_{33} - \frac{A_{22}E_{32}^2}{\kappa_2} \right) \end{bmatrix}. \quad (\text{A.4})$$

Appendix B

$$\xi_1^{(0)} = \frac{A_{11}E_{31}^2R + (2A_{11}B_{12} - 2A_{12}B_{11} - A_{11}N_x^0R)X_{11} + (A_{11}D_{11} - B_{11}^2)RX_{33}}{(B_{11}^2 - A_{11}D_{11})RX_{11}} \quad (\text{B.1})$$

$$\xi_2^{(0)} = \frac{(A_{12}^2 - A_{11}A_{22})X_{11} + R(2A_{12}B_{11} - 2A_{11}B_{12} + A_{11}N_x^0R)X_{33}}{(B_{11}^2 - A_{11}D_{11})R^2X_{11}}, \quad (\text{B.2})$$

$$\xi_3^{(0)} = \frac{(-A_{12}^2 + A_{11}A_{22})X_{33}}{(B_{11}^2 - A_{11}D_{11})R^2X_{11}}, \quad (\text{B.3})$$

$$\xi_4^{(0)} = 0 \quad \text{and} \quad \xi_5^{(0)} = 0. \quad (\text{B.4})$$

Appendix C

$$\begin{aligned} \xi_1 = & \frac{1}{(B_{11}^2 - A_{11}D_{11})R^6(D_{66} + 2B_{66}R + A_{66}R^2)X_{11}} \\ & \times \left\{ -(B_{66}^2D_{11} - 2B_{11}B_{66}D_{12} + B_{11}^2D_{22} - A_{66}D_{11}D_{66})n^2X_{11} \right. \\ & - 2A_{12}B_{11}D_{66}RX_{11} - 2(B_{11}^2B_{22} + A_{12}B_{66}D_{11})n^2RX_{11} \\ & - 2B_{11}[2B_{66}^2 - (A_{12} + A_{66})(D_{12} + 2D_{66})]n^2RX_{11} - 4A_{12}B_{11}B_{66}R^2X_{11} \\ & - [B_{11}(A_{22}B_{11} - 4A_{12}B_{66}) + A_{12}(A_{12} + 2A_{66})D_{11}]n^2R^2X_{11} \\ & - 2A_{12}A_{66}B_{11}R^3X_{11} - B_{12}^2n^2(D_{11} - 2B_{11}R)X_{11} \\ & + 2B_{12}n^2[-(A_{12} + A_{66})D_{11}R + B_{66}(-D_{11} + B_{11}R) + B_{11}(D_{12} + D_{66} + A_{12}R^2)]X_{11} \\ & - B_{11}^2D_{66}n^2R^2X_{22} - 2B_{11}^2B_{66}n^2R^3X_{22} - A_{66}B_{11}^2n^2R^4X_{22} \\ & - B_{11}^2R^2[D_{66} + R(2B_{66} + A_{66}R)]X_{33} + A_{11}(-D_{12}^2 + D_{12}D_{22})n^2X_{11} \\ & + A_{11}D_{66}[-2D_{12}n^2X_{11} + 2B_{12}(1 - 2n^2)RX_{11} \\ & \quad + R^2(E_{31}^2 + 4A_{66}n^2X_{11} - N_x^0X_{11} + D_{11}n^2X_{22} + D_{11}X_{33})] \\ & + A_{11}R[-4B_{66}^2n^2RX_{11} + n^2(2B_{22}D_{11} - 2B_{12}D_{12} - B_{12}^2R + A_{22}D_{11}R)X_{11} \\ & - 4B_{12}B_{66}R(-1 + n^2)X_{11} + 2B_{66}R^2(E_{31}^2 - N_x^0X_{11} + D_{11}n^2X_{22} + D_{11}X_{33}) \\ & + A_{66}R(2D_{12}n^2X_{11} + 2B_{12}RX_{11}) \\ & \quad \left. + A_{66}R^3(E_{31}^2 - N_x^0X_{11} + D_{11}n^2X_{22} + D_{11}X_{33}) \right\}, \quad (\text{C.1}) \end{aligned}$$

$$\begin{aligned} \xi_2 = & \frac{1}{(B_{11}^2 - A_{11}D_{11})R^4(D_{66} + 2B_{66}R + A_{66}R^2)X_{11}} \\ & \times \left\{ -2B_{12}^2n^2(-1 + n^2)RX_{11} \right. \end{aligned}$$

$$\begin{aligned}
& -2A_{12}B_{11}n^2R[E_{31}E_{32}R^2 + (-1+n^2)(D_{22}+B_{22}R)X_{11} \\
& \quad - D_{66}R^2X_{22} + (D_{12}+2D_{66})n^2R^2X_{22}] \\
& + B_{11}^2n^2R[E_{32}^2 + n^2(D_{22}+2B_{22}R+A_{22}R^2)X_{22}] + A_{12}^2D_{66}R^2X_{11} \\
& + A_{12}^2n^2R^2[2(D_{12}+2D_{66})(-1+n^2)X_{11} + R^2(E_{31}^2 - N_x^0X_{11} + D_{11}n^2X_{22})] \\
& + A_{66}2A_{12}E_{31}^2n^2R^4 \\
& + A_{66}(D_{12}^2n^4 - D_{11}D_{22}n^4 - 2B_{22}D_{11}n^4R - 2A_{12}D_{12}n^2R^2 - A_{22}D_{11}n^4R^2 \\
& \quad + 4A_{12}D_{12}n^4R^2 + A_{12}^2R^2 - 2A_{12}n^2N_x^0R^4)X_{11} \\
& + 2A_{12}A_{66}D_{11}n^4R^4X_{22} - 2A_{66}D_{12}D_{66}n^4X_{11} \\
& + A_{66}D_{66}n^2R^2[E_{31}^2 - (-4A_{12}+8A_{12}n^2+N_x^0)X_{11} + n^2(D_{11}+4B_{11}R)X_{22}] \\
& + 2A_{66}B_{11}n^2R[D_{22}n^2X_{11} + B_{22}(1+n^2)RX_{11} \\
& \quad + R^2(E_{31}E_{32} + A_{22}X_{11} + D_{12}n^2X_{22} - A_{12}R^2X_{22})] \\
& - A_{11}D_{22}n^2R^2[(E_{31}^2 + A_{66}n^2X_{11} - N_x^0X_{11} + D_{11}n^2X_{22}) + D_{66}n^2X_{11}] \\
& + A_{11}D_{12}^2n^4R^2X_{22} + 2A_{11}D_{66}E_{31}E_{32}n^2R^2 \\
& - A_{11}D_{66}R(-1+2n^2)[-A_{22}R + 2n^2(B_{22}+A_{22}R)]X_{11} \\
& - A_{11}D_{66}n^2R^4X_{22}(4A_{66}n^2 - N_x^0) \\
& - 2A_{11}D_{12}n^2R[-E_{31}E_{32}R + (-1+n^2)(B_{22}+A_{22}R)X_{11} \\
& \quad + n^2R(-D_{66}+A_{66}R^2)X_{22}] \\
& - A_{11}D_{11}n^4R^3(2B_{22}+A_{22}R)X_{22} - A_{11}D_{11}n^2R^2E_{32}^2 \\
& - 2A_{11}R^3B_{22}n^2[E_{31}^2 + (A_{66}-N_x^0)X_{11}] \\
& - A_{11}R^4[A_{22}(A_{66}X_{11} + E_{31}^2n^2 - N_x^0n^2X_{11}) + A_{66}n^2(2E_{31}E_{32} - N_x^0R^2X_{22})] \\
& + R^2[B_{11}^2D_{22} - A_{66}D_{11}D_{66} + A_{11}(D_{12}^2 - D_{11}D_{22} + 2D_{12}D_{66})]n^2X_{33} \\
& - 2[-B_{11}^2B_{22} + A_{11}B_{22}D_{11} + (A_{12}+A_{66})B_{11}(D_{12}+2D_{66})]n^2R^3X_{33} \\
& + 2A_{12}B_{11}D_{66}R^3X_{33} + [A_{12}^2D_{11} + 2A_{12}A_{66}D_{11} + A_{22}(B_{11}^2 - A_{11}D_{11}) \\
& \quad - 2A_{11}A_{66}(D_{12}+2D_{66})]n^2R^4X_{33} \\
& + A_{11}D_{66}N_x^0R^4X_{33} + R^2(2A_{12}A_{66}B_{11}R^3 + A_{11}A_{66}N_x^0R^4)X_{33} - 2B_{66}^2D_{12}n^4X_{11} \\
& + B_{66}^2n^2[E_{31}^2R^2 + 4A_{12}(1-2n^2)R^2X_{11} - N_x^0R^2X_{11} \\
& \quad + R^2(D_{11}+4B_{11}R+4A_{11}R^2)(n^2X_{22}+X_{33})] \\
& + B_{12}^2n^2[D_{66}n^2X_{11} + 4B_{66}(1-2n^2)RX_{11} + E_{31}^2R^2 + 4A_{66}R^2X_{11} \\
& \quad - 2A_{12}(-1+n^2)R^2X_{11} - N_x^0R^2X_{11} \\
& \quad + R^2(D_{11}-2B_{11}R+A_{11}R^2)(n^2X_{22}+X_{33})] \\
& - 2B_{12}B_{66}^2n^2(-1+4n^2)RX_{11} - 2B_{12}B_{66}D_{12}n^4X_{11}
\end{aligned}$$

$$\begin{aligned}
& + 2B_{12}B_{66}n^2R^2[(A_{12} - 4A_{12}n^2 - N_x^0)X_{11} + E_{31}^2 \\
& \quad + (D_{11}n^2 - B_{11}n^2R - 2A_{11}R^2 + 2A_{11}n^2R^2)X_{22}] \\
& - 2B_{12}B_{66}R^2[-D_{11}n^2 + 2A_{11}R^2 + n^2R(B_{11} - 2A_{11}R)]X_{33} \\
& - 2A_{11}B_{12}n^2R[-E_{31}E_{32}R^2 - (-1 + n^2)(D_{22} + B_{22}R)X_{11} \\
& \quad + (D_{66} - D_{12}n^2 + 2D_{66}n^2)R^2X_{22}] \\
& - 2A_{66}B_{12}n^2R[(D_{66} - 2D_{12}n^2 + 2D_{66}n^2)X_{11} \\
& \quad + R^2(-E_{31}^2 + N_x^0X_{11} - D_{11}n^2X_{22} + A_{11}R^2X_{22})] \\
& - 2B_{12}R^3[-A_{66}D_{11}n^2 + A_{11}(D_{66} - D_{12}n^2 - 2D_{66}n^2 + A_{66}R^2)]X_{33} \\
& + 2A_{12}B_{12}n^2R[(-D_{12} - D_{66} + D_{12}n^2 + 2D_{66}n^2)X_{11} \\
& \quad + R^2(E_{31}^2 + 2A_{66}X_{11} - N_x^0X_{11} + D_{11}n^2X_{22} + D_{11}X_{33})] \\
& + 2B_{11}B_{12}B_{22}(-1 + n^2)n^2RX_{11} \\
& - 2B_{11}B_{12}n^2R^2[E_{31}E_{32} + A_{22}(1 - n^2)X_{11} + (D_{12} + B_{66} + A_{12}R^2)(n^2X_{22} + X_{33})] \\
& + 2B_{66}(A_{12}^2 - A_{11}A_{22})R^3X_{11} \\
& + 2B_{66}n^4[A_{11}R(D_{22} + 2B_{22}R)X_{11} + B_{11}(D_{22} + 3B_{22}R + 2A_{22}R^2)X_{11} \\
& \quad + A_{12}D_{11}R^3X_{22} - B_{11}R^2(D_{12} + 2A_{12}R^2)X_{22}] \\
& + 4A_{12}B_{11}B_{66}R^4X_{33} + 2A_{11}B_{66}N_x^0R^5X_{33} - 4A_{12}^2B_{66}n^2R^3X_{11} \\
& + 2A_{11}B_{66}n^2R^3(2A_{22}X_{11} + N_x^0R^2X_{22}) \\
& - 2A_{12}B_{66}n^2R[D_{12}X_{11} - R^2(E_{31}^2 - N_x^0X_{11} + D_{11}X_{33})] \\
& - 2B_{11}B_{66}n^2R[B_{22}X_{11} + E_{31}E_{32}R + A_{22}RX_{11} \\
& \quad + D_{12}RX_{33} + 2A_{12}R^3(-X_{22} + X_{33})], \quad (C.2)
\end{aligned}$$

$$\begin{aligned}
\xi_3 = & \frac{1}{(B_{11}^2 - A_{11}D_{11})R^6(D_{66} + 2B_{66}R + A_{66}R^2)X_{11}} \\
& \times \{ 2B_{66}^2E_{31}E_{32}n^4R^2 - B_{66}^2n^2[D_{22}n^4 + (1 - 2n)^2R(A_{22}R - 2B_{22}n^2 - 2A_{22}n^2R)]X_{11} \\
& - B_{66}^2n^4R^2[2D_{12}n^2 - (4A_{12} - 8A_{12}n^2 - N_x^0)R^2]X_{22} - 2A_{12}^2B_{66}n^2(1 - 2n^2)R^5X_{22} \\
& - 2A_{11}B_{66}n^2R^3[E_{32}^2n^2 + D_{22}n^4X_{22} + 2B_{22}n^4RX_{22} + A_{22}(-1 + 2n^2)R^2X_{22}] \\
& - 2B_{11}B_{66}E_{32}^2n^4R^2 - 2B_{11}B_{66}n^4R^2[D_{22}n^2 + B_{22}(-1 + 3n^2)R + A_{22}(-1 + 2n^2)R^2]X_{22} \\
& + 2A_{12}B_{66}n^2R[E_{31}E_{32}R^2 + (-1 + n^2)(-B_{22}R + D_{22}n^2 + 2B_{22}n^2R)X_{11} \\
& \quad + n^2R^2(D_{12} + N_x^0R^2)X_{22}] \\
& - A_{12}(-1 + n^2)n^2R^2[2E_{32}R(-B_{11}E_{32} + A_{12}E_{31}R) + A_{12}D_{22}(-1 + n^2)X_{11}]
\end{aligned}$$

$$\begin{aligned}
& -A_{12}^2 D_{66} n^2 R^4 X_{22} - A_{12} n^4 R^3 [2A_{12}(D_{12} + 2D_{66})(-1 + n^2)R \\
& \quad - A_{12} N_x^0 R^3 - 2B_{11}(-1 + n^2)(D_{22} + B_{22}R)] X_{22} \\
& - A_{11} n^2 R^2 [-D_{66} E_{32}^2 n^2 - A_{22} D_{22}(1 - n^2)X_{11} + 2A_{22} E_{31} E_{32}(1 - n^2)R^2 \\
& \quad + E_{32}^2 N_x^0 R^2 - A_{22} D_{22} n^4 X_{11} + B_{22}^2 (1 - n^2)^2 X_{11} \\
& \quad + n^2 R^2 (2A_{22} D_{12} - 2A_{22} D_{12} n^2 + D_{22} N_x^0 + A_{22} N_x^0 R^2) X_{22}] \\
& + A_{11} D_{66} n^2 R^2 [D_{22} n^4 + (-1 + 2n^2)R(-A_{22}R + 2B_{22}n^2 + 2A_{22}n^2 R)] X_{22} \\
& - 2A_{11} B_{22} n^2 R^3 [E_{31} E_{32}(1 - n^2) + n^2(D_{12} - D_{12} n^2 + N_x^0 R^2) X_{22}] \\
& + B_{66}^2 n^2 R^2 [2D_{12} n^2 + A_{12}(-4 + 8n^2)R^2 + N_x^0 R^2] X_{33} - 2B_{11} B_{66} D_{22} n^4 R^2 X_{33} \\
& + 2B_{66} [B_{11} B_{22} + A_{12} D_{12} - (3B_{11} B_{22} + A_{11} D_{22})n^2] n^2 R^3 X_{33} \\
& + 2B_{66} [A_{22} B_{11} - 2(A_{22} B_{11} + A_{11} B_{22})n^2] n^2 R^4 X_{33} \\
& + 2B_{66} [(A_{12}^2 - A_{11} A_{22})(-1 + 2n^2) + A_{12} n^2 N_x^0] R^5 X_{33} - A_{12}^2 D_{66} R^4 X_{33} \\
& - A_{12}^2 D_{66} R^4 X_{33} + A_{12} [-2A_{12}(D_{12} + 2D_{66})(-1 + n^2)R + A_{12} N_x^0 R^3 \\
& \quad + 2B_{11}(-1 + n^2)(D_{22} + B_{22}R)] n^2 R^3 X_{33} \\
& + A_{11} D_{22} (D_{66} n^4 - n^2 N_x^0 R^2) R^2 X_{33} \\
& + 2A_{11} B_{22} [-D_{12} - D_{66} + (D_{12} + 2D_{66})n^2 - N_x^0 R^2] n^2 R^3 X_{33} \\
& + A_{11} A_{22} [D_{66}(1 - 2n^2)^2 + 2D_{12}(-1 + n^2)n^2 - N_x^0 n^2 R^2] R^4 X_{33} \\
& + 2B_{12}^3 n^2 (-1 + n^2) R^3 (n^2 X_{22} + X_{33}) \\
& + B_{12}^2 n^2 R^2 [- (D_{66} n^2 + 4B_{66} R - 8B_{66} n^2 R + 2A_{12} R^2 \\
& \quad - 2A_{12} n^2 R^2 - N_x^0 R^2) (n^2 X_{22} + X_{33}) - A_{22}(-1 + n^2)^2 X_{11}] \\
& + 2B_{12} B_{66}^2 n^2 (-1 + 4n^2) R^3 (n^2 X_{22} + X_{33}) \\
& + 2B_{12} B_{66} n^2 R [-B_{12} n^2 (-1 + n^2) X_{11} + A_{22}(-1 + 3n^2 - 2n^4) R X_{11} + E_{31} E_{32} n^2 R \\
& \quad + (D_{12} n^2 R - A_{12} R^3 + 4A_{12} n^2 R^3 + N_x^0 R^3) (n^2 X_{22} + X_{33})] \\
& + 2A_{11} B_{12} n^2 R^2 [E_{31} E_{32}(1 - n^2) R + B_{22}(1 - n^2)^2 X_{11} \\
& \quad + R(D_{12} + D_{66} - (D_{12} + 2D_{66})n^2 + N_x^0 R^2) (n^2 X_{22} + X_{33})] \\
& + 2A_{11} B_{12} n^2 R^3 (1 - n^2) [E_{32}^2 + (D_{22} + B_{22}R) (n^2 X_{22} + X_{33})] \\
& + 2B_{11} B_{12} n^2 R^3 (1 - n^2) [(B_{22} + A_{22}R) (n^2 X_{22} + X_{33})] \\
& + A_{66} D_{22} n^4 [D_{66} n^2 X_{11} - 2B_{12}(-1 + n^2) R X_{11}] \\
& + A_{66} D_{22} n^4 R^2 [-2A_{12}(-1 + n^2) X_{11} + E_{31}^2 - N_x^0 X_{11} \\
& \quad + (D_{11} + 2B_{11} R + A_{11} R^2) (n^2 X_{22} + X_{33})] \\
& - 2A_{66} D_{12} n^4 R [E_{31} E_{32} R + (1 - n^2)(B_{22} + A_{22}R) X_{11} \\
& \quad + D_{66} n^2 R - A_{12} R^3 X_{22} + 2n^2 R^2 (B_{12} + A_{12}R) X_{22}]
\end{aligned}$$

$$\begin{aligned}
& -2A_{66}D_{12}n^2R^2[D_{66}n^2 - A_{12}R^2 + 2n^2R(B_{12} + A_{12}R)]X_{33} - A_{66}D_{12}^2n^4R^2(n^2X_{22} + X_{33}) \\
& + A_{66}D_{66}n^2R[-2E_{31}E_{32}n^2R + 2B_{22}n^2(-1 + 2n^2)X_{11} + A_{22}(1 - 2n^2)^2RX_{11} \\
& \quad - R^2(-2B_{12} + 8B_{12}n^2 - 4A_{12}R + 8A_{12}n^2R + N_x^0R)(n^2X_{22} + X_{33})] \\
& + A_{66}D_{11}n^4R^2[E_{32}^2 + R(2B_{22} + A_{22}R)(n^2X_{22} + X_{33})] \\
& + A_{66}n^2R^3[-4B_{12}^2n^2RX_{22} + 2B_{11}n^2(E_{32}^2 + A_{22}R^2X_{22})] \\
& + A_{66}n^2R^4[2A_{12}E_{31}E_{32} + A_{22}E_{31}^2n^2 - 4A_{12}E_{31}E_{32}n^2 + A_{11}E_{32}^2n^2 - A_{22}n^2N_x^0X_{11} \\
& \quad + (-A_{12}^2 + A_{11}A_{12} + 2A_{12}n^2N_x^0)R^2X_{22}] \\
& + 2A_{66}B_{12}n^2R^3[-A_{22}X_{11} + n^2(-2E_{31}E_{32} + A_{22}X_{11} - 2A_{12}R^2X_{22} + N_x^0R^2X_{22})] \\
& + A_{66}R^4[-4B_{12}^2n^2 + 2n^2(A_{22}B_{11} - 2A_{12}B_{12} + B_{12}N_x^0)R \\
& \quad + (-A_{12}^2 + A_{11}A_{12} + 2A_{12}n^2N_x^0)R^2]X_{33} \\
& + 2A_{66}B_{22}n^2R^3[A_{12}X_{11} + E_{31}^2n^2 - (A_{12} + N_x^0)n^2X_{11} \\
& \quad + n^2R(B_{11} + B_{11}n^2 + A_{11}R)X_{22} + R(B_{11} + B_{11}n^2 + A_{11}R)X_{33}]\}, \quad (C.3)
\end{aligned}$$

$$\begin{aligned}
\xi_4 = & \frac{1}{(B_{11}^2 - A_{11}D_{11})R^6(D_{66} + 2B_{66}R + A_{66}R^2)X_{11}} \\
& \times \{B_{66}^2E_{32}^2n^6 + B_{66}^2n^2(n^2X_{22} + X_{33})[D_{22}n^4 + (-1 + 2n^2)(-A_{22}R^2 + 2B_{22}n^2R + 2A_{22}n^2R^2)] \\
& \quad - 2B_{66}(-1 + n^2)n^2R[A_{12}E_{32}^2n^2 - B_{12}(-A_{22}R + B_{22}n^2 + 2A_{22}n^2R)(n^2X_{22} + X_{33}) \\
& \quad + A_{12}(-B_{22}R + D_{22}n^2 + 2B_{22}n^2R)(n^2X_{22} + X_{33})] \\
& + A_{66}n^4[-2A_{12}E_{32}^2R^2 + 2A_{12}E_{32}^2n^2R^2 + E_{32}^2N_x^0R^2 + B_{22}^2X_{11} - 2B_{22}^2n^2X_{11} + B_{22}^2n^4X_{11} \\
& \quad - A_{22}(-1 + n^2)(2E_{31}E_{32}R^2 - D_{22} + D_{22}n^2X_{11}) \\
& \quad + D_{22}n^2(-2A_{12} + 2A_{12}n^2 + N_x^0)R^2X_{22} \\
& \quad + A_{22}n^2R^2(2D_{12} - 2D_{12}n^2 + N_x^0R^2)X_{22} \\
& \quad + 2B_{12}(-1 + n^2)R(E_{32}^2 + D_{22}n^2X_{22} - A_{22}R^2X_{22})] \\
& + 2A_{66}B_{12}n^2R(-1 + n^2)(D_{12}n^2 - A_{22}R^2)X_{33} \\
& + A_{66}n^4R^2[D_{22}(-2A_{12} + 2A_{12}n^2 + N_x^0) + A_{22}(2D_{12} - 2D_{12}n^2 + N_x^0R^2)]X_{33} \\
& - 2A_{66}B_{22}E_{31}E_{32}n^4(-1 + n^2)R \\
& - 2A_{66}B_{22}n^2R[A_{12}R^2 + D_{12}(-1 + n^2)n^2 - (A_{12} + N_x^0)n^2R^2](n^2X_{22} + X_{33}) \\
& - A_{66}D_{66}n^2[D_{22}n^4 + (-1 + 2n^2)R(-A_{22}R + 2B_{22}n^2 + 2A_{22}n^2R)](n^2X_{22} + X_{33}) \\
& - A_{66}D_{66}E_{32}^2n^6 \\
& + (-1 + n^2)^2n^2R^2[A_{22}B_{12}^2(n^2X_{22} + X_{33}) - 2A_{12}B_{12}B_{22}(n^2X_{22} + X_{33})]
\end{aligned}$$

$$+ A_{12}^2(E_{32}^2 + D_{22}n^2X_{22} + D_{22}X_{33}) + A_{11}B_{22}^2(n^2X_{22} + X_{33}) \\ - A_{11}A_{22}(E_{32}^2 + D_{22}n^2X_{22} + D_{22}X_{33})\}], \quad (C.4)$$

$$\xi_5 = \frac{1}{(B_{11}^2 - A_{11}D_{11})R^6(D_{66} + 2B_{66}R + A_{66}R^2)X_{11} \\ \times \{A_{66}n^4(1 - n^2)^2[-B_{22}^2(n^2X_{22} + X_{33}) + A_{22}E_{32}^2 + A_{22}D_{22}(n^2X_{22} + X_{33})]\}}. \quad (C.5)$$

Acknowledgments

This work was supported by the National Natural Science Foundation of China (Grant 11672054); the Key Program of Natural Science Foundation of Liaoning Province of China (Grant 20170540186); High Level Talents Support Plan of Dalian of China (Grant 2017RQ111); Dalian Innovation Foundation of Science and Technology (Grant 2018J11CY005) and the Fundamental Research Funds for the Central Universities (Grant DUT17LK57).

References

- [Ansari et al. 2016] R. Ansari, T. Pourashraf, R. Gholami, and A. Shahabodini, “Analytical solution for nonlinear postbuckling of functionally graded carbon nanotube-reinforced composite shells with piezoelectric layers”, *Compos. B Eng.* **90** (2016), 267–277.
- [Chen and Zhao 2009] W. Q. Chen and L. Zhao, “The symplectic method for plane elasticity problem of functionally graded materials”, *Acta Mech. Sinica* **41**:4 (2009), 588–594. in Chinese.
- [Chen et al. 1996] C.-Q. Chen, Y.-P. Shen, and X.-M. Wang, “Exact solution of orthotropic cylindrical shell with piezoelectric layers under cylindrical bending”, *Int. J. Solids Struct.* **33**:30 (1996), 4481–4494.
- [Dai and Zheng 2011] H.-L. Dai and H.-Y. Zheng, “Buckling and post-buckling analyses for an axially compressed laminated cylindrical shell of FGM with PFRC in thermal environments”, *Eur. J. Mech. A Solids* **30**:6 (2011), 913–923.
- [Dai et al. 2013] H.-L. Dai, T. Dai, and H.-Y. Zheng, “Creep buckling and post-buckling analyses for a hybrid laminated viscoelastic FGM cylindrical shell under in-plane loading”, *Int. J. Mech. Mater. Des.* **9**:4 (2013), 309–323.
- [Dong and Wang 2007] K. Dong and X. Wang, “Wave propagation characteristics in piezoelectric cylindrical laminated shells under large deformation”, *Compos. Struct.* **77**:2 (2007), 171–181.
- [Fan and Wang 2016] Y. Fan and H. Wang, “The effects of matrix cracks on the nonlinear bending and thermal postbuckling of shear deformable laminated beams containing carbon nanotube reinforced composite layers and piezoelectric fiber reinforced composite layers”, *Compos. B Eng.* **106** (2016), 28–41.
- [Farajpour et al. 2017] A. Farajpour, A. Rastgoo, and M. Mohammadi, “Vibration, buckling and smart control of microtubules using piezoelectric nanoshells under electric voltage in thermal environment”, *Physica B* **509** (2017), 100–114.
- [Fard and Bohlooly 2017] K. M. Fard and M. Bohlooly, “Postbuckling of piezolaminated cylindrical shells with eccentrically/concentrically stiffeners surrounded by nonlinear elastic foundations”, *Compos. Struct.* **171** (2017), 360–369.
- [Ganesan and Kadoli 2003] N. Ganesan and R. Kadoli, “Buckling and dynamic analysis of piezothermoelastic composite cylindrical shell”, *Compos. Struct.* **59**:1 (2003), 45–60.
- [Ghorbanpour Arani et al. 2012a] A. Ghorbanpour Arani, S. Amir, A. R. Shajari, and M. R. Mozdianfar, “Electro-thermo-mechanical buckling of DWBNNTs embedded in bundle of CNTs using nonlocal piezoelectricity cylindrical shell theory”, *Compos. B Eng.* **43**:2 (2012), 195–203.
- [Ghorbanpour Arani et al. 2012b] A. Ghorbanpour Arani, S. Shams, S. Amir, and M. J. Maboudi, “Buckling of piezoelectric composite cylindrical shell under electro-thermo-mechanical loading”, *J. Solid Mech.* **4**:3 (2012), 296–306.

- [Ghorbanpour Arani et al. 2014] A. Ghorbanpour Arani, A. A. M. Barzoki, and R. Kolahchi, "Nonlinear dynamic buckling of viscous-fluid-conveying PNC cylindrical shells with core resting on visco-Pasternak medium", *J. Solid Mech.* **6**:3 (2014), 265–277.
- [Ghorbanpour Arani et al. 2016] A. Ghorbanpour Arani, M. Jamali, M. Mosayyebi, and R. Kolahchi, "Wave propagation in FG-CNT-reinforced piezoelectric composite micro plates using viscoelastic quasi-3D sinusoidal shear deformation theory", *Compos. B Eng.* **95** (2016), 209–224.
- [Hajmohammad et al. 2017] M. H. Hajmohammad, M. S. Zarei, A. Nouri, and R. Kolahchi, "Dynamic buckling of sensor/functionally graded-carbon nanotube-reinforced laminated plates/actuator based on sinusoidal-visco-piezoelectricity theories", *J. Sandw. Struct. Mater.* (2017), 1099636217720373.
- [Hajmohammad et al. 2018] M. H. Hajmohammad, M. B. Azizkhani, and R. Kolahchi, "Multiphase nanocomposite viscoelastic laminated conical shells subjected to magneto-hygrothermal loads: dynamic buckling analysis", *Int. J. Mech. Sci.* **137** (2018), 205–213.
- [Hussein and Heyliger 1998] M. Hussein and P. Heyliger, "Three-dimensional vibrations of layered piezoelectric cylinders", *J. Eng. Mech. (ASCE)* **124**:11 (1998), 1294–1298.
- [Jamal-Omidi and Shayanmehr 2017] M. Jamal-Omidi and M. Shayanmehr, "An experimental study on the nonlinear free vibration response of epoxy and carbon fiber-reinforced composite containing single-walled carbon nanotubes", *J. Vib. Control* **24**:19 (2017), 4529–4540.
- [Kamarian et al. 2018] S. Kamarian, M. Shakeri, and M. H. Yas, "Natural frequency analysis and optimal design of CNT/fiber/polymer hybrid composites plates using mori-tanaka approach, GDQ technique, and firefly algorithm", *Polym. Compos.* **39**:5 (2018), 1433–1446.
- [Ke et al. 2014] L. L. Ke, Y. S. Wang, and J. N. Reddy, "Thermo-electro-mechanical vibration of size-dependent piezoelectric cylindrical nanoshells under various boundary conditions", *Compos. Struct.* **116** (2014), 626–636.
- [Keleshteri et al. 2017] M. M. Keleshteri, H. Asadi, and Q. Wang, "Postbuckling analysis of smart FG-CNTRC annular sector plates with surface-bonded piezoelectric layers using generalized differential quadrature method", *Comput. Methods Appl. Mech. Eng.* **325** (2017), 689–710.
- [Kheibari and Beni 2017] F. Kheibari and Y. T. Beni, "Size dependent electro-mechanical vibration of single-walled piezoelectric nanotubes using thin shell model", *Mater. Des.* **114** (2017), 572–583.
- [Khoa et al. 2019] N. D. Khoa, H. T. Thiem, and N. D. Duc, "Nonlinear buckling and postbuckling of imperfect piezoelectric S-FGM circular cylindrical shells with metal-ceramic-metal layers in thermal environment using Reddy's third-order shear deformation shell theory", *Mech. Adv. Mater. Struct.* **26**:3 (2019), 248–259.
- [Lang and Xuewu 2013] Z. Lang and L. Xuewu, "Buckling and vibration analysis of functionally graded magneto-electro-thermo-elastic circular cylindrical shells", *Appl. Math. Model.* **37**:4 (2013), 2279–2292.
- [Leissa 1993] A. W. Leissa, *Vibration of shells*, Acoustical Society of America, New York, 1993.
- [Li et al. 2015] R. Li, P. Wang, Y. Tian, B. Wang, and G. Li, "A unified analytic solution approach to static bending and free vibration problems of rectangular thin plates", *Sci. Rep.* **5** (2015), 17054.
- [Lim and Xu 2010] C. W. Lim and X. S. Xu, "Symplectic elasticity: theory and applications", *Appl. Mech. Rev. (ASME)* **63**:5 (2010), 050802–10.
- [Mehralian and Tadi Beni 2016] F. Mehralian and Y. Tadi Beni, "Size-dependent torsional buckling analysis of functionally graded cylindrical shell", *Compos. B Eng.* **94** (2016), 11–25.
- [Mehralian and Tadi Beni 2017a] F. Mehralian and Y. Tadi Beni, "Molecular dynamics analysis on axial buckling of functionalized carbon nanotubes in thermal environment", *J. Mol. Model.* **23**:12 (2017), 330.
- [Mehralian and Tadi Beni 2017b] F. Mehralian and Y. Tadi Beni, "Thermo-electro-mechanical buckling analysis of cylindrical nanoshell on the basis of modified couple stress theory", *J. Mech. Sci. Technol.* **31**:4 (2017), 1773–1787.
- [Mehralian and Tadi Beni 2018] F. Mehralian and Y. Tadi Beni, "Buckling of bimorph functionally graded piezoelectric cylindrical nanoshell", *Proc. Inst. Mech. Engineer. Part C: J. Mech. Eng. Sci.* **232**:19 (2018), 3538–3550.
- [Mehralian et al. 2016a] F. Mehralian, Y. Tadi Beni, and R. Ansari, "On the size dependent buckling of anisotropic piezoelectric cylindrical shells under combined axial compression and lateral pressure", *Int. J. Mech. Sci.* **119** (2016), 155–169.

- [Mehralian et al. 2016b] F. Mehralian, Y. Tadi Beni, and R. Ansari, “Size dependent buckling analysis of functionally graded piezoelectric cylindrical nanoshell”, *Compos. Struct.* **152** (2016), 45–61.
- [Mehralian et al. 2017a] F. Mehralian, Y. Tadi Beni, and M. K. Zeverdejani, “Calibration of nonlocal strain gradient shell model for buckling analysis of nanotubes using molecular dynamics simulations”, *Physica B* **521** (2017), 102–111.
- [Mehralian et al. 2017b] F. Mehralian, Y. Tadi Beni, and M. K. Zeverdejani, “Nonlocal strain gradient theory calibration using molecular dynamics simulation based on small scale vibration of nanotubes”, *Physica B* **517** (2017), 61–69.
- [Mirzavand and Eslami 2007] B. Mirzavand and M. R. Eslami, “Thermal buckling of simply supported piezoelectric FGM cylindrical shells”, *J. Therm. Stresses* **30**:11 (2007), 1117–1135.
- [Mirzavand and Eslami 2011] B. Mirzavand and M. R. Eslami, “A closed-form solution for thermal buckling of piezoelectric FGM hybrid cylindrical shells with temperature dependent properties”, *Mech. Adv. Mater. Struct.* **18**:3 (2011), 185–193.
- [Mirzavand et al. 2010] B. Mirzavand, M. R. Eslami, and M. Shakeri, “Dynamic thermal postbuckling analysis of piezoelectric functionally graded cylindrical shells”, *J. Therm. Stresses* **33**:7 (2010), 646–660.
- [Mirzavand et al. 2013] B. Mirzavand, M. R. Eslami, and J. N. Reddy, “Dynamic thermal postbuckling analysis of shear deformable piezoelectric-FGM cylindrical shells”, *J. Therm. Stresses* **36**:3 (2013), 189–206.
- [Mirzavand et al. 2016] B. Mirzavand, P. Rezapour, and M. Bohllooly, “Thermal buckling of shallow/nonshallow piezoelectric-composite cylindrical shells”, *Mech. Adv. Mater. Struct.* **23**:10 (2016), 1236–1243.
- [Mohammadimehr et al. 2014] M. Mohammadimehr, M. Moradi, and A. Loghman, “Influence of the elastic foundation on the free vibration and buckling of thin-walled piezoelectric-based FGM cylindrical shells under combined loadings”, *J. Solid Mech.* **6**:4 (2014), 347–365.
- [Mohammadimehr et al. 2016] M. Mohammadimehr, B. Rousta Navi, and A. Ghorbanpour Arani, “Modified strain gradient Reddy rectangular plate model for biaxial buckling and bending analysis of double-coupled piezoelectric polymeric nanocomposite reinforced by FG-SWNT”, *Compos. B Eng.* **87** (2016), 132–148.
- [Mosallaie Barzoki et al. 2012] A. A. Mosallaie Barzoki, A. Ghorbanpour Arani, R. Kolahchi, and M. R. Mozdianfard, “Electro-thermo-mechanical torsional buckling of a piezoelectric polymeric cylindrical shell reinforced by DWBNNTs with an elastic core”, *Appl. Math. Model.* **36**:7 (2012), 2983–2995.
- [Mosallaie Barzoki et al. 2013] A. A. Mosallaie Barzoki, A. Ghorbanpour Arani, R. Kolahchi, M. R. Mozdianfard, and A. Loghman, “Nonlinear buckling response of embedded piezoelectric cylindrical shell reinforced with BNNT under electro-thermo-mechanical loadings using HDQM”, *Compos. B Eng.* **44**:1 (2013), 722–727.
- [Ni et al. 2017] Y. Ni, Z. Tong, D. Rong, Z. Zhou, and X. Xu, “A new Hamiltonian-based approach for free vibration of a functionally graded orthotropic circular cylindrical shell embedded in an elastic medium”, *Thin-Walled Struct.* **120** (2017), 236–248.
- [Ni et al. 2018] Y. Ni, Z. Tong, D. Rong, Z. Zhou, and X. Xu, “Accurate thermal buckling analysis of functionally graded orthotropic cylindrical shells under the symplectic framework”, *Thin-Walled Struct.* **129** (2018), 1–9.
- [Ninh 2018] D. G. Ninh, “Nonlinear thermal torsional post-buckling of carbon nanotube-reinforced composite cylindrical shell with piezoelectric actuator layers surrounded by elastic medium”, *Thin-Walled Struct.* **123** (2018), 528–538.
- [Pietrzakowski 2008] M. Pietrzakowski, “Piezoelectric control of composite plate vibration: effect of electric potential distribution”, *Comput. Struct.* **86**:9 (2008), 948–954.
- [Rafiee et al. 2013] M. Rafiee, J. Yang, and S. Kitipornchai, “Thermal bifurcation buckling of piezoelectric carbon nanotube reinforced composite beams”, *Comput. Math. Appl.* **66**:7 (2013), 1147–1160.
- [Rafiee et al. 2014] M. Rafiee, X. Q. He, and K. M. Liew, “Non-linear dynamic stability of piezoelectric functionally graded carbon nanotube-reinforced composite plates with initial geometric imperfection”, *Int. J. Non-Linear Mech.* **59** (2014), 37–51.
- [Rafiee et al. 2019] M. Rafiee, F. Nitzsche, and M. R. Labrosse, “Fabrication and experimental evaluation of vibration and damping in multiscale graphene/fiberglass/epoxy composites”, *J. Compos. Mater.* **53**:15 (2019), 2105–2118.
- [Rotter 2014] J. M. Rotter, “Cylindrical shells under axial compression”, pp. 66–111 in *Buckling of thin metal shells*, edited by J. G. Teng and J. M. Rotter, CRC Press, 2014.
- [SafarPour et al. 2019] H. SafarPour, B. Ghanbari, and M. Ghadiri, “Buckling and free vibration analysis of high speed rotating carbon nanotube reinforced cylindrical piezoelectric shell”, *Appl. Math. Model.* **65** (2019), 428–442.

- [Sahmani et al. 2016] S. Sahmani, M. M. Aghdam, and A. H. Akbarzadeh, "Size-dependent buckling and postbuckling behavior of piezoelectric cylindrical nanoshells subjected to compression and electrical load", *Mater. Des.* **105** (2016), 341–351.
- [Salehi-Khojin and Jalili 2008] A. Salehi-Khojin and N. Jalili, "Buckling of boron nitride nanotube reinforced piezoelectric polymeric composites subject to combined electro-thermo-mechanical loadings", *Compos. Sci. Technol.* **68**:6 (2008), 1489–1501.
- [Saviz et al. 2007] M. R. Saviz, M. Shakeri, and M. H. Yas, "Electroelastic fields in a layered piezoelectric cylindrical shell under dynamic load", *Smart Mater. Struct.* **16**:5 (2007), 1683–1695.
- [Shen 2001] H.-S. Shen, "Postbuckling analysis of axially-loaded laminated cylindrical shells with piezoelectric actuators", *Eur. J. Mech. A Solids* **20**:6 (2001), 1007–1022.
- [Shen 2002a] H.-S. Shen, "Postbuckling of laminated cylindrical shells with piezoelectric actuators under combined external pressure and heating", *Int. J. Solids Struct.* **39**:16 (2002), 4271–4289.
- [Shen 2002b] H.-S. Shen, "Thermal postbuckling analysis of laminated cylindrical shells with piezoelectric actuators", *Compos. Struct.* **55**:1 (2002), 13–22.
- [Shen 2005] H.-S. Shen, "Postbuckling of axially loaded FGM hybrid cylindrical shells in thermal environments", *Compos. Sci. Technol.* **65**:11-12 (2005), 1675–1690.
- [Shen 2009] H.-S. Shen, "A comparison of post-buckling behavior for FGM cylindrical shells with piezoelectric fiber reinforced composite actuators", *J. Eng. Mater. Technol. (ASME)* **131**:3 (2009), 031010–031010–11.
- [Shen 2010] H.-S. Shen, "Buckling and postbuckling of anisotropic laminated cylindrical shells with piezoelectric fiber reinforced composite actuators", *Mech. Adv. Mater. Struct.* **17**:4 (2010), 268–279.
- [Shen and Li 2002] H.-S. Shen and Q. S. Li, "Postbuckling of cross-ply laminated cylindrical shells with piezoelectric actuators under complex loading conditions", *Int. J. Mech. Sci.* **44**:8 (2002), 1731–1754.
- [Shen and Noda 2007] H.-S. Shen and N. Noda, "Postbuckling of pressure-loaded FGM hybrid cylindrical shells in thermal environments", *Compos. Struct.* **77**:4 (2007), 546–560.
- [Shen and Xiang 2007] H.-S. Shen and Y. Xiang, "Postbuckling of pressure-loaded piezolaminated cylindrical shells with temperature dependent properties", *Int. J. Struct. Stab. Dyn.* **7**:1 (2007), 1–22.
- [Sheng and Wang 2010] G. G. Sheng and X. Wang, "Thermoelastic vibration and buckling analysis of functionally graded piezoelectric cylindrical shells", *Appl. Math. Model.* **34**:9 (2010), 2630–2643.
- [Sun et al. 2013] J. Sun, X. Xu, and C. W. Lim, "Accurate symplectic space solutions for thermal buckling of functionally graded cylindrical shells", *Compos. B Eng.* **55** (2013), 208–214.
- [Sun et al. 2014a] J. Sun, X. Xu, and C. W. Lim, "Buckling of functionally graded cylindrical shells under combined thermal and compressive loads", *J. Therm. Stresses* **37**:3 (2014), 340–362.
- [Sun et al. 2014b] J. Sun, X. Xu, and C. W. Lim, "Torsional buckling of functionally graded cylindrical shells with temperature-dependent properties", *Int. J. Struct. Stab. Dyn.* **14**:01 (2014), 1350048.
- [Sun et al. 2016] J. Sun, X. Xu, C. W. Lim, Z. Zhou, and S. Xiao, "Accurate thermo-electro-mechanical buckling of shear deformable piezoelectric fiber-reinforced composite cylindrical shells", *Compos. Struct.* **141** (2016), 221–231.
- [Sun et al. 2018] J. Sun, Z. Wang, Z. Zhou, X. Xu, and C. W. Lim, "Surface effects on the buckling behaviors of piezoelectric cylindrical nanoshells using nonlocal continuum model", *Appl. Math. Model.* **59** (2018), 341–356.
- [Tadi Beni and Mehralian 2016] Y. Tadi Beni and F. Mehralian, "The effect of small scale on the free vibration of functionally graded truncated conical shells", *J. Mech. Mater. Struct.* **11**:2 (2016), 91–112.
- [Tadi Beni et al. 2015] Y. Tadi Beni, F. Mehralian, and H. Razavi, "Free vibration analysis of size-dependent shear deformable functionally graded cylindrical shell on the basis of modified couple stress theory", *Compos. Struct.* **120** (2015), 65–78.
- [Tadi Beni et al. 2016] Y. Tadi Beni, F. Mehralian, and H. Zeighampour, "The modified couple stress functionally graded cylindrical thin shell formulation", *Mech. Adv. Mater. Struct.* **23**:7 (2016), 791–801.
- [Tan and Tong 2001a] P. Tan and L. Tong, "Micro-electromechanics models for piezoelectric-fiber-reinforced composite materials", *Compos. Sci. Technol.* **61**:5 (2001), 759–769.
- [Tan and Tong 2001b] P. Tan and L. Tong, "Micromechanics models for non-linear behavior of piezo-electric fiber reinforced composite materials", *Int. J. Solids Struct.* **38**:50-51 (2001), 8999–9032.

- [Teng 1996] J. G. Teng, “Buckling of thin shells: recent advances and trends”, *Appl. Mech. Rev. (ASME)* **49**:4 (1996), 263–274.
- [Teng and Rotter 2014] J. G. Teng and J. M. Rotter, “Buckling of thin shells: an overview”, pp. 25–65 in *Buckling of thin metal shells*, CRC Press, 2014.
- [Ueberschlag 2001] P. Ueberschlag, “PVDF piezoelectric polymer”, *Sens. Rev.* **21**:2 (2001), 118–126.
- [Wang 2002] Q. Wang, “On buckling of column structures with a pair of piezoelectric layers”, *Eng. Struct.* **24**:2 (2002), 199–205.
- [Wang and Qin 2007] J.-S. Wang and Q.-H. Qin, “Symplectic model for piezoelectric wedges and its application in analysis of electroelastic singularities”, *Philos. Mag.* **87**:2 (2007), 225–251.
- [Wu and Chang 2014] C.-P. Wu and S.-K. Chang, “Stability of carbon nanotube-reinforced composite plates with surface-bonded piezoelectric layers and under bi-axial compression”, *Compos. Struct.* **111** (2014), 587–601.
- [Wu et al. 2016] H. Wu, S. Kitipornchai, and J. Yang, “Thermo-electro-mechanical postbuckling of piezoelectric FG-CNTRC beams with geometric imperfections”, *Smart Mater. Struct.* **25**:9 (2016), 095022.
- [Yamaki 1984] N. Yamaki, *Elastic stability of circular cylindrical shells*, North-Holland, Amsterdam, 1984.
- [Yang et al. 2015] J. Yang, L.-L. Ke, and C. Feng, “Dynamic buckling of thermo-electro-mechanically loaded FG-CNTRC beams”, *Int. J. Struct. Stab. Dyn.* **15**:8 (2015), 1540017.
- [Yao et al. 2009] W. Yao, W. Zhong, and C. W. Lim, *Symplectic elasticity*, World Scientific, 2009.
- [Zeighampour and Tadi Beni 2014] H. Zeighampour and Y. Tadi Beni, “Cylindrical thin-shell model based on modified strain gradient theory”, *Int. J. Eng. Sci.* **78** (2014), 27–47.
- [Zhu et al. 2017] C.-S. Zhu, X.-Q. Fang, and J.-X. Liu, “Surface energy effect on buckling behavior of the functionally graded nano-shell covered with piezoelectric nano-layers under torque”, *Int. J. Mech. Sci.* **133** (2017), 662–673.

Received 27 Jan 2019. Revised 5 Jun 2019. Accepted 12 Jun 2019.

SHENGBO ZHU: zhushengbo@mail.dlut.edu.cn

State Key Laboratory of Structural Analysis for Industrial Equipment and Department of Engineering Mechanics,
Dalian University of Technology, Dalian, 116023, China

YIWEN NI: nyw2009213@mail.dlut.edu.cn

State Key Laboratory of Structural Analysis for Industrial Equipment and Department of Engineering Mechanics,
Dalian University of Technology, Dalian, 116024, China

JIABIN SUN: jbsun1983@dlut.edu.cn

State Key Laboratory of Structural Analysis for Industrial Equipment and School of Ocean Science and Technology,
Dalian University of Technology, Panjin, 124221, China

ZHENZHEN TONG: tongzhzh@163.com

College of Locomotive and Rolling Stock Engineering, Dalian Jiaotong University, Dalian, 116028, China

ZHENHUAN ZHOU: zhouzh@dlut.edu.cn

State Key Laboratory of Structure Analysis for Industrial Equipment and Department of Engineering Mechanics,
Dalian University of Technology, Dalian, 116024, China

XINSHENG XU: xsxu@dlut.edu.cn

Department of Engineering Mechanics, Dalian University of Technology, State Key Laboratory for Structural Analysis for
Industrial Equipment, Dalian, 116024, China

THERMOELASTIC FRACTURE INITIATION: THE ROLE OF RELAXATION AND CONVECTION

LOUIS M. BROCK

An isotropic, thermoelastic solid is at rest at uniform (absolute) temperature, and contains a semi-infinite, closed plane crack. Thermal relaxation governs, and crack surfaces are subject to convection. In-plane and compressive point forces, applied to each face of the crack initiate transient 3D extension. Wiener–Hopf equations are formulated in integral transform space from expressions whose inverses are dynamically similar and valid for short times. The solutions, upon inversion, are subjected to the dynamic energy release rate criteria, with kinetic energy included. A differential equation for crack edge contour is produced, and demonstrates that a certain type of point-force time variation can indeed cause a constant extension rate. Calculations for the pure compression case show that variation in crack growth rate with convection is not necessarily monotonic. A finite measure of crack edge thermal response for pure compression is provided by the temperature norm. Calculations indicate even greater sensitivity to thermal convection.

Introduction

Crack edge location in a transient 3D study is defined by a (possibly non-rectilinear) contour in the crack plane. As an illustration, the semi-infinite, planar crack in an unbounded thermoelastic solid is treated in [Brock 2017]. Fracture is driven by mixed-mode, point force loading on the crack faces, and crack extension rate is constant and well below Rayleigh and body-wave speed. Fracture initiation is the focus, and is governed by dynamic energy release rate [Freund 1972; 1990] with kinetic energy included [Gdoutos 1993]. Therefore:

- Thermal relaxation [Ignaczak and Ostoja-Starzewski 2010] can be important.
- Asymptotic forms of the governing equations for thermal relaxation are viable.
- Only knowledge of solution behavior near the crack edge is required.

The possibility that discontinuities in temperature and heat flux, as well as in displacement, occur is considered. Therefore analysis is based on the related, but unmixed, boundary-value problem of such discontinuities prescribed on a plane in a crack-free solid. The analytical solution in transform space is obtained and asymptotic forms whose inverses are valid for short times used to address the fracture problem. The displacement discontinuity corresponding to crack extension direction can be resolved in crack-opening, (in-plane) sliding and (in-plane) tearing modes. The fracture problem can thus be reduced to four equations of the Wiener–Hopf type [Morse and Feshbach 1953] and two of them are coupled. Solutions to the equations are then inverted, and subjected to the dynamic energy release rate. A nonlinear, first-order differential equation for the (dimensionless) speed parameter that defines the crack

Keywords: thermoelastic, relaxation, transient, fracture, discontinuity, convection.

edge contour results. Study shows that, in particular, a certain point-force loading history produces a parameter that can vary with direction, but is time-independent.

It is noted that crack-surface thermal convection is not addressed in [Brock 2017]. Moreover the restriction that crack extension rates be “well below” critical values simplified analysis of the Wiener–Hopf equations, but is not required for their solution. This paper therefore also addresses the situation treated in [Brock 2017], but crack extension rate is only required to be constant and subcritical, and thermal convection is possible. Two sets of assumptions are now listed explicitly. If loading is only in-plane:

- Crack surface friction can be neglected.
- Across the crack plane, temperature is continuous and heat flux is allowed.

With or without in-plane loading, if compression loading is present:

- Thermal convection, subject to thermal relaxation, occurs on the crack faces.
- A temperature discontinuity between crack faces can exist.
- Net heat flux across the crack itself cannot occur.

It will be seen that the latter assumption set gives, in contrast to [Brock 2017], three uncoupled sets of equations in integral transform space. A single equation for the displacement discontinuity due to in-plane tearing comprises one set. Two coupled equations for crack opening involve displacement discontinuity and discontinuity in temperature of the two crack faces, and comprise the second set. The third set consists of two coupled equations for in-plane sliding that involve displacement discontinuity and the average of the two crack face temperatures. Equations are of the Wiener–Hopf type.

Problem statement

An unbounded, thermoelastic solid is at rest for time $t \leq 0$ and uniform (absolute) temperature T_0 prevails. In terms of Cartesian basis $\mathbf{x}_0 = \mathbf{x}_0(x_k^0)$, $k = (1, 2, 3)$ the closed, plane crack occupies region A_C ($x_3^0 = 0$, $x_1^0 = 0$), with rectilinear boundary C ($x_1^0, x_3^0 = 0$). Shear and compressive point forces appear for $t > 0$ on both crack faces ($x_1^0 = 0^-, x_2^0 = 0$, $x_3^0 = 0^\pm$). Brittle fracture is instantaneous, and the crack extends outward from $\mathbf{x}_0 = 0$. The crack now occupies region $A_C + \delta A$. Boundary C is assumed to now include a concave bulge centered on the point-force sites:

$$\sqrt{(x_1^0)^2 + (x_2^0)^2} = l(\psi, t), \quad l(\psi, t) = V(\psi)t, \quad (1a)$$

$$0 < V < V^*, \quad \psi = \tan^{-1} \frac{x_2^0}{x_1^0} (|\psi| < \pi/2). \quad (1b)$$

Equation (1) implies a dynamically similar fracture process, and (speed parameter) V is subcritical, i.e., lies below V^* , the minimum of Raleigh and body wave speeds.

Displacement $\mathbf{u}(u_k)$, traction $\mathbf{T}(\sigma_{ik})$ and Θ , the change in temperature from T_0 , are field variables. For the solid with thermal relaxation governed by the Lord–Shulman (LS) model [Lord and Shulman

1967; Ignaczak and Ostoj-Starzewski 2010]:

$$\nabla \cdot \mathbf{T} - \rho D_0^2 \mathbf{u} = 0, \quad (2a)$$

$$(k_T \nabla^2 - \rho C_E D_0 P_0) \Theta + \mu \alpha_D T_0 D_0 P_0 (\nabla \cdot \mathbf{u}) = 0, \quad (2b)$$

$$\frac{1}{\mu} \mathbf{T} = \left[\frac{2\nu}{1-2\nu} (\nabla \cdot \mathbf{u}) \mathbf{1} - \alpha_D \Theta \right] + \nabla \mathbf{u} + \mathbf{u} \nabla = 0, \quad (2c)$$

$$P_0 = 1 + t_0 D_0. \quad (2d)$$

In (2) Θ and components (u_k, σ_{ik}) are functions of (\mathbf{x}_0, t) , and $(\nabla, \nabla^2, \mathbf{1})$ respectively are gradient and Laplacian operators and identity tensor. Symbol $(D_0 f, \dot{f})$ signifies time differentiation in basis \mathbf{x}_0 , and t_0 is thermal relaxation time. It is noted that (2) describes the classical (Fourier model) solid [Boley and Weiner 1960] when $P_0 = 1$. Constants (μ, ρ, ν) represent shear modulus, mass density and Poisson's ratio, and (k_T, C_E, α_D) are thermal conductivity, specific heat at constant strain, and coefficient of (volumetric) thermal expansion. Homogeneity of (2a) and (2b) reflects the absence of thermal and mechanical body forces. In particular, the solid contains no internal heat source or sink.

For convenience temporal behavior is described in terms of variable $s = V_R t$, operator $D_0 = V_R D$ and parameters:

$$P_0 = 1 + h_0 D, \quad (3a)$$

$$V_R = \sqrt{\frac{\mu}{\rho}}, \quad V_D = C_D V_R, \quad C_D = \sqrt{2 \frac{1-\nu}{1-2\nu}}, \quad \varepsilon = \frac{\mu T_0}{\rho C_E} \alpha_D^2, \quad (3b)$$

$$h = \frac{k_T}{C_E \sqrt{\mu \rho}}, \quad h_0 = V_R t_0. \quad (3c)$$

In (3) ε is the dimensionless thermal coupling constant, and (h, h_0) are thermoelastic characteristic lengths. Symbols (V_R, V_D) are, respectively, rotational speed and isothermal dilatational speed. In regard to subcritical speed, it will be seen that subsonic ($< V_R$) Rayleigh speeds exist. These depend on both material properties and the nature of the point forces. Equations (2a) and (2b) can be partially uncoupled and for $s > 0$ give, in view of (3)

$$\mathbf{u} = \mathbf{u}_R + \mathbf{u}_D, \quad (4a)$$

$$(\nabla^2 - D^2) \mathbf{u}_R = 0, \quad \nabla \cdot \mathbf{u}_R = 0, \quad (4b)$$

$$(c_D^2 \nabla^2 - D^2) \mathbf{u}_D - \alpha_D \nabla \Theta = 0, \quad (4c)$$

$$[(c_D^2 \nabla^2 - D^2)(h \nabla^2 - D P_0) - \varepsilon D P_0 \nabla^2](\mathbf{u}_D, \Theta) = 0. \quad (4d)$$

For $x_3^0 = 0 \pm$, $(x_1^0, x_2^0) \in A_C + \delta A$ ($s > 0$):

$$\sigma_{3k} = -F_k \delta(x_1^0) \delta(x_2^0), \quad \partial_3 \Theta = \mp \chi P_0 \Theta. \quad (5a)$$

For $x_3^0 = 0$, $(x_1^0, x_2^0) \notin A_C + \delta A$ ($s > 0$):

$$[u_k] = [\sigma_{3k}] = [\Theta] = [\partial_3 \Theta] = 0. \quad (5b)$$

In (5a) and (5b) $k = (1, 2, 3)$ and $\partial_k f = \partial f / \partial x_k^0$. Force F_k is a positive constant and χ is the (positive)

convection constant, with dimensions of inverse length. Symbol δ in (5a) denotes Dirac function, and $[f] = f^{(+)} - f^{(-)}$ where $f^{(\pm)} = f(x_1^0, x_2^0, 0 \pm, s)$. Moreover $[u_k]$ must vanish continuously on C , but $[\Theta]$ can exhibit (integrable) singular behavior. It is noted that two other relations also arise for $x_3^0 = 0$, $(x_1^0, x_2^0) \in A_C + \delta A$ ($s > 0$):

$$[\partial_3 \Theta] + 2\chi P_0 \langle \Theta \rangle = 0, \quad \langle \partial_3 \Theta \rangle + \chi P_0 [\Theta] = 0. \quad (5c)$$

In (5c) $\langle f \rangle = \frac{1}{2}(f^{(+)} + f^{(-)})$ is the average taken over $(x_1^0, x_2^0) \in A_C + \delta A$. For $s \leq 0$ $(\mathbf{u}, \mathbf{T}, \Theta) \equiv 0$, and for finite $s > 0$ $(\mathbf{u}, \mathbf{T}, \Theta)$ must be bounded as $|\mathbf{x}_0| \rightarrow \infty$.

Discontinuity problem

A common practice for solving crack problems is to represent the relative motion of crack faces as unknown discontinuities in displacement; see, e.g., [Barber 1992]. To implement that procedure here, a more general problem is considered: The unbounded solid is again at rest at uniform (absolute) temperature T_0 but for $(x_3^0 = 0, s > 0)$ discontinuities $([u_k], [\Theta], [\partial_3 \Theta])$ are imposed. For $(x_1^0, x_2^0) \notin A_C + \delta A$ and $(x_1^0, x_2^0) \in A_C + \delta A$, respectively the discontinuities vanish and are continuous functions of (x_1^0, x_2^0, s) . They vanish for $s \leq 0$, and are bounded in $A_C + \delta A$ for $\sqrt{(x_1^0)^2 + (x_2^0)^2} \rightarrow \infty$ ($s > 0$). Therefore, as in the crack problem, $(\mathbf{u}, \mathbf{T}, \Theta) \equiv 0$ for $s \leq 0$, and are bounded as $|\mathbf{x}_0| \rightarrow \infty$ for finite $s > 0$.

Transform solution

An effective procedure (e.g., [Brock and Achenbach 1973]) for 2D transient study of semi-infinite crack extension at constant speed employs coordinates that translate with the crack edge, and unilateral temporal and bilateral spatial integral transform [Sneddon 1972]. In view of (1) a translating basis \mathbf{x} is defined for $|\psi| < \pi/2$ as

$$x_1 = x_1^0 - [c(\psi) \cos \psi] s, \quad x_2 = x_2^0 - [c(\psi) \sin \psi] s, \quad x_3 = x_3^0, \quad (6a)$$

$$c(\psi) = \frac{V(\psi)}{V_S}, \quad Df = \partial_S f - c(\psi)(\partial_1 f \cos \psi + \partial_2 f \sin \psi), \quad (6b)$$

$$\partial_S = \frac{\partial f}{\partial s}, \quad \partial_k f = \frac{\partial f}{\partial x_k} \quad k = (1, 2, 3). \quad (6c)$$

The temporal Laplace transform operation is

$$L(f) = \hat{f} = \int f(s) \exp(-ps) ds. \quad (7a)$$

Integration is over positive real s and $\text{Re}(p) > 0$. A double spatial integral transform and inversion, respectively, can be defined [Sneddon 1972] by

$$\tilde{f}(p, q_1, q_2) = \iint \hat{f}(p, x_1, x_2) \exp[-p(q_1 x_1 + q_2 x_2)] dx_1 dx_2, \quad (7b)$$

$$\hat{f}(p, x_1, x_2) = \left(\frac{P}{2\pi i}\right)^2 \iint \tilde{f}(p, q_1, q_2) \exp[p(q_1 x_1 + q_2 x_2)] dq_1 dq_2. \quad (7c)$$

Integration in (7b) is over real (x_1, x_2) ; integration in (7c) is along the imaginary (q_1, q_2) -axes. It is noted that (\mathbf{x}, s) have dimensions of length, p has dimensions of inverse length, and (q_1, q_2) are dimensionless. Because (1) involves a speed that varies with direction, application of (7a) and (7b) to (2)–(4) and discontinuity restraints for $(x_3^0, x_3) = 0$ is complicated. Despite use of ψ the discontinuity problem is not axially symmetric. However, 3D studies of sliding and rolling contact [Brock 2012] and crack growth [Brock 2017] suggest transformations:

$$\text{Im}(q_1) = \text{Im}(q) \cos \psi, \quad \text{Im}(q_2) = \text{Im}(q) \sin \psi, \quad (8a)$$

$$x_1 = x \cos \psi, \quad x_2 = x \sin \psi. \quad (8b)$$

Here $\text{Re}(q) = 0+$, $|\text{Im}(q)|$, $|x| < 0$ and $|\psi| < \pi/2$. Parameters (x, ψ) and (q, ψ) resemble quasi polar coordinates, i.e.,

$$dx_1 dx_2 = |x| dx d\psi, \quad dq_1 dq_2 = |q| dq d\psi. \quad (8c)$$

The uncoupling effect of (8) leads to the combination

$$\tilde{f}(p, q_1, q_2) \rightarrow \bar{f}(p, q, \psi), \quad (9a)$$

$$\hat{f}(p, x, \psi) = -\frac{p^2}{2\pi} \int \frac{|q|}{q} \bar{f}(p, q, \psi) \exp(pqx) dq. \quad (9b)$$

Integration is along the positive ($\text{Re}(q) = 0+$) side of the $\text{Im}(q)$ -axis.

In view of (6)–(8) and (9a), equation (4) gives a corresponding set in transform space by making formal substitutions:

$$\nabla \rightarrow (pq \cos \psi, pq \sin \psi, \partial_3), \quad D \rightarrow pQ, \quad \nabla^2 \rightarrow \partial_3^2 + p^2 q^2, \quad (10a)$$

$$P_0 \rightarrow \bar{P}_0 = 1 + h_0 pQ, \quad (10b)$$

$$Q = 1 - cq. \quad (10c)$$

Set elements that correspond to (4b)–(4d) are homogeneous, ordinary differential equations in x_3 , with characteristic functions $pB(q)$ and $pA_{\pm}(p, q)$:

$$B(q) = \sqrt{Q^2 - q^2}, \quad (11a)$$

$$A_{\pm}(p, q) = \sqrt{\left(\frac{2Q}{\Gamma_{\pm} \pm \Gamma_{-}}\right)^2 - q^2}, \quad (11b)$$

$$\Gamma_{\pm} = \sqrt{(c_D \pm \sqrt{hpQ/\bar{P}_0})^2 + \varepsilon}. \quad (11c)$$

The solutions to the differential equations are

$$\bar{\mathbf{u}}_R = \left[U_1^{(\pm)}, U_2^{(\pm)}, (\pm) \frac{q}{B} (U_1^{(\pm)} \cos \psi + U_2^{(\pm)} \sin \psi) \right] \exp(-pB|x_3|), \quad (12a)$$

$$\bar{\mathbf{u}}_D = \bar{\mathbf{u}}_+ + \bar{\mathbf{u}}_-, \quad (12b)$$

$$\bar{\mathbf{u}}_{\pm} = [q \cos \psi, q \sin \psi, (\mp) A_{\pm}] U_{\pm}^{(\pm)} \exp(-pA_{\pm}|x_3|), \quad (12c)$$

$$\bar{\Theta} = \bar{\Theta}_+ + \bar{\Theta}_-, \quad (13a)$$

$$\bar{\Theta}_\pm = -C_\pm \frac{Q^2}{\alpha_D} p U_\pm^{(\pm)} \exp(-p A_\pm |x_3|), \quad (13b)$$

$$C_\pm = 1 - \left(\frac{2c_D}{\Gamma_+ \pm \Gamma_-} \right)^2, \quad C_+ - C_- = \frac{\Gamma_+ \Gamma_-}{hpQ} \bar{p}_0. \quad (13c)$$

Here $(U_\pm^{(\pm)}, U_1^{(\pm)}, U_2^{(\pm)})$ are unknown functions of (p, q, ψ) and (\pm) signifies $x_3 > 0(+)$, $x_3 < 0(-)$. Equations (12a), (12c) and (13b) are bounded for $\text{Re}(p) > 0$ as $|x_3| \rightarrow \infty$ when $\text{Re}(A_\pm, B) \geq 0$ in the cut q -plane. Imposition of discontinuities $([u_k], [\Theta], [\partial_3 \Theta])$ for $(x_3^0, x_3) = 0$ leads to equations in transform space that can be solved for the unknown functions. The results are presented in Appendix A, where it proves convenient to use displacement discontinuities $(\Delta_O, \Delta_T, \Delta_S)$ that for given $|\psi| < \pi/2$, correspond to crack opening and in-plane sliding and tearing, respectively:

$$\Delta_O = [u_3], \quad \begin{bmatrix} \Delta_S \\ \Delta_T \end{bmatrix} = \begin{bmatrix} \cos \psi & \sin \psi \\ \sin \psi & -\cos \psi \end{bmatrix} \begin{bmatrix} [u_1] \\ [u_2] \end{bmatrix}. \quad (14)$$

Asymptotic analysis

Focus in this paper is upon fracture initiation, i.e., small t (small s). The LS model [Lord and Shulman 1967] is robust in this regard. Indeed calculations [Brock 2009; Ignaczak and Ostoj a-Starzewski 2010] indicate that $h \approx O(10^{-9})$ m and $h_0 \approx O(10^{-10})$ m, so that in view of (7a) transform expressions valid for $|h_0 p| \gg 1$ suffice, i.e., $s/h_0 \ll 1$. Therefore (12), (13) and entries in Appendix A are modified by employing asymptotic forms of (11b) and (11c):

$$A_\pm(p, q) \rightarrow A_\pm(q) = \sqrt{\frac{Q^2}{c_\pm^2} - q^2}, \quad (15a)$$

$$C_\pm = 1 - \frac{c_D^2}{c_\pm^2}, \quad c_\pm = \frac{1}{2}(\Gamma_+ \pm \Gamma_-), \quad C_+ - C_- = \lambda \Gamma_+ \Gamma_-, \quad (15b)$$

$$\Gamma_\pm = \sqrt{\left(\frac{1}{\sqrt{\lambda}} \pm c_D \right)^2 + \varepsilon}, \quad \lambda = \frac{h_0}{h}. \quad (15c)$$

Equation (11a) and dimensionless terms c_\pm in (15) show that solution behavior involves body wave speeds $(V_R, V_\pm = c_\pm V_R)$, where $1 < c_- < c_+$. Data from, e.g., [Brock 2009; Ignaczak and Ostoj a-Starzewski 2010] suggest moreover that $c_+ > c_D$, $c_- \approx c_D$ —so that V_+ is larger than isothermal dilatational wave speed $V_D = c_D V_R$ while V_- is approximately the same. Bounded behavior for $(\hat{u}_k, \hat{\Theta})$ as $|x_3| \rightarrow \infty$ requires in light of (12) and (13) that $\text{Re}(A_\pm) > 0$ and $\text{Re}(B) > 0$ in the q -plane with, respectively, branch cuts:

$$\text{Im}(q) = 0, \quad \frac{-1}{c_\pm - c} < \text{Re}(q) < \frac{1}{c_\pm + c}, \quad (16a)$$

$$\text{Im}(q) = 0, \quad \frac{-1}{1 - c} < \text{Re}(q) < \frac{1}{1 + c}. \quad (16b)$$

It is noted that (16) is valid only for $c < 1$; i.e., $V(\psi) < V_R$ ($|\psi| < \pi/2$).

Application to fracture problem

In order that (12)–(15) and results in Appendix A represent the (asymptotic) transform solution for the fracture problem, the transforms of (5a) must be satisfied. It is noted that (5a) is incorporated in general formulas for ($s > 0$, $x_3 = 0\pm$):

$$\sigma_{3k} = \sigma_{3k}^0 - F_k \delta(x_1^0) \delta(x_2^0), \quad (17a)$$

$$\partial_3 \Theta = \partial_3 \Theta_0 \mp \chi P_0 \Theta^{(\pm)}, \quad (17b)$$

$$\Theta = \Theta_0 + \Theta^{(\pm)}. \quad (17c)$$

Here σ_{3k}^0 and $(\partial_3 \Theta_0, \Theta_0)$ respectively represent σ_{3k} for $|x_3| = 0$, $x > 0$ and $(\partial_3 \Theta, \Theta)$ for $x > 0$ in a region generated behind wave front $c_+ s - x - cs > 0$. Thus the corresponding transforms exist for $\text{Re}(q) > -1/(c_+ - c)$. The Dirac function term has transform

$$-\frac{F_k}{pQ} (\text{Re}(q) < 1/c). \quad (17d)$$

Terms $(\Delta_O, \Delta_S, \Delta_T, \Theta^{(\pm)}, \partial_3 \Theta^{(\pm)})$ and related terms $([\Theta], \langle \Theta \rangle, [\partial_3 \Theta], \langle \partial_3 \Theta \rangle)$ occur for $x < 0$ in a region generated behind wave front $c_+ s + x + cs > 0$. Thus the corresponding transforms exist for $\text{Re}(q) < 1/(c_+ + c)$. These behaviors show that

$$(\bar{\sigma}_{3k}^0, \bar{\partial}_3 \Theta_0, \bar{\Theta}_0) \quad \text{and} \quad (\bar{\Delta}_O, \bar{\Delta}_S, \bar{\Delta}_T, \bar{\Theta}^{(\pm)}, \bar{\partial}_3 \Theta^{(\pm)}, F_k/pQ)$$

are analytic in halves of the q -plane that overlap in the strip $-1/(c_+ - c) < \text{Re}(q) < 1/(c_+ + c)$. In view then, of (2c), (11)–(17) and Appendix A, three sets of transform equations of the Wiener–Hopf type can be generated. These are given in Appendix B where, in light of (14), it has proved convenient to introduce traction terms:

$$\sigma_O = \sigma_{33}^0, \quad \begin{bmatrix} \sigma_S \\ \sigma_T \end{bmatrix} = \begin{bmatrix} \cos \psi & \sin \psi \\ \sin \psi & -\cos \psi \end{bmatrix} \begin{bmatrix} \sigma_{31}^0 \\ \sigma_{32}^0 \end{bmatrix}. \quad (18)$$

Coefficients $(M_O(q), M_S(q))$ in (B.2) and (B.3) exhibit behavior:

$$M_O \left(\frac{\pm 1}{c_O \pm c} \right) = 0, \quad M_O \approx \frac{bR_O}{a_+ a_-} \sqrt{q} \sqrt{-q} \quad (|q| \rightarrow \infty), \quad (19a)$$

$$R_O = \frac{1}{c^2} \left[4a_+ a_- - \frac{K^2}{\lambda \Gamma_+ \Gamma_- b} (C_+ a_+ - C_- a_-) \right], \quad R_O(\pm c_O) = 0, \quad (0 < c_O < 1), \quad (19b)$$

$$M_S \left(\frac{\pm 1}{c_S \pm c} \right) = 0, \quad M_S \approx \frac{R_S}{b} \sqrt{q} \sqrt{-q} \quad (|q| \rightarrow \infty), \quad (20a)$$

$$R_S = \frac{1}{c^2} \left[\frac{4b}{\lambda \Gamma_+ \Gamma_-} (C_+ a_+ - C_- a_-) - K^2 \right], \quad R_S(\pm c_S) = 0, \quad (0 < c_S < 1). \quad (20b)$$

Behavior of coefficients ($m_O(q)$, $m_S(q)$, $n_O(q)$, $n_S(q)$) is given by

$$m_O \approx \mp i m_3 \quad (|q| \rightarrow \infty), \quad m_3 = \frac{\chi h K}{c \Gamma_+ \Gamma_-} \left(\frac{1}{a_+} - \frac{1}{a_-} \right), \quad (21a)$$

$$m_S \approx \pm i m_{12} \quad (|q| \rightarrow \infty), \quad m_{12} = \frac{1}{\lambda c^2 \Gamma_+ \Gamma_-} (a_+ - a_-), \quad (21b)$$

$$n_O \approx \mp i q n_3 \quad (|q| \rightarrow \infty), \quad n_3 = \frac{\varepsilon K}{\Gamma_+ \Gamma_-} \left(\frac{1}{a_+} - \frac{1}{a_-} \right), \quad (21c)$$

$$n_S \approx \pm i q^2 n_{12} \quad (|q| \rightarrow \infty), \quad n_{12} = \frac{2\varepsilon}{\Gamma_+ \Gamma_-} (a_+ - a_-). \quad (21d)$$

Notation $\pm i$ denotes $\text{Im}(q) < 0$ and $\text{Im}(q) > 0$, respectively, in expressions for (m_O , m_S , n_O , n_S). In (19)–(21):

$$a_{\pm}(c) = \sqrt{1 - \frac{c^2}{c_{\pm}^2}}, \quad b(c) = \sqrt{1 - c^2}, \quad K(c) = c^2 - 2. \quad (22a)$$

Here (b , a_{\pm}) arise as factors of (B , A_{\pm}) for $|q| \rightarrow \infty$. Expressions (M_S , M_O) and (R_S , R_O) are Rayleigh functions of respectively, q and c . Data from, e.g., [Brock 2009; Ignaczak and Ostoja-Starzewski 2010] indicate that in general

$$0 < c_O < c_S < 1 < c_- < c_+, \quad c_- \approx c_D - . \quad (22b)$$

In addition to body wave speeds, therefore, solution behavior for the fracture problem is influenced by Rayleigh speeds ($V_O = c_O V_R$, $V_S = c_S V_R$). In light of (22b) subcritical speed is defined as $V(\psi) < V_O$ ($|\psi| < \pi/2$).

Solution: Wiener–Hopf problem (tearing mode)

Solution of Wiener–Hopf equation (B.1a) involves manipulations that produce left- and right-hand sides that are analytic in overlapping regions of the complex q -plane. That is, the two sides are analytic continuations of each other. To this end (B , A_{\pm}) are written as products ($B^+ B^-$, $A_{\pm}^+ A_{\pm}^-$) where

$$B^+ = \sqrt{1 + q(1 - c)}, \quad B^- = \sqrt{1 - q(1 + c)}, \quad (23a)$$

$$A_{\pm}^+ = \sqrt{\frac{1}{c_{\pm}} + q \left(1 - \frac{c}{c_{\pm}} \right)}, \quad A_{\pm}^- = \sqrt{\frac{1}{c_{\pm}} - q \left(1 + \frac{c}{c_{\pm}} \right)}. \quad (23b)$$

Factors B^+ and B^- are analytic in overlapping portions of the q -plane:

$$\text{Re}(q) > \frac{-1}{1 - c}, \quad \text{Re}(q) < \frac{1}{1 + c}. \quad (23c)$$

In similar fashion factors A_{\pm}^+ and A_{\pm}^- are analytic in overlapping portions:

$$\text{Re}(q) > \frac{-1}{c_{\pm} - c}, \quad \text{Re}(q) < \frac{1}{c_{\pm} + c}. \quad (23d)$$

For $|q| \rightarrow \infty$ (B^\pm, A_\pm^+, A_\pm^-) generate factors

$$b^\pm(c) = \sqrt{1 \mp c}, \quad a_\pm^+(c) = \sqrt{1 - \frac{c}{c_\pm}}, \quad a_\pm^-(c) = \sqrt{1 + \frac{c}{c_\pm}}. \quad (24)$$

Manipulations of (B.1a) in view of (23a) and (23c) lead to

$$\frac{\bar{\sigma}_T}{B^+} - \frac{F_T}{pQ} \left(\frac{1}{B^+} - \sqrt{c} \right) = -\mu p B^- \bar{\Delta}_T + \sqrt{c} \frac{F_T}{pQ}. \quad (25)$$

Analytic continuation requires that the two sides of (25) be equal to the same entire function. Restrictions on $[u_k]$ noted in connection with (5) imply that $pq\bar{\Delta}_T$, and therefore the right-hand side of (25), vanish for $|q| \rightarrow \infty$. In light of Liouville's theorem [Morse and Feshbach 1953] the entire function must vanish. Equation (25) then gives

$$\bar{\sigma}_T = \frac{F_T}{pQ} - \sqrt{c} B^+ \frac{F_T}{pQ}, \quad p\bar{\Delta}_T = \frac{\sqrt{c}}{p^2 Q B^-} \frac{F_T}{\mu}. \quad (26a)$$

Imposition of fracture criteria such as dynamic energy release rate [Freund 1990] requires only knowledge of $(\sigma_T, D_0 \Delta_T)$ near crack contour C , i.e., $\sqrt{x^2 + x_3^2} \approx 0$, $|\psi| < \pi/2$. Therefore transform behavior for $|q| \rightarrow \infty$ suffices and, in view of (6b), (26a) gives

$$\bar{\sigma}_T \approx \frac{F_T b^+}{p\sqrt{qc}}, \quad pQ\bar{\Delta}_T \approx \frac{-F_T}{\mu p b^- \sqrt{-qc}}. \quad (26b)$$

Solution: Wiener–Hopf problem (crack-opening mode)

Two coupled equations, (B.2a) and (B.2b), are involved in this instance. In view of (19)–(21), (M_O, m_O, n_O) can be expressed as products $(M_O^+ M_O^-, m_O^+ m_O^-, n_O^+ n_O^-)$. The factors are analytic in overlapping halves $\text{Re}(q) > -1/(c_+ - c)(+)$ and $\text{Re}(q) < 1/(c_+ + c)(-)$ of the complex q -plane. Based on a standard procedure [Morse and Feshbach 1953; Achenbach 1976] the factors are found to be

$$M_O^+ = \frac{B^+ G_O^+}{A_+^+ A_-^+} \left(\frac{1}{c_O - c} + q \right), \quad M_O^- = R_O \frac{B^- G_O^-}{A_+^- A_-^-} \left(\frac{1}{c_O + c} - q \right), \quad (27a)$$

$$m_O^+ = \frac{A_-^+}{a_-^+ G^+}, \quad m_O^- = -m_3 \frac{a_-^- G^-}{A_-^-}, \quad (27b)$$

$$n_O^+ = \frac{A_-^+}{a_-^+ G^+}, \quad n_O^- = -n_3 q \frac{a_-^- G^-}{A_-^-}. \quad (27c)$$

Term (G_O^\pm, G^\pm) is given in Appendix C, and it is noted that $(M_O^+, m_O^+, n_O^+) \geq 0$. Equation (B.2a) can

therefore be put in the form

$$\frac{\bar{\sigma}_O}{P_O^+} - \frac{F_3}{pQ} \left(\frac{1}{P_O^+} - \frac{c}{P_3} \right) = -\mu p \bar{\Delta}_O \frac{M_O^-}{2} \lambda_O^+ + \mu \alpha_D \langle \bar{\Theta} \rangle \frac{m_O^-}{\lambda_O^+} + \frac{F_3}{pQ P_O}, \quad (28a)$$

$$P_O^+ = \sqrt{M_O^+ m_O^+}, \quad \lambda_O^+ = \sqrt{\frac{M_O^+}{m_O^+}}, \quad (28b)$$

$$P_3 = \sqrt{c} P_O^+ \left(\frac{1}{c} \right) = \frac{1}{\sqrt{c_O - c}} \sqrt{\frac{g_O^+ c_O}{g^+ a_-^+}}, \quad g_O^+ = G_O^+ \left(\frac{1}{c} \right), \quad g^+ = G^+ \left(\frac{1}{c} \right). \quad (28c)$$

The left-hand side of (28a) is analytic for $\text{Re}(q) > -1/(c_+ - c)$. Equations (28b), (28c), (C.2) and (C.3) and behavior expected for σ_O suggest that this side vanishes for $|q| \rightarrow \infty$. Setting the right-hand side of (28a) to zero leads to a quadratic equation in λ_O^+ . The solution is itself an equation of the Wiener–Hopf type; i.e., λ_O^+ is set equal to a combination of terms that are analytic in the overlapping region $\text{Re}(q) < 1/(c_+ + c)$. Both sides must be analytic continuations of the same bounded entire function. For $|q| \rightarrow \infty$:

$$\lambda_O^+ \rightarrow J_3 = \sqrt{\frac{b^+}{a_+^+ a_-^+}}. \quad (29)$$

Equation (29) identifies this function as a constant, so that (28a) now takes the classic [Morse and Feshbach 1953] form:

$$\frac{\bar{\sigma}_O}{P_O^+} - \frac{F_3}{pQ} \left(\frac{1}{P_O^+} - \frac{c}{P_3} \right) = -\mu p \bar{\Delta}_O \frac{M_O^- J_3}{2} + \mu \alpha_D \langle \bar{\Theta} \rangle \frac{m_O^-}{J_3} + \frac{c F_3}{pQ P_3}. \quad (30)$$

In view of the behavior noted for the left-hand side of (28a), the bounded entire function for (30) vanishes. Thus (30) defines $\bar{\sigma}_O$ and provides a linear equation for $(\bar{\Delta}_O, \langle \bar{\Theta} \rangle)$. Use of that in (B.2b) gives

$$\alpha_D \bar{\Theta}_O = -\frac{n_O}{J_3 M_O^-} \frac{\sqrt{c} F_3}{\mu p Q P_3} + \alpha_D \langle \bar{\Theta} \rangle W, \quad W = N_O - \frac{n_O m_O^-}{J_3^2 M_O^-}. \quad (31)$$

Rearrangement of (31) into a form analogous to (30) is possible, but coefficient W leads to a complicated expression. For $|q| \rightarrow \infty$ however, the resulting form, and its counterpart for (30), combine to give more tractable forms:

$$\bar{\sigma}_O \approx \frac{J_3 F_3}{P_3 p \sqrt{q c}}, \quad p Q \bar{\Delta}_O \approx -\frac{F_3 D_3}{\mu p \sqrt{-q}}, \quad (32a)$$

$$\alpha_D \bar{\Theta}_O \approx \frac{\sqrt{c} J_3 F_3}{m_3 P_3} \frac{h \chi}{\Gamma_+ \Gamma_-} \left(\frac{C_-}{a_-} - \frac{C_+}{a_+} \right) \frac{1}{\mu p \sqrt{q}}, \quad \alpha_D \langle \bar{\Theta} \rangle \approx \frac{F_3 E_3}{\mu p \sqrt{-q}} \exp(\mp i \Psi_3), \quad (32b)$$

$$D_3 = \frac{2a_+ a_-}{b R_O} \frac{\sqrt{c} J_3}{P_3} \cos \Psi_3, \quad E_3 = \frac{h \chi}{\Gamma_+ \Gamma_-} \frac{c J_3}{m_3 P_3} \left(\frac{C_+}{a_+} - \frac{C_-}{a_-} \right) \cos \Psi_3, \quad (32c)$$

$$\Psi_3 = \tan^{-1} \frac{h \chi}{\Gamma_+ \Gamma_-} \left[\left(\frac{C_+}{a_+} - \frac{C_-}{a_-} \right) c + \frac{\varepsilon K^2}{c \Gamma_+ \Gamma_-} \frac{(a_+ - a_-)^2}{b a_+ a_- R_O} \right]. \quad (32d)$$

In (32b) (\mp) signifies $\text{Im}(q) > 0$ and $\text{Im}(q) < 0$ respectively.

Solution: Wiener–Hopf problem (sliding mode)

Equations (B.3a) and (B.3b) govern in this instance, but the method of solution closely mirrors that for the crack-opening mode. For $|q| \rightarrow \infty$:

$$\bar{\sigma}_S \approx \frac{-\sqrt{b^+} F_S}{P_{12} p \sqrt{q}}, \quad p Q \bar{\Delta}_S \approx \frac{F_S D_{12}}{\mu p \sqrt{-q}}, \quad (33a)$$

$$\alpha_D \bar{\partial}_3 \Theta_0 \approx \frac{-F_S}{2\mu m_{12}} \left(\frac{C_+}{a_+} - \frac{C_-}{a_-} \right) \frac{pq}{\sqrt{b^+} P_{12} p \sqrt{q}}, \quad \alpha_D |\bar{\Theta}| \approx -\frac{F_S F_{12}}{\mu p \sqrt{-q}}, \quad (33b)$$

$$D_{12} = \frac{2b}{P_{12}} \sqrt{\frac{c}{b^+}} \frac{C_+ a_+ - C_- a_-}{2bm_{12} n_{12} \lambda \Gamma_+ \Gamma_- + R_S (C_+ a_+ - C_- a_-)}, \quad E_{12} = \frac{1}{P_{12} m_{12} \sqrt{b^+}}. \quad (33c)$$

Term (P_{12}, m_{12}, n_{12}) in (33) correspond to (P_3, m_3, n_3) and are given by

$$P_{12} = \frac{1}{\sqrt{c_S - c}} \sqrt{\frac{g_S^+ c_S}{g^+ a_+^+}}, \quad g_S^+ = G_S^+ \left(\frac{1}{c} \right), \quad (34a)$$

$$m_{12} = \frac{a_+ - a_-}{\lambda c^2 \Gamma_+ \Gamma_-}, \quad n_{12} = \frac{2\varepsilon}{\Gamma_+ \Gamma_-} (a_+ - a_-). \quad (34b)$$

Term G_S^\pm is defined in Appendix C.

Solution behavior in crack plane near C

Equations (26b), (32) and (33) involve linear combinations of three types of transform. The types and corresponding inverses are given in Appendix D. It proves convenient to now introduce some generality by considering point-force loads that are not temporal step-functions. That is $F_k \rightarrow F_k(s)$ $F_k(0) = 0$. It is also noted that $\bar{D}_0 f = V_R \bar{D} f = V_R p Q \bar{f}$. Thus ahead of the extending crack ($x \rightarrow 0+$, $|\psi| < \pi/2$) (26b), (32), (33) and (D.3) give by convolution:

$$\sigma_O \approx \frac{-J_3 K_O}{\pi P_3 \sqrt{cx}}, \quad \sigma_S \approx \frac{\sqrt{b^+} K_S}{\pi P_{12} \sqrt{cx}}, \quad \sigma_T \approx \frac{-b^+ K_T}{\pi \sqrt{cx}}, \quad (35a)$$

$$\alpha_D \Theta_0 \approx \frac{c^2 J_3}{\pi K P_3} \frac{C_+ a_- - C_- a_+}{a_+ - a_-} \frac{K_O}{\mu \sqrt{cx}}, \quad (35b)$$

$$\alpha_D \partial_3 \Theta_0 \approx -\frac{\partial}{\partial x_0} \frac{c}{\pi P_{12} \sqrt{b^+}} \frac{C_+ a_+ - C_- a_-}{2\lambda \Gamma_+ \Gamma_-} \frac{K_S}{\mu \sqrt{cx}}. \quad (35c)$$

For $(x \rightarrow 0-, |\psi| < \pi/2)$:

$$D_0 \Delta_O \approx \frac{D_3}{\pi} \frac{V_R K_O}{\mu \sqrt{-x}}, \quad D_0 \Delta_S \approx -\frac{D_{12}}{\pi} \frac{V_R K_S}{\mu \sqrt{-x}}, \quad D_0 \Delta_T \approx \frac{1}{\pi b^- \sqrt{c}} \frac{V_R K_T}{\mu \sqrt{-x}}, \quad (36a)$$

$$\alpha_D \langle \Theta \rangle \approx \frac{-E_3}{\pi} \cos \Psi_3 \frac{V_R K_O(s)}{\mu \sqrt{-x}}, \quad \alpha_D |\Theta| \approx \frac{E_{12}}{\pi} \frac{V_R K_S(s)}{\mu \sqrt{-x}}. \quad (36b)$$

In (35) and (36):

$$K_O = \frac{d}{ds} \int \frac{dF_3}{du} \frac{du}{\sqrt{s-u}}, \quad K_S = \frac{d}{ds} \int \frac{dF_S}{du} \frac{du}{\sqrt{s-u}} \quad (0 < u < s), \quad (37a)$$

$$K_T = \frac{d}{ds} \int \frac{dF_T}{du} \frac{du}{\sqrt{s-u}} \quad (0 < u < s). \quad (37b)$$

Velocity and temperature change near C

In regard to solution behavior near C for $|x_3| \geq 0$, temperature change Θ and particle velocity in terms of components $(D_0 u_S, D_0 u_T, D_0 u_3)$ can be obtained from expressions (12)–(14) that are evaluated for $|q| \rightarrow \infty$ in terms (A.1)–(A.3), (15), (26), (32), (33) and relation

$$D_0 \begin{bmatrix} u_S \\ u_T \end{bmatrix} = D_0 \begin{bmatrix} \cos \psi & \sin \psi \\ \sin \psi & -\cos \psi \end{bmatrix} \begin{bmatrix} u_1 \\ u_2 \end{bmatrix}. \quad (38)$$

The resulting expressions for $(\bar{D}_0 u_S, \bar{D}_0 u_T, \bar{D}_0 u_3)$ are linear combinations of two transform types. The types and corresponding inversions are given in Appendix D. Response near C is made clearer in terms of local coordinates (r, ψ, ϕ) , where $(r \rightarrow 0+, |\psi| < \pi/2, |\phi| < \pi)$ and

$$x = r \cos \phi, \quad x_3 = r \sin \phi. \quad (39)$$

In light of (39) term $1/\sqrt{x - i\omega}$ in Appendix D gives for $\omega = (b, a_{\pm})$ respectively:

$$\frac{1}{\sqrt{2r}}(B^{[+]} + iB^{[-]}), \quad B^{[\pm]} = \frac{1}{B_{\Phi}} \sqrt{B_{\Phi}^{[\pm]} \cos \phi}, \quad B_{\Phi} = \sqrt{1 - c^2 \sin^2 \phi}, \quad (40a)$$

$$\frac{1}{\sqrt{2r}}(A_{\pm}^{[+]} + iA_{\pm}^{[\pm]}), \quad A_{\pm}^{[\pm]} = \frac{1}{A_{\Phi}^{\pm}} \sqrt{A_{\Phi}^{\pm} [\pm] \cos \phi}, \quad A_{\Phi}^{\pm} = \sqrt{1 - \frac{c^2}{c_{\pm}^2} \sin^2 \phi}. \quad (40b)$$

Generalization $F_k \rightarrow F_k(s)$, $F_k(0) = 0$ is again made, and it can then be shown in view of (40) that for $(r \approx 0+, |\psi| < \pi/2, |\phi| < \pi)$:

$$\begin{aligned} \alpha_D \Theta \approx & \frac{1}{2\pi \Gamma_+ \Gamma_-} \frac{K_S}{\mu \sqrt{2r}} \left[\frac{2\varepsilon}{c} D_{12} (A_-^{[-]} - A_+^{[-]}) + \frac{E_{12}}{\lambda} (C_- A_-^{[-]} - C_+ A_+^{[-]}) \right] \\ & + \frac{\varepsilon K D_3}{2\pi c \Gamma_+ \Gamma_-} \frac{K_O}{\mu \sqrt{2r}} \left(\frac{A_+^{[+]}}{a_+} - \frac{A_-^{[+]}}{a_-} \right) \\ & + \frac{h\chi c E_3}{\pi \Gamma_+ \Gamma_-} \frac{K_O}{\mu \sqrt{2r}} \left[\left(\frac{A_-^{[+]}}{a_-} - \frac{A_+^{[+]}}{a_+} \right) \cos \Psi_3 + \left(\frac{A_-^{[-]}}{a_-} - \frac{A_+^{[-]}}{a_+} \right) \sin \Psi_3 \right], \quad (41) \end{aligned}$$

$$D_0 u_T \approx -\frac{V_R}{\pi \mu} \sqrt{c} \frac{B^{[-]}}{2b^-} \frac{K_T}{\sqrt{2r}}, \quad (42a)$$

$$\begin{aligned} D_0 u_S \approx & \frac{V_R}{\pi \mu c^2} \left[b D_3 B^{[+]} \frac{K_O}{\sqrt{2r}} - K D_{12} B^{[-]} \frac{K_S}{\sqrt{2r}} \right] \\ & + \frac{V_R}{2\pi \mu c^2 \lambda \Gamma_+ \Gamma_-} \frac{K_S}{\sqrt{2r}} \left[2D_{12} (C_- A_+^{[-]} - C_+ A_-^{[-]}) + c E_{12} (A_-^{[-]} - A_+^{[-]}) \right] \\ & + \frac{V_R K D_3}{2\pi \mu c^2 \lambda \Gamma_+ \Gamma_-} \frac{K_O}{\sqrt{2r}} \left(\frac{C_+}{a_-} A_-^{[+]} - \frac{C_-}{a_+} A_+^{[+]} \right) \\ & + \frac{V_R h \chi \lambda E_3}{\pi \mu \Gamma_+ \Gamma_-} \frac{K_O}{\sqrt{2r}} \left[\left(\frac{A_-^{[+]}}{a_-} - \frac{A_+^{[+]}}{a_+} \right) \cos \Psi_3 + \left(\frac{A_-^{[-]}}{a_-} - \frac{A_+^{[-]}}{a_+} \right) \sin \Psi_3 \right], \quad (42b) \end{aligned}$$

$$\begin{aligned} D_0 u_3 \approx & \frac{V_R}{\pi \mu c^2} \left[\frac{K}{b} D_{12} B^{[+]} \frac{K_S}{\sqrt{2r}} + D_3 B^{[-]} \frac{K_O}{\sqrt{2r}} \right] \\ & + \frac{V_R}{2\pi \mu c^2 \lambda \Gamma_+ \Gamma_-} \frac{K_S}{\sqrt{2r}} [a_- A_-^{[+]} (2C_- D_{12} - c E_{12}) + a_+ A_+^{[+]} (2C_+ D_{12} - c E_{12})] \\ & + \frac{V_R K D_3}{2\pi \mu c^2 \lambda \Gamma_+ \Gamma_-} \frac{K_O}{\sqrt{2r}} (C_+ A_-^{[-]} - C_- A_+^{[-]}) \\ & + \frac{V_R h \chi \lambda E_3}{\pi \mu \Gamma_+ \Gamma_-} \frac{K_O}{\sqrt{2r}} [(A_+^{[-]} - A_-^{[-]}) \cos \Psi_3 + (A_-^{[+]} - A_+^{[+]}) \sin \Psi_3]. \quad (42c) \end{aligned}$$

Preliminary comments

The coupling of (χ, Ψ_3) with K_O in (35), (36), (41) and (42) shows that crack opening (and therefore convection) indeed occurs only when compressive load $F_3(s)$ is present. These equations also show that introduction of components that align with coordinates (x, ψ, x_3) allow an uncoupling into three modes of fracture. However classical definitions [Freund 1990] of in-plane modes are made in terms of the normal and tangent to the crack edge, and designated as Modes II and III, respectively. Here crack edge orientation is controlled by $V(\psi)$. In terms of (35a) and (36a) for example

$$\begin{bmatrix} \sigma_{II} \\ \sigma_{III} \end{bmatrix} = \mathbf{M}_C \begin{bmatrix} \sigma_S \\ \sigma_T \end{bmatrix}, \quad \begin{bmatrix} D_0 \Delta_{II} \\ D_0 \Delta_{III} \end{bmatrix} = \mathbf{M}_C \begin{bmatrix} D_0 \Delta_S \\ D_0 \Delta_T \end{bmatrix}, \quad (43a)$$

$$\mathbf{M}_C = \begin{bmatrix} \cos \psi_C & -\sin \psi_C \\ \sin \psi_C & \cos \psi_C \end{bmatrix}, \quad \psi_C = \tan^{-1} \frac{dc}{cd\psi}. \quad (43b)$$

Dynamic energy release rate criterion

Equation (43) need not be employed if the imposed fracture criterion is based on scalar products, i.e., dynamic energy release rate [Freund 1990]. If kinetic energy is included [Gdoutos 1993; Brock 2017] it

can be shown that here the criterion can be written:

$$D_0 \iint_{\delta A} e_F dx_1^0 dx_2^0 - \iint_{\mathcal{I}} \sigma_{3k}^0 D_0 \Delta_k dx_1^0 dx_2^0 - D_0 \iiint_{123} \frac{\rho}{2} D_0 u_k D_0 u_k dx_1^0 dx_2^0 dx_3^0 = 0, \quad (44a)$$

$$\sigma_{3k}^0 D_0 \Delta_k = \sigma_O D_0 \Delta_O + \sigma_S D_0 \Delta_S + \sigma_T D_0 \Delta_T, \quad (44b)$$

$$D_0 u_k D_0 u_k = (D_0 u_O)^2 + (D_0 u_S)^2 + (D_0 u_T)^2. \quad (44c)$$

In (44a) e_F is the surface energy per unit area in area δA , and is generally viewed as constant [de Boer et al. 1988; Skriver and Rosenggaard 1992]. Fracture zone \mathcal{I} is a strip of infinitesimal thickness in the $x_1^0 x_2^0$ -plane that straddles the portion of C that borders δA . In view of the singular behavior seen in (35) and (36) it can be shown [Freund 1972] that integration yields a finite value. Subscript 123 signifies integration over the solid, but the singular behavior exhibited in (42) demonstrates that the volume integral can be confined to a tube of radius $r_C \rightarrow 0$ that is centered on, and encloses, the crack edge C . Analysis [Brock 2017] shows that these produce a single integration with respect to ψ on the left-hand side of (44a). That is, (44a) is satisfied if the integrand vanishes for all $|\psi| < \pi/2$. However the integrand cannot, in general, vanish for constant e_F and time-invariant crack-extension rate; compare [Achenbach and Brock 1973]. An exception, featured in [Brock 2017], is case $3F_k(s) = 2f_k s^{3/2}$, i.e.,

$$K_O = \pi f_3, \quad K_S = \pi(f_1 \cos \psi + f_2 \sin \psi), \quad K_T = \pi(f_1 \sin \psi - f_2 \cos \psi). \quad (45)$$

Here f_k is constant and $f_3 \geq 0$. This analysis concerns fracture initiation, and appropriate asymptotic forms such as (15) have been employed. So, the exception is here taken to represent only the initial loading behavior. A focus is, moreover, on the role of crack surface convection. The observation concerning (K_O, Ψ_3) made above suggests that consideration of the pure-compression case ($f_1 = f_2 = 0$) is sufficient in this regard. In view of (35), (36), (42) and (45) formula (44a) produces the equation:

$$\frac{f_3^2 c}{2\pi\mu} \frac{J_3 D_3}{P_3} + \left[e_F + \frac{f_3^2}{(2\pi)^2 \mu} \int_{\Phi} (Q_O^2 + Q_S^2) \cos \phi d\phi \right] \sqrt{c^2 + \left(\frac{dc}{d\psi} \right)^2} = 0, \quad (46a)$$

$$Q_O = \frac{D_3}{c^2} \left[B^{[-]} + \frac{K}{2\lambda\Gamma_+\Gamma_-} (C_+ A_-^{[-]} - C_- A_+^{[-]}) \right] + \frac{h\chi\lambda}{\Gamma_+\Gamma_-} [(A_+^{[-]} - A_-^{[-]}) \cos \Psi_3 + (A_-^{[+]} - A_+^{[+]}) \sin \Psi_3], \quad (46b)$$

$$Q_S = \frac{D_3}{c^2} \left[bB^{[+]} + \frac{K}{2\lambda\Gamma_+\Gamma_-} \left(\frac{C_+}{a_-} A_-^{[+]} - \frac{C_-}{a_+} A_+^{[+]} \right) \right] + \frac{h\chi\lambda}{\Gamma_+\Gamma_-} \left[\left(\frac{A_-^{[+]}}{a_-} - \frac{A_+^{[+]}}{a_+} \right) \cos \Psi_3 + \left(\frac{A_-^{[-]}}{a_-} - \frac{A_+^{[-]}}{a_+} \right) \sin \Psi \right]. \quad (46c)$$

Subscript Φ in (46a) signifies integration over range $|\phi| < \pi$. Absence of ψ in (46a) implies that $dc/d\psi = 0$; i.e., the crack edge forms a semicircle of radius cs about the point force. Equation (46a) then reduces to a transcendental algebraic relation for constant c :

$$e_F + \frac{f_3^2}{2\pi\mu} \left[\frac{J_3 D_3}{P_3} + \frac{1}{2\pi} \int_{\Phi} (Q_O^2 + Q_S^2) \cos \phi d\phi \right] = 0. \quad (46d)$$

Thermal response on C

Equation (41) describes unbounded temperature change along crack edge C . As with dynamic energy release rate a finite measure is possible, in this case by considering the norm of crack edge temperature change:

$$\|\Theta\| = \sqrt{\int_C \Theta^2 dl}. \quad (47)$$

The line integration in (47) for given $|\psi| < \pi/2$ is around the surface of the tube of radius $r_C \rightarrow 0$ that is involved in analysis of (44a). Thus (41) governs and $dl = r_C d\phi$. For pure compression ($f_1 = f_2 = 0$) equation (47) gives

$$\|\Theta\| = \frac{f_3}{\mu\alpha_D} \frac{1}{\sqrt{2} \Gamma_+ \Gamma_-} \left[\int_\Phi d\phi \left(\frac{K D_3}{2c} Q_D + h\chi c E_3 Q_E \right)^2 \right]^{1/2}, \quad (48a)$$

$$Q_D = \frac{A_+^{[+]}}{a_+} - \frac{A_-^{[+]}}{a_-}, \quad Q_E = \left(\frac{A_-^{[-]}}{a_-} - \frac{A_+^{[-]}}{a_+} \right) \sin \Psi_3 - Q_D \cos \Psi_3. \quad (48b)$$

Illustration of convection effect

Convection is represented in (46) and (48) by $h\chi$, a dimensionless constant that plays a role similar to that of the Biot number in classical thermoelasticity [Boley and Weiner 1960]. As noted above, results here are valid for subcritical speed $V(\psi)$, i.e., $c(\psi) < (c_3, c_{12})$. In contrast results in [Brock 2017] require that $c(\psi) < 0.3$. Imposing a similar requirement here, $c < 0.4$, does allow an explicit, asymptotic representation of convection effect. In particular, expansions of (46b), (46c) and (48b) in powers of c allow closed-form integration with respect to ϕ . Equations (46d) and (48a) become

$$(c_D^2 E_0 + E_1 + E_2 h^2 \chi^2) c^2 + \left[\frac{2\mu e_F}{\pi f_3^2} c_O \left(1 - \frac{1}{c_D^2} \right) - \frac{1}{c_O} + \frac{\sqrt{\lambda}}{2c_D} \Gamma_+ \right] c_D^2 c - c_D^2 \approx 0, \quad (49a)$$

$$\|\Theta\| \approx \frac{7c^{3/2}}{4\mu\alpha_D} \sqrt{\frac{\pi}{2}} \frac{f_3}{c_O} \left(\frac{\varepsilon\lambda}{c_D^2 - 1} + h\chi c^{3/2} \right). \quad (49b)$$

The (positive) coefficients (E_0, E_1, E_2) are given in Appendix E. Equation (49) indicates that for $c \rightarrow 0$ convection parameter $h\chi$ diminishes in importance. More insight is possible by calculation of c and the corresponding $\|\Theta\|$. Convection parameters $h\chi$ are based on Biot parameter values featured in [Boley and Weiner 1960]. Values for loading parameter f_3 are based on those in [Brock 2017], as are the material constants for a generic solid at room temperature:

$$\begin{aligned} \mu &= 79 \text{ GPa}, & e_F &= 2.2 \text{ J/m}^2, & V_R &= 3094 \text{ m/s}, \\ c_D &= 2, & c_+ &= 4.5452, & c_- &= 1.997, & c_O &= 0.9332, \\ T_0 &= 294 \text{ K}, & \alpha_D &= 89.6 \cdot 10^{-6} \text{ K}^{-1}, & \varepsilon &= 0.05044, \\ h &= 3.1862 \cdot 10^{-9} \text{ m}, & h_0 &= 1.547 \cdot 10^{-10} \text{ m}. \end{aligned}$$

Combinations of $(h\chi, f_3)$ chosen are such that quadratic (49a) yields solutions $0 < c < 0.4$. Calculations for $(c, \|\Theta\|)$ are displayed in Tables 1 and 2. Entries in Table 1 indicate that c tends to increase by orders

f_3 (N/m ^{3/2})	$h\chi = 0$	$h\chi = 10$	$h\chi = 50$	$h\chi = 65$	$h\chi = 80$
$1 \cdot 10^4$	0.00129249	0.00129248	0.001292476	0.00129247	0.00129225
$2 \cdot 10^4$	0.00518312	0.00518309	0.00518323	0.00518174	0.00518103
$5 \cdot 10^4$	0.0327376	0.0327294	0.0325396	0.0323988	0.0322297
$1 \cdot 10^5$	0.123558	0.123168	0.115141	0.110192	0.10563
$1 \cdot 10^6$	0.381241	0.2869926	0.2869926	0.250029	0.2194334

Table 1. Values of c for various $(h\chi, f_3)$.

f_3 (N/m ^{3/2})	$h\chi = 0$	$h\chi = 10$	$h\chi = 50$	$h\chi = 65$	$h\chi = 80$
$1 \cdot 10^4$	$1.215 \cdot 10^{-11}$	$1.907 \cdot 10^{-10}$	$4.674 \cdot 10^{-10}$	$5.712 \cdot 10^{-10}$	$5.663 \cdot 10^{-8}$
$2 \cdot 10^4$	$1.951 \cdot 10^{-9}$	$1.088 \cdot 10^{-8}$	$4.657 \cdot 10^{-8}$	$5.99 \cdot 10^{-8}$	$7.325 \cdot 10^{-8}$
$5 \cdot 10^4$	$7.747 \cdot 10^{-8}$	$5.694 \cdot 10^{-6}$	$2.767 \cdot 10^{-5}$	$3.549 \cdot 10^{-5}$	$4.325 \cdot 10^{-5}$
$1 \cdot 10^5$	$1.136 \cdot 10^{-6}$	$5.997 \cdot 10^{-4}$	$2.446 \cdot 10^{-3}$	$2.787 \cdot 10^{-3}$	$2.974 \cdot 10^{-3}$
$1 \cdot 10^6$	$6.132 \cdot 10^{-5}$	0.16846	0.37872	0.32555	0.27085

Table 2. Values of $\|\Theta\|$ (K m^{1/2}) for various $(h\chi, f_3)$.

of magnitude with increases in f_3 . Variation in c with $h\chi$ is not however monotonic for given f_3 . Indeed, for higher f_3 -values a marked decrease occurs in c for higher $h\chi$ -values. Table 2 entries indicate that $\|\Theta\|$ also tends to increase with increasing f_3 . $\|\Theta\|$ is even more sensitive than c to variations in $h\chi$, and especially in f_3 . Another contrast: except at the highest f_3 -value, monotonic increases in $\|\Theta\|$ occur with increasing $h\chi$. Variations noted in Tables 1 and 2 can be a matter of significant figures. The trends described seem however to be clear.

Some summary comments

This paper addresses a problem similar to that found in [Brock 2017]. However crack surface thermal convection is now considered and crack extension rate need only be subcritical, not well below Rayleigh and body wave speed. In addition formulation of the governing Wiener–Hopf equations in integral transform space differs. Because the requirement on speed is relaxed moreover, the equations yield solutions that are more robust. Analysis of the inverses that result, and calculations for the pure compression case, indicate that:

- Effect of convection is less important at low crack extension rates.
- Increase in point force magnitude does in general increase crack extension rate.
- For given force, variation in rate with convection may not be monotonic.
- At higher forces, increases in convection can decrease extension rate.
- Thermal response, in terms of crack edge temperature norm, is similar.
- Norm variation with changes in convection is however more pronounced.

Appendix A

$$U_1^{(\pm)} = \frac{qB}{Q^2} \bar{\Delta}_O \cos \psi (\pm) \left(\frac{T \bar{\Delta}_S}{2Q^2} \cos \psi + \frac{\bar{\Delta}_T}{2} \sin \psi \right), \quad (\text{A.1a})$$

$$U_2^{(\pm)} = \frac{qB}{Q^2} \bar{\Delta}_O \sin \psi (\pm) \left(\frac{T \bar{\Delta}_S}{2Q^2} \sin \psi - \frac{\bar{\Delta}_T}{2} \cos \psi \right), \quad (\text{A.1b})$$

$$U_+^{(\pm)} = \frac{hp}{Q \bar{P}_0 \Gamma_+ \Gamma_- A_+} \left(\frac{\alpha_D}{p^2} [\bar{\partial}_3 \Theta] + C_- T \bar{\Delta}_O \right) (\mp) \frac{hp}{Q \bar{P}_0 \Gamma_+ \Gamma_-} \left(\frac{\alpha_D}{p} [\bar{\Theta}] + 2C_- q \bar{\Delta}_S \right), \quad (\text{A.2a})$$

$$U_-^{(\pm)} = \frac{-hp}{Q \bar{P}_0 \Gamma_+ \Gamma_- A_-} \left(\frac{\alpha_D}{p^2} [\bar{\partial}_3 \Theta] + C_+ T \bar{\Delta}_O \right) (\pm) \frac{hp}{Q \bar{P}_0 \Gamma_+ \Gamma_-} \left(\frac{\alpha_D}{p} [\bar{\Theta}] + 2C_+ q \bar{\Delta}_S \right), \quad (\text{A.2b})$$

$$T = Q^2 - 2q^2. \quad (\text{A.3})$$

In view of (5c), equations (A.1) and (A.2) are subject to constraints:

$$[\bar{\partial}_3 \Theta] + 2\chi \bar{P}_0 \langle \bar{\Theta} \rangle = 0, \quad \langle \bar{\partial}_3 \Theta \rangle = \chi \bar{P}_0 [\bar{\Theta}]. \quad (\text{A.4})$$

Appendix B

Tearing mode response is governed by

$$\bar{\sigma}_T - \frac{F_T}{pQ} = -\mu p \bar{\Delta}_T B, \quad (\text{B.1a})$$

$$F_T = F_1 \sin \psi - F_2 \cos \psi. \quad (\text{B.1b})$$

Crack-opening mode response is governed by the coupled set

$$\bar{\sigma}_O - \frac{F_3}{pQ} = -\mu p \bar{\Delta}_O \frac{M_O}{2} + \mu \alpha_D \langle \bar{\Theta} \rangle m_O, \quad (\text{B.2a})$$

$$\alpha_D \bar{\Theta}_0 = -p \bar{\Delta}_O \frac{n_O}{2} + \alpha_D \langle \bar{\Theta} \rangle N_O. \quad (\text{B.2b})$$

Sliding mode response is governed by the coupled set

$$\bar{\sigma}_S - \frac{F_S}{pQ} = -\mu p \bar{\Delta}_S \frac{M_S}{2} + \mu \alpha_D [\bar{\Theta}] m_S, \quad (\text{B.3a})$$

$$\alpha_D \bar{\partial}_3 \bar{\Theta}_0 = p^2 \bar{\Delta}_S \frac{n_S}{2} + p \alpha_D [\bar{\Theta}] N_S, \quad (\text{B.3b})$$

$$F_S = F_1 \cos \psi + F_2 \sin \psi. \quad (\text{B.3c})$$

Coefficients in (B.2) and (B.3) are

$$M_O = \frac{1}{Q^2} \left[4q^2 B + \frac{T^2}{\lambda \Gamma_+ \Gamma_-} \left(\frac{C_+}{A_-} - \frac{C_-}{A_+} \right) \right], \quad (\text{B.4a})$$

$$M_S = \frac{1}{Q^2} \left[\frac{T^2}{B} + \frac{4q^2}{\lambda \Gamma_+ \Gamma_-} (C_+ A_- - C_- A_+) \right], \quad (\text{B.4b})$$

$$N_O = -1 + \frac{\chi h Q}{\Gamma_+ \Gamma_-} \left(\frac{C_+}{A_+} - \frac{C_-}{A_-} \right), \quad (\text{B.4c})$$

$$N_S = \frac{1}{2} \left[\chi h_0 Q + \frac{1}{\lambda \Gamma_+ \Gamma_-} (C_- A_- - C_+ A_+) \right], \quad (\text{B.4d})$$

$$m_O = \frac{\chi T h}{\Gamma_+ \Gamma_- \beta} \left(\frac{1}{A_+} - \frac{1}{A_-} \right), \quad m_S = \frac{1}{\lambda \Gamma_+ \Gamma_-} \frac{q}{Q^2} (A_+ - A_-), \quad (\text{B.5a})$$

$$n_O = -\frac{\varepsilon T}{\Gamma_+ \Gamma_-} \left(\frac{1}{A_+} - \frac{1}{A_-} \right), \quad n_S = -\frac{2\varepsilon q}{\Gamma_+ \Gamma_-} (A_+ - A_-). \quad (\text{B.5b})$$

Appendix C

$$\ln G_O^\pm(q) = \frac{1}{\pi} \int \frac{\Phi_O du}{(u \mp c)(qu \pm Q)}, \quad \ln G_S^\pm(q) = \frac{1}{\pi} \int \frac{\Phi_S du}{(u \mp c)(qu \pm Q)}. \quad (\text{C.1a})$$

Integration is over range $1 < u < c_+$, where for $c_- < u < c_+$:

$$\Phi_O = \tan^{-1} \left(\frac{4a_+ \beta \lambda}{C_- K^2} \Gamma_+ \Gamma_- + \frac{C_+ a_+}{C_- \alpha_-} \right), \quad \Phi_S = \tan^{-1} \frac{4C_- a_+ \beta}{4C_+ \alpha_- \beta + \lambda K^2 \Gamma_+ \Gamma_-}. \quad (\text{C.1b})$$

For $1 < c < c_-$:

$$\Phi_O = \tan^{-1} \frac{K^2}{4\lambda \beta \Gamma_+ \Gamma_-} \left(\frac{C_+}{a_-} - \frac{C_-}{a_+} \right), \quad \Phi_S = \tan^{-1} \frac{4\beta}{\lambda K^2 \Gamma_+ \Gamma_-} (C_- a_+ - C_+ a_-). \quad (\text{C.1c})$$

$$G^\pm(q) = \frac{1}{\pi} \int \tan^{-1} \frac{a_+}{\alpha_-} \frac{du}{(u \mp c)(qu \pm Q)} \quad (c_- < u < c_+). \quad (\text{C.2})$$

In (C.1) and (C.2) $a_\pm = a_\pm(u)$ and [see (24)] $K = K(u)$. Moreover

$$\beta = \sqrt{u^2 - 1}, \quad \alpha_- = \sqrt{\frac{u^2}{c_-^2} - 1}. \quad (\text{C.3})$$

Appendix D

Equations (26b), (32) and (33) involve three basic types of transform function. These types, and the corresponding inverses generated by (9b) are

$$\frac{1}{p\sqrt{q}} \rightarrow -\sqrt{\frac{p}{\pi x}} \quad (x > 0), \quad (\text{D.1a})$$

$$\frac{1}{p\sqrt{-q}} \rightarrow -\sqrt{\frac{p}{\pi|x|}} \quad (x < 0), \quad (\text{D.1b})$$

$$\frac{\exp(\mp i\Psi_3)}{p\sqrt{-q}} \rightarrow -\sqrt{\frac{p}{\pi|x|}} \cos \Psi_3 \quad (x < 0). \quad (\text{D.1c})$$

In view of (38) it can be shown that $(\bar{D}_0 u_S, \bar{D}_0 u_T, \bar{D}_0 u_O)$ are linear combinations of two types of transforms. The types, and their inversions generated by use of (9b) are

$$\left[\frac{1}{p\sqrt{q}}, \frac{(\pm)}{p\sqrt{-q}} \right] \exp(-p\omega\sqrt{q}\sqrt{-q}) \rightarrow -\sqrt{\frac{p}{\pi}} [\text{Re}, \text{Im}] \frac{1}{\sqrt{x-i\omega}}, \quad (\text{D.2a})$$

$$\left[\frac{1}{p\sqrt{q}}, \frac{(\pm)}{p\sqrt{-q}} \right] \exp((\mp)i\Psi_3 - p\omega\sqrt{q}\sqrt{-q}) \rightarrow \sqrt{\frac{p}{\pi}} [\text{Re}, \text{Im}] \frac{\exp(-i\Psi_3)}{\sqrt{x-i\omega}}, \quad (\text{D.2b})$$

$$\omega = (b, a_{\pm})|x_3|. \quad (\text{D.2c})$$

On the left-hand (transform) sides of (D.2a) and (D.2b) (\pm) signifies $\text{Im}(q) > 0$ and $\text{Im}(q) < 0$, respectively. In view of (7a) moreover \sqrt{p} is the transform of

$$\frac{d}{ds} \left(\frac{1}{\sqrt{\pi s}} \right) \quad (s > 0). \quad (\text{D.3})$$

Appendix E

$$E_0 = \frac{1}{8(c_D^2 - 1)} \left[\frac{3}{4} \left(23 + \frac{3}{2} (13c_D^2) \right) + \frac{c_D^2 - 32}{c_D^2 - 1} \right], \quad (\text{E.1a})$$

$$E_1 = 4c_D^2 + (1 + \lambda c_F^2) \left[1 - \frac{1}{c_D^2 - 1} \left(\frac{1}{2} + \frac{1}{c_D^2} \right) \right] + \frac{2c_D^2}{c_O} \left(1 - \frac{\sqrt{\lambda}}{c_D} \Gamma_+ \right) + \frac{c_D^2}{c_D^2 - 1} (7 + 3\lambda), \quad (\text{E.1b})$$

$$E_2 = (c_D \lambda)^2 \left[1 - \frac{\varepsilon \lambda}{2c_D^2 (c_D^2 - 1)} \right]^2. \quad (\text{E.1c})$$

In (E.1b) $c_F = \sqrt{c_D^2 + \varepsilon}$, where $V_D = c_F V_R$ is dilatational wave speed in classical thermoelasticity; see, e.g., [Brock 2009].

References

[Achenbach 1976] J. D. Achenbach, *Wave propagation in elastic solids*, vol. 16, North-Holland Series in Applied Mathematics and Mechanics, North-Holland, Amsterdam, 1976.

- [Achenbach and Brock 1973] J. D. Achenbach and L. M. Brock, “On quasistatic and dynamic fracture”, pp. 529–541 in *Proceedings of an international conference on Dynamic Crack Propagation*, edited by G. C. Sih, Springer, Dordrecht, 1973.
- [Barber 1992] J. R. Barber, *Elasticity*, vol. 12, Solid Mechanics and its Applications, Kluwer, Dordrecht, 1992.
- [Boley and Weiner 1960] B. A. Boley and J. H. Weiner, *Theory of thermal stresses*, Wiley, New York, 1960.
- [Brock 2009] L. M. Brock, “Basic problems of coupled thermoelasticity with thermal relaxation and pre-stress: aspects observed in exact and asymptotic solutions”, *J. Therm. Stresses* **32**:6-7 (2009), 593–622.
- [Brock 2012] L. M. Brock, “Two cases of rapid contact on an elastic half-space: sliding ellipsoidal die, rolling sphere”, *J. Mech. Mater. Struct.* **7**:5 (2012), 469–483.
- [Brock 2017] L. M. Brock, “Transient analysis of fracture initiation in a coupled thermoelastic solid”, *J. Mech. Mater. Struct.* **12**:5 (2017), 667–688.
- [Brock and Achenbach 1973] L. M. Brock and J. D. Achenbach, “Extension of an interface flaw under the influence of transient waves”, *Int. J. Solids Struct.* **9**:1 (1973), 53–68.
- [de Boer et al. 1988] F. R. de Boer, W. C. M. Mattens, R. Boom, A. R. Miedema, and A. K. Niessen, *Cohesion in metals*, North-Holland, Amsterdam, 1988.
- [Freund 1972] L. B. Freund, “Energy flux into the tip of an extending crack in an elastic solid”, *J. Elasticity* **2**:4 (1972), 341–349.
- [Freund 1990] L. B. Freund, *Dynamic fracture mechanics*, Cambridge Monographs on Mechanics, Cambridge University Press, Cambridge, 1990.
- [Gdoutos 1993] E. E. Gdoutos, *Fracture mechanics: an introduction*, vol. 14, Solid Mechanics and its Applications, Kluwer, Dordrecht, 1993.
- [Ignaczak and Ostoja-Starzewski 2010] J. Ignaczak and M. Ostoja-Starzewski, *Thermoelasticity with finite wave speeds*, Oxford University Press, 2010.
- [Lord and Shulman 1967] H. W. Lord and Y. Shulman, “A generalized dynamical theory of thermoelasticity”, *J. Mech. Phys. Solids* **15**:5 (1967), 299–309.
- [Morse and Feshbach 1953] P. M. Morse and H. Feshbach, *Methods of theoretical physics*, McGraw-Hill, New York, 1953.
- [Skriver and Rosengaard 1992] H. L. Skriver and N. M. Rosengaard, “Surface energy and work function of elemental metals”, *Phys. Rev. B* **46**:11 (1992), 7157–7168.
- [Sneddon 1972] I. N. Sneddon, *The use of integral transforms*, McGraw-Hill, New York, 1972.

Received 28 Jan 2019. Revised 5 May 2019. Accepted 11 May 2019.

LOUIS M. BROCK: louis.brock@uky.edu

Department of Mechanical Engineering, University of Kentucky, 151 Ralph G. Anderson Building, Lexington, KY 40506-0503, United States

DEVELOPMENT OF FRACTURE MECHANICS MODEL OF BEAM RETROFITTED WITH CFRP PLATE SUBJECTED TO CYCLIC LOADING

SHAHRIAR SHAHBAZPANAHI AND HUNAR FARID HAMA ALI

A new finite element model was proposed to simulate a concrete beam retrofitted by carbon fiber reinforced polymer (CFRP) composite under cyclic loading. A link element was introduced as interface element to model crack propagation based on the cohesive law in the concrete material. Then the mass and the damping matrix of the link element were defined. A bar element was implemented to simulate the CFRP and then the energy release rates was determined. The load-displacement of the beam was compared with the existing experimental test data and conventional fracture mechanics models carried out using ABAQUS software. The load-displacement curves found by the proposed model were in reasonable agreement with the results of existing experimental data (5.4%–7.6% difference) while conventional fracture mechanics models carried out by the software ABAQUS showed a greater difference (15.2%–24% difference) when compared to the previous experimental tests.

1. Introduction

Fracture mechanics theory is considered to be a more accurate method for predicting crack growth, because this method is similar to the physical reality of crack propagation [Shi 2009]. Two methods are now available for fracture analysis in concrete structures. These can be broadly categorized into linear and nonlinear fracture mechanics. For the first time, linear fracture mechanics was implemented to investigate the crack growth in warships [Esfahani 2007]. In this method, a constant factor was used on the stress around the real crack [Shahbazpanahi 2017]. This constant factor was known as the intensity factor of the stress. The linear fracture mechanics of this theory create stress-singularity in the real crack. Studies such as [Raghu and Renuka 2007; Wu et al. 2011; Pietruszczak and Haghighat 2015], have used linear fracture mechanics to study crack growth. Kaplan [1961] demonstrated that linear fracture mechanics was not able to analyze the crack propagation of concrete beams with normal size [Shi et al. 2001]. Therefore, Hillerborg et al. [1976] presented the crack propagation method on the concrete beam according to nonlinear fracture mechanics. This investigation introduced the fracture region in front of real crack [Fischer and Bohse 2014]. This large and variable region was known as the fracture process zone (FPZ). This zone has the ability to transfer stresses [Shahbazpanahi et al. 2015]. Hence, a study on the role of the FPZ is indispensable for predicting and preventing crack propagation under static loading [Tryding and Ristinmaa 2017]. Although more techniques of the crack propagation have been developed in fracture mechanics, crack modeling for predicting the behavior of concrete structures is still far from satisfactory. Fracture mechanics has been used to simulate crack propagation in the concrete material with softening behavior [Kirane and Bažant 2015; Dong et al. 2016]. Griffith theory can be implemented to

Keywords: ABAQUS, beam, cyclic loading, cohesive, CFRP, propagation.

evaluate the crack growth criterion in the FPZ [Shahbazpanahi 2017]. This theory explains that the energy release rate must be bigger than the critical fracture energy to grow the crack [Ouzaa and Benmansour 2014; Biscaia et al. 2013a]. Based on Griffith theory, for the first time, a cohesive model was suggested to model the FPZ in [Hillerborg et al. 1976]. In the suggested model in [Hillerborg et al. 1976], the stress at the tip of the crack reaches the tensile strength [Dong et al. 2017]. The total area of the stress-opening of the crack is the critical fracture energy. This model was implemented to simulate the crack propagation in normal-size structures. The cohesive model was used in [Dugdale 1960] to study crack propagation in brittle material and by using this method, mesh sensitivity was reduced. Many investigations have been done to improve the cohesive model. The model proposed in [Hillerborg et al. 1976] has been usually implemented because of its practicality and economic considerations [Palmieri and Lorenzis 2014]. Discrete cohesive zone model (DCZM) is one of the most used elements for simulating the cohesive zone. The DCZM was used in some investigations in the review because this model was well-matched with the finite element method [Xie and Waas 2006; Xu et al. 2011; Simon and Kishen 2017]. Also, one of the methods for the crack propagation modeling in the DCZM was the modified crack closure integral method. It can be calculated by the virtual crack closure technique (VCCT). This technique calculates the energy used for closing the crack by multiplying the nodal force and displacement opening. This method is computationally inexpensive and provided satisfactory results [Xie et al. 2006; Xie and Biggers Jr. 2006].

Furthermore, carbon fiber reinforced plastic (CFRP) plate can be used in flexure to prevent flexural crack of a reinforced concrete (RC) beam. Modeling of CFRP retrofitted beams under cyclic loading and investigating of the effect of CFRP plate on the crack propagation criterion in the concrete material is important. Hence, it is necessary to introduce a numerical model to predict the crack propagation of CFRP retrofitted beams under cyclic loading.

A large number of studies on structural behavior of CFRP-strengthened RC beams have recently been reported [Bruno et al. 2013; Carloni and Subramaniam 2013; Abbass et al. 2014; Martinelli and Caggiano 2014; Aravind et al. 2015; Baji et al. 2015]. Many numerical models have been developed for structural analyses of CFRP-strengthened RC beams [Pan and Wu 2014; Zheng et al. 2015; Bruno et al. 2017]. However, most of them are about the analysis of the structural behavior under static loading or the bond-slip of the CFRP. The effects of the CFRP retrofitting on the flexural crack growth criterion under dynamic loading have not been studied based on the literature review.

This paper deals with the accurate stiffness, new mass and damping matrix of the interface element to model the FPZ, material model of the concrete, material model the CFRP plate and new the crack propagation criterion of the flexural-retrofitted RC beam. To obtain the energy release rates in the concrete material, the link element was used. Then, mass and damping matrix of the link element was defined. A bar element was implemented to simulate the CFRP and then the energy dissipation rate by the CFRP was computed. The comparison of the results obtained by proposed model and the available experimental test data were discussed.

2. Methods and materials

In the proposed model, a link elements boundary was used to model crack propagation. The link element defends the softening behavior of the stress-opening of the crack in the submaterial.

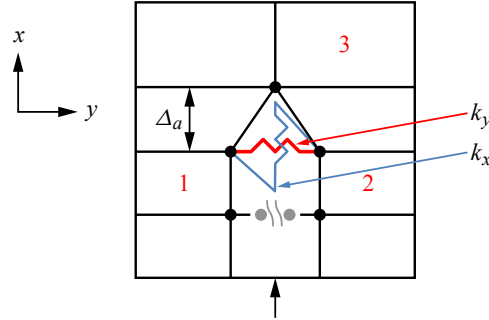


Figure 1. Spring interface element between two nodes.

2.1. Interface element. A nonlinear link is located between two nodes (Figure 1). These nodes are placed in front of crack to model the FPZ. At the beginning of the analysis, the coordinates of joints 1 and 2 are same. The stiffness matrix of the interface element is

$$K = \begin{bmatrix} k_x & 0 & -k_x & 0 \\ 0 & k_y & 0 & -k_y \\ -k_x & 0 & k_x & 0 \\ 0 & -k_y & 0 & k_y \end{bmatrix}, \quad (1)$$

where k_x is normal and k_y is shear stiffness values. In the proposed model, the k_x is obtained from the stress versus crack opening of the concrete material. In this study, k_x and k_y , obtained in [Shahbazpanahi et al. 2012], were used to model the crack softening behavior of subconcrete. The variation of the length of the FPZ was considered to predict the crack propagations.

2.2. Mass matrix and damping matrix in the concrete. Cracks require special modeling if subjected to repeated loading. In the proposed model, the prediction of crack propagation was modeled as subjected to cyclic loading. An improved damping matrix was developed based on the correct stiffness matrix. This damping matrix improves the prediction of the crack propagation subjected to cyclic loading and is more accurate than other existing models. In this study, the mass matrix, M_1 , of the interface element to model crack propagation in concrete is given by

$$M_1 = \frac{1}{2} \rho_1 w_c \begin{bmatrix} 1 & 0 & 0 & 0 \\ 0 & 1 & 0 & 0 \\ 0 & 0 & 1 & 0 \\ 0 & 0 & 0 & 1 \end{bmatrix}, \quad (2)$$

where ρ_1 is mass density of concrete. The Rayleigh damping matrix in concrete, C_1 , is a linear combination of the mass and stiffness matrices, that is,

$$C_1 = \alpha_1 M_1 + \beta_1 K, \quad (3)$$

where α_1 and β_1 are the damping coefficients. These damping coefficients are calculated automatically from modal analysis with initial stiffness by FEAPpv program.

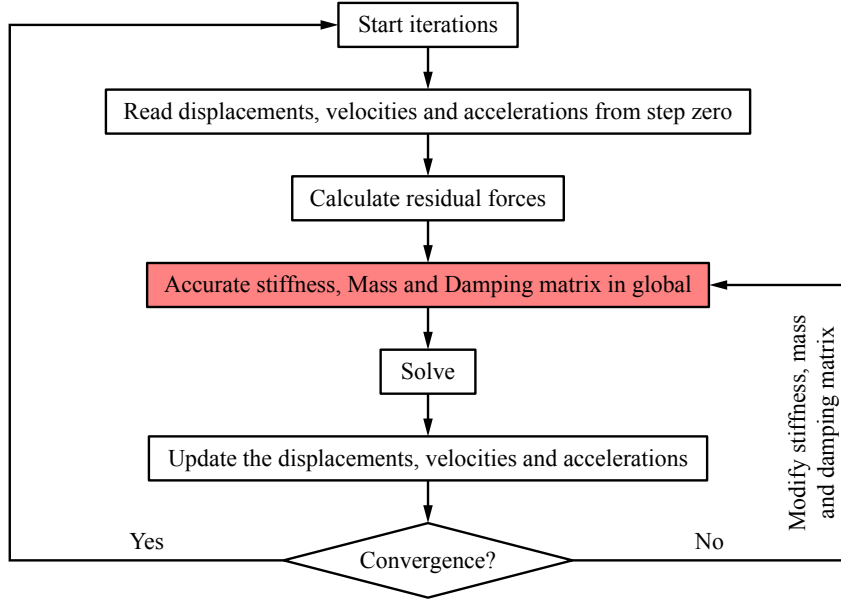


Figure 2. The Newmark's flowchart at each time step.

FEAPpv (Finite Element Analysis Program, Personal Version) was designed for research use [Taylor 2009]. A problem is solved by using a command language concept in FEAPpv. In this program, the solution algorithm is written by the user. Therefore, each user may define a solution strategy that meets specific needs. The system includes sufficient commands that can be used for applications in structural or fluid mechanics, heat transfer, and other areas that require solutions modeled by differential equations, including those for steady-state and transient problems. Users may also add new features for model description and command language statements to meet specific application requirements.

2.3. Time integration. The global equation system is

$$\mathbf{M}\ddot{\mathbf{U}}_t + \mathbf{C}\dot{\mathbf{U}}_t + \mathbf{K}\mathbf{U}_t = \mathbf{F}_t, \quad (4)$$

where \mathbf{M} , \mathbf{K} and \mathbf{C} are the assembled as global mass, stiffness and damping matrices, \mathbf{F}_t is the global load vector, \mathbf{U}_t , $\dot{\mathbf{U}}_t$ and $\ddot{\mathbf{U}}_t$ are the global nodal displacement, nodal velocity and nodal acceleration vectors, respectively. Equation (4) can be solved using standard time integration algorithms. The Newmark method was used in this study to solve dynamic equation. Figure 2 shows the Newmark's flowchart at each time step to solve the dynamic equation.

2.4. Energy release rate in the concrete material. To describe the crack propagation criterion in the fracture process at the crack tip, Griffith energy approach can be used. This approach states that the energy release rate, which is required to form the crack, must be sufficiently larger than the critical fracture energy. The energy release rate is defined as the amount of energy stored in the FPZ [Lee et al. 2010]. Hence, to study the crack state, the crack propagation criterion can be defined in terms of the energy release rate.

Strain energy release rate for the mixed-mode in the concrete was assumed to be the same as Mode I magnitude [Bocca et al. 1991]. Strain energy release rate for Mode I, due to this force, based on VCCT, is

$$G_I = \frac{k_x(u_1 - u_3)^2}{2B\Delta_a}, \quad (5)$$

where Δ_a is mesh size and B is the thickness of the beam. The equation (5) can be applied for mixed-mode and multiple-crack fracture problems. A single-active crack mode strategy following [Shi 2009] is used to simulate multiple cracks. The DCZM element depends on the coordinates of the nodes [Xie and Waas 2006]. Also, u_1 , u_3 and Δ_a depend on the mesh size, however k_x is a material property and it is independent of mesh size. In the results section, mesh-size sensitivity will be done to investigate how results obtained from (5) are mesh-size dependent.

During cyclic loading, the stiffness of concrete was degraded. To determine effective stiffness of concrete under cyclic loading, the stiffness of concrete was proposed as

$$k_N = \left(1 - 0.33 \frac{N}{N_f}\right) k_x, \quad (6)$$

where k_N is the effective stiffness of concrete at N cycles. N_f is the number of loading cycles to failure [Li et al. 2017] and the strain energy release rate at N cycles is

$$G_{I_N} = \frac{k_N(u_1 - u_3)^2}{2B\Delta_a}. \quad (7)$$

2.5. The CFRP effect on flexural crack propagation. The CFRP effect on a flexural crack in the concrete is necessary to prevent growth and improve load bearing. A numerical model based on nonlinear fracture mechanics should be developed to obtain the mechanical response of the CFRP on the FPZ. Let us consider a CFRP reinforced RC beam (see Figure 3). The use of CFRP will increase the rate of energy dissipation and the toughness of concrete structures [Wu and Bailey 2005]. The amount of energy dissipated in the system can be determined by calculating the change in the potential energy of the system. When reloading is applied, the energy dissipation rate of flexural-strengthened members by CFRP is

$$R = \frac{E_F(u_8 - u_{10})(u_{12} - u_{14})}{2b_f L'}, \quad (8)$$

where E_F is the Young's modulus of CFRP, b_f is the width of the CFRP, and u_8 and u_{10} are the displacements in the x direction for nodes 4 and 5, respectively (Figure 3), and u_{12} and u_{14} are the displacements in the x direction for nodes 6 and 7, respectively. L' is the length variation of crack propagation.

Equation (8) is used to estimate the effect of the CFRP as the crack propagates in the concrete beam. This relationship shows that, when the FPZ length increases and the crack opening in concrete is small, the effect of the CFRP on preventing crack propagation is relatively small. Finally, as the FPZ length reaches a constant value and the crack opening increases, the role of the CFRP in resisting crack growth increases. So far, no model has presented a convincing equation for estimating the effect of the CFRP on crack propagation. Given that the CFRP is not located in the crack tip, the rate of energy dissipation due to the moment of the couple caused by the CFRP force is ignored. The energy criterion of crack

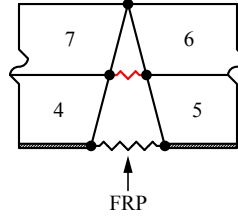


Figure 3. Modeling of flexural strengthened members by CFRP.

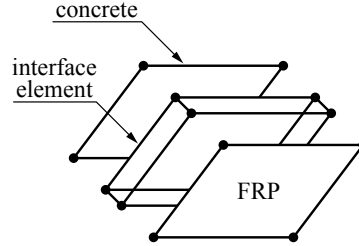


Figure 4. Interface element for modeling bond slip of CFRP.

propagation can be expressed as

$$G_{IN} - R > G_C. \quad (9)$$

Here, R and G_{IN} are based on the size of the mesh. These equations are adopted with the assumption that behavior outside FPZ is linearly elastic. Energy release rate is used to manage convergence in a nonlinear process to a fixed solution. It is assumed that in unloading paths, the effect of the FRP on unloading stiffness is less important and ignored.

2.6. Interface of CFRP bond-slip. Many researchers proposed constitutive models to simulate the bond behavior between an FRP and concrete [Ferracuti et al. 2007; Ko and Sato 2007; Biscaia et al. 2013b]. In this study, a constitutive model was used in [Nakaba et al. 2001]. Figure 4 shows the eight-node interface element for transferring shear in nodal forces between four-node isoparametric quadrilateral element concrete and CFRP elements. In the present study, stress-slip is defined by (10), as used by Nakaba et al.:

$$\frac{\tau}{\tau_{\max}} = \frac{s}{s_{\max}} \cdot \frac{n}{(n+1) + (s/s_{\max})^n}, \quad (10)$$

where τ and s are bond stress and slip between concrete and CFRP, respectively, τ_{\max} is maximum shear stress, s_{\max} is the slip at maximum shear stress and n is a constant.

Two-dimensional plane stress finite elements are applied to analyze crack propagation. The CFRP behavior is elastic but elastic-perfect plastic is considered to model the behavior of steel bars. Four-node isoparametric elements are used for bulk concrete with linear elastic and isotropic behavior. The bar elements are employed to simulate CFRP and longitudinal steel.

material	specifications (mm)	modulus of elasticity (MPa)	compressive strength (MPa)	yield point (MPa)	ultimate tensile strain
concrete	$h = 200, b = 100$	29.45	40.0	–	–
steel	bar dia. = 2×12 mm	$2 \cdot 10^5$	–	415	–
CFRP	$t = 0.13$	$2.40 \cdot 10^5$	–	–	0.00152

Table 1. Material properties of the beam tested in [Kesavan et al. 2013].

3. Results and discussion

In this study, two CFRP-strengthened RC beams are modeled and discussed. The first example is the beam as tested in [Kesavan et al. 2013]. A four-point bending concrete beam strengthened with the CFRP plate on tension face under cyclic loading from that paper was modeled to verify our proposed numerical model. The thickness and width of the CFRP plates were 0.13 mm and 50 mm, respectively. The experimental test results have shown that failure was observed with the debonding of the CFRP plate, and also the model showed that CFRP plate debonding occurred. The CFRP plate increased the bearing capacity by 23% in the proposed model. The material properties of the beam tested in [Kesavan et al. 2013] are summarized in Table 1.

Also, to validate the proposed model, three-dimensional finite element modeling of beams by ABAQUS software was employed. Software, such as ABAQUS, applies linear fracture mechanics to model crack propagation. The proposed model can be compared to the conventional CZM approach used in analysis software such as the FEA software ABAQUS. The beam was modeled by ABAQUS software with 3469 C3D8R elements. An isometric view of the model, cross section of the beam, is shown in Figure 5. The CFRP plate was also set at specific positions to strengthen the beam as shown in Figure 6.

Figure 7 compares the load versus deflection for a beam subjected to cyclic loading obtained by the proposed model, ABAQUS software data and with the results of experimental data in [Kesavan et al. 2013]. Results from the proposed model are in good agreement with those of Kesavan et al. It can be observed that failure load in the proposed model was predicted within 5.4%–7.6% of the experimental data. It can be seen that the push of the curve by the proposed model were similar to the experimental data. However, the push of the curve by the ABAQUS software overestimated the experimental results.

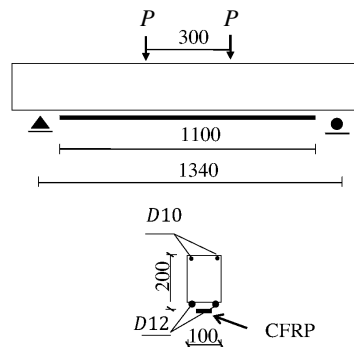


Figure 5. Details and dimensions of the beam strengthened with the CFRP plate tested [Kesavan et al. 2013].

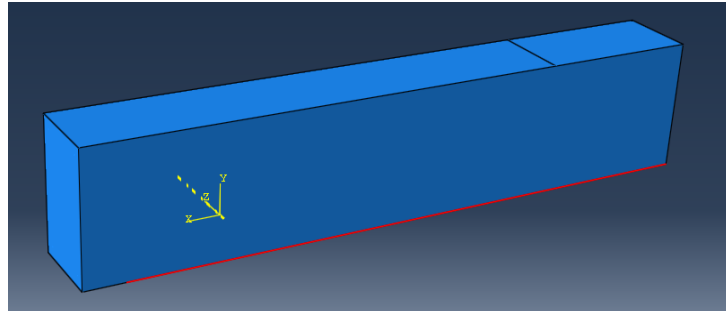


Figure 6. The beam modeled by ABAQUS software.

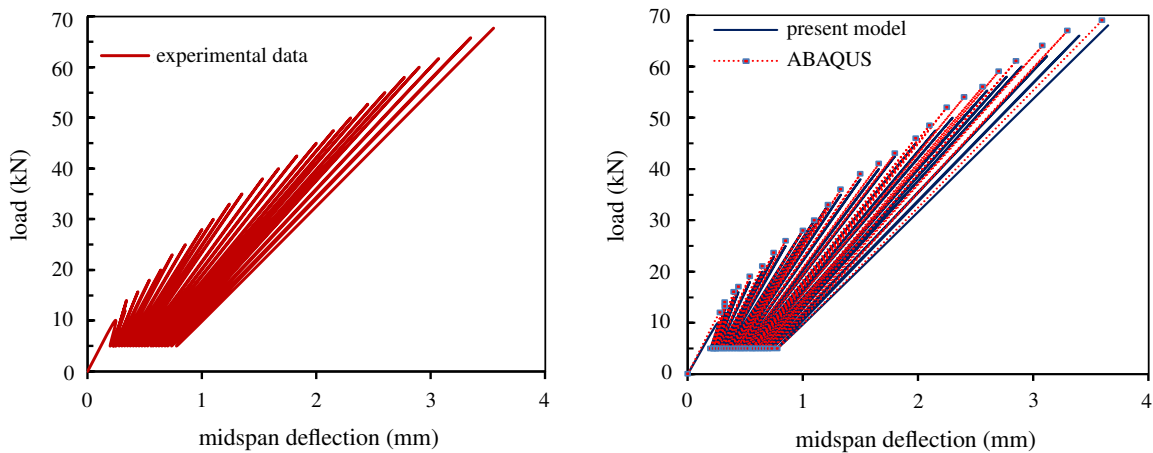


Figure 7. Load-deflection curve: experimental data in [Kesavan et al. 2013] (left) and proposed model and ABAQUS software data (right).

ABAQUS software data shows a greater margin of difference (15.2%–24%) compared to experimental data from [Kesavan et al. 2013].

Figure 8 illustrates the crack pattern of the beam, as modeled. As shown in Figure 8 (left), the flexural

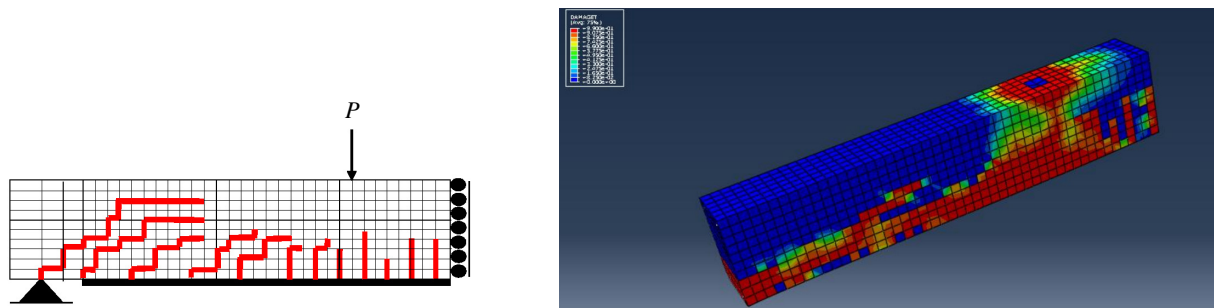


Figure 8. Crack patterns of the beam predicted by the proposed model (left) and ABAQUS (right).

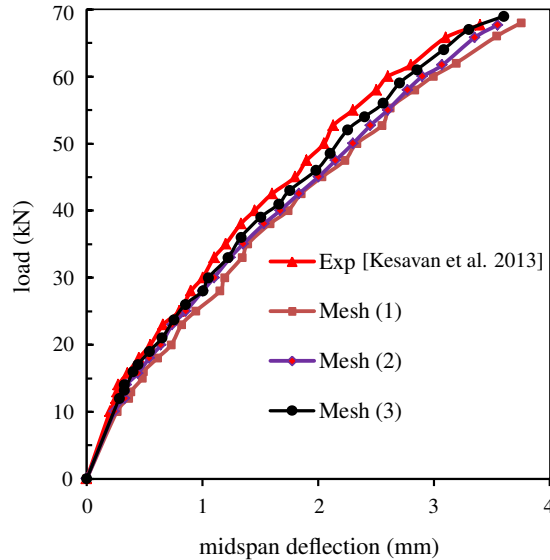


Figure 9. Comparisons pushover of load-deflection between three different meshes.

cracks have not propagated into the upper half of the beam. The proposed model predicted five flexural cracks and five flexural-shear cracks. Within the shear span, the proposed model predicted five flexural-shear cracks compared with two flexural-shear cracks observed in the ABAQUS simulation. However, the flexural-shear cracks intersected together in the ABAQUS software. The number of shear cracks is two in the proposed model compared with one shear crack predicted using ABAQUS. In both cases, shear cracks propagated in the upper half of the beam depth. In the ABAQUS simulation, the real crack is shown in red lines, while the FPZ propagation elements are displayed in green color. It should be noted that the crack path is smooth, but the crack path is illustrated by unconventional lines in this study. In the ABAQUS software, the degradation of the damage is characterized by damage variables from 0 to 0.1. If tensile damage obtained from the software is greater than 0.1, damage occurred. The results from Figure 8 (left) showed that the maximum value of the tensile damage parameter is $0.407 > 0.1$. Therefore, the tensile damage occurred along the red lines as shown in Figure 8 (right). The test showed that failure occurred with the debonding of CFRP plate. However, the model showed that CFRP plate debonding occurs at failure load.

Figure 9 shows the pushover of the load—the midspan deflection with different mesh to study mesh-size sensitivity and to check (5). Mesh 1 had 955 elements (element average size is $18 \text{ mm} \times 16 \text{ mm}$, with a finer mesh of $14 \text{ mm} \times 10 \text{ mm}$). Mesh 2 had 1,344 elements (element average size is $14 \text{ mm} \times 12 \text{ mm}$, with a finer mesh of $12 \text{ mm} \times 8 \text{ mm}$). Mesh 3 had 1,862 elements (element average size is $12 \text{ mm} \times 8 \text{ mm}$, with a finer mesh of $10 \text{ mm} \times 8 \text{ mm}$). The approximate matching of the three curves demonstrates the independence of the model from mesh size and shows that the model exhibited fast convergence. The results in mesh 3 were close to the experimental result (up to 95%).

Another example is a full-scale simply supported beam with four-point load strengthened by the CFRP plate which was tested in [Heffernan and Erki 2004]. A CFRP-strengthened RC beam under a cyclic load as in that article is modeled by using the proposed model. The details of reinforcement

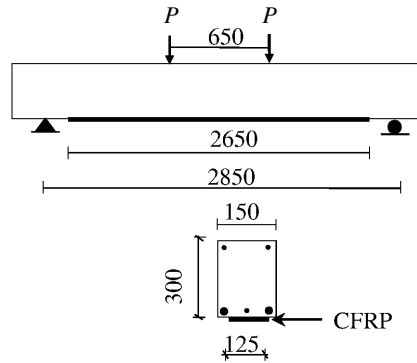


Figure 10. Details of the beam strengthened with the CFRP plate tested in [Heffernan and Erki 2004].

and dimensions of the beam are illustrated in Figure 10. The beam has three longitudinal steel rods of diameter 25.2 mm in tensile side and the compressive side of the RC beam consists of two longitudinal rods of diameter 11.3 mm. The beam span length and width are 2850 mm and 300 mm, respectively. The material properties of this beam are summarized in Table 2.

The critical strain energy for Mode I in concrete and the elastic opening are $0.07 \text{ N} \cdot \text{mm}^{-1}$ and 0.077 mm, respectively. The maximum shear stress between the concrete and the CFRP, and the maximum slip are 5.95 MPa and 0.044 mm, respectively.

The central deflection and number of loading cycles curves observed in the previous experimental test [Heffernan and Erki 2004], the proposed model and the ABAQUS software for the beam strengthened by CFRP are shown in Figure 11. The results of the proposed model are close to that of the experimental results. This finding indicates that the proposed model is validated by the test results. The yield point of the curve in the proposed model is similar to its counterpart in the experimental test results (8%–11% difference). However, this point obtained in the simulations by ABAQUS software is higher than that in the experimental test results (18%–21% difference). The accuracy of the proposed model is also confirmed by the close value of the failure load obtained from the proposed model and the experimental test. The difference in load failure of the beam strengthened by CFRP is 8.4%. Compared with the experimental test, the difference of load failure as analyzed by the ABAQUS software is over-predicted (18%–25% difference).

Figure 12 (left) illustrates an initial mesh and crack paths for the beam by the proposed model at the failure load. The crack pattern predicted by ABAQUS is shown in Figure 12 (right). It can be observed from Figure 12 (left) that five flexural cracks occur at midspan perpendicular to the axis in the beam

material	specifications (mm)	modulus of elasticity (MPa)	compressive strength (MPa)	yield point (MPa)	ultimate tensile strain
concrete	$h = 300, b = 150$	29.45	37.0	–	–
steel	area = 700 mm^2	$2 \cdot 10^5$	–	400	–
CFRP	area = 89.4 mm^2	$2.33 \cdot 10^5$	–	–	0.00175

Table 2. Material properties of the beam tested in [Heffernan and Erki 2004].

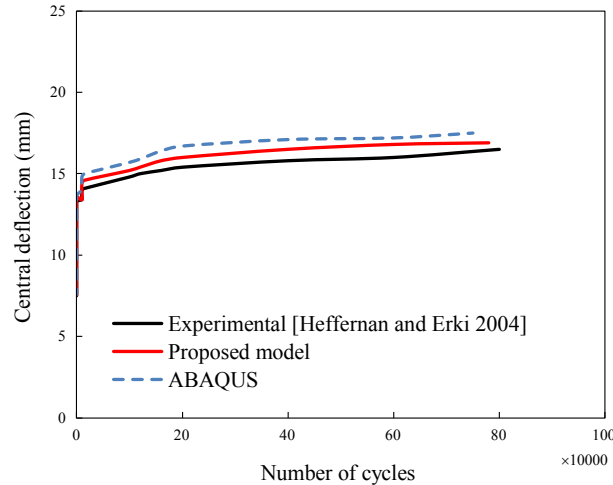


Figure 11. Comparing results for the CFRP-strengthened beam.

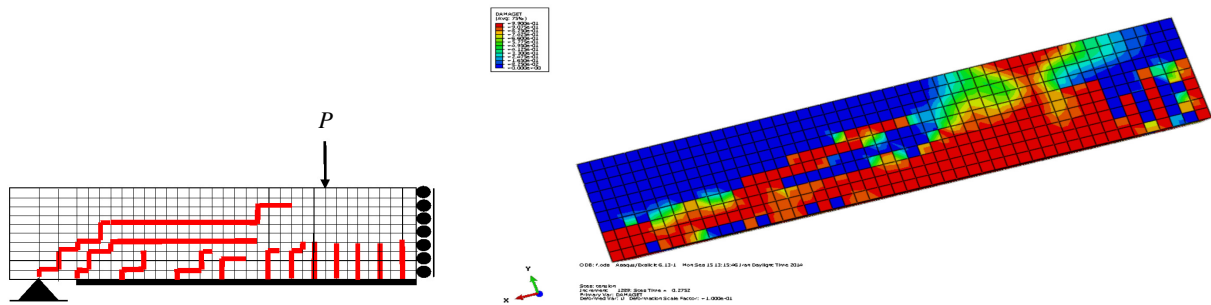


Figure 12. Crack patterns of the beam predicted by the proposed model (left) and ABAQUS (right).

strengthened by CFRP. It is interesting to observe that the crack propagation is controlled by the CFRP plate before into the upper half of the beam. There are five flexural-shear cracks in the shear span of the beam. The two main diagonal shear cracks are formed at the support in the beam. This finding may be compared with the predicted results by ABAQUS software results that only a shear crack was observed in the vicinity of the support shown in Figure 12 (right). The shear cracks grew directly which are followed by a slowly inclining slope towards the loading point. In both the proposed model and ABAQUS software results, there are two shear cracks as shown in Figures 12 (left) and 12 (right), respectively. Crack length was 9.7 mm at 40 kN load in the vicinity of the midspan and 162.7 mm at 120 kN load. Shear cracks started at approximately 180 kN load at the support and expanded upward as load increased.

Based on the proposed model, the effect of CFRP length on the flexural crack propagation is studied. The finding from this parametric study can be used for efficient design of RC beam strengthened by CFRP plate under cyclic loading. The program computed the changing length of CFRP plate while other parameters remained unchanged. Varying lengths of CFRP are 2450 mm, 2550 mm, 2650 mm, 2750 mm and 2850 mm (equal to length of the beam). The influence of the varying lengths of CFRP on the biggest

flexural crack length is shown in Figure 13. As expected, the load capacity increases with the increase length of CFRP plate. It is found that the flexural crack length of the beam strengthened with CFRP decreases with the increase in length of CFRP at the same load. For 2450 mm and 2550 mm lengths of CFRP plate, the crack propagates to the half of the beam while the crack propagation arrests in the beam strengthened by 2650 mm, 2750 mm and 2850 mm lengths. It can be seen that after the crack propagated at a certain point, the load capacity is climbed for 2650 mm, 2750 mm and 2850 mm lengths of CFRP plate. This phenomenon may be due to increase of the slip when the length of CFRP plates increase.

4. Conclusion

A new finite element model was proposed to simulate concrete beam retrofitted by CFRP composite under cyclic loading. A link element was introduced as interface element to model crack propagation based on the cohesive law in the concrete material. Then the mass and the damping matrix of the link element were defined. A bar element was implemented to simulate the CFRP and then the energy release rates was determined. The load-displacement of the beam were compared with the existing experimental test data and conventional fracture mechanics models based on linear fracture mechanics carried out using ABAQUS software. It was observed that the results from the proposed model are in good agreement with the results of previous experimental data (5.4%–7.6% difference). The ABAQUS software data shows a greater difference (15.2%–24% difference) compared to previous experimental test data. The results of the proposed model are close to that of the previous experimental results. This finding indicates that the proposed model was validated by the test results. The yield point of the curve in the proposed model was similar to its counterpart in the experimental test results (8% to 11% difference). However, this point obtained in the simulations by ABAQUS software was higher than that in the experimental test results (18% to 21% difference). The accuracy of the proposed model was also confirmed by the close value of the failure load obtained from the proposed model and the experimental test. The differences of beam with strengthened by CFRP are 8.4% in terms of load failure. Comparing with experimental test, the

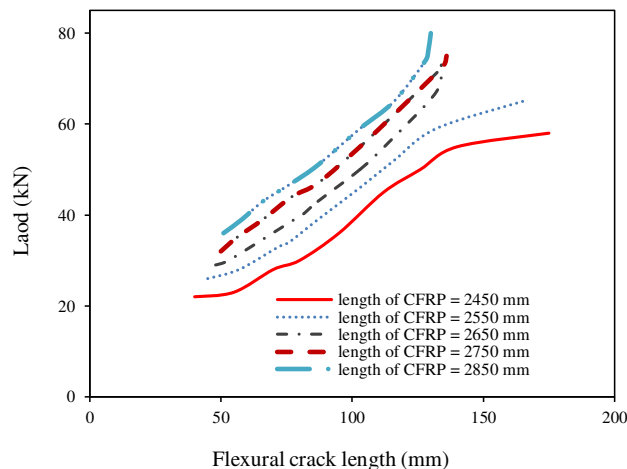


Figure 13. Load vs. largest flexural crack length with different lengths of CFRP plates.

differences of load failure as analyzed via ABAQUS was over-predicted (18% to 25% difference). As expected, the load capacity increases with the increase length of CFRP plate. It is interesting to observe that the crack propagation was controlled with CFRP plate before into the upper half of the beam. In one of the beams, there were five flexural-shear cracks in the shear span of the beam. The two main diagonal shear cracks were formed at the support in the beam. This finding may be compared with the predicted results by ABAQUS software results that only a shear crack was observed in the vicinity of the support. Also, it was found that the flexural crack length of the beam strengthened with CFRP decreases with the increase in length of CFRP at the same load. The mesh-size sensitive analysis demonstrates that the model is independent on mesh size and shows that the model exhibited fast convergence.

References

- [Abbass et al. 2014] M. M. Abbass, V. Matsagar, and A. K. Nagpal, "Bond-slip response of FRP sheets or plates bonded to reinforced concrete beam under dynamic loading", pp. 1959–1969 in *Advances in Structural Engineering*, edited by V. Matsagar, Springer, New Delhi, 2014.
- [Aravind et al. 2015] N. Aravind, A. K. Samanta, D. K. S. Roy, and J. V. Thanikal, "Flexural strengthening of reinforced concrete (RC) beams retrofitted with corrugated glass fiber reinforced polymer (GFRP) laminates", *Curved Layered Struct.* **2**:1 (2015), 244–253.
- [Baji et al. 2015] H. Baji, A. Eslami, and H. R. Ronagh, "Development of a nonlinear FE modelling approach for FRP-strengthened RC beam-column connections", *Structures* **3** (2015), 272–281.
- [Biscaia et al. 2013a] H. C. Biscaia, C. Chastre, and M. A. G. Silva, "Linear and nonlinear analysis of bond-slip models for interfaces between FRP composites and concrete", *Compos. B Eng.* **45**:1 (2013), 1554–1568.
- [Biscaia et al. 2013b] H. C. Biscaia, C. Chastre, and M. A. G. Silva, "Nonlinear numerical analysis of the debonding failure process of FRP-to-concrete interfaces", *Compos. B Eng.* **50** (2013), 210–223.
- [Bocca et al. 1991] P. Bocca, A. Carpinteri, and S. Valente, "Mixed mode fracture of concrete", *Int. J. Solids Struct.* **27**:9 (1991), 1139–1153.
- [Bruno et al. 2013] D. Bruno, F. Greco, and P. Lonetti, "A fracture-ALE formulation to predict dynamic debonding in FRP strengthened concrete beams", *Compos. B Eng.* **46** (2013), 46–60.
- [Bruno et al. 2017] D. Bruno, F. Greco, S. L. Feudo, and P. N. Blasi, "Edge debonding prediction in beams strengthened by FRP composite plates", pp. 105–124 in *Models, simulation, and experimental issues in structural mechanics*, edited by M. Frémond et al., Springer Series in Solid and Structural Mechanics **8**, Springer, 2017.
- [Carloni and Subramaniam 2013] C. Carloni and K. V. Subramaniam, "Investigation of sub-critical fatigue crack growth in FRP/concrete cohesive interface using digital image analysis", *Compos. B Eng.* **51** (2013), 35–43.
- [Dong et al. 2016] W. Dong, D. Yang, X. Zhou, G. Kastiukas, and B. Zhang, "Experimental and numerical investigations on fracture process zone of rock-concrete interface", *Fatigue Fract. Eng. Mater. Struct.* **40**:5 (2016), 820–835.
- [Dong et al. 2017] W. Dong, Z. Wu, X. Zhou, L. Dong, and G. Kastiukas, "FPZ evolution of mixed mode fracture in concrete: experimental and numerical", *Eng. Failure Analysis* **75** (2017), 54–70.
- [Dugdale 1960] D. S. Dugdale, "Yielding of steel sheets containing slits", *J. Mech. Phys. Solids* **8**:2 (1960), 100–104.
- [Esfahani 2007] M. R. Esfahani, *Fracture mechanics of concrete*, Tehran Polytechnic press, Tehran, 2007.
- [Ferracuti et al. 2007] B. Ferracuti, M. Savoia, and C. Mazzotti, "Interface law for FRP-concrete delamination", *Compos. Struct.* **80**:4 (2007), 523–531.
- [Fischer and Bohse 2014] G. Fischer and J. Bohse, "Observation and analysis of fracture processes in concrete with acoustic emission (AE) and digital image correlation (DIC)", pp. 1–8 in *31st Conference of the European Working Group on Acoustic Emission* (Dresden, Germany), 2014.
- [Heffernan and Erki 2004] P. J. Heffernan and M. A. Erki, "Fatigue behavior of reinforced concrete beams strengthened with carbon fiber reinforced plastic laminates", *J. Compos. Constr. (ASCE)* **8**:2 (2004), 132–140.

- [Hillerborg et al. 1976] A. Hillerborg, M. Mod  er, and P.-E. Petersson, "Analysis of crack formation and crack growth in concrete by means of fracture mechanics and finite elements", *Cem. Concr. Res.* **6**:6 (1976), 773–781.
- [Kaplan 1961] M. Kaplan, "Crack propagation and the fracture concrete", *ACI J.* **58**:11 (1961), 591–610.
- [Kesavan et al. 2013] K. Kesavan, K. Ravisankar, R. Senthil, and A. K. F. Ahmed, "Experimental studies on performance of reinforced concrete beam strengthened with CFRP under cyclic loading using FBG array", *Measurement* **46**:10 (2013), 3855–3862.
- [Kirane and Ba  ant 2015] K. Kirane and Z. P. Ba  ant, "Size effect in Paris law for quasibrittle materials analyzed by the microplane constitutive model M7", *Mech. Res. Commun.* **68** (2015), 60–64.
- [Ko and Sato 2007] H. Ko and Y. Sato, "Bond stress-slip relationship between FRP sheet and concrete under cyclic load", *J. Compos. Constr. (ASCE)* **11**:7 (2007), 419–426.
- [Lee et al. 2010] J. H. Lee, R. M. Chacko, and M. M. Lopez, "Use of mixed-mode fracture interfaces for the modeling of large-scale FRP-strengthened beams", *J. Compos. Constr. (ASCE)* **14**:6 (2010), 845–855.
- [Li et al. 2017] D. Li, P. Huang, X. Guo, X. Zheng, J. Lin, and Z. Chen, "Fatigue crack propagation behavior of RC beams strengthened with CFRP under cyclic bending loads", *Fatigue Fract. Eng. Mater. Struct.* **41**:1 (2017), 212–222.
- [Martinelli and Caggiano 2014] E. Martinelli and A. Caggiano, "A unified theoretical model for the monotonic and cyclic response of FRP strips glued to concrete", *Polymers* **6**:2 (2014), 370–381.
- [Nakaba et al. 2001] K. Nakaba, K. K., T. Furuta, and K. Yoshizawa, "Bond behavior between fiber-reinforced polymer laminates and concrete", *ACI Struct. J.* **98**:3 (2001), 359–367.
- [Ouzaa and Benmansour 2014] K. Ouzaa and M. B. Benmansour, "Cracks in continuously reinforced concrete pavement", *Arab. J. Sci. Eng.* **39**:12 (2014), 8593–8608.
- [Palmieri and Lorenzis 2014] V. Palmieri and L. D. Lorenzis, "Multiscale modeling of concrete and of the FRP-concrete interface", *Eng. Fract. Mech.* **131** (2014), 150–175.
- [Pan and Wu 2014] J. Pan and Y.-F. Wu, "Analytical modeling of bond behavior between FRP plate and concrete", *Compos. B Eng.* **61** (2014), 17–25.
- [Pietruszczak and Haghghat 2015] S. Pietruszczak and E. Haghghat, "Modeling of fracture propagation in concrete structures using a constitutive relation with embedded discontinuity", *Studia Geotechnica et Mechanica* **36**:4 (2015), 27–33.
- [Raghu and Renuka 2007] P. B. K. Raghu and D. M. V. Renuka, "Extension of FCM to plain concrete beams with vertical tortuous cracks", *Eng. Fract. Mech.* **74**:17 (2007), 2758–2769.
- [Shahbazpanahi 2017] S. Shahbazpanahi, "Mechanical analysis of a shear-cracked RC beam", *Acta Scientiarum. Technol.* **39**:3 (2017), 285–290.
- [Shahbazpanahi et al. 2012] S. Shahbazpanahi, A. A. A. Ali, F. N. Aznieta, and A. Kamgar, "A simple method to model crack propagation in concrete", *Constructii J.* **13**:1 (2012), 41–50.
- [Shahbazpanahi et al. 2015] S. Shahbazpanahi, A. A. A. Ali, A. Kamgar, and N. Farzadnia, "Fracture mechanic modeling of fiber reinforced polymer shear-strengthened reinforced concrete beam", *Compos. B Eng.* **68** (2015), 113–120.
- [Shi 2009] Z. Shi, *Crack analysis in structural concrete: theory and applications*, Butterworth-Heinemann, Burlington, USA, 2009.
- [Shi et al. 2001] Z. Shi, M. Ohtsu, M. Suzuki, and Y. Hibino, "Numerical analysis of multiple cracks in concrete using the discrete approach", *J. Struct. Eng. (ASCE)* **127**:9 (2001), 1085–1091.
- [Simon and Kishen 2017] K. M. Simon and J. M. C. Kishen, "A multiscale approach for modeling fatigue crack growth in concrete", *Int. J. Fatigue* **98** (2017), 1–13.
- [Taylor 2009] L. R. Taylor, *FEAPpv source: a finite element analysis program*, University of California, Berkeley, 2009.
- [Tryding and Ristinmaa 2017] J. Tryding and M. Ristinmaa, "Normalization of cohesive laws for quasi-brittle materials", *Eng. Fract. Mech.* **178** (2017), 333–345.
- [Wu and Bailey 2005] Z. J. Wu and C. G. Bailey, "Fracture resistance of a cracked concrete beam post-strengthened with FRP sheets", *Int. J. Fract.* **135** (2005), 35–49.
- [Wu et al. 2011] Z. Wu, H. Rong, J. Zheng, F. Xu, and W. Dong, "An experimental investigation on the FPZ properties in concrete using digital image correlation technique", *Eng. Fract. Mech.* **78**:17 (2011), 2978–2990.

- [Xie and Biggers Jr. 2006] D. Xie and S. B. Biggers Jr., “Progressive crack growth analysis using interface element based on the virtual crack closure technique”, *Finite Elem. Anal. Des.* **42**:11 (2006), 977–984.
- [Xie and Waas 2006] D. Xie and A. M. Waas, “Discrete cohesive zone model for mixed-mode fracture using finite element analysis”, *Eng. Fract. Mech.* **73**:13 (2006), 1783–1796.
- [Xie et al. 2006] D. Xie, A. G. Salvi, C. Sun, A. M. Waas, and A. Caliskan, “Discrete cohesive zone model to simulate static fracture in 2D triaxially braided carbon fiber composites”, *J. Compos. Mater.* **40**:22 (2006), 2025–2046.
- [Xu et al. 2011] F. Xu, Z. Wu, J. Zheng, Y. Zhao, and K. Liu, “Crack extension resistance curve of concrete considering variation of FPZ length”, *J. Mater. Civ. Eng. (ASCE)* **23**:5 (2011), 703–710.
- [Zheng et al. 2015] J.-J. Zheng, J.-G. Dai, and X.-L. Fan, “Fracture analysis of FRP-plated notched concrete beams subjected to three-point bending”, *J. Eng. Mech. (ASCE)* **142**:3 (2015), 1–10.

Received 11 Feb 2019. Revised 21 Apr 2019. Accepted 12 May 2019.

SHAHRIAR SHAHBAZPANAHI: sh.shahbazpanahi@gmail.com

Department of Civil Engineering, Sanandaj Branch, Islamic Azad University, Sanandaj, Iran

HUNAR FARID HAMA ALI: hunar.hamaali@uoh.edu.iq

Department of Building and Construction Engineering, University of Halabja, Kurdistan, Iraq

ASSESSMENT OF DEGRADATION OF RAILROAD RAILS: FINITE ELEMENT ANALYSIS OF INSULATED JOINTS AND UNSUPPORTED SLEEPERS

HOSSAM ELSAYED, MOHAMED LOTFY, HAYTHAM ZOHNY AND HANY SOBHY

This research investigates the response of rail material using an elastic-plastic finite-element framework. The implications of unsupported sleepers and insulated rail joints which represent sources of stiffness discontinuity in railroad lines were included. The nonlinear response of wheel-rail material was considered. The developed finite-element model has been supported by an analytical method to assess the onset of fatigue cracks in rails. Deflections, strains, stresses, and crack initiation parameters were obtained. The results showed good compatibility with the field observations, Hertz's theory, and equivalent studies. The findings showed the high sensitivity of plastic flow and rail material fatigue to the value of rail deflection which on the contrary has a meagre impact on the magnitudes of stresses. In addition, insulated rail joints due to stress singularity have a hurtful influence on the quantities of stresses, plastic deformation, and fatigue life. However, this effect plummets with increasing depth. For all cases, cracks initiate at the rail's surface knowing that the simulated friction coefficient between wheel and rail is 0.35 and the applied wheel load is 110 kN. Additionally, 15 mm depth is enough to study the nonlinear characteristics of rail materials. And finally, unsupported sleepers accelerate the electrical failure, which causes troublesome traffic disturbances, at insulated rail joints.

1. Introduction

Deterioration of rails is a critical and growing issue for railways across the world. Zerbsta et al. [2009] stated that in Great Britain over the last century the failures of rails per train kilometre have been raised more than twice. In Egypt, for reasons still not rigorously identified, rail fracture is inevitable and frequent every year (see Figure 1) with a plethora of replacements taking place prior to the complete damage (not included in Figure 1). This problem is not only contributing to increasing the annual costs of maintenance [Cannon et al. 2003] but also it may cause catastrophic incidents such as the derailment of Hatfield train in the UK which resulted in four fatalities and over seventy casualties [Zerbsta et al. 2009]. This issue reaches its maxima at the locations where the track loses its stiffness continuity. Such discontinuity can be found at the insulated rail joints (IRJs) (or in short insulated joints) which are used to control the railway signalling system of most modern rail networks. At any IRJ, it is required to have two rails electrically insulated from each other with an insulating material which always has lower stiffness than the adjacent rails inducing high-stress concentration at IRJ's zone. Zong and Dhanasekar [2014] highlighted that the average life of IRJs is 20% compared with conventional rails, making their replacement about 20%–50% of the entire track replacements. Another source of stiffness irregularity appears at unsupported sleepers (or hanging sleepers), which refer to sleepers connected to the rail

Keywords: unsupported sleeper, railway model, wheel-rail contact, insulated rail joints, crack initiation, fatigue of rails.

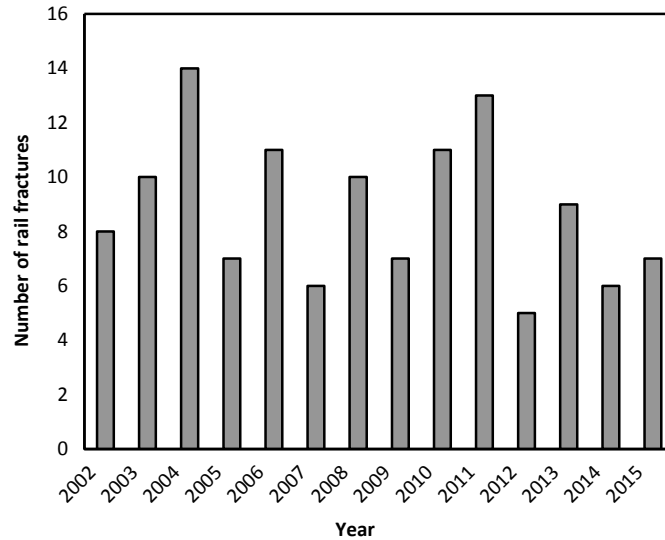


Figure 1. Variation of the number of rail fractures per year in the first line of Cairo Metro in Egypt [El-sayed et al. 2018a].

without any support from the ballast. This fault is created by the uneven settlement of the ballast or the underneath material layer formed during service life due to irregularity in track stiffness [Lundqvist and Dahlberg 2005]. This defect exists in all ballasted railroad lines. Augustin et al. [2003] claimed that in reality up to 50% of sleepers are partially or fully hanging. Olsson and Zackrisson [2002] found by field measurements very frequent small gaps among sleepers and ballast, with different size of these gaps of the same sleeper. Ishida et al. [1999] explained with an analytical dynamic model the baleful effect of unsupported sleepers on the fatigue life of rail welds, rail deflection, and rail bending stress.

The likelihood of the occurrence of hanging sleepers at IRJs is high. This can be explained in Figure 2. The reduction of stiffness at IRJ's location intensifies the dynamic forces [Wen et al. 2005; Cai et al. 2007; Pang and Dhanasekar 2006], causing track deterioration through a various number of failure modes [Mandal and Peach 2010; Rathod et al. 2012; El-sayed et al. 2018b]; e.g., squashing, spalling, rolling contact fatigue, plastic flow in the proximity of the joint, and sleepers' failure. These failure forms make a ferocious cycle with the quantity of impact load. As the train-track dynamic load escalated, the nonuniform deformation of the ballast increases [Zhang et al. 2008; Grassie and Cox 1985], producing unsupported sleepers' defect. In the literature, most of the efforts investigate either the effects of unsupported sleepers [Ishida et al. 1999; Zhang et al. 2008; Grassie and Cox 1985; Bezin et al. 2009] or IRJs [Chen and Chen 2006; Chen and Kuang 2002; Zong and Dhanasekar 2012; Sandström and Ekberg 2009] on the behaviour of railway track. However, both issues jointly should be studied for real knowledge of the mechanisms of rail's failure. Likewise, although the fatigue life and stress-strain states have been extensively explored for conventional rails [El-sayed et al. 2018a; Ringsberg 2001; Ringsberg et al. 2000; Ringsberg and Josefson 2001] and rails at traditionally bolted joints [Wen et al. 2005; Cai et al. 2007; Mohammadzadeh et al. 2013], the impact of IRJs and hanging sleepers simultaneously and separately on these dilemmas is questionable.

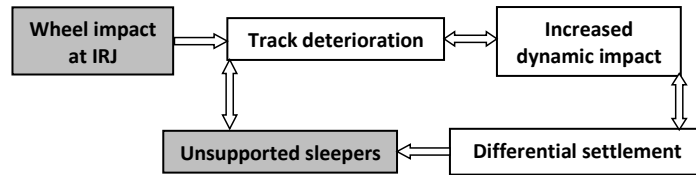


Figure 2. The process of unsupported sleepers' formation at IRJ.

This research focuses on examining the influence of IRJs in collaboration with hanging sleepers on the rail material response and comparing the results with that acquired from each issue individually. To this end, numerical simulations were implemented in which different scenarios for comparison purpose were created accounting for both normal and jointed tracks in the absence and presence of hanging sleepers considering the whole track response. The plastic deformation, realistic contact geometry, and rail bending were considered, which are necessary to get authentic findings. The numerical results were discussed and compared against field investigation, Hertz's theory, and equivalent studies. Likewise, they were incorporated with a fatigue life criterion to get predictions of the initiation of fatigue cracks in rails.

2. Modelling of wheel-track system

To achieve the research objective, a three-dimensional (3D) finite element (FE) model was performed considering the full wheel-track system with the implementation of an elastic-plastic material model using ABAQUS/Explicit code [Dassault Systèmes 2014]. The introduced model is based on specifications of a sector of railroad track existing in Cairo Metro (CM), Egypt; it is hereafter named the test site and it is depicted minutely in [Egyptian National Railways 2004]. At the test site, the standard 1435 mm gauge is used. A 54E1 (UIC54) standard rail profile (Figure 3, second row, left) with an inclination of 1 : 20 is applied and supported by monoblock concrete sleepers (Figure 3, third row). The sleeper spacing is 0.6 m and each sleeper is embedded into a ballast layer, which has a depth of 0.3 m. The sleeper is separated from the rail bottom with a layer of compressible material (rail pad) of 5 mm height and a steel plate of 14 mm thickness. The wheel has a nominal radius R_w of 510 mm (Figure 3, second row, right), subjected to a vertical static load equal to 110 kN when there are 13 passengers per meter square in the motorcoach. The peak permissible (design) speed of the trains passing the test site is 100 km/h while the operational speed is 80 km/h.

2.1. Modelling of normal track. The normal track model here refers to the track with no irregularity. Referring to Figure 3, two FE models were created namely "global model" and "submodel". The global model is used to account for the bending line of rail. The influence of rail pads, sleepers, ballast, and subgrade was considered (see Figure 3, top row, left). The rail pad was connected with the rail and sleeper in both vertical and transverse directions. The steel base plate existing under the rail pad was disregarded since its impact on the rail bending is quite small because of its higher stiffness compared with other components beneath the rail. The ballast and subgrade layers were connected by tie constraints with no longitudinal displacement permitted at the ends of the two layers. The base of the model and the ends of the rail were fixed in all directions. Symmetry of the track system was presumed so that only one wheel and a half-straight track were modelled with symmetry boundary condition assigned at the

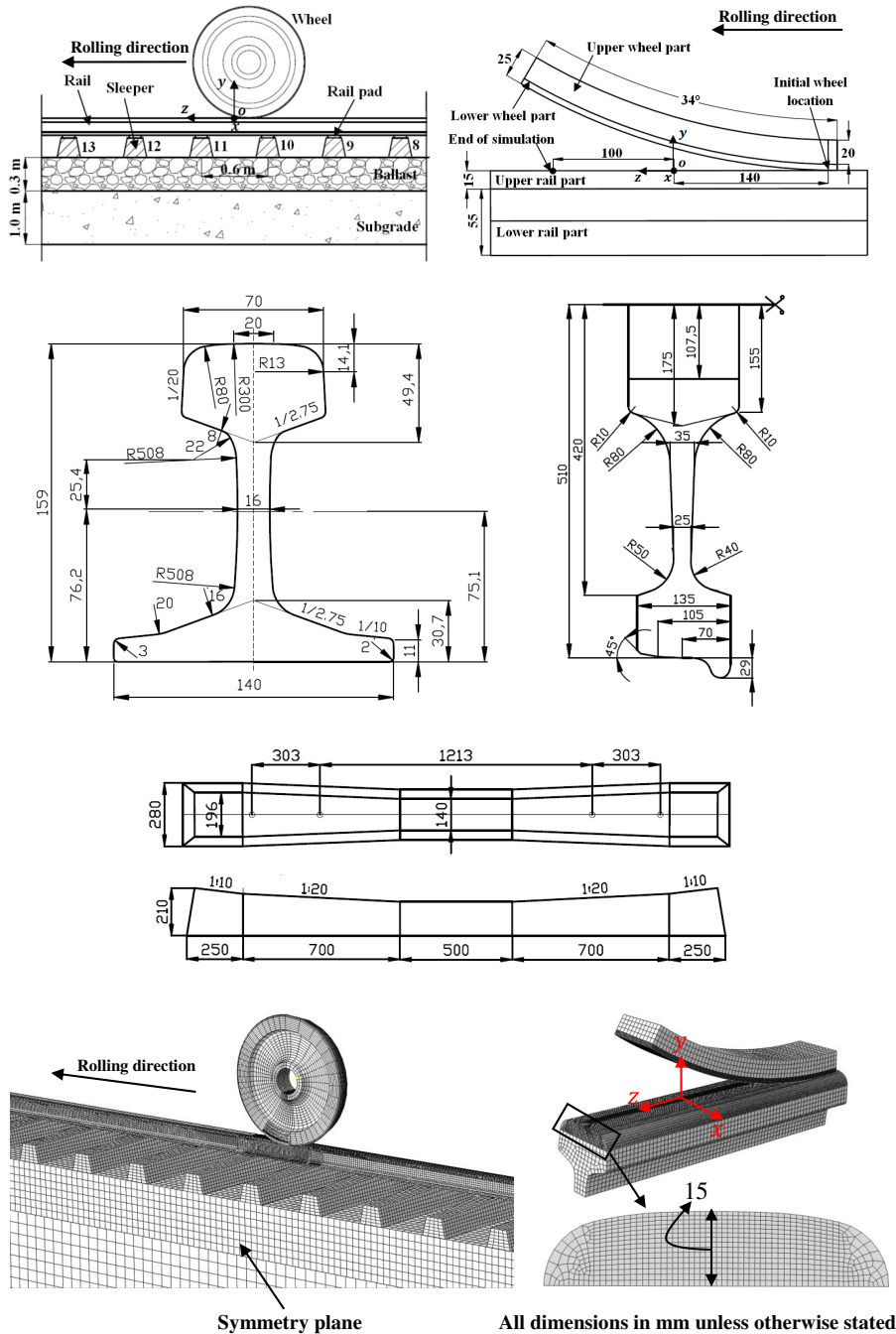


Figure 3. Wheel-track interaction model. Top row: schematic diagram of a part of the global FE model (left) and representation of the wheel-rail FE model in submodel (right). Second row: rail profile (left) and wheel profile (right). Third row: dimensions of a concrete monoblock sleeper (the plane is drawn above the longitudinal view). Bottom row: meshing of a section of the global model (left) and meshing of submodel (right).

symmetry plane. This system was modelled for a length of 20 sleeper spans which is long enough to simulate the track response [Sadeghi 1997]. Such large FE model prohibits element size to be refined to a desirable level due to barriers of calculation time which passively affects the fineness of local stresses and strains generated at the region of wheel-rail interface. Accordingly, using submodeling approach, which enables examining a local sector of the entire model with a much finer mesh and with no disregard of the rail bending line [Dassault Systèmes 2014], another FE model dubbed as “submodel” was created. This model as clarified in Figure 3 (top row, right) is composed of only a limited sector of the wheel and rail. The response of rail’s boundaries with time in submodel was acquired from the global model. For the same reason of calculation time, the rolling distance in both models was restrained to 240 mm. The initial contact position among wheel-rail was taken at 140 mm away from the origin o of coordinate system xyz defined in Figure 3 (top row) where the origin o is located at the middle-top point of the 54E1 (UIC54) profile, at the mid-side of the two middle sleepers, i.e., sleeper 10 and sleeper 11. The current and previous studies [El-sayed et al. 2018a; 2018b] have shown that this length using the explicit analysis method in case of elastic-plastic behaviour can give reliable results. The meshed geometry is demonstrated in Figure 3 (bottom row, left and right) for the global model and submodel, respectively. The modelled wheel and rail parts were meshed with first-order brick elements (Type C3D8) with fine elements, $2\text{ mm} \times 2\text{ mm} \times 2\text{ mm}$ and $1\text{ mm} \times 1\text{ mm} \times 0.8\text{ mm}$ in the global model and submodel, in x , y , z , respectively, at the contact area; while, coarse mesh was allowed at other noncontacting regions. The mesh transition among regions of different element characteristics was managed using tie constraints. For other components reduced integrated solid elements (Type C3D8R) were preferred since they minify the time of calculation and exhibit no shear locking. The material parameters of the FE model are given in Table 1, in which the variables defining the nonlinear response of wheel-rail materials are also presented. These parameters obtained from [El-sayed et al. 2018a] are compatible with the test site’s specifications. The elastic-plastic behaviour was implemented only in submodel at the contact spot; i.e., the upper rail part and the lower wheel part (Figure 3, top row, right). Other than that, the elastic response was applied.

2.2. Modelling of unsupported sleepers. As presented in Figure 4, two hanging sleepers were considered to be unsupported; namely sleeper 10 and sleeper 11, the two middle sleepers. These hanging sleepers were modelled by introducing a gap with 2 mm and 4 mm between the two sleepers and the ballast bed. Shi et al. [2012], according to measurement carried out by Guangzhou Railway Corporation in China [Li and Sun 1992] clarified that the range of small gaps among sleepers and ballast is 2 mm to 4 mm. In the simulation, the interaction between the hanging sleepers and ballast was activated only when the prescribed gap was closed. The transition from the normal track sector to the unsupported one was not studied; only the unsupported area was elucidated to explore the effect of increased deflection on material failure.

2.3. Modelling of jointed railway track. As clarified in Figure 5 (left), the modelled IRJ as utilized at the test site is composed of an insulating material inserted between two rail sections. This layer is made of fibreglass material and its width is 8 mm. To secure the joint, two steel joint bars are fastened to the rails with epoxy adhesive and six pretensioned bolts. The adhesive layers were presumed to have a thickness of 3 mm. The joint bar has nonuniform cross-sections as seen in Figure 5 (right), shaped with thicker mid-section (width = 48 mm) to provide additional strength and deflection resistance at the joint’s region. In the simulation, the end post and adhesive layers were assumed to be fully bonded with

Part	Parameter (Unit)	Value
Wheel (grade R7)	Mass density, ρ_w (kg/m ³)	7850
	Elastic modulus, E_w (MPa)	205000
	Poisson's ratio, ν_w	0.3
	Yield stress, σ_{yw} (MPa)	316
	Kinematic hardening parameter, γ	401
	Kinematic hardening modulus, C (MPa)	137000
Rail (grade 900A)	Mass density, ρ_r (kg/m ³)	7800
	Elastic modulus, E_r (MPa)	206000
	Poisson's ratio, ν_r	0.28
	Yield stress, σ_{yr} (MPa)	379
	Kinematic hardening parameters, $\gamma_1, \gamma_2, \gamma_3$	55, 600, 2000
	Kinematic hardening modules, C_1, C_2, C_3 (MPa)	24750, 60000, 200000
	Isotropic hardening parameter, R	500
	Isotropic hardening modulus, Q_∞ (MPa)	-189
Rail pad	Mass density, ρ_p (kg/m ³)	950
	Elastic modulus, E_p (MPa)	800
	Poisson's ratio, ν_p	0.46
Sleeper	Mass density, ρ_c (kg/m ³)	2300
	Elastic modulus, E_c (MPa)	36000
	Poisson's ratio, ν_c	0.3
Ballast	Mass density, ρ_b (kg/m ³)	1800
	Elastic modulus, E_b (MPa)	170
	Poisson's ratio, ν_b	0.3
Subgrade	Mass density, ρ_s (kg/m ³)	1600
	Elastic modulus, E_s (MPa)	30
	Poisson's ratio, ν_s	0.25

Table 1. Material parameters applied in the numerical simulations [El-sayed et al. 2018a].

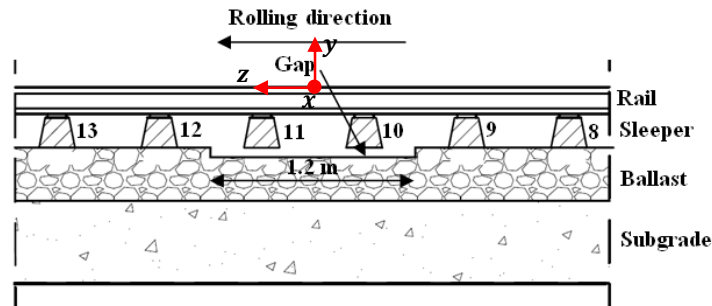
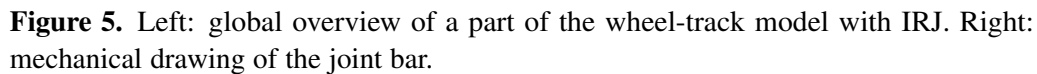


Figure 4. Schematic drawing of hanging sleepers.



2.4. Applied loads. Loads and rolling of the wheel were negotiated by three quantities F_y , V , and ω defined at the central point of the wheel. This point was rigidly linked by tie constraints with all nodes of the closest side of the wheel part (see Figure 5, left). Here, F_y is the vertical force taken equivalent to 110 kN. Displacement of the wheel was achieved by imposing a translational velocity V at the wheel centre. To simulate pure rolling, an angular velocity ω equal to V/R_w was applied. Since the trains at the site concerned move with a design speed of 100 km/h, a translational velocity of 100 km/h with an angular one equal 54.5 rad/s were applied to the wheel. The wheel was not allowed to move in the lateral direction and no lateral forces were applied to the model. For insulated joint's scenarios, in the global model, the bolt pretension load generated from bolt tightening was considered. The bolt pretension P_b can be defined as [Wen et al. 2005]

where K_b is the coefficient of the bolt torque moment T , and D is the bolt diameter. Here, the selected values are $T = 500 \text{ Nm}$ [Wen et al. 2005], $K_b = 0.2$ [Wen et al. 2005], and $D = 32 \text{ mm}$ according to IRJ's design used in CM.

2.5. Wheel-track interaction. In the FE-software, the interface was defined by surface-to-surface discretization algorithm. One surface of this approach is called “master surface” and the other is “slave surface”. Contact was then achieved by forbidding nodes of the slave surface in each increment from penetrating the master segment using a penalty algorithm which imposes normal springs among the penetrating nodes and the master surface. The contact force is equal to the product of contact stiffness and penetration distance. Isotropic Coulomb’s friction model was adopted to simulate the tangential behaviour with a limiting shear stress value of μP at the contacting nodes where slip takes place. Here, μ is the friction coefficient, and P is the interface pressure. If the frictional stress is lower than μP , a penalty algorithm was used to ensure that no slip occurs. The value of μ was selected as 0.35 for wheel-rail interface [Harrison et al. 2002], 0.3 for rail-rail pad and rail pad-sleeper interfaces [Zhang 2015], 0.7 for sleeper-ballast layer interface [Zhang 2015], and 0.4 for bolts-joint bars and bolts-rails interfaces [Cai et al. 2007]. The finite sliding option was permitted during analysis to define the relative sliding among the two contacting bodies. The wheel-rail contact position was presumed at the lateral centre of the rail profile against the wheel tread.

3. Results and discussion

The results are discussed for the performed scenarios, which are:

Scenario 1: Normal track.

Scenario 2: Track with two hanging sleepers of 2 mm gap size.

Scenario 3: Track with an IRJ.

Scenario 4: Incorporation of scenario 2 with scenario 3.

Scenario 5: Track with two unsupported sleepers of 4 mm gap size.

Scenario 6: Integration of scenario 3 with scenario 5.

The last two scenarios are presented only when there is an obvious impact of increasing gap size from 2 mm to 4 mm.

3.1. Displacement. As depicted in Figure 6 (left), the crest downward displacement of scenario 1 is 1.95 mm which is concurrent with El-sayed et al. [2018a] with 8% difference owing to the finer meshing implemented in this study. Another reason is that in [El-sayed et al. 2018a] the length of the modelled track is equivalent to 32 sleeper spans being different from the FE model created here in which 20 sleepers were utilized. In scenario 2, the climax downward deflection is 3.87 mm, extensively higher compared with that acquired from scenario 1 due to low stiffness. This abrupt change of rail displacement at the region of hanging sleepers would cause undesirable effects on ride comfort and safety. However, the impact of IRJ on the magnitude of this component is relatively small (not exceed 2.7%). This means that such joint bar design (see Figure 5, right) provides adequate stiffness to the rail joint in the vertical direction. The impact of gap size on the peak values of rail deflection is clarified in Figure 6 (right). It is obvious that the relationship between gap size and rail downward deflection is nonlinear. As the gap size increased from 2 mm to 4 mm, the maximum downward deflection raised only by 16.6% in the absence of IRJ and by 13.7% in the presence of IRJ. This behaviour is probably due to the impact of the adjacent sleepers. Adding these findings to that obtained in [Ishida et al. 1999], it can be concluded that there

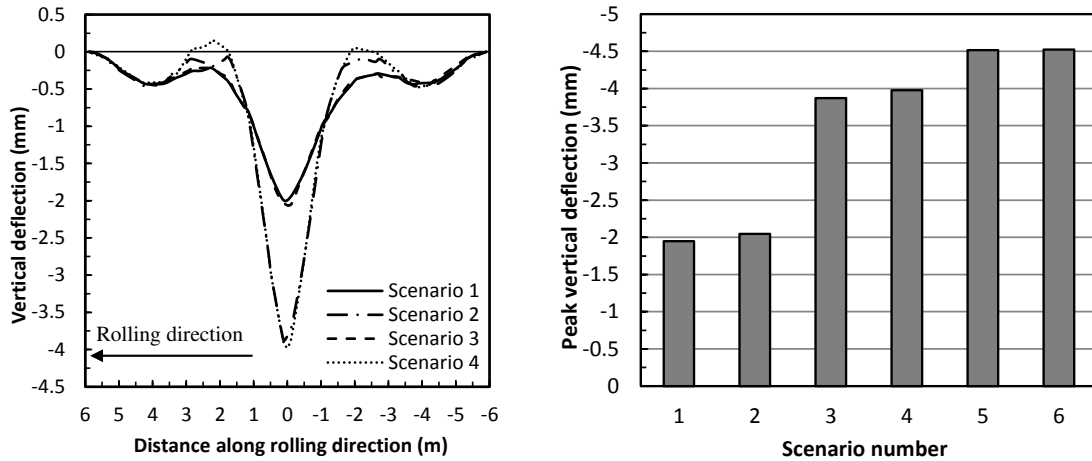


Figure 6. Left: deflection of rail for the first four scenarios. Right: effect of gap size on the maximum downward deflection of the rail.

is a gap size above which the rail deflection is unchanging, and the unsupported sleepers don't touch the ballast. Figure 7 depicts the residual longitudinal deformation at the end of the loading step at IRJ's region for scenario 3 and scenario 4 as obtained from submodel analysis. As clarified, the width of end post dwindled due to the axial deformation of rail material adjacent to IRJ's zone. The peak reduction of IRJ's width for both scenarios occurred at $y = -0.8$ mm with a magnitude equal to 0.1874 mm and 0.2486 mm for scenario 3 and scenario 4, respectively, meaning that hanging sleepers can markedly accelerate the electrical deterioration of IRJs, which occurs if the two rails at IRJ's zone touched each other when the track of this section is not occupied. This electrical problem causes troublesome traffic disturbances.

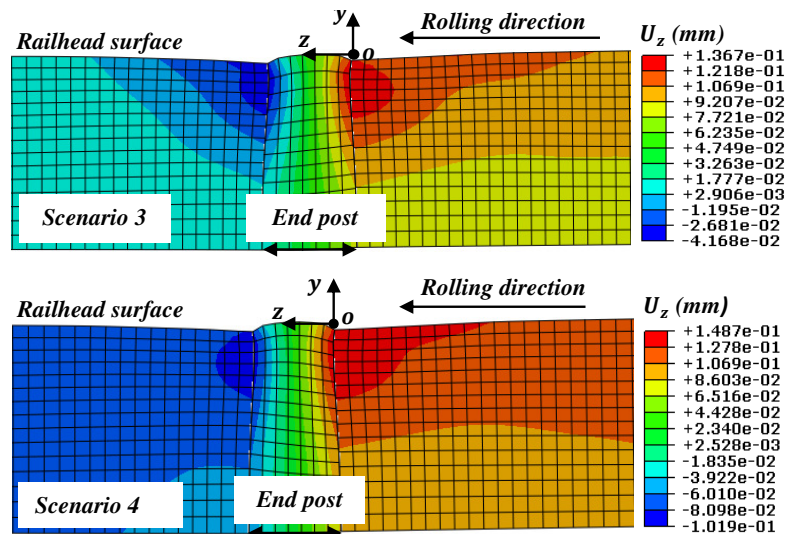


Figure 7. Residual longitudinal deformation at IRJ's region (deformation scale factor = 10).

3.2. Surface pressure. The interface pressure distribution at the position which has peak value during rolling contact is plotted in Figure 8. However, it should be recognized that as the rail is discretely supported, the contact characteristics alter with the change of contact position, see Figure 12 (left) for more clarification. As depicted in scenario 1, the normal pressure is maxima when $P = 1000$ MPa distributed over a contact area of 21.49 mm and 18.01 mm in z -direction and x -direction, respectively. Compared with Hertz's theory which is based on elastic behaviour assumption, refer to [Johnson 1985] for detailed illustration, the present FE model as depicted in Figure 9, owing to the consideration of plastic deformation, showed a lower pressure value with a larger contact patch in both directions. These findings are in good agreement with that obtained in [Yan and Fischer 2000]. On the contrary with scenario 1, the peak magnitude of pressure is largely unaffected by the existence of hanging sleepers, the difference is only 1.67%, but the position of this value is different, it appeared closer to the track origin. This position remained the same as the gap size increased from 2 mm to 4 mm. For scenario 3, as expected a high impact on interface pressure parameters (shape and magnitude) due to edge effect was obtained. The entity of IRJ raised the peak value of interface pressure to 1172 MPa, which is 17.2% larger than that computed from scenario 1. Moreover, the contact spot became wider in z -direction and in x -direction as well. In scenario 4, case of hanging sleepers with IRJ, the pressure value increased by 4.35% from that determined in scenario 3 with no change in the location of crest pressure value.

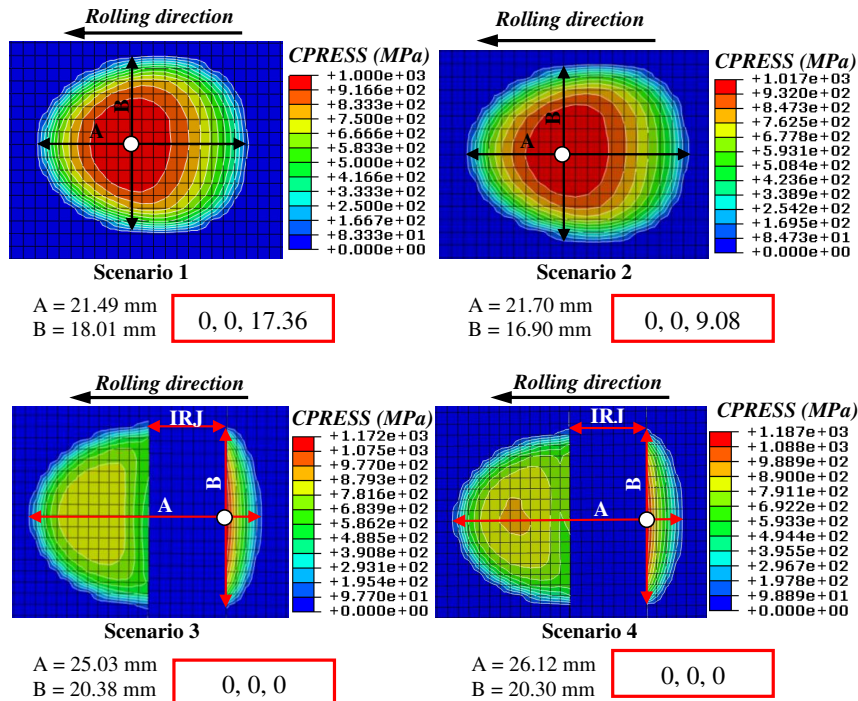


Figure 8. Interface pressure's distribution for the first four scenarios when the contact pressure reached its climax value. Note, A and B represent dimensions of the contact patch in rolling and lateral directions, respectively, and the white point shows the position of peak pressure value whose coordinates are drawn in a red box.

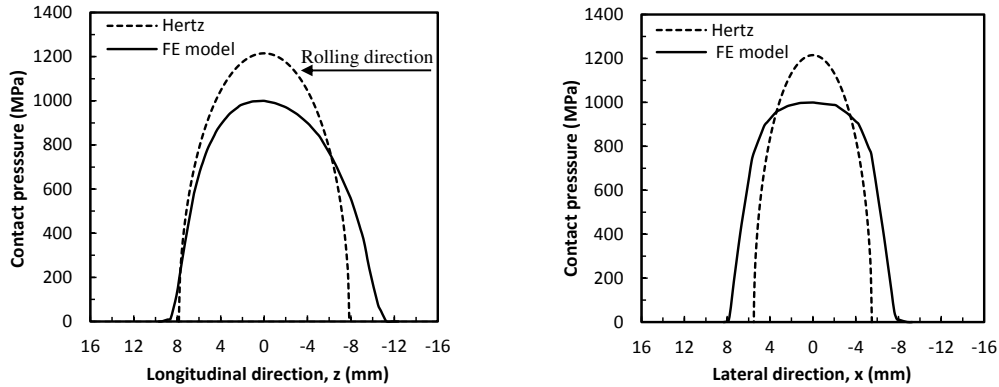


Figure 9. Distribution of contact pressure acquired from the FE model in scenario 1 and Hertz's theory: along the rolling axis (left) and along the lateral axis (right). Here, the origin is placed at the crest P value.

The tangential stress distribution at the crest normal pressure position is delineated in Figure 10. In scenario 1 and scenario 2, the magnitude of surface shear stress is lower than μP along the contact spot. This means that the contact patch is totally in stick due to the free-rolling condition. The reason for the small negative tangential stress quantity, existing in the leading edge of the contact patch, is that the tangential force is negligible at this location, case of frictionless contact. However, in scenario 3 and scenario 4, despite free-rolling, the tangential stress distribution coincides with the corresponding μP curve up to rail edge 1 where interfacial shear stress hit its maximum magnitude. Furthermore, because of the significant reduction of interface pressure at the end post as presented in Figure 8, the direction of surface shear stress is opposite on both sides of the IRJ correlating well with the results gained in [Chen and Chen 2006]. The effect of hanging sleepers on increasing the tangential stress of IRJ's scenarios is only obvious on the left side of the IRJ. These results reveal the meagre effect of rail deflection on wheel-rail contact characteristics.

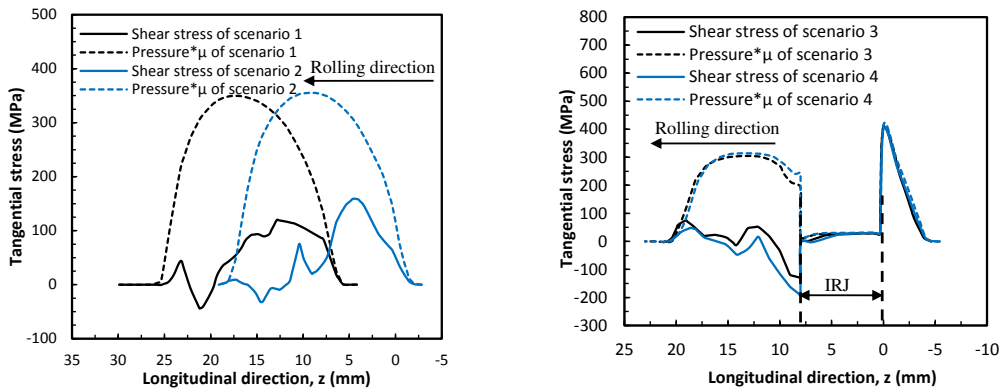


Figure 10. Surface shear stress distribution along the z -axis: for scenarios without IRJ (left) and for IRJ's scenarios (right). Solid lines represent the tangential shear stress (τ_{yz}) and dashed lines represent the interface pressure multiplied by μ (i.e., $P\mu$).

3.3. Stress analysis. Figure 11 depicts the contours of von Mises stress σ_e in x - y plane from the FE model together with the distribution of σ_e along the rail depth at $x = 0$ for the four main scenarios. These plots were drawn when σ_e reached its maximum value. As clarified, the crest value of σ_e (denoted by black point) formed at the rail's surface with a value equal 514.8 MPa and 506.5 MPa in scenario 1 and scenario 2, respectively, noticeably larger than the yield strength of rail material which is 379 MPa in this analysis. In addition, in both scenarios the magnitudes of σ_e remain almost constant to some millimetres beneath the rail surface. This could increase the probability of both surface and subsurface damage initiation. For IRJ's scenarios, the peak σ_e magnitude located at the rail's top surface at $z = 0$, then it decreased rapidly. Compared with scenario 1, the vicinity of IRJ again due to edge effect increased the summit σ_e magnitude by 46.36% and 43.42% in scenario 3 and scenario 4, respectively. However, at subsurface depths, approximately 4 mm below the surface, the behaviour reversed. Moreover, the effect of hanging sleepers on this component is quite small along the upper rail part, being analogous with the results presented in Section 3.2. This means that von Mises stress magnitude is highly influenced by the contact characteristics and rail displacement has a minuscule impact on this quantity.

Figure 12 (left) indicates the crest von Mises stress σ_e magnitude in a strip of surface nodes along the travelling direction at $x = 0$. The peak stress of a node is the maximum stress the node experienced in the time history. As observed, for all given scenarios the characteristics of von Mises stress, such as values and shapes (not shown in the figure), differ with time even with smooth rail surface. This is because of both the vibrations of the track system which are inherent in the explicit model and the change of contact spot position on a discretely supported system. The results showed that, the oscillation amplitude of σ_e in scenario 1 is 47.01 MPa, 10.53% of the mean value which equal 446.55 MPa. For scenario 2, the oscillation amplitude is 69.11 MPa, 15.80% of the mean value that is equivalent to 437.41 MPa. This implies that on the contrary to the normal track, the stress oscillation increases in case of unsupported sleepers. In the IRJ's scenarios, the entity of insulating layer changed drastically the oscillation amplitude which equals 253.52 MPa and 239.1 MPa in scenario 3 and scenario 4, respectively, in the studied strip.

3.4. Plastic strain analysis. As seen in Figure 12 (right), the maximum value of equivalent plastic strain ε_{eff} in the first two scenarios appeared at subsurface and at different longitudinal position, precisely at $y = -2.54$ mm and $z = 35.20$ mm for scenario 1 and at $y = -4.19$ mm and $z = 74.36$ mm for scenario 2. These results contradict with the von Mises stress contours depicted in Figure 11 in which the peak stress is on the surface. This behaviour occurs because of the rail deflection. El-sayed et al. [2018a] compared a FE model that considered rail bending with another one that neglected this factor and the results explained that a 1.805 mm vertical deflection makes the maximum ε_{eff} quantity appearing at subsurface; while the zenith von Mises stress value is on the top. In addition, the peak ε_{eff} value is 0.009625 and 0.013018 in scenario 1 and scenario 2, respectively; i.e., the hanging sleepers alone incremented the crest ε_{eff} value by 35.25%. The increase of gap size from 2 mm to 4 mm reduced the crest ε_{eff} value for unsupported sleepers' scenarios without IRJ by 21.67% and made the maximum value appearing at $y = -4.25$ mm and $z = 22.75$ mm. These findings emphasise that the ε_{eff} quantity is sensitive to the value of vertical rail displacement. By combining these outcomes with that computed in [El-sayed et al. 2018a], one can conclude that the plastic deformation in continuous rails increases as the rail deflection rises to a certain value, then the plastic flow reduces again. However, this quantity is largely uninfluenced by the presence of hanging sleepers alongside IRJ. For scenario 3 and scenario 4, the climax value of ε_{eff} emerged at

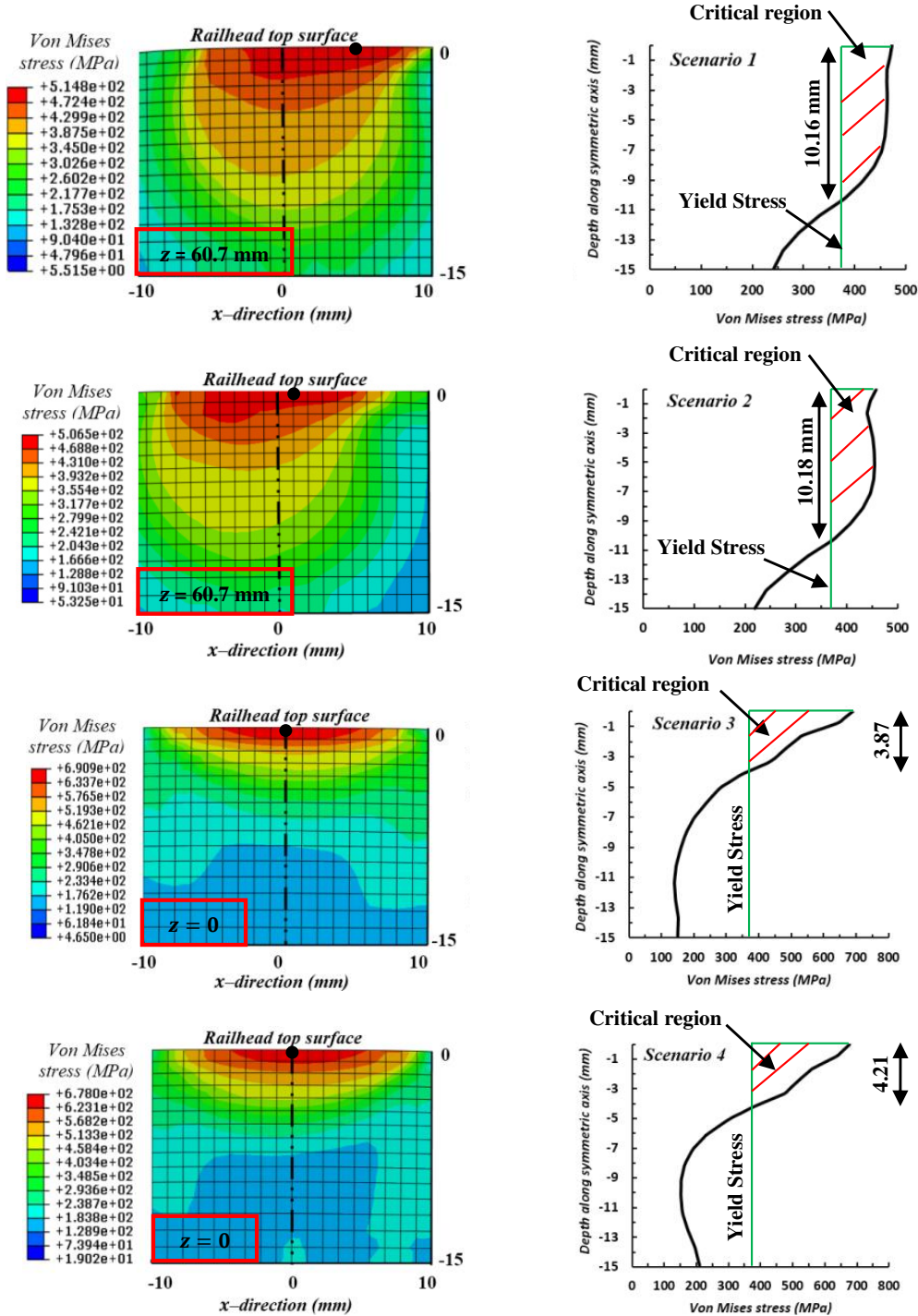


Figure 11. Contours of von Mises stress in x-y plane associated with the variation of σ_e along the rail depth at $x = 0$ for the first four studied scenarios. The red box denotes the position of section in the longitudinal direction.

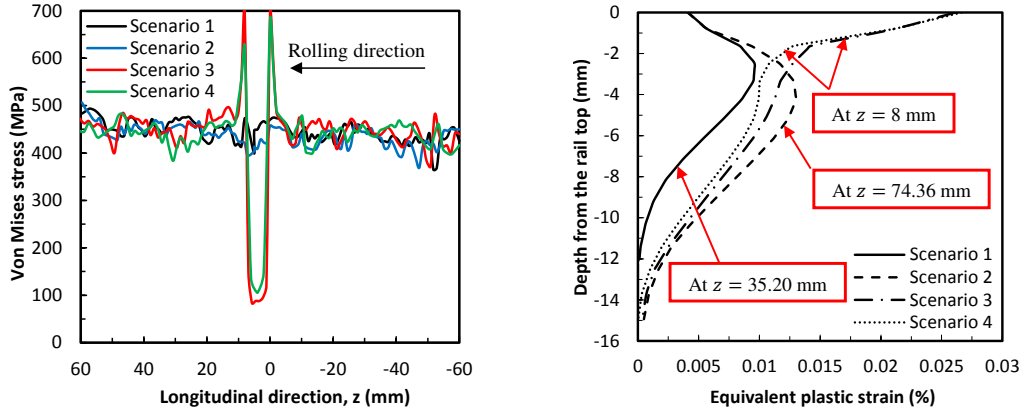


Figure 12. Left: peak von Mises stress of a strip of surface nodes in the travelling direction at $x = 0$. Right: variation of equivalent plastic strain ε_{eff} with rail depth for the first four scenarios at the location where the peak magnitude of ε_{eff} is observed.

the top of rail edge 2, which is slightly larger than that obtained at rail edge 1, see Figure 13 for more illustration, with a magnitude equal 0.026117 and 0.026633. These values are corresponding to 2.71 and 2.77 times of that computed from scenario 1. Then, the quantity of ε_{eff} decreased swiftly like the trend of von Mises stress seen in Figure 11. With regard to the dimensions of plastic region, the depth of plastic zone is 11.97 mm in scenario 1; whilst for those scenarios which include either hanging sleeper defect or IRJ, the depth of plastic zone exceeded with a quite small value the 15 mm depth which signifies that the presumed dimensions of plastic layer implemented in this research are widely adequate to recognize the nonlinear response of rail material.

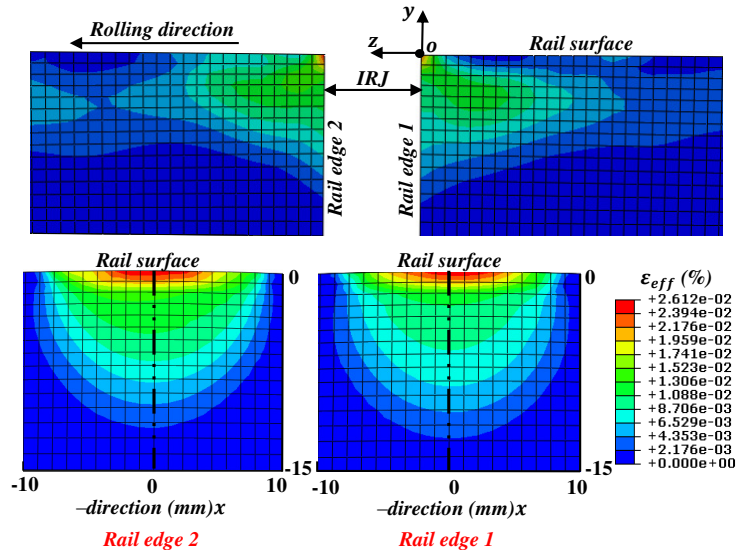


Figure 13. Contours of equivalent plastic strain ε_{eff} at the perfect insulated joint scenario (scenario 3).

4. Fatigue crack initiation analysis

4.1. Fatigue Model. The high stresses induced by wheel-rail interface could increase the likelihood of damage initiation. Subsequently, with time, this leads to rail fracture and vehicle derailment. Therefore, it is necessary to quantify the fatigue impact. The results extracted from the FE model (Figure 14, for instance), revealed the multiaxial and nonproportional state of both stress and strain of the elements at the contact region. Hence, in the present study, the critical plane concept together with the multiaxial fatigue criterion proposed in [Jiang and Sehitoglu 1999] was employed to identify the effect of hanging sleepers and IRJs on the reliability of rail steel against crack initiation due to fatigue. Such combination has been shown to fit very well with experimental findings regarding both fatigue life and crack plane orientation [Chen et al. 1999; Varvani-Farahani 2000]. This method can be expressed with the multiaxial fatigue parameter

$$FP = \langle \sigma_{\max} \rangle \frac{\Delta \varepsilon}{2} + J \Delta \tau \Delta \gamma. \quad (2)$$

At a material plane under consideration, $\Delta \varepsilon$ is the range of the normal strain, and σ_{\max} is the largest normal stress with $\langle \sigma_{\max} \rangle = \sigma_{\max}/2$ for $\sigma_{\max} > 0$ and $\langle \sigma_{\max} \rangle = 0$ for $\sigma_{\max} \leq 0$. Furthermore, $\Delta \tau$ is the range of shear stress, $\Delta \gamma$ is the range of shear strain, and J is a material parameter.

The fatigue parameter FP is related to the fatigue initiation life Nf via the relation

$$FP_{\max} = \frac{(\tau'_f)^2}{G_r} (2Nf)^{2b} + \tau'_f \gamma'_f (2Nf)^{b+c}, \quad (3)$$

where FP_{\max} is the peak fatigue parameter corresponding to the critical plane; τ'_f , γ'_f , b , and c are material parameters; $G_r = E_r/2(1 + \nu_r)$ is the shear modulus of rail. The mechanical properties used in fatigue calculations are $b = -0.089$, $c = -0.559$, $\gamma'_f = 15.45$, $\tau'_f = 468$ MPa, and $J = 0.2$ [Ringsberg 2001]. Nevertheless, the grade of rail steel employed at the test site is 900A, the prescribed values of fatigue parameters are corresponding to BS11 normal grade steel owing to lack of experimental data of grade 900A and the wide analogy of the mechanical properties of both two grades [Ringsberg et al. 2000; Ringsberg and Josefson 2001].

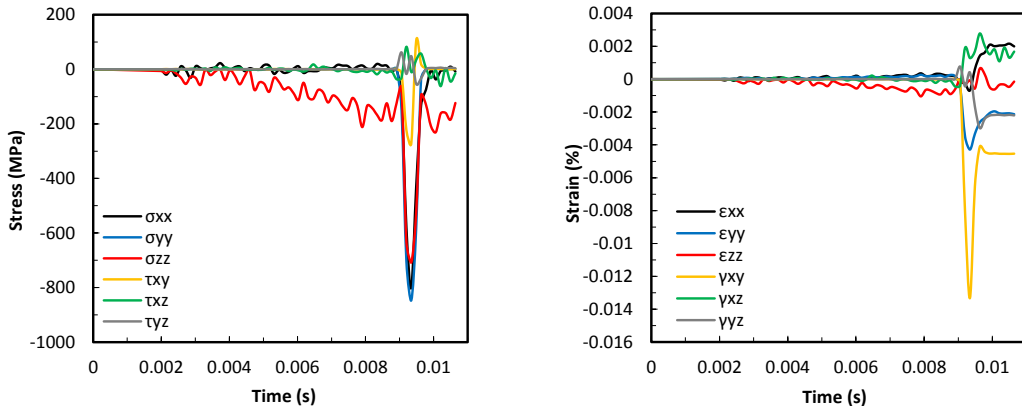


Figure 14. Variation of stress and strain components with time for the element experiencing peak von Mises stress in scenario 2.

4.2. Numerical predictions of fatigue impact. In the current research, the crack plane and the highest damage parameter were identified by the rotation of stress and strain tensors at an equal increment (1 degree) for a set of points suffering from maximum von Mises stress, at which damage is quite probable. Shear stress range $\Delta\tau$ and shear strain range $\Delta\gamma$ in (2) were identified by means of the longest chord method [Papadopoulos 1998]. The first part of (2) was removed due to the compression state of the three normal stress components (Figure 14). The crack plane was identified by two angles depicted in Figure 15. Angle θ is the angle between the normal vector \vec{n} and z -axis; whilst angle φ is the angle between z -axis and crack plane. The variations of FP with the angles θ and φ for scenario 1 and scenario 2 as two samples are presented in Figure 16. These plots refer to the most critical point in each scenario where FP_{\max} is obtained.

As shown in Table 2, the critical plane in scenario 1 occurred at $\theta = 111^\circ$, $\varphi = 87^\circ$, and $d = 0$. Field results presented in Figure 17 (left) indicate that the predominant orientation of cracks on the surface, corresponding to angle θ , lies between 113° and 123° which is in a good correlation with that predicted. Note that, the cracks at the test site were deemed to be initiated after being visible on the rail surface, but theoretically the crack may be treated to be initiated when its length is between 0.1 mm–0.5 mm

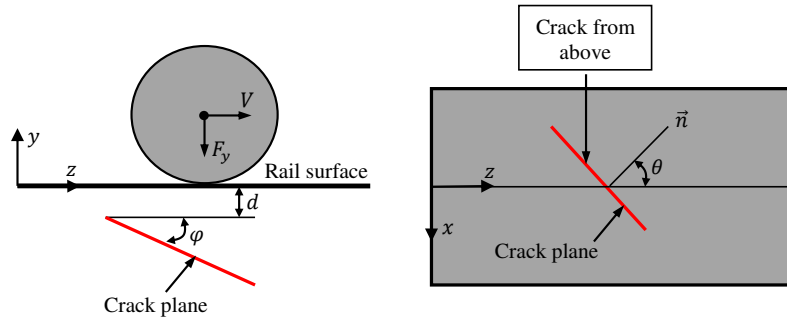


Figure 15. Definition of crack plane angles in the railhead.

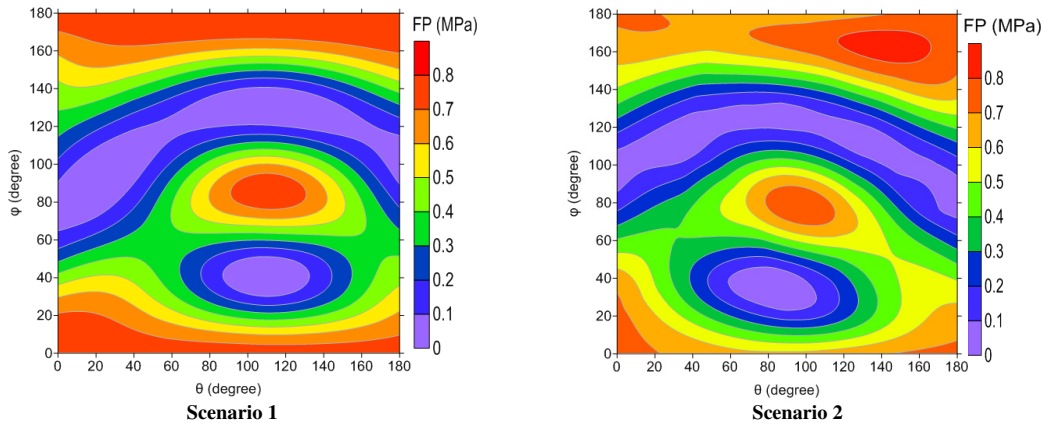


Figure 16. Variation of fatigue parameter with plane orientation in the first two scenarios for the critical point that showed the highest fatigue parameter value.

Scenario number	Description Hanging sleepers (gap size)	IRJ	θ (degree)	φ (degree)	Coordinates			FP_{\max} (MPa)	$N_r \cdot 10^5$ (passage)
					x	y	z		
1	No	No	111	87	0	0	60.72	0.7812	10.54
2	Yes (2 mm)	No	144	162	2.97	0	57.34	0.8403	9.176
3	No	Yes	174	111	0	0	0	2.3319	1.498
4	Yes (2 mm)	Yes	156	24	0	0	0	2.4152	1.412
5	Yes (4 mm)	No	84	84	1.86	0	58.46	0.8683	8.628
6	Yes (4 mm)	Yes	153	27	0	0	0	2.3059	1.527

Table 2. Predicted results of crack angles, crack coordinates, maximum fatigue parameter, and crack initiation life in each studied case.

[Ringsberg 2001]. However, angle φ contradicts with that estimated in [El-sayed et al. 2018a] where $\varphi = 9^\circ\text{--}27^\circ$. This is likely because of cyclic loading on material hardening considered in [El-sayed et al. 2018a] and disregarded in the present research. Likewise, the FP_{\max} computed at the critical plane is 0.7812 MPa. This maximum quantity causes the crack to initiate after $1.054 \cdot 10^6$ wheel passages. Upon data collected from the test site about traffic volume, approximately 18576 axles pass the test site per day. This means that the crack in the studied loading condition initiates after 56 days, but this is a critical value because in this research the highest possible wheel load was chosen, and the action of wear which can mitigate rail material fatigue [Wang et al. 2009] was overlooked. This implies that the cracks in the test site probably initiate after the predicted period. In scenario 2 compared with scenario 1, a high deviation of the critical plane angles with a slight difference in position was observed. In addition, the FP_{\max} in this scenario is higher than that evaluated from scenario 1 by 7.56%, which is corresponding to 12.94% reduction in the fatigue life. As the gap size increased from 2 mm to 4 mm, the fatigue life reduced again by 6.35%.

In scenario 3, the predicted location of cracks and the angle θ at the IRJ correlate well with the observations, see Figure 17 (right) as an example. Generally, it is obvious that in IRJ's scenarios the life

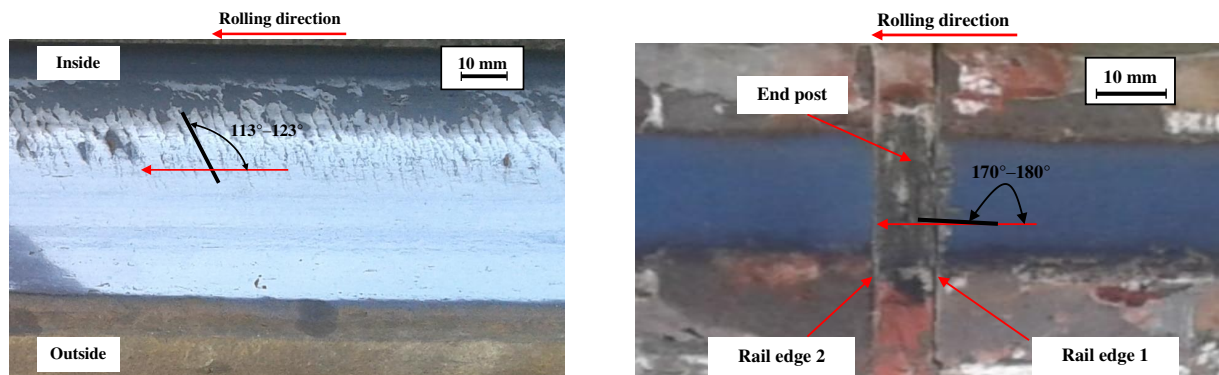


Figure 17. Observed defects on the railhead surface at the test site at the initiation stage: at a normal rail (left) and at an IRJ after three days of installation in the field (right). The given angle range is the predominate values along the test site.

of fatigue largely declines and the position of FP_{\max} occurs at the surface of rail edge 1. The main cause of this is ratchetting, excessive plastic flow.

5. Conclusions

The behaviour of rail material in both normal and jointed railway tracks with and without hanging sleepers was analysed considering different scenarios. A three-dimensional finite-element model was built to compute displacements, stresses, and strains. The finite-element results were incorporated with a multiaxial fatigue model to comprehend the mechanism of crack initiation in rails. The main findings are summed up as follows:

- In comparison with the normal track model, the track with hanging sleepers exhibits higher magnitudes of deflection, stress oscillation (as quantified by von Mises stress), and plastic strain. In addition, unsupported sleepers reduce the fatigue life of the rail material.
- The quantity and position of plastic flow are highly sensitive to the value of rail deflection. On the contrary, the interface parameters (interface pressure, tangential stress, and contact area) and von Mises stress values are largely unaffected by this factor.
- At insulated joints, stiffness discontinuity at end post has a detrimental impact on the rail material, particularly at rail's edges. From the studied case compared with the normal track model, the model with insulated joint mounted the peak magnitudes of interface pressure, von Mises stress, and plastic strain by 17.2%, 46.36%, and 177%, respectively. In addition, due to the ratchetting response of the material at rail's edges, the fatigue life is severely reduced.
- The seriousness of insulated joints is increased if integrated with hanging sleepers. The increments due to this incorporation for the case of 2 mm gap size in comparison with the perfect insulated track model in rail deflection, joint width reduction, and fatigue life are 94.43%, 32.66%, and 6.09%, respectively. However, a marginal increase in the fatigue life was found in the model of insulated joint with 4 mm gap size. The higher reduction of the joint width in the entity of hanging sleepers accelerates the deterioration of insulated joints from the electrical viewpoint.
- Based on the obtained results, it is recommended that the track maintenance operators should consider a strategy to avoid the appearance or development of hanging sleepers.

References

- [Augustin et al. 2003] S. Augustin, G. Gudehus, G. Huber, and A. Schünemann, "Numerical model and laboratory tests on settlement of ballast track", pp. 317–336 in *System dynamics and long-term behaviour of railway vehicles, track and subgrade*, vol. 6, edited by K. Popp and W. Schiehlen, Lecture Notes in Applied Mechanics, Springer, Berlin, Heidelberg, 2003.
- [Bezin et al. 2009] Y. Bezin, S. D. Iwnicki, M. Cavalletti, E. de Vries, F. Shahzad, and G. Evans, "An investigation of sleeper voids using a flexible track model integrated with railway multi-body dynamics", *Proc. Inst. Mech. Eng. F* **223**:6 (2009), 597–607.
- [Cai et al. 2007] W. Cai, Z. Wen, X. Jin, and W. Zhai, "Dynamic stress analysis of rail joint with height difference defect using finite element method", *Eng. Fail. Anal.* **14**:8 (2007), 1488–1499.
- [Cannon et al. 2003] D. F. Cannon, K.-O. Edel, S. L. Grassie, and K. Sawley, "Rail defects: an overview", *Fatigue Fract. Eng. Mater. Struct.* **26** (2003), 865–887.

- [Chen and Chen 2006] Y.-C. Chen and L.-W. Chen, “Effects of insulated rail joint on the wheel/rail contact stresses under the condition of partial slip”, *Wear* **260**:11-12 (2006), 1267–1273.
- [Chen and Kuang 2002] Y. C. Chen and J. H. Kuang, “Contact stress variations near the insulated rail joints”, *Proc. Inst. Mech. Eng. F* **216**:4 (2002), 265–273.
- [Chen et al. 1999] X. Chen, S. Xu, and D. Huang, “A critical plane-strain energy density criterion for multiaxial low-cycle fatigue life under non-proportional loading”, *Fatigue Fract. Eng. Mater. Struct.* **22** (1999), 679–686.
- [Dassault Systèmes 2014] Dassault Systèmes, *ABAQUS analysis user’s guide*, 6.14, Dassault Systèmes Simulia Corp, 2014, Available at http://130.149.89.49:2080/v6.14/pdf_books/ANALYSIS_4.pdf.
- [Egyptian National Railways 2004] Egyptian National Railways, *Guidelines for railways and switches maintenance*, Railway Engineering Department, 2004.
- [El-sayed et al. 2018a] H. M. El-sayed, M. Lotfy, H. N. El-din Zohny, and H. S. Riad, “Prediction of fatigue crack initiation life in railheads using finite element analysis”, *Ain Shams Eng. J.* **9**:4 (2018), 2329–2342.
- [El-sayed et al. 2018b] H. M. El-sayed, M. Lotfy, H. N. El-din Zohny, and H. S. Riad, “A three dimensional finite element analysis of insulated rail joints deterioration”, *Eng. Fail. Anal.* **91** (2018), 201–215.
- [Grassie and Cox 1985] S. L. Grassie and S. J. Cox, “The dynamic response of railway track with unsupported sleepers”, *Proc. Inst. Mech. Eng. D* **199**:2 (1985), 123–136.
- [Harrison et al. 2002] H. Harrison, T. McCanney, and J. Cotter, “Recent developments in coefficient of friction measurements at the rail/wheel interface”, *Wear* **253**:1-2 (2002), 114–123.
- [Ishida et al. 1999] M. Ishida, T. Moto, A. Kono, and Y. Jin, “Influence of loose sleeper on track dynamics and bending fatigue of rail welds”, *Q. Rep. RTRI* **40**:2 (1999), 80–85.
- [Jiang and Sehitoglu 1999] Y. Jiang and H. Sehitoglu, “A model for rolling contact failure”, *Wear* **224**:1 (1999), 38–49.
- [Johnson 1985] K. L. Johnson, *Contact mechanics*, Cambridge University Press, Cambridge, 1985.
- [Li and Sun 1992] Z. F. Li and J. G. Sun, “Maintenance and cause of unsupported sleeper”, *China Railway Building* **2** (1992), 15–17.
- [Lundqvist and Dahlberg 2005] A. Lundqvist and T. Dahlberg, “Load impact on railway track due to unsupported sleepers”, *Proc. Inst. Mech. Eng. F* **219**:2 (2005), 67–77.
- [Mandal and Peach 2010] N. K. Mandal and B. Peach, “An engineering analysis of insulated rail joints: a general perspective”, *Int. J. Eng. Sci. Technol.* **2**:8 (2010), 3964–3988.
- [Mohammadzadeh et al. 2013] S. Mohammadzadeh, M. Sharavi, and H. Keshavarzian, “Reliability analysis of fatigue crack initiation of railhead in bolted rail joint”, *Eng. Fail. Anal.* **29** (2013), 132–148.
- [Olsson and Zackrisson 2002] E. L. Olsson and P. Zackrisson, “Long-term measurement results”, technical report 2B/000120/T2/DA for the EUROBALT II Project, Final report, Banverket, Borlänge, 2002.
- [Pang and Dhanasekar 2006] T. Pang and M. Dhanasekar, “Dynamic finite element analysis of the wheel-rail interaction adjacent to the insulated rail joints”, in *Proc. of the 7th International Conference of Contact Mechanics and Wear of Wheel/Rail Systems (CM 2006)* (Brisbane), 2006.
- [Papadopoulos 1998] I. V. Papadopoulos, “Critical plane approaches in high-cyclic fatigue on the definition of the amplitude and mean value of the shear stress acting on the critical plane”, *Fatigue Fract. Eng. Mater. Struct.* **21** (1998), 269–285.
- [Rathod et al. 2012] C. Rathod, D. Wexler, T. Chandra, and H. Li, “Microstructural characterisation of railhead damage in insulated rail joints”, *Mater. Sci. Forum* **706-709** (2012), 2937–2942.
- [Ringsberg 2001] J. W. Ringsberg, “Life prediction of rolling contact fatigue crack initiation”, *Int. J. Fatigue* **23**:7 (2001), 575–586.
- [Ringsberg and Josefson 2001] J. W. Ringsberg and B. L. Josefson, “Finite element analyses of rolling contact fatigue crack initiation in railheads”, *Proc. Inst. Mech. Eng. F* **215**:4 (2001), 243–259.
- [Ringsberg et al. 2000] J. W. Ringsberg, H. Bjarnehed, A. Johansson, and B. L. Josefson, “Rolling contact fatigue of rails — finite element modelling of residual stresses, strains and crack initiation”, *Proc. Inst. Mech. Eng. F* **214**:1 (2000), 7–19.
- [Sadeghi 1997] J. Sadeghi, *Investigation of characteristics and modeling of railway track system*, Ph.D. thesis, Department of Civil and Mining Engineering, University of Wollongong, 1997, Available at <https://ro.uow.edu.au/theses/1249/>.

- [Sandström and Ekberg 2009] J. Sandström and A. Ekberg, “Numerical study of the mechanical deterioration of insulated rail joints”, *Proc. Inst. Mech. Eng. F* **223**:3 (2009), 265–273.
- [Shi et al. 2012] J. Shi, A. H. Chan, and M. P. N. Burrow, “Influence of unsupported sleepers on dynamic responses of railroad embankment below a heavy haul railway line using simulation techniques”, in *Proc. of Rail Research UK Association Annual Conference*, 2012.
- [Varvani-Farahani 2000] A. Varvani-Farahani, “A new energy-critical plane parameter for fatigue life assessment of various metallic materials subjected to in-phase and out-of-phase multiaxial fatigue loading conditions”, *Int. J. Fatigue* **22**:4 (2000), 295–305.
- [Wang et al. 2009] W. J. Wang, J. Guo, Q. Y. Liu, M. H. Zhu, and Z. R. Zhou, “Study on relationship between oblique fatigue crack and rail wear in curve track and prevention”, *Wear* **267**:1-4 (2009), 540–544.
- [Wen et al. 2005] Z. Wen, X. Jin, and W. Zhang, “Contact-impact stress analysis of rail joint region using the dynamic finite element method”, *Wear* **258**:7-8 (2005), 1301–1309.
- [Yan and Fischer 2000] W. Yan and F. D. Fischer, “Applicability of the Hertz contact theory to rail-wheel contact problems”, *Arch. Appl. Mech.* **70**:4 (2000), 255–268.
- [Zerbsta et al. 2009] U. Zerbsta, R. Lundénb, K.-O. Edel, and R. A. Smith, “Introduction to the damage tolerance behaviour of railway rails – a review”, *Eng. Fract. Mech.* **76**:17 (2009), 2563–2601.
- [Zhang 2015] Z. Zhang, *Finite element analysis of railway track under vehicle dynamic impact and longitudinal loads*, Master’s thesis, Civil & Environmental Engineering, University of Illinois at Urbana-Champaign, 2015, Available at <https://www.ideals.illinois.edu/handle/2142/89060>.
- [Zhang et al. 2008] S. Zhang, X. Xiao, Z. Wen, and X. Jin, “Effect of unsupported sleepers on wheel/rail normal load”, *Soil Dyn. Earthq. Eng.* **28**:8 (2008), 662–673.
- [Zong and Dhanasekar 2012] N. Zong and M. Dhanasekar, “Analysis of rail ends under rail contact loading”, *Int. J. Mechan. Mechatron. Eng.* **6**:8 (2012), 1469–1477.
- [Zong and Dhanasekar 2014] N. Zong and M. Dhanasekar, “Experimental studies on the performance of rail joints with modified wheel/railhead contact”, *Proc. Inst. Mech. Eng. F* **228**:8 (2014), 857–877.

Received 18 Mar 2019. Revised 29 Jun 2019. Accepted 12 Aug 2019.

HOSSAM ELSAYED: hossam.mohamed91@eng.suez.edu.eg
Civil Engineering Departement, Faculty of Engineering, Suez Canal University, Ismailia 41522, Egypt

MOHAMED LOTFY: lotfytaha@cu.edu.eg
Aerospace Department, Faculty of Engineering, Cairo University, Giza 12316, Egypt

HAYTHAM ZOHNY: hnozohny@eng.asu.edu.eg
Public Works Departement, Faculty of Engineering, Ain Shams University, Cairo 11517, Egypt

HANY SOBHY: hanysobhyr@eng.asu.edu.eg
Public Works Departement, Faculty of Engineering, Ain Shams University, Cairo 11517, Egypt

SUBMISSION GUIDELINES

ORIGINALITY

Authors may submit manuscripts in PDF format online at the Submissions page. Submission of a manuscript acknowledges that the manuscript is original and has neither previously, nor simultaneously, in whole or in part, been submitted elsewhere. Information regarding the preparation of manuscripts is provided below. Correspondence by email is requested for convenience and speed. For further information, write to contact@msp.org.

LANGUAGE

Manuscripts must be in English. A brief abstract of about 150 words or less must be included. The abstract should be self-contained and not make any reference to the bibliography. Also required are keywords and subject classification for the article, and, for each author, postal address, affiliation (if appropriate), and email address if available. A home-page URL is optional.

FORMAT

Authors can use their preferred manuscript-preparation software, including for example Microsoft Word or any variant of \LaTeX . The journal itself is produced in \LaTeX , so accepted articles prepared using other software will be converted to \LaTeX at production time. Authors wishing to prepare their document in \LaTeX can follow the example file at www.jomms.net (but the use of other class files is acceptable). At submission time only a PDF file is required. After acceptance, authors must submit all source material (see especially Figures below).

REFERENCES

Bibliographical references should be complete, including article titles and page ranges. All references in the bibliography should be cited in the text. The use of Bib \TeX is preferred but not required. Tags will be converted to the house format (see a current issue for examples); however, for submission you may use the format of your choice. Links will be provided to all literature with known web locations; authors can supply their own links in addition to those provided by the editorial process.

FIGURES

Figures must be of publication quality. After acceptance, you will need to submit the original source files in vector format for all diagrams and graphs in your manuscript: vector EPS or vector PDF files are the most useful. (EPS stands for Encapsulated PostScript.)

Most drawing and graphing packages—Mathematica, Adobe Illustrator, Corel Draw, MATLAB, etc.—allow the user to save files in one of these formats. Make sure that what you’re saving is vector graphics and not a bitmap. If you need help, please write to graphics@msp.org with as many details as you can about how your graphics were generated.

Please also include the original data for any plots. This is particularly important if you are unable to save Excel-generated plots in vector format. Saving them as bitmaps is not useful; please send the Excel (.xls) spreadsheets instead. Bundle your figure files into a single archive (using zip, tar, rar or other format of your choice) and upload on the link you been given at acceptance time.

Each figure should be captioned and numbered so that it can float. Small figures occupying no more than three lines of vertical space can be kept in the text (“the curve looks like this:”). It is acceptable to submit a manuscript with all figures at the end, if their placement is specified in the text by means of comments such as “Place Figure 1 here”. The same considerations apply to tables.

WHITE SPACE

Forced line breaks or page breaks should not be inserted in the document. There is no point in your trying to optimize line and page breaks in the original manuscript. The manuscript will be reformatted to use the journal’s preferred fonts and layout.

PROOFS

Page proofs will be made available to authors (or to the designated corresponding author) at a Web site in PDF format. Failure to acknowledge the receipt of proofs or to return corrections within the requested deadline may cause publication to be postponed.

Journal of Mechanics of Materials and Structures

Volume 14, No. 3

May 2019

-
- Experimental and numerical energy absorption study of aluminum honeycomb structure filled with graded and nongraded polyurethane foam under in-plane and out-of-plane loading**
ALIREZA MOLAIEE and SEYED ALI GALEHDARI 309
- Transient thermal stresses in a laminated spherical shell of thermoelectric materials**
YUE LIU, KAIFA WANG and BAOLIN WANG 323
- Tuning the propagation characteristics of the trapped and released strongly nonlinear solitary waves in 1-D composite granular chain of spheres** BIN WU, HEYING WANG, XIUCHENG LIU, MINGZHI LI, ZONGFA LIU and CUNFU HE 343
- Accurate buckling analysis of piezoelectric functionally graded nanotube-reinforced cylindrical shells under combined electro-thermo-mechanical loads**
SHENGBO ZHU, YIWEN NI, JIABIN SUN,
ZHENZHEN TONG, ZHENHUAN ZHOU and XINSHENG XU 361
- Thermoelastic fracture initiation: the role of relaxation and convection**
LOUIS M. BROCK 393
- Development of fracture mechanics model of beam retrofitted with CFRP plate subjected to cyclic loading**
SHAHRIAR SHAHBAZPANAHI and HUNAR FARID HAMA ALI 413
- Assessment of degradation of railroad rails: finite element analysis of insulated joints and unsupported sleepers** HOSSAM ELSAYED, MOHAMED LOTFY, HAYTHAM ZOHNHY and HANY SOBHY 429



1559-3959(2019)14:3;1-V